Modélisation et contrôle d'une main anthropomorphe actionnée par des tendons antagonistes

Maxime Chalon

ParisTech
INSTITUT DES SCIENCES ET TECHNOLOGIES
PARIS INSTITUTE OF TECHNOLOGY

MINES ParisTech

École doctorale n°432 :
Sciences des Métiers de l'Ingénieur

Doctorat ParisTech

T H È S E

pour obtenir le grade de docteur délivré par

l'École nationale supérieure des mines de Paris

Spécialité «Informatique temps-réel, robotique et automatique»

présentée et soutenue publiquement par

Maxime CHALON

le 2 octobre 2013

Modélisation et contrôle d'une main anthropomorphe actionnée par des tendons antagonistes

∼ ∼ ∼

Modeling and control of an antagonistically actuated tendon driven anthropomorphic hand

Directeur de thèse : **Brigitte d'ANDREA-NOVEL**

Jury

Maxime GAUTIER, Professeur, Faculté des Sciences et Techniques, Université de Nantes	Rapporteur
Claudio MELCHIORRI, Professeur, Faculty of Engineering, University of Bologna	Rapporteur
Brigitte d'ANDREA-NOVEL, Professeur, MINES ParisTech	Examinateur
Markus GREBENSTEIN, Dr. Institute of Robotics and Mechatronics, DLR	Examinateur
Christian OTT, Dr.-Ing. Institute of Robotics and Mechatronics, DLR	Examinateur
Véronique PERDEREAU, Professeur, Université Pierre et Marie Curie	Examinateur

T H È S E

MINES ParisTech
Centre de robotique (CAOR)
60, boulevard Saint-Michel 75272 Paris cedex 06

Acknowledgment

To give acknowledgment to all the persons that supported this work is without a doubt a challenge on its own. I decided to list the people that helped under all forms, without specific order or importance. If you are missing, please be sure that it was not intentional. Thanks to: Brigitte d'Andreas-Novel for being my professor during this work. Jens Reinecke for the unbelievable number of hours spent in experimenting together. Werner Friedl for building all the test setups and designing the forearm. Alex Dietrich for correcting so well all the little details and for the discussion on the possible control methods. Thanks to Thomas Wimbock with whom I started at DLR and that supported me for my first papers. Markus Grebenstein for creating this fantastic system. Alin Albu-Schaeffer for giving me the chance of working in DLR and more generally to all the colleagues I have been discussing with.

Contents

List of Figures

List of Tables

Résumé

Ce chapitre résume les points importants de chaque chapitre de ce manuscrit.

Introduction

Pour commencer, une courte présentation de DLR ainsi que du récent système bras-main (appelé Hand Arm System) est donnée.

Ce nouveau système a la particularité d'être mécaniquement flexible. Cette flexibilité intrinsèque offre la possibilité de stocker de l'énergie à court terme et remplit ainsi deux fonctions essentielles pour un robot humanoïde: les impacts sont filtrés et les performances dynamiques sont augmentées. Dans cette thèse, on se concentre plus particulièrement sur la main. Chacun des 19 degrés de liberté est actionné par deux tendons flexibles antagonistes. La rigidité des tendons étant non linéaire il est possible, tout comme peut le faire l'être humain, de co-contracter les " muscles " et ainsi de modifier la rigidité mécanique. Il est donc possible d'ajuster la rigidité des doigts afin de s'adapter au mieux aux tâches à effectuer. Cependant, cette flexibilité entraine de nouveau défis de modélisation et de contrôle.

De nombreuses mains robotiques ont été développées au centre de robotique de DLR et dans d'autres laboratoires à l'international. Le système est unique à la fois par sa complexité, utilisant 42 moteurs et plus de 200 capteurs, et par sa construction mécanique unique. Les travaux publiés se concentrent majoritairement sur le problème de la répartition des forces internes ou alors du contrôle d'articulation flexible mais peu de travaux considèrent les deux problèmes simultanément. Les travaux sont présentés en deux parties. La première se concentre sur la modélisation tandis que la seconde concerne le contrôle. Autant que possible, des simulations et des mesures sont réalisées afin de vérifier la validité des hypothèses.

Modeling and identification

Cette première partie vise à établir des modèles mécaniques pour l'ensemble des sous-systèmes. Puisque le système comporte plus de 50 moteurs et 200 capteurs, une démarche *bottom-up* est utilisée.

Modeling approach

Les méthodes utilisées pour la modélisation sont présentées. La cinématique est construite grâce à des transformations homogènes. Pour le modèle dynamique deux approches principales sont présentées. Les avantages et désavantages de plusieurs méthodes sont discutés. Finalement, il est vérifié

que les termes représentant les forces de Coriolis et centrifuge peuvent être négligés.

Motor model

Le système utilise un total de 38 moteurs pour tirer et relâcher les tendons. Il est important de disposer d'un modèle précis du comportement des moteurs afin de pouvoir contrôler les forces ou les positions des tendons. Un modèle des frottements périodiques générés par l'engrenage harmonique est établi et il est montré qu'un compensateur permet de réduire sensiblement les vibrations.

Tendon model

Les articulations sont actionnées par des tendons flexibles. Le déplacement et la force d'un tendon sont mesurés par un capteur magnétique placé sur le ressort. Le ressort est linéaire mais est placé dans un mécanisme générant une relation non linéaire. Le mécanisme est modélisé et des mesures sont effectuées pour sélectionner les paramètres du modèle.

Finger model

La structure mécanique des doigts est similaire à l'exception du pouce et de l'articulation distale de l'annulaire. Le chapitre propose un modèle cinématique pour chacun des doigts. Les équations qui permettent de transformer les forces et les positions des tendons pour obtenir le couple et la rigidité de l'articulation sont établies. Les articulations des doigts ne disposent pas de capteur, cependant puisque huit tendons sont utilisés pour actionner quatre articulations, un algorithme est nécessaire pour évaluer la position des doigts à partir du déplacement des tendons. Le cas spécial du pouce est présenté car l'insertion des tendons est différente afin de produire une force suffisante pour s'opposer aux autres doigts. La relation géométrique non linéaire entre le déplacement des tendons et le déplacement des articulations requière un algorithme particulier. L'algorithme est présenté accompagné de simulations visant à estimer sa vitesse de convergence.

Wrist model

L'ensemble des tendons est guidée au travers du poignet. Cependant, puisqu'il est mécaniquement impossible de faire passer tous les tendons par un unique centre de rotation, un déplacement du poignet implique un déplacement des tendons. Si le déplacement n'est pas compensé, un mouvement des doigts est perceptible. La modélisation de la cinématique du poignet est présentée étape par étape. Finalement, des mesures sont effectuées et comparées aux simulations.

Control

La seconde partie utilise les modèles pour établir les lois de contrôle. Les premiers chapitres présentent deux problèmes spécifiques aux systèmes actionnés par tendons. Ensuite, un régulateur pour la force des tendons est développé et expérimenté. Dans un premier temps, un contrôleur pour la force des tendons est construit. Ensuite, similaire aux approches proposées dans la littérature, un contrôleur en cascade, basé sur le régulateur de force des tendons, est présenté et analysé. Afin de s'affranchir de l'hypothèse de cascade, une approche classique de placement de pôles est envisagée. Le choix des gains étant une étape critique pour un système avec 38 moteurs, une méthode de contrôle optimal basé sur les équations de Riccati est proposée. Puisque que le système est non linéaire, la méthode SDRE (State Dependant Riccati Equation) est utilisée. Les méthodes proposées jusqu'à ce point sont linéaires ou du moins, motivées par une approche linéaire. Afin d'explorer de nouvelles possibilités, une approche strictement non linéaire est exposée. La méthode porte le nom de backstepping. Finalement, la question du choix des gains pour le backstepping est détaillée et une méthode est proposée pour automatiser ce choix.

Tendon force distribution

Comme pour la majorité des systèmes actionnés par tendons, il est primordial de s'assurer que les forces des tendons restent bornées. Dépasser la force maximale admissible augmente le risque de rupture. Inversement, une force trop faible augmente le risque qu'un tendon quitte ses guides. Dans un système actionné par des tendons antagonistes flexibles, il existe une infinité de combinaison de forces qui produisent les mêmes couples. Il est possible d'ajuster la rigidité mécanique du système en modifiant les forces internes. Le chapitre présente plusieurs formulations du problème et discute plusieurs méthodes permettant de distribuer les forces.

Stiffness correction

Les tendons étant flexibles, ils apportent une flexibilité mécanique aux doigts. De plus, en pratique, un contrôleur d'impédance est utilisé pour augmenter les possibilités d'ajustement. Cependant, puisque la flexibilité mécanique et la flexibilité apportée par le contrôleur sont connectées en série, l'utilisateur perçoit une combinaison des deux. Le chapitre modélise cette connexion et propose un contrôleur adaptatif afin de produire la flexibilité désirée par l'utilisateur.

Joint torque observer

Aucun capteur n'est placé en dehors de l'avant bras ce qui confère aux doigts une excellente robustesse. Ils sont à la fois résistants aux impacts et insensibles à la poussière et à l'humidité. En contre partie, les frottements induits par les articulations et qui ne sont pas mesurés, réduisent la sensibilité des doigts. Il est possible d'estimer les frottements des articulations en ajoutant des capteurs de contrainte sur la structure des doigts. Il est ainsi possible d'analyser la contribution des frottements des articulations et d'estimer les gains possibles par une amélioration des articulations.

Tendon control

Bien que de nombreuses approches soient disponibles, la plupart des contrôleurs sont basés sur un contrôle de la force des tendons. Ce chapitre établi plusieurs lois de contrôle pour la régulation de la force des tendons. Puisque la rigidité des tendons est non linéaire, la réponse d'un contrôleur linéaire dépend du point de fonctionnement. Une modification du contrôleur, inspirée par la méthode de " Gain Scheduling " est proposée et les expériences confirment que la méthode est effective.

Two time scale approach

La méthode la plus directe pour créer un contrôleur d'impédance pour les articulations consiste à considérer deux problèmes indépendants. Le premier consiste à calculer un couple de référence pour les articulations, tandis que le second consiste à générer les forces correspondantes pour les tendons. La stabilité du système est simple à prouver s'il est admis que les échelles de temps sont suffisamment différentes. Les échelles de temps dépendent de la rigidité mécanique du système et donc la validité de l'approche dépend des contraintes internes. Une analyse plus complexe grâce à la théorie des systèmes en cascade permet de garantir la stabilité en contrepartie d'un choix plus difficile des matrices de gains.

Pole placement

Pour des systèmes d'ordre élevé, il est difficile de choisir les gains de retour d'état. Dans le cas d'une approche linéaire il est possible de placer les pôles du système afin de garantir sa stabilité. Il suffit pour cela de choisir les gains pour obtenir des parties réelles négatives pour les pôles. Bien que théoriquement correct, la méthode ne prend pas en compte les limites réelles du système tel que les délais de calculs, le bruit de mesure ou encore la saturation des actionneurs. En conséquence, la méthode est délicate à utiliser car des pôles peu réalistes nécessitent une action de contrôle impossible à réaliser.

Optimal control

Le chapitre étudie la question du choix des gains en utilisant des résultats de contrôle optimal. Grâce aux équations de Riccati il est possible d'obtenir les gains optimaux pour le contrôle du système linéaire.

State-Dependent Riccati Equation

Les équations de Riccatti ne s'appliquent qu'à des systèmes linéaires. Néanmoins, une extension aux systèmes non linéaire a été proposé sous le nom de State-Dependent Riccati Equation. Elle consiste à linéariser le système en tout point et à appliquer la méthode de Riccati. Des simulations sont présentées pour évaluer le gain de performance par rapport à la méthode de Riccati utilisée pour le système nominal.

Backstepping

Le backstepping est une méthode de contrôle non linéaire pouvant s'appliquer à une large gamme de systèmes. Elle présente l'avantage de ne pas nécessiter de linéarisation et permet d'établir la stabilité du système en boucle fermée. Un contrôleur d'impédance est souhaité pour les articulations et donc le backstepping est modifié pour produire le comportement attendu. La méthode est appliquée pas à pas à des systèmes de plus en plus complexes. La stabilité est établie par construction au travers d'une fonction de Lyapunov. Des expériences et les simulations correspondantes sont présentées et attestent de l'applicabilité de la méthode. Finalement, la méthode est appliquée à une articulation antagoniste et des mesures confirment qu'un contrôleur d'impédance est obtenu et a une performance supérieure aux contrôleurs précédant.

Optimal Backstepping

Le contrôleur de backstepping a une très bonne performance mais, tout comme le placement de pôle, est difficile à paramétrer. Le chapitre propose d'identifier les gains du contrôleur à ceux d'un contrôleur d'état optimal. Le résultat est une méthode permettant de sélectionner automatiquement les gains en fonction de matrices de coût.

Conclusion

Le Hand Arm System est un nouveau système qui permet d'explorer de nouvelles méthodes de manipulation de par sa robustesse et son dynamisme. Le travail présenté dans ce manuscrit s'est concentré sur la main et le poignet.

Il couvre la modélisation et le contrôle. De nombreuses expériences et simulations sont présentées et il est montré que des méthodes non linéaires peuvent être appliquées afin de maximiser les performances.

1 Introduction

1.1 DLR

The work presented in this thesis is realized at the Institute of Robotics and Mechatronics of the German Aerospace Center (Deutsche Luft and Raumfahrt DLR). The institute focuses on research in the field of robotics, ranging from industrial robot control to innovative biped platform and targets service robotic applications as well as space robotics. About 300 reseachers and students are working on mechanical design, electronics, control, perception, and planning. The institute is located near Munich (Oberpfaffenhofen) in Germany (cf. Fig. 1.1).

Figure 1.1: Aerial View of the DLR site in Oberpfaffenhofen (courtesy of DLR)

1.2 The Hand Arm System

The Hand Arm System (cf. Fig. 1.2) is composed of an arm, a wrist and a hand [1]. The arm has five degrees of freedom[1] (DoFs) for the arm motion and five DoFs for the adjustement of the stiffness, thus actuated by a total of 10 motors. The wrist is actuated by four motors, in a helping antagonism configuration [2], and provides 2 DoFs of motion and 2 DoFs of stiffness. Finally, the hand is composed of 5 fingers and 19 joints, with 4-4-4-3-4 DoFs of motion (and 4-4-4-3-4 DoFs for adjusting the stiffness), actuated by 38 motors located in the forearm. The motor motion is transferred to the finger joints by tendons. A tendon is routed through a pulley/spring mechanism that provides a mean to adjust the joint stiffness by changing the tendon pretension [3]. Similarily, all joints of the arm are equiped with nonlinear spring mechanism, thus are able to modify the arm mechanical

[1] In robotics, the number of degree freedom is the mininal number of parameters needed to describe the geometric configuration of a system.

stiffness. The system is the basis for a new generation of humanoid robots.

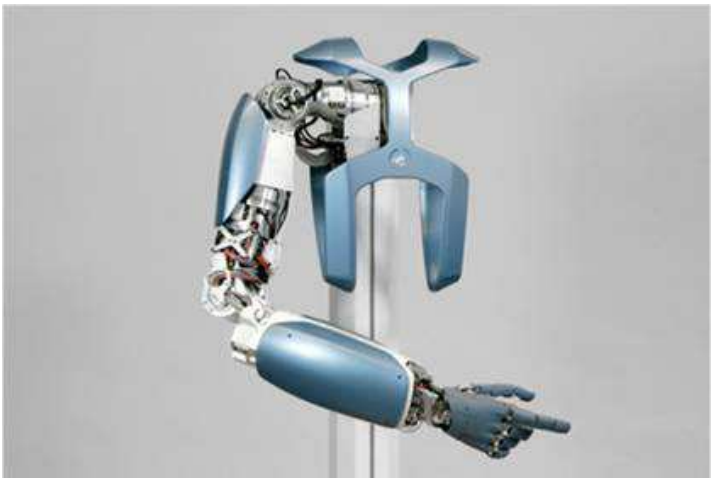

Figure 1.2: General View of the System

Not only it is looking human in size and shape, but it can also compete with the human in terms of force, accuracy and speed. The design and the realization of a system of such a complexity was only possible because of the very high integration of all components and a tight collaboration between the team members. From the concepts to the final system, the entire robot has been design and manufactured in DLR, ensuring the quality and the fit of all components.

1.3 Motivation

1.3.1 Robustness

It seems that several major challenges in robotics such as grasping, manipulation and mobility are still not tackled because the robustness of robots is often too limited. Considering the fact that the failure rate increases with the robot complexity, the number of parts and the diminution of part size, it is not surprising that hands are often in need for maintenance, severely restricting the operational time and the associated progress. One of the major targets of the development of the Hand Arm System is to develop a humanoid robotic system that is able to operate in a partially unknown environment, which poses strong demands on the robustness of the design. Hard collisions with other objects are unavoidable and the successful operation of such a system is strongly related to the ability to withstand those collisions, and impacts, without severe damage or functional impairments.

Generally, the system complexity of robotic systems has been drastically increasing, simultaneously rising the risk of system failure. A single colli-

sion during operation may lead to a significant maintenance time and the associated costs. Therefore, application developers have to be conservative when testing new methods and strategies. This slows down progress and hardly gives a chance to develop radically different control/motion planning strategies. In robotic hands, the impact tolerance plays an even more dominant role than in robot arms since during grasp acquisition or tactile exploration, the fingers are strongly exposed and a fragile hardware simply prohibits many strategies.

The elasticity in the fingers increases the robustness. An experiment showing how the fingers resisted to the impact of a hammer hit has been realized. In a similar fashion, the arm has been hit by a baseball bat and the joints accelerations were recorded. The measurements demonstrated that, without the mechanical compliance, the system could not continue operating (the impact exceeds the gear box peak load capability). Those experiments have a good media impact, moreover, they demonstrate that the *fragility* of non-industrial robots can be greatly improved without significant increase in weight, size or cost (often at the expense of control complexity). Several videos demonstrating the robustness of the system have been released on public media platforms such as YouTube (e. g. YouTube: Robot Arm Using a Hammer).

1.3.2 Dynamics

Interesting to notice, is the fact that the dynamic capabilities of current state-of-the-art robots are not comparable to human capabilities in terms of speed at the same inertial properties [4]. Particularly in cyclic tasks (e. g. running) or highly dynamic tasks (throwing, kicking), the energy the actuators can provide during peak loads without getting too bulky and heavy is not sufficient. In contrast to the classical *stiff robots*, elastic actuation can generate more output power, for a short time, than the maximum motor power. It enables to consider an entirely new set of mechanical designs, motion control schemes, and control strategies. For example, by explicitly controlling the potential energy that can be stored in the joint and transforming it to kinetic energy, i. e. link speed. This explicit use of the elasticity for highly dynamic motions constitutes a major step for equipping service robots with human like motion capabilities. Some initial work done in [5–7], identified this property and used it on a rather conceptual level. More recently, several control schemes were proposed to explicitly maximize the dynamic range of variable stiffness robots [5, 8–10].

These recent works show very promising results that pose several new research questions; How to optimize the control to maximize the power output during explosive motions (e. g. throwing a ball), how to damp the oscillations resulting from the low mechanical stiffness, and how to set the stiffness in order to achieve energy efficient motions. The, short term, energy storage

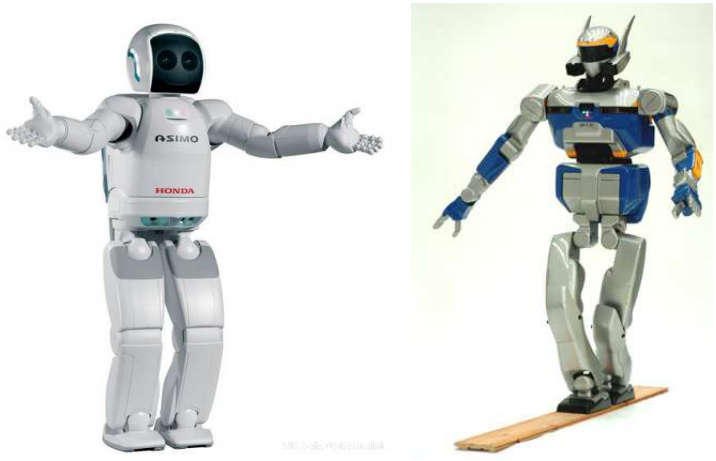

(a) Asimo (b) HRP II

Figure 1.3: Left: Humanoid Asimo from Honda. Right: Second version of the HRP humanoid from Kawada Industries

capabilities may fundamentally change the motion generation paradigms. Elasticity is a mean to control oscillatory behavior explicitly and not only a desirable feature for high bandwidth compliant behavior.

1.4 State of the art

This section presents a state of the art of humanoid robotics. First humanoid robots are presented along with their most important characteristics. In a second point, the focus goes to the robotic hands that have been designed. Ranging from designs close to the two jaw grippers up to the more advanced anthropomorphic hand designs. Design methods and grasps planning references are given. The third point concentrates on the design, selection, and evaluation of serial elastic elements and adjustable stiffness mechanisms. Finally, the fourth point presents control approaches. Several of the approaches are implemented and evaluated in the control part of the thesis.

1.4.1 Humanoids

Well-known humanoid robots like Honda's Asimo (cf. Fig. 1.3a, [11]) or the HRP 2 developed by Kawada Industries (cf. Fig. 1.3b, [12, 13]) are two examples of robots with rigid joints and links.

There is only a rather limited number of complete humanoids (that is with legs and arms) because of the complexity of building a lightweight structure that still moves fast enough to allow for proper control (e. g. bal-

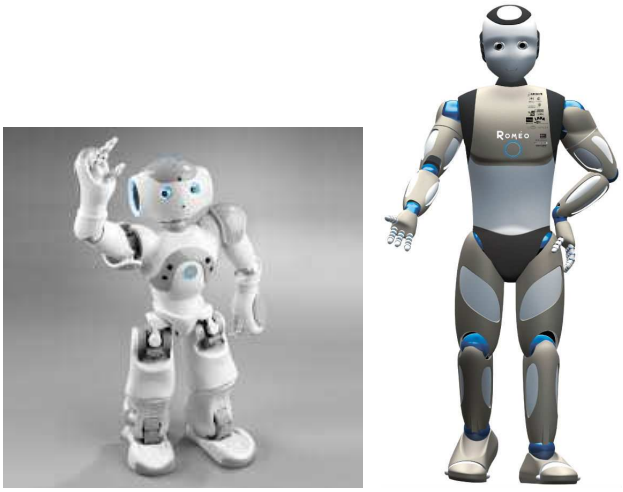

(a) Nao (b) Romeo

Figure 1.4: Left: Nao, a small (50cm) humanoid robot from Aldebaran Robotics. Right: Romeo, a large scale (1.43m) version of Nao presented in 2012.

ancing). Moreover, the robustness of these systems regarding collisions is low, requiring very cautious operation and planning.

One the contrary, there exist numerous platform that have been developed to study two arms control such as the humanoid upper body Robonaut and the manipulation platform Justin (cf. Fig. 1.6a, cf. Fig. 1.6b). Many upper body humanoid projects are eventually mounted on a wheeled platform. The main reason is that mobile platforms are able to carry large loads and their control is well understood. Moreover, their limited capabities in outdoor environment are not a severe drawback since indoor applications are representing a large market (eg. household, worker assistance). Robots with mobile platform are becoming increasingly important, e. g. in the context of healthcare assistance (cf. Fig. 1.5). A very important community is growing around the platform PR2 developed at Willow Garage.

Finally, there exists a catergory of robots dedicated to entertainment or teaching (cf. Fig. 1.4a). Despite their limited payload that prevents them from doing much more than moving themselves, they are commercially available system that are getting increasingly popular. They allow to develop software such as artificial intelligence, navigation, or vision processing, without the time consuming part of developing hardware.

In general, the systems are fragile and are not meant to withstand impacts. Therefore, several systems increased their tolerance to impacts by introducing serial elastic actuators. One good example is the Robonaut R2 that uses serial elastic actuators (SEA) to increase its robustness to impacts.

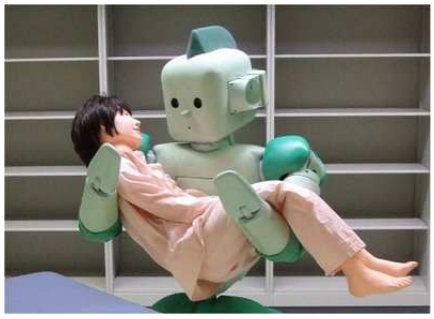

Figure 1.5: Ri Man, a health care robot designed by Riken in Japon

(a) Robonaut

(b) Justin

Figure 1.6: Two upper humanoids, left: Robonaut is developed by NASA/JPL [14]. Right: Justin is developed by DLR

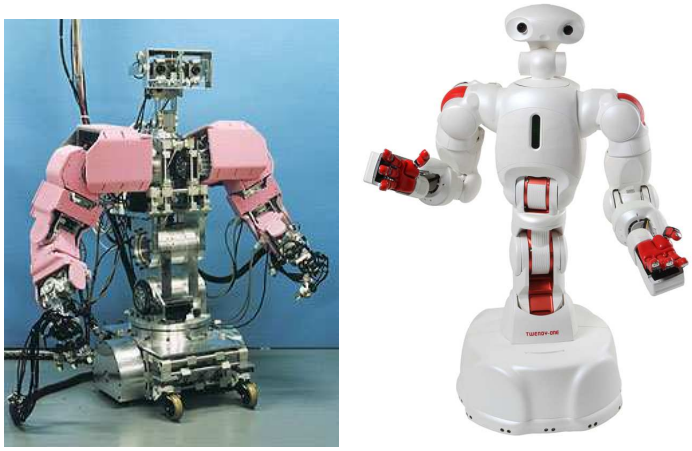

(a) Wendy (b) TwendyOne

Figure 1.7: Wendy, one of the first humanoid robot with adjustable stiffness in the joints. TwendyOne is the succesor of Wendy, its stiffness elements have been removed to gain space.

It is interesting to notice that, by using a spring mechanism, the position difference between the input and output of the mechanism provides a measure of the joint torque without any strain gauges. The use of flexible joints poses the question of the choice of the appropriate stiffness. Intuitively, there exist stiffness settings adapated to each task (e. g. precision picking vs. ball throwing). One solution is to use a brake to bypass all, or part, of the spring. An other solution is to introduce a second, smaller, actuator to adjust the stiffness. The Waseda robot Wendy (cf. Fig. 1.7a, [15]) is considered to be the first humanoid with slowly adjustable mechanical joint stiffness. In the subsequent version, TwendyOne, the adjustability was removed in order to save space in the arms (cf. Fig. 1.7b, [16]). The Hand Arm System includes nonlinear elements, in the arm an adjuster motor is used. For the lower arm rotation, a helping antagonism configuration is used. Finally, in the fingers, an antagonistic configuration is used.

1.4.2 Hands

The design of a robotic hand is a great challenge since it requires a large number of degrees of freedom integrated in a reduced space. Maybe motivated by the human hand amazing skills, many robot hands have been developed in the last three decades. They are ranging from the most simple two jaw grippers to the most advance hand equiped with five fingers and precision sensing.

The first designs of robotic hands used tendons to remotely actuate the

finger joints. The Utah-MIT hand is one of the first robot hand designed with two tendons attached to each joint to tackle the issue of slack (cf. Fig. 1.8a, [17]). The fingers of the JPL/Stanford hand are using a $N + 1$ configuration[2] in order to reduce the number of tendons (cf. Fig. 1.8b, [19]).

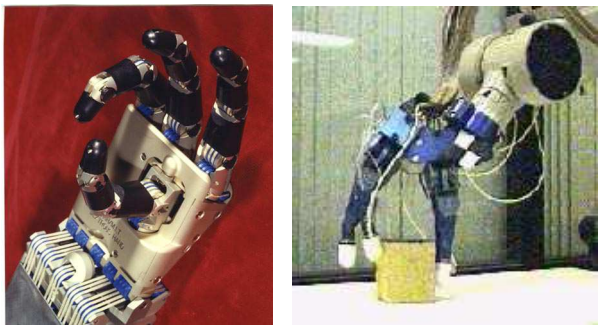

(a) Utah-MIT hand (b) JPL/Standord, N+1 tendon driven hand

Figure 1.8: Two early tendon driven hands

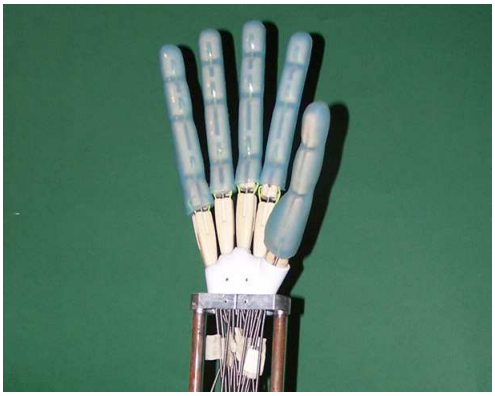

Figure 1.9: Third version of the University of Bologna hand (UB3). Sheaths are used to give the tendons.

Tendon driven robot hands, e. g. the UB Hand III, have been presented that use sheath-guided tendons, however with the drawback of introducing a large amount of friction into the system (cf. Fig. 1.9, [20, 21]).

[2]The minimum number of tendons to indenpendently move n joints is $n + 1$. It is proved that using more than $2n$ tendons is necessarily redundant. A finger using $n + 1$ (resp. $2n$) is commonly referred to as a $n + 1$ tendon configuration (resp. $2n$ tendon configuration). However, between $n + 1$ and $2n$ the number of tendons can simplify the design, or can create interesting couplings [18].

Figure 1.10: Dexhand a space qualifiable hand from DLR

The main reason for the use of tendon, at that time, was that it was impossible to integrate the drives within the hand or in the joints. The advances in mechatronics such as gear box size reduction, power density increase, communication speed increase and, generally, increased availabilty of computation power allowed to build modular hands that integrate the whole drive system within the hand, e. g. the DLR Hand II [22] and the TwendyOne hand [16]. More recently, the Dexhand, an outer space qualifiable dexterous hand was presented (cf. Fig. 1.10, [23,24]). The drives of the Dexhand are in the palm and the power and control systems are housed in the wrist. However, despite the progress of mechatronics, the size of those robotic hands is still larger than their human counterpart. In order to reach human like fingertip force and maintain a short wrist (that improves manipulability), the 38 drives of the hand of the Hand Arm System are located in the forearm.

The Robonaut R2 also contains serial elastic actuators. Furthermore, it is equipped with dexterous hands that are remotely actuated in the forearm [14]. The hands of the Obrero robot are using low mechanical impedance and serial elastic actuators to detect contact and conform to the grasped objects. The hands of the iCub are smaller than human hands and tendon driven. It is a completely open source platform created at the Italian Institute of Technology (IIT).

The humanoid Kenta with a tendon driven spine was developed to be more human like than other humanoids [25] and more recently the robot Kojiro was built that consists of 109 tendon drives (cf. Fig. 1.11, [26]). Underactuation is primarily studied in the field of robotic protestics. Indeed, the limited control input and the maximum allowed weight leads to a reduction of the number of actuators. Systems like the cyberhand [27] or the Ottobock prosthesis [28] have been designed to be robust and used easily by the amputee while providing appropriate cosmetic appearance.

Beside these humanoid systems, bio-inspired robotic hands replicating the anatomy of the human hand have been proposed. The anatomically

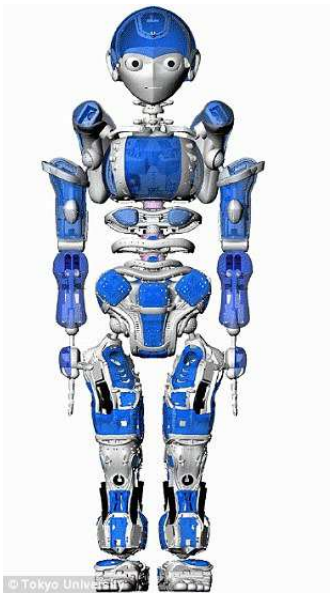

Figure 1.11: Kojiro

correct testbed (ACT) Hand [29] and the Shadowhand [30, 31] are both tendon driven hands. The ACT Hand focuses on the one-to-one copy of the human tendon kinematics. The Shadowhand is based on either pneumatic muscles or DC motors. Both are driven by an external actuation unit, not integrated in a hand-arm system. They both have a limited maximum fingertip force and remain fragile w. r. t. impacts.

The kinematic structure is the most important design choice and one of the key challenges in robot hand design. A large number of kinematics, mainly based on empirical results, can be found. They are mostly designed to fit the special needs of existing robot hands like data glove calibration or animation purpose [20].

Alternatively, kinematics can be derived from the analysis of human kinematics. In [32], Giurintano and Hollister developed a five link kinematics for the thumb based on cadaver analysis to reproduce the motion of the human thumb as close as possible. Stillfried measured the kinematics of a human hand using MRI[3] data and segmentation algorithms to extract the bones motions and therefore the hand kinematics. The institute of Ergonomics of the technical university of Munich synthesized a kinematic model of the whole human body to realize the *RAMSIS* system[4].

Optimization is another promising but complex mean to derive hand kinematics. Santos and Valero-Cuevas [33] modeled the kinematics of Giur-

[3]Magnetic Resonance Imaging

[4]The RAMSIS model is used mainly to realise ergonomic interfaces, e. g. in automobile industry.

intano and Hollister using DH-parameters and optimised these using cadaver test data from [32] and Monte Carlo Simulation. They optimised the found kinematics using Markov Chain Monte Carlo Simulation within a space of 50 parameters [34].

Once the kinematics is obtained, or during its optimization, it can be evaluated by using several approaches. Examples of such methods are:

- mathematical criteria
  - manipulability ellipsoids [35, 36]
  - dexterous workspace [37]
  - grasp stability [38]
- evaluation tools
  - graps planners
  - experiments

Miller and Allen developed a complete simulation environment : GraspIt! It can, among other things, simulate hands in contact situations and determine grasp quality indices [39]. A motion planning software developed by Rosen Diankov [40] provides a number of metrics calculation that can be used to rank the grasps. Thus, used on a large number of grasps, can be indirectly used to evaluate the quality of the kinematics.

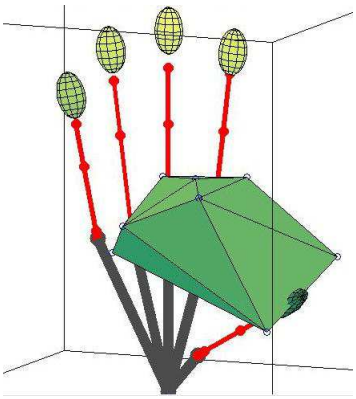

Figure 1.12: Workspace analysis for the thumb of the hand of the Hand Arm System [41].

1.4.3 Soft robotics

The design of the Hand Arm System is mainly driven by the insight that todays humanoid robot systems are not robust enough to be operated in unstructured environments, where collisions cannot be avoided. This lack

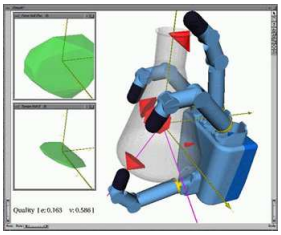

Figure 1.13: Simulation tool for grasp evaluation: GraspIt!

of robustness slows down the development of applications in particular using methods that require unsuccessful tasks such as reinforcement learning. Therefore, it seems that

future robotic systems have to be able to store energy

to meet these requirements [42].

In the recent years a lively discussion about the motivation of variable stiffness robots has been led debating their advantages and disadvantages with respect to human interactions and especially safety (e. g. *STIFF* and *THE* European projects).

In the design of serial elastic actuators the trade-off between robustness/mechanical compliance and task performance/mechanical stiffness has to be fixed. In order to postpone this decision, variable stiffness actuators have been proposed [43–49]. More recently, a European project *VIACTORS* was conducted to evaluate the state of the art concerning the variable stiffness actuators. A valuable output of this project was the definition of a specification datasheet for variable stiffness mechanisms (cf. Fig. 1.14).

Using the specification sheets of the mechanisms it is possible to compare, at least globally, the mechanisms. A few of those mechanisms are depicted in Fig. 1.15a, Fig. 1.15b, Fig. 1.15, Fig. 1.16a , and Fig. 1.16b.

Control This section gives an overview of the work done in the last decades in terms of control for nonlinear flexible joints. The references are organized in the same order as the control sections.

The use of tendons to actuate the fingers has a number of advantages. However, because tendons can only pull, it is critical to maintain a minimum pulling force on all tendons to avoid issues related to tendon slack. Early work on tendon driven mechanism was introduced in the field of manipulation [50] and formalized by Kobayashi [18]. He proposed a number of definitions for the properties of tendon driven systems, such as tendon controllability and tendon redundancy. In [51], tendon driven mechanisms are studied with the help of oriented graphs.

More recently, in the context of the development of the Hand Arm System, work on the stiffness and torque workspace of tendon driven mecha-

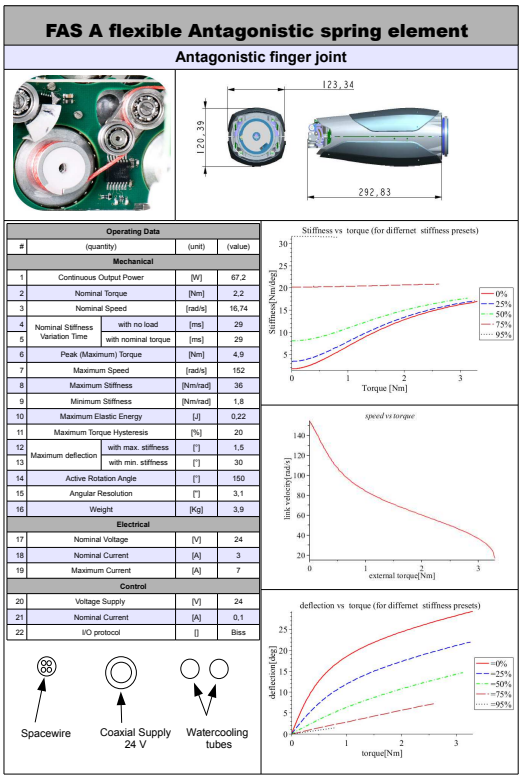

Figure 1.14: Datasheet format created in the VIACTOR project. Example of the tendon mechanism used in the hand of the Hand Arm System (FAS).

nism with nonlinear flexible elements was presented in [41]. Similar work on the achievable Cartesian stiffness of flexible joint robot is found in [52]. In [53, 54], it is shown that the tendon force distribution problem can be simplified if the tendon stiffness is linear in the tendon force. In [55], experimental work on the implementation of the tendon force distribution algorithm was reported.

In case of small size robots, the friction plays an important role. Unfortunaly, due to the system size and low serie production, the accurate identification of friction is not a simple task. A complete parameter identification method developed for the LWR (Light-Weight Robot) is presented in [56]. Offline identification methods are time consuming and, often, require assumptions on the friction model [57]. If link side torque sensing is available, it is possible to build an online stiffness observer [58]. Moreover, it is shown in [59] that the joint stiffness can be estimated online.

(a) FSJ

(b) FAS

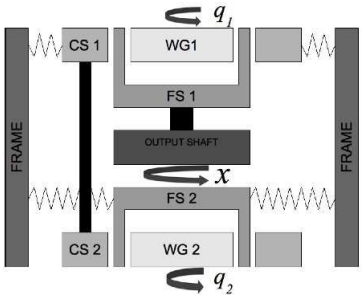

Figure 1.15: VSA-HD.

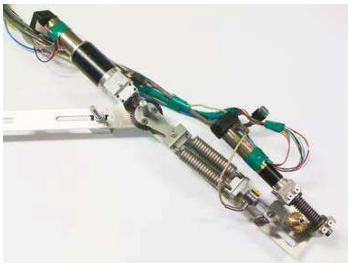

(a) Macceppa

(b) AWAS II

When considering flexibility in robots, two main branches are considered. Flexible link control, where the links themselves are flexing under external loads such as gravity, and flexible joint control, where the links are rigid and the joints have a flexible behavior. Most of the publications about flexible joint control deal with flexibility introduced by the drive train. Consequently, most of the papers are stiffness/inertia ratios that are several orders of magnitude higher than in the case of the Hand Arm System. When the joint deflection of a robot due to its own weigth is large, the local approximation of the Jacobian are not valid and it becomes challenging to derive global controllers [60]. The, usually simple, gravity compensation is not neccessarily simple since the joint stiffness needs to fullfill new conditions [61, 62] (intuitively, the stiffness should be stronger that the gravity field). The design of traking controller for flexible joint robots has been reported in [63, 64]. The application of flexible joint control to the active damping of an light weight robot is reported by A. Albu Schäffer in [65, 66].

Extensive work on the impedance control of redundant flexible joint robot has been done by Ott in [67, 68]. Between 1990 and 2000, passivity based control of flexible joint system was considered in [69, 70] as well as for a more general class of systems [71–73]. Passivity based control is applied to hand control in [74], and to telemanipulation in [72,75,76]. Damping control for highly flexible robots is considered in [77], where a feedback is used to decouple the dynamics by double diagonalization, compute a proper damping with a pole identification method and apply the controller in the original coordinates.

Impedance control [78] and admittance control [79] have both been applied to tendon control systems. The goal is usually to provide compliance to help in case of inaccuracies in the models or in the sensors. Controllers are used to provide a tendon compliance or to provide a link compliance. In both cases the sensing of the tendon force is required. The Robonaut research group has published serveral papers on the control of the, not antagonistically, tendon driven fingers [80, 81]. Control of a joint driven by antagonistic tendon is presented in [82]. Work on the modeling and control of the hand of the University of Bologna is reported in [83].

Several nonlinear control methods have been applied to the control of flexible joint control. Examples of such methods are: feedback linearization, Lyapunov redesign, backstepping or sliding mode control. This thesis uses the backstepping method as described in [84, p.489]. In [68, 85], the method is applied to flexible joint control, however limited to the case of linear stiffness and non-antagonistic actuator configurations.

Generally, optimal control method are challenging to implement in real-time, unless closed form solution can be obtained (e. g. optimality of the bang-bang control for some problems [86]). Direct methods to solve the optimal control problem are reported as early as 1960 (cf. [87]). It has been applied to a very large variety of offline optimization problem such as space

shuttle trajectory, ship maneuver or throwing problem [88]. However, expect for simple cases, the equations can not be solved analytically and do not give any further insight on the required inputs. Numerical methods are required to construct solutions. Unfortunatly, they require forward and backward integrations and are generally extremely expensive to compute.

An intermediate way between the linear optimal control (Riccati equations) and the optimal nonlinear control (HBJ equations), has been proposed around 1962 by Pearson [89] under the name of State Dependant Riccati Equation (SDRE). It has been expanded by Wernly [90] and popularized by Cloutier [91–95]. The method is an intuitive extension of the Algebraic Riccati Equation, applied to a pointwize linearized system. Existance of a SDRE stabilizing feedback is discussed in [96]. The method offers only limited theoretical results for global stability (an excellent survey is provided in [97]) but proved to be effective in practice.

1.5 Organization of the work

The Hand Arm System is a major development achieved by a team of about 20 persons. Thus, parts of the system have been presented in different conferences and journals [1, 3, 98]. The work of this thesis is divided into two main parts: the **modeling** and the **control**. Figure 1.16 depicts the organization of the works and the logical links between the different chapters.

1.5.1 Modeling

The **modeling** part intends to present the hand of the Hand Arm System in details and constructs, step by step, a kinematic and a dynamic model of the motors, the tendons, the springs, the fingers and the wrist. It follows a bottom up approach and thus starts with the motors.

First, a motor model is proposed and verified with a set of identification experiments. Due to their very small size and their high gear ratio, the motors have significant friction. The identification and compensation of the frictional effect is proposed and experimentally verified.

Next, the tendon actuation and the nonlinear spring elements are introduced. The nonlinear spring mechanism is modeled and, similar to the motor modeling, a set of simulations and experiments are carried out to verify its validity. Because the tendon force measurements are performed into the forearm, the friction introduced by the guidings from the fingers to the spring mechanisms is critical. A deep understanding of the friction behavior is paramount to the proper operation of the fingers. Therefore, a set of measurements with different pulley materials, grove shapes, tendon material and sliding surfaces is performed in order to establish a model. Although the system is already built, the precise knowledge of the influence of the different parameters allows to verify the calculated values. The results

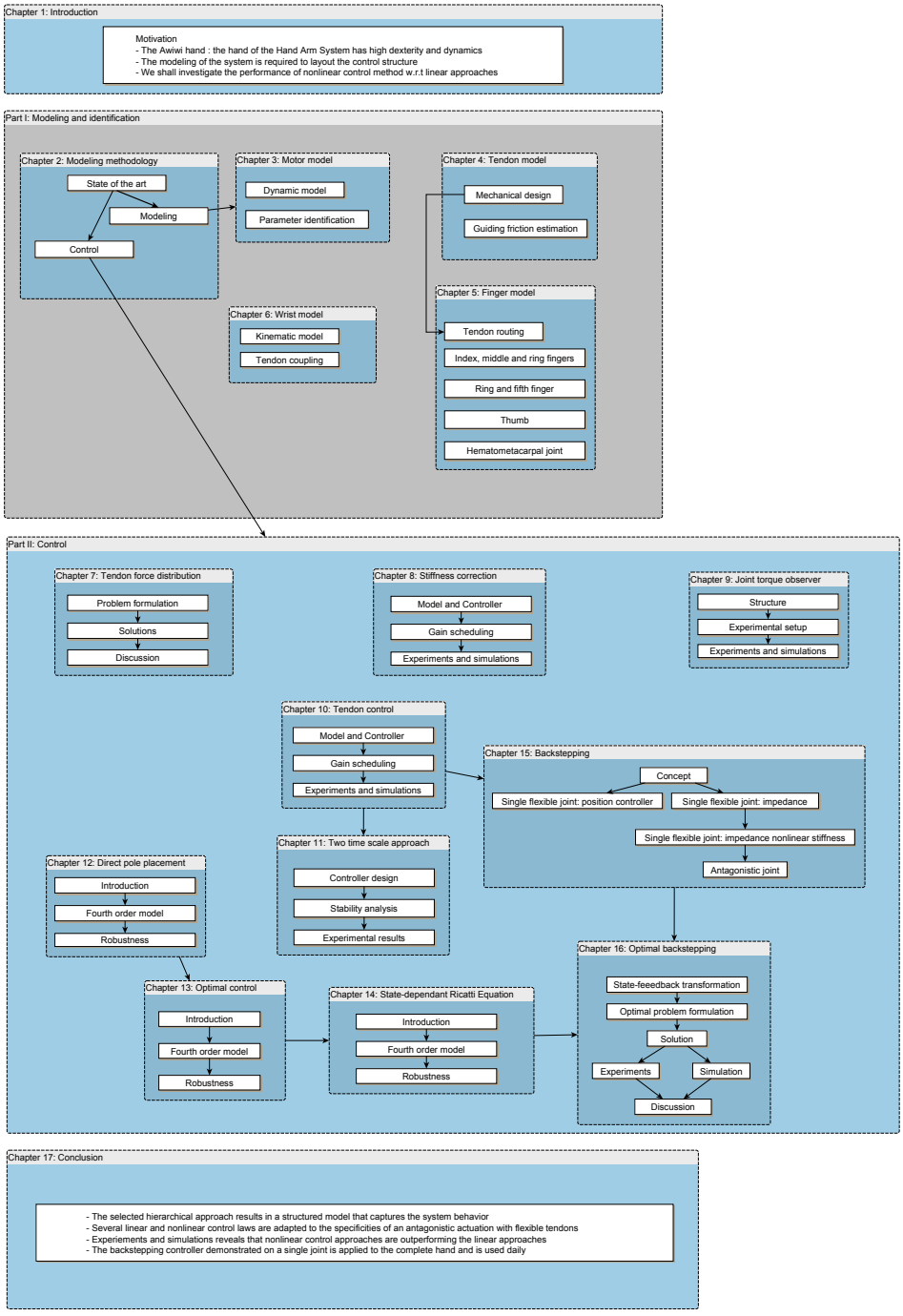

Figure 1.16: Overview of the structure of the thesis

are a very important tool for the mechanical designers that are seeking a continuous improvement of the system.

The kinematics and the dynamics of the fingers are similar to the case of a serial robot. The kinematics of the finger actuation, from the motor displacements to the fingertip frames are derived using homogeneous transformations. The Lagrange and the Newton-Euler methods are presented. A short discussion of their respective strength is given. Simulations are performed to highlight the fact that the Coriolis and centrifugal effects are negligible (at the considered speeds). It does confirm that the governing factor is the mass matrix. The fingers are moved by moving the tendons. Therefore, it is necessary to establish the relationship between the motor motion and the joint motion. The specificities of each fingers are treated in dedicated sections. The fingers have no electronics or cables, conferring them an impressive robustness, it implies however that the link position must be estimated. In the case of the finger, a possible solution is to use a pseudo inverse of the coupling matrix. The thumb actuation is using a tensegrity structure (uncommon for robotic hands) that provides good strength and range of motion. However, because of its nonlinear geometry it implies that the relationship between displacement of the motors and displacement of the link is position dependent. A numerical algorithm is developed and evaluated to estimate, in real-time, the link position. Finally, the ability to adjust the stiffness is studied. The analysis reveals that the stiffness transformation between the tendons and the links is obtained with the coupling matrix. The position dependency of the thumb coupling matrix implies that the derivative of the coupling matrix influences the joint stiffness.

All tendons must cross the wrist to go from the motors to the finger insertion points. By doing so, a coupling between the wrist motion and the tendon displacement is introduced. Although negligible in the flexion/extension direction, the effect is major during the abduction/adduction motions (sideway motions). Consequently, the guidance through the wrist is modeled and included in the kinematic chain of the tendons. The wrist mechanism itself is a double inverted parallelogram and its kinematic modeling is explained step by step. Experiments and simulations are compared and confirm the validity of the model.

1.5.2 Control

The control of robots with a high number of degree of freedom and nonlinear components is a globally unsolved problem. Although linear control methods have been successfully applied on slightly nonlinear system, highly nonlinear plants remain difficult to control. In the **control** part, the challenges related to the tendon actuation and elastic joint control are treated. Approaches from the linear control theory as well as the nonlinear control theory are used. Since the Hand Arm System is an important research plat-

form for DLR, the objective of the control part is to derive a controller that is theoretically solid and practically performs well. Therefore, some methods such as Immersion and Invariance control are not applied since that are unlikely to be implementable on a real-time system (considering the 38 actuators). Simulation are systematically performed because they are cheaper, faster, and less risky than real experiments. However, they might not be as accurate in capturing the details as experiments are (there always exist unmodeled effects). Therefore, simulated results are, as much as possible, compared to the experimental results. It allows to gain confidence in the modeling and the simulations as well as to detect unmodeled effects that need to be included in the simulations.

A first section presents the problem of distributing the tendon internal forces, while satisfying secondary constraints and boundary conditions.

The second section proposes to adjust the controller stiffness on line in order to achieve the user desired fingertip stiffness. Indeed, the controller and the mechanism are connected in series. Therefore, a change of the mechanical stiffness can be compensated by the controller in order to obtain a given fingertip *effective* stiffness. Experimental results show that the method is effective, however, the stability analysis is not provided in this thesis.

According to the modeling part, the friction in the guidings and the joints is not negligible. The third section introduces a link side torque sensor, based on strain gauges, and proposes a link side friction observer. The purpose of the section is to appreciate the contribution of the friction. That is, what would be the performance without friction and is it worth trying to reduce it. The link side sensing is temporary since it significantly reduces the robustness of the fingers. Experiments and simulations confirm that tracking and regulation are improved.

The fourth section concentrates on the force control of the tendons. Initially, the equations of a state feedback controller are derived and implemented. The nonlinearity of the plant leads to a limited performance of the controller when the working point is far from the reference plant. Thus, an adaptive gain design, using the gain scheduling method is proposed. It is verified that, indeed, the scheduled controller is well adapted for all working points.

Motivated by the effectiveness of the gain scheduled tendon controller, a two time scale approach is presented in the fifth section. It consists in treating the tendon control problem and the link control problem as two separated plants. The assumption that the time scales are sufficiently different and that the solution have the required properties (e. g. boundedness) allows to use the singular perturbation theory. The stability of the controllers is proved (under the separation assumption). However, the experimental results demonstrate that the assumption is not valid, especially when the system is rigid. Consequently, a more global approach of the system is done. A system consisting of a motor, a link, and a flexible joint is con-

sidered. Based on its state description, a direct pole placement method is applied. A numerical sensitivity analysis shows that the choice of the poles is critical. Moreover, the previous approaches are not restricting the amplitude of the control input, thus leading to saturation effects that are not included in the stability analysis. To account for the amplitude of the input, the optimal control theory, such as the Riccati equations, is an adapted tool. Simulations are performed and shows that input amplitude is indeed reduced.

Section six applies a purely nonlinear control method, known as the backstepping method, to a flexible joint. It has the advantage of explicitely accounting for the nonlinear effects. It is pointed out in most of the control literature that the backstepping method is able to profit from the *good* nonlinearities (whereas the feedback linearization cancels all nonlinearities). The method is applied on systems of increasing complexity. The controller equations are derived, implemented, simulated and experimented on a test system with a single flexible joint driven by a single motor and with a linear flexible joint. The method reveals to perform well. Therefore, the equations are modified to be applied on the same test system with nonlinear flexibility. It exhibits good perfomance too. Nonetheless, the fingers of the Hand Arm System are driven by two motors in an antagonistic configuration. Thus, the backstepping method must be adapted to be applied to the real system. An adaptation is proposed that consists in sharing the desired torque between the motors and neglecting the influence of the antagonist motor. Simulations and experiments are carried and demonstrate the effectiveness of the method.

Although the backstepping method is practically very successful, it requires to select several gain matrices. The sensor noise, the unmodeled effects, and the computation delays prohibit the use of arbitrarily large gains. The theory, however, only requires positive definiteness of the gains. Therefore, the seventh section considers the *novel* problem of computing somehow optimal gains for the backstepping. The proposed method first uses the State Dependent Riccati Equation (SDRE) theory in order to compute the, locally, optimal state feedback gains. Then, a numerical solver is used to find the backstepping gains that would result in a state feedback control close (w. r. t. some arbitrary metric) to the optimal one.

Part I

Modeling and identification

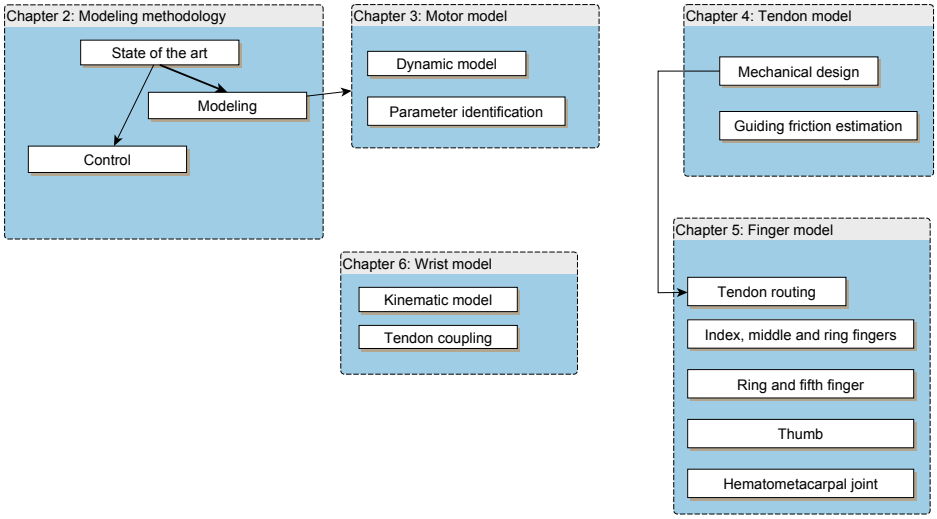

Figure 1.17: Overview of the structure of the modeling part

In this part, the mechanical modeling of the hand is conducted. The modeling starts with the motors and is progressively extended to the fingers. The nonlinear spring mechanisms and the tendons are modeled. Experiments are performed step by step to verify the models. modeling. The logical links between the different chapters of this part are depicted in Fig. 1.17.

In the first chapter, the general methodology is presented. Dynamics modeling methods such as the Lagrangian and the Newton-Euler methods are introduced and are later used to establish the dynamic model for the fingers. The second chapter details the modeling of the motors. A precise modeling of the friction and a set of friction compensation methods is proposed. Experimental results are reported that confirm the benefits of the compensations.

The third chapter concentrates on the modeling of the tendon behavior. A complete characterization of several tendon types and materials is performed. A tendon model is established such that the mechanical designer has the tools to decide between the use of pullies guidings or sliding surfaces.

The fourth chapter presents the kinematic modeling of the fingers. However, because each finger has a slightly different design (e. g. the thumb tensegrity structure or the underactuated joints), the specificities of each finger are detailed in separate chapters. The couplings between the motor motion and the finger motion are derived and the pseudo inverse matrix is used to estimate the link side position from the tendon displacements. A dynamic model of the index finger is presented and several simulations are performed to derive a simplified dynamic model.

Finally, the wrist kinematic modeling is reported in the fifth chapter. The influence of the wrist motion on the tendon displacement is analyzed. Simulations and experiments are performed to show that the kinematic model can be successfully used to compensate the wrist coupling.

2 Modeling approaches

This chapter reports the different methods used to create the kinematic models and the dynamic models of the fingers. In the first section, the generic symbols and units used in the thesis are reported. The second section presents the kinematic modeling. The third section presents two well known dynamic modeling methods. Finally, a short discussion summarizes the chapter.

2.1 Symbols and units

The units used through the thesis comply with the international units and are reported in table 2.1.

2.2 Kinematic modeling approaches

Robotic manipulators represent a subclass of mechanisms that have a specific mechanical structure. Most often, they consist of a serial connection of links connected by revolute or prismatic joints. Although other types of joint exist, the use of electromotors for the actuation and ball bearings for the guidings leads to those two principal types. The transformation of the robot end-effector is obtained by cumulating the transformation of each link in the chain, starting from the base. Homogeneous transformation matrices are used to establish kinematic models. It circumvents the ambiguity of the Denavit-Hartenberg [99] notation while having negligible impact on the real-time system. Indeed, the implementation is performed through the use of formal manipulation softwares (Maple^{TM}) and C language export.

2.3 Dynamic modeling approaches

Dynamic modeling approaches are used to established the dynamic equations of motion in the form

$$\boldsymbol{M}(\boldsymbol{q})\ddot{\boldsymbol{q}} + \boldsymbol{C}(\boldsymbol{q}, \dot{\boldsymbol{q}})\dot{\boldsymbol{q}} + \boldsymbol{g}(\boldsymbol{q}) = \boldsymbol{\tau}, \tag{2.1}$$

where $n \in \mathbb{N}$ is the number of links, $\boldsymbol{M}(\boldsymbol{q}) \in \mathbb{R}^{n\times n}$, $\boldsymbol{C}(\boldsymbol{q}, \dot{\boldsymbol{q}}) \in \mathbb{R}^{n\times n}$, $\boldsymbol{g}(\boldsymbol{q}) \in \mathbb{R}^n$ are respectively the inertia matrix, the Coriolis and centrifugal effects and the gravity torque covector. $\boldsymbol{q} \in \mathbb{R}^n$ and $\boldsymbol{\tau} \in \mathbb{R}^n$ are the joint position and the motor torque vector.

A dynamic model of the system is paramount for any analysis and controller design. Numerous techniques have been developed to establish the system of second order differential equations, such as Lagrange-Euler, recursive Lagrangian and Newton-Euler methods. Each approach leads to the

Description	Unit	Symbol
Time	seconds	[s]
Length	meters	[m]
Mass	kilograms	[kg]
Angle	radians	[rad]
Torque	Newton meter	[Nm]
Force	Newton	[N]
Linear velocity	meters per second	[m/s]
Angular velocity	radians per second	[rad/s]
Linear acceleration	meters per second squared	[m/s^2]
Angular acceleration	radians per second squared	[rad/s^2]
Linear stiffness	Newton per meter	[N/m]
Angular stiffness	Newton meter per radian	[Nm/rad]

Table 2.1: Symbols and units

same behavior [100], but the computation burdens are different. One can refer to [101] for a comparison of the different methods applied on different types of robot.

2.3.1 Newton-Euler approach

The Newton-Euler method is a recursive method based on the equilibrium of forces and torques. In numerous papers and text books, the method is used to establish the dynamic equations. The equations reported here are based on Craig [102]. Several software packages such as Symoro+ [103] have been developed based on this algorithm, in order to simplify the modeling process. More recently, in [104] De Luca proposed to modify the genuine method in order to reduce the computational effort to obtain the Coriolis/centrifugal and inertia matrices.

The Newton-Euler method proceeds in two phases: first the velocity and acceleration are computed from base to end-effector. Then, the forces and torques are computed from end-effector to base.

Base equations

A free body of mass $m \in \mathbb{R}^+$ subject to a force $\boldsymbol{F} \in \mathbb{R}$ acting on the center of mass results in an acceleration $\boldsymbol{a} \in \mathbb{R}$ according to Newton's law

$$\boldsymbol{F} = m\boldsymbol{a}. \tag{2.2}$$

Similarily for the torque, Euler's equation gives

$$\boldsymbol{N} = \boldsymbol{I}\dot{\boldsymbol{\omega}} + \boldsymbol{\omega} \times \boldsymbol{I}\boldsymbol{\omega}, \tag{2.3}$$

where $\boldsymbol{N} \in \mathbb{R}$ is the body torque. $\boldsymbol{I} \in \mathbb{R}$ and $\boldsymbol{\omega} \in \mathbb{R}$ are the link inertia expressed at the center of mass and the angular velocity.

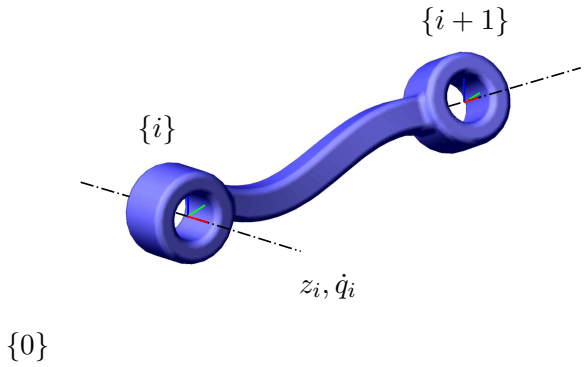

Figure 2.1: Isolated link i

Forward equations

The position, velocity and acceleration of all links are propagated from bottom to end-effector. Considering a chain of $n \in \mathbb{N}$ bodies connected with n revolute joints. Starting from the base link $< 0 >$ attached to frame $\{0\}$ (cf. Fig. 2.1) up to the end effector link $< n >$ attached to frame $\{n\}$. The velocities and accelerations of the link are obtained from the previous link with

$$ {}^{i+1}\boldsymbol{v}_{i+1} = {}^{i+1}_{i}\mathbf{R}[{}^{i}\boldsymbol{v}_i + ({}^{i}\boldsymbol{\omega}_i \times {}^{i}\boldsymbol{p}_{i+1,i})], \tag{2.4} $$

and

$$ {}^{i+1}\boldsymbol{a}_{i+1} = {}^{i+1}_{i}\mathbf{R}[{}^{i}\dot{\boldsymbol{\omega}}_i \times {}^{i}\boldsymbol{p}_{i+1,i} + {}^{i}\boldsymbol{\omega}_i \times ({}^{i}\boldsymbol{\omega}_i \times {}^{i}\boldsymbol{p}_{i+1,i}) + {}^{i}\boldsymbol{a}_i], \tag{2.5} $$

where $\forall i \in [0 \dots n-1]$, ${}^{i}\boldsymbol{v}_i \in \mathbb{R}^3$ is the linear velocity of link i with respect to the frame $\{0\}$ expressed in $\{i\}$. ${}^{i}\boldsymbol{\omega}_i \in \mathbb{R}^3$ is the the angular velocity of link i with respect to $\{0\}$ expressed in $\{i\}$, ${}^{i}\boldsymbol{p}_{i+1,i} \in \mathbb{R}^3$ is the vector between the rotation center of body $< i >$ and body $< i+1 >$ rotation points, expressed in $\{i\}$.

Similarily, ${}^{i}\boldsymbol{a}_i \in \mathbb{R}^3$ is the linear acceleration of link i with respect to $\{0\}$ expressed in $\{i\}$ and ${}^{i}\dot{\boldsymbol{\omega}}_i \in \mathbb{R}^3$ is the angular acceleration of the link i expressed in $\{i\}$.

The angular velocities in world coordinates are transformed with

$$ {}^{0}\boldsymbol{\omega}_{i+1} = {}^{0}\boldsymbol{\omega}_i + \dot{q}_{i+1}{}^{0}\boldsymbol{z}_{i+1} \tag{2.6} $$

In the previous link coordinates,

$$ {}^{i+1}\boldsymbol{\omega}_{i+1} = {}^{i+1}_{i}\mathbf{R}{}^{i}\boldsymbol{\omega}_i + \dot{q}_{i+1}{}^{i+1}\boldsymbol{z}_{i+1}, \tag{2.7} $$

$\forall i \in [1 \dots n]$, ${}^{0}\boldsymbol{\omega}_i \in \mathbb{R}^3$(resp. ${}^{i}\boldsymbol{\omega}_i \in \mathbb{R}^3$), denotes the angular velocity of link i with respect to $\{0\}$ (resp. $\{i\}$), ${}^{0}\boldsymbol{z}_{i+1} \in \mathbb{R}^3$ (resp. ${}^{i+1}\boldsymbol{z}_{i+1} \in \mathbb{R}^3$) is the rotation axis expressed in $\{0\}$ (resp. $\{i+1\}$) and $\dot{q}_{i+1} \in \mathbb{R}$ is the rotational velocity of link $i+1$ with respect to the link i (i. e. the joint velocity).

The angular accelerations are:

$$^{i+1}\dot{\boldsymbol{\omega}}_{i+1} = {}^{i+1}_{i}\mathbf{R}\,{}^{i}\dot{\boldsymbol{\omega}}_{i} + {}^{i+1}_{i}\mathbf{R}\,{}^{i}\boldsymbol{\omega}_{i} \times \dot{q}_{i+1}\,{}^{i+1}\boldsymbol{z}_{i+1} + \ddot{q}_{i+1}\,{}^{i+1}\boldsymbol{z}_{i+1}, \tag{2.8}$$

where $\ddot{q}_i \in \mathbb{R}$ is the rotational acceleration of link $i+1$ with respect to link i (i. e. the joint acceleration).

In order to apply Newton's law, all linear accelerations must be expressed at the center of mass of each link. Recalling,

$$^{i}\boldsymbol{v}_{c,i} = {}^{i}\boldsymbol{v}_{i} + {}^{i}\boldsymbol{\omega}_{i} \times {}^{i}\boldsymbol{p}_{c,i}, \tag{2.9}$$

where $\forall i \in [1 \dots n]$, ${}^{0}\boldsymbol{p}_{c,i} \in \mathbb{R}^3$ is the vector from the origin to the center of mass of the link, expressed in $\{0\}$ and $\boldsymbol{v}_{c,i} \in \mathbb{R}^3$ is the linear velocity of the center of mass of the link i.

$$^{i}\boldsymbol{a}_{c,i} = {}^{i}\boldsymbol{a}_{i} + {}^{i}\dot{\boldsymbol{\omega}}_{i} \times {}^{i}\boldsymbol{p}_{c,i} + {}^{i}\boldsymbol{\omega}_{i} \times {}^{i}\boldsymbol{\omega}_{i} \times {}^{i}\boldsymbol{p}_{c,i}, \tag{2.10}$$

where $\forall i \in [1 \dots n]$, $\boldsymbol{a}_{c,i} \in \mathbb{R}^3$ is the linear acceleration of the center of mass of the link i.

At the end of the forward procedure, all velocities and accelerations of the center of mass of the links are expressed recursively with respect to the previous link. The laws of Euler and Newton yield

$$^{i+1}\boldsymbol{F}_{i+1} = m^{i+1}_{i+1}\boldsymbol{a}_{c,i+1} \tag{2.11}$$

$$^{i+1}\boldsymbol{N}_{i+1} = \boldsymbol{I}_{i+1}\,{}^{i+1}\dot{\boldsymbol{\omega}}_{i+1} + {}^{i+1}\boldsymbol{\omega}_{i+1} \times \boldsymbol{I}_{i+1}\,{}^{i+1}\boldsymbol{\omega}_{i+1} \tag{2.12}$$

where all inertia matrices $\boldsymbol{I}_i \in \mathbb{R}^{3\times3}, \forall i \in [1 \dots n]$ are expressed at the center of mass of the links.

Backward equations

In the backward phase, the forward equations are substituted in the Newton law of equilibrium in order to express the link's angular and linear accelerations depending on the joint torques and the gravity field. Expressing the force and torque balance yields

$$^{i}\boldsymbol{f}_{i} = {}_{i+1}^{i}\mathbf{R}\,{}^{i+1}\boldsymbol{f}_{i+1} + {}^{i}\boldsymbol{F}_{i}, \tag{2.13}$$

where $\boldsymbol{f}_i \in \mathbb{R}, i \in [1 \dots n]$ is the force exerted on link i by link $i-1$. Similarily the torque balance gives

$$^{i}\boldsymbol{\eta}_{i} = {}^{i}\boldsymbol{N}_{i} + {}_{i+1}^{i}\mathbf{R}\,{}^{i+1}\boldsymbol{\eta}_{i+1} + {}^{i}\boldsymbol{p}_{c,i} \times {}^{i}\boldsymbol{F}_{i} + {}^{i}\boldsymbol{p}_{i+1} \times {}_{i+1}^{i}\mathbf{R}\,{}^{i+1}\boldsymbol{f}_{i+1}, \tag{2.14}$$

where $\boldsymbol{\eta}_i \in \mathbb{R}, i \in [1 \dots n]$ is the torque exerted on link i by link $i-1$.

Finally, the joint torques are obtained as

$$\boldsymbol{\tau}_{i} = {}^{i}\boldsymbol{\eta}_{i}^{T\,i}\boldsymbol{z}_{i}. \tag{2.15}$$

2.3.2 Lagrange approach

The Lagrange method is based upon the fact that the change of energy of the system is equal to the power exchange with the environment. More formally, by introducing $\mathcal{L} = E_v - E_c$ the difference between the kinetic energy E_v and the potential energy E_c(elastic or gravity), and in the absence of frictional losses (also called the Rayleigh dissipation terms), the joint torques τ_i are directly obtained as:

$$\frac{d}{dt}\left(\frac{\partial \mathcal{L}}{\partial \dot{q}_i}\right) - \frac{\partial \mathcal{L}}{\partial q_i} = \tau_i, \quad \forall i \in [1 \dots n] \tag{2.16}$$

for a system with n degrees of freedom, where $\boldsymbol{q}$ is the state variable and $\mathcal{L}$ is the Lagragian of the system. Collecting the terms allows to write the dynamic equation as

$$\boldsymbol{M}(\boldsymbol{q})\ddot{\boldsymbol{q}} + \boldsymbol{C}(\boldsymbol{q}, \dot{\boldsymbol{q}})\dot{\boldsymbol{q}} + \boldsymbol{g}(\boldsymbol{q}) = \boldsymbol{\tau}_{ext}, \tag{2.17}$$

where $\boldsymbol{q} \in \mathbb{R}^n$ is the state vector, $\boldsymbol{M}(\boldsymbol{q}) \in \mathbb{R}^{n \times n}$ is the inertia matrix and $\boldsymbol{C}(\boldsymbol{q}, \dot{\boldsymbol{q}}) \in \mathbb{R}^n$ is the matrix of Coriolis and centrifugal terms. $\boldsymbol{g}(\boldsymbol{q}) \in \mathbb{R}^n$ is the covector of the gravity torques and $\boldsymbol{\tau}_{ext} \in \mathbb{R}^n$ is the covector of externally applied torques.

Deriving the dynamics equations with the Lagragian method mainly consists of expressing the Lagrangian $\mathcal{L}$ of the mechanical system and symbolically deriving the expressions for the torques $\tau_i, i \in [1 \dots n]$. The method can be applied to any not non-holonomic mechanism structure. It is a systematic method and can be applied programatically. However, applied without further considerations, the method generates computationally more expensive forms.

2.4 Discussion

The most important conclusion is, that, on the one hand the Lagrange-Euler method (very structured) leads to computationally expensive formulations. On the other hand the Newton-Euler methodology leads to more efficient computation forms (but is not well structured). Indeed, it is reported in [102] that the Lagrangian approach has a $O(n^3)$ complexity while the recursive Euler-Newton method is of complexity $O(n)$. Nonetheless, it should be noted that once the closed form equations are obtained, simplifications (factorization or code optimization) can lead to more efficient implementations. In this thesis, the Lagragian approach is selected, since, by observing the closed form structure, more insight into the possible control scheme is gained.

3 Motor model

Motors are the foundation layer of robotic systems. Highly dynamic motors are allowing to have high fast and precise positioning. This section models the motors used in the forearm to pull the tendons. The aim is to obtain a reliable dynamic motor model, and if possible to improve the motor behavior through the use of friction compensation or ripple (periodic disturbances) compensation mechanisms. Friction modeling and compensation techniques are presented in [57, 105–109]. The motors used have been designed and manufactured by a spin-off company of the Institute of Robotics and Mechatronics [110]. Figure 3.1 shows the motor, the power electronics, and the communication module. The motors are classified as PMSM (permanent magnet synchronous motors). The current control loop is executed in the communication electronics FPGA (Fast Programmable Gate Array: Xilinx Spartan 3e XCS500EP132) at 100kHz. All motor modules are connected to a data collector board via a BiSS (Bidirectional Synchronous Serial interface [111]). The data collector board features two FPGAs (V5LX50) and communicates with the real-time computer via an optical SpaceWire connexion (space qualified ESA standard [112]).

3.1 Dynamic model

The motors are modeled as a second order system with a velocity and position dependent friction (cf. Fig. 3.2). The total inertia expressed in the output shaft velocity is obtained from the fixed gear ratio α_{gear} (neglecting the harmonic drive elasticity) between input shaft and output shaft by considering the energy mapping.

$$B = B_{motor}\alpha_{gear}^{-2} + B_{gearbox}, \tag{3.1}$$

where $B \in \mathbb{R}$ is the total motor inertia seen at the output shaft. $B_{motor} \in \mathbb{R}$ is the motor shaft inertia alone. $B_{gearbox} \in \mathbb{R}$ is the inertia of the output

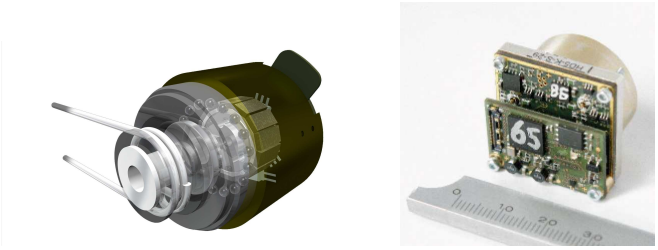

(a) Render (b) Photograph

Figure 3.1: Rendered motor module and real motor module

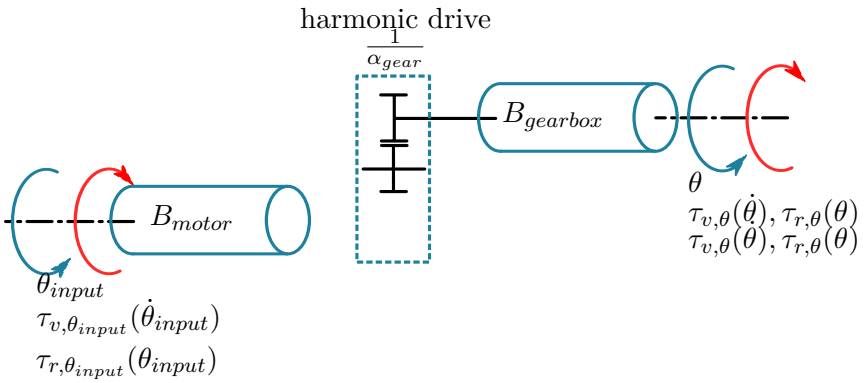

Figure 3.2: Model of the Permanent Magnet Synchronous Motors (PMSM) with a harmonic drive. The friction terms before and after the gear box are separated.

Table 3.1: Different contributions to the total motor friction

Description	Symbol
$\tau_{\mathrm{v}}(\dot{\theta}_{\mathrm{input}}) \in \mathbb{R}$	Velocity dependent friction due to the input shaft
$\tau_{\mathrm{v}}(\dot{\theta}) \in \mathbb{R}$	Velocity dependent friction due to the output shaft
$\tau_{\mathrm{r,input}}(\theta_{\mathrm{input}}) \in \mathbb{R}$	Position dependent friction due to the input shaft
$\tau_{\mathrm{r}}(\theta) \in \mathbb{R}$	Position dependent friction due to the output shaft

gear alone and $\alpha_{gear} \in \mathbb{R}$ is the gear ratio of the harmonic drive from input to output velocity. Practically, the total inertia only depends on the input shaft inertia since the gear ratio is 1/100. In the absence of external forces, the equation of dynamics is

$$B\ddot{\theta} = \tau_{friction}(\theta, \dot{\theta}) + \tau_m, \tag{3.2}$$

where $\theta \in \mathbb{R}$ is the rotor position with respect to the stator. $\tau_m \in \mathbb{R}$ is the electromagnetic torque. The frictional torque $\tau_{friction}(\theta, \dot{\theta}) \in \mathbb{R}$ can be separated into the motor shaft and output shaft term as well as the velocity or position dependent terms leading to

$$\tau_{friction}(\theta, \dot{\theta}) = \tau_v(\dot{\theta}_{input}) + \tau_{r,input}(\theta_{input}) + \tau_v(\dot{\theta}) + \tau_r(\theta) \tag{3.3}$$

where the terms are defined in Table 3.1.

The motor velocity and the output velocity are related by the fixed gear ratio $\dot{\theta} = \alpha_{\mathrm{gear}}\dot{\theta}_{\mathrm{input}}$. Hence, only one velocity dependent term is kept (that accounts for both). The total frictional effects are consequently written:

$$\tau_{\mathrm{friction}}(\theta, \dot{\theta}) = \tau_{\mathrm{r,input}}(\theta_{input}) + \tau_{\mathrm{v}}(\dot{\theta}) + \tau_{\mathrm{r}}(\theta). \tag{3.4}$$

Using the velocity relation between $\dot{\theta}$ and $\dot{\theta}_{\mathrm{input}}$, the motor dynamics are

$$B\ddot{\theta} = \tau_{\mathrm{v}}(\dot{\theta}) + \tau_{\mathrm{r,input}}(\alpha_{\mathrm{gear}}^{-1}\theta) + \tau_{\mathrm{r}}(\theta) + \tau_{\mathrm{m}} \tag{3.5}$$

Description	Unit	Symbol
Inertia	kilogram meter square	$[kgm^2]$
Motor constant	Newton meter per ampere	$[Nm/A]$
Static friction torque	Newton meter	$[Nm]$
Viscous friction torque	Newton meter per radian per second	$[Nm/(rad/s)]$

Table 3.2: Parameters to be identified

where $B \in \mathbb{R}$ is the total motor inertia, $\theta \in \mathbb{R}$ is the output shaft position w. r. t. some arbitrary origin. $\tau_{\mathrm{v}}(\dot{\theta}) \in \mathbb{R}$ is the velocity dependent friction torque due to input and output viscous effects. $\tau_{\mathrm{r}}(\theta) \in \mathbb{R}$ (resp. $\tau_{\mathrm{r,input}}(\alpha_{\mathrm{gear}}^{-1}\theta) \in \mathbb{R}$) is the friction torque depending on the output (resp. input) shaft position.

3.2 Parameter identification

The unknown parameters of equation (3.5) (listed in table 3.2) must be either identified or neglected. In case of large uncertainties it is better to neglect frictional terms rather than over compensating them. Indeed, the energy introduced to compensate the friction may lead to the loss of mechanical passivity [113].

To identify the motor parameters of Table 3.2, several experiments are conducted:

- constant velocity square waves (for velocity dependent friction)
- constant torque impulse (for inertia modeling)
- constant velocity with Coulomb and viscous friction compensation (for ripple identification)

Inertia and torque constant The inertia and the motor electromagnetic constant (current to torque relationship) are linearly dependent in the dynamic equations. Therefore, either the inertia or the torque constant must be measured externally. The torque constant was determined by a direct torque measurement at the motor output shaft and is assumed to be constant among all the motors. The inertia was obtained from a current step response experiment, based on the model

$$B\ddot{\theta} = \tau_{\mathrm{m}}, \tag{3.6}$$

where $B \in \mathbb{R}$ is the inertia along the rotation axis, $\theta \in \mathbb{R}$ is the position of the motor shaft w. r. t. some arbitrary origin and $\tau_{\mathrm{m}} \in \mathbb{R}$ is the electromagnetic torque. This identification neglects the viscous friction and the stick-slip friction. The inertia value obtained by this method is comparable to the value obtained from the CAD data.

Table 3.3: Parameters of the friction model

Parameter	Unit	Value
γ_1	$[rad/s]^{-1}$	10
γ_2	$[Nm]$	0.5586
γ_3	$[Nm][rad/s]^{-1}$	0.0356

Friction At constant velocity, one can write (under the assumption that the friction is uniquely velocity dependent):

$$0 = \tau_{\mathrm{v}}(\dot{\theta}) + \tau_{\mathrm{r,input}}(\alpha_{\mathrm{gear}}^{-1}\theta) + \tau_{\mathrm{r}}(\theta) + \boldsymbol{\tau}_{\mathrm{m}} \tag{3.7}$$

where $\theta \in \mathbb{R}$ is the position of the motor shaft w. r. t. some arbitrary origin. $\tau_{\mathrm{v}}(\dot{\theta}) \in \mathbb{R}$ is the velocity dependent friction torque due to input and output viscous effects. $\tau_{\mathrm{r}}(\theta) \in \mathbb{R}$ (resp. $\tau_{\mathrm{r,input}}(\alpha_{\mathrm{gear}}^{-1}\theta) \in \mathbb{R}$) is the friction torque depending on the output (resp. input) shaft position and $\tau_{\mathrm{m}} \in \mathbb{R}$ is the electromagnetic torque.

Therefore, the friction parameters can be estimated for a given velocity $\dot{\theta}$ by driving at different constant speeds (as depicted in Fig. 3.3a). The steady-state motor torque for each velocity is obtained by an average filter applied to a few motor periods (the position dependent input and output torques $\tau_{\mathrm{r,input}}, \tau_{\mathrm{r}}$ are periodic) and repeating the measurements with different speeds leads to the Figure 3.3b.

To maintain the central symmetry and provide smoothness, the friction model is selected as

$$\hat{\tau}_{friction}(\dot{\theta}) = atan(\gamma_1\dot{\theta})\gamma_2 + \gamma_3\dot{\theta}, \tag{3.8}$$

where $\hat{\tau}_{\mathrm{friction}}(\dot{\theta}) \in \mathbb{R}$ is the estimated friction torque at a given velocity $\dot{\theta}$. The position dependent terms are neglected. The parameters γ_1, γ_2 and γ_3 for one specific motor are reported in Table 3.3.

Ripple The motor ripple (periodic disturbances) is generated by a magnetic or a mechanical effect and therefore is mainly position dependent. A compensation for the magnetic ripple is proposed and implemented in [114]. Bearing friction models and compensation schemes are discussed in [57] and harmonic drive specific friction is treated in [115]. Because two bearings are used (the motor shaft bearings and the output shaft bearing), two periodic disturbances appear on the motor torque. It is possible to cancel or at least to reduce the disturbances by applying a correct feedforward signal. In Figure 3.4a and 3.4b, 10 measurements with the same desired velocity are depicted and confirm the repeatability of the disturbances. In each of them the measurement was triggered on the same motor position. The measurements demonstrate that the position dependent friction effects are strongly repeatable.

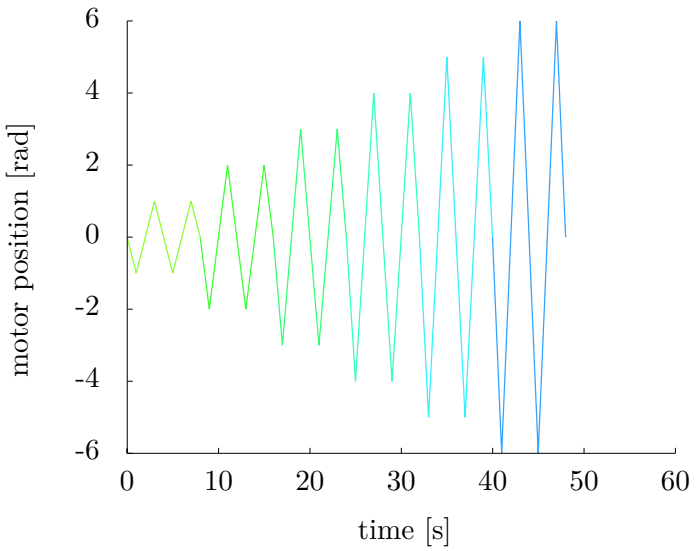

(a) Position profiles used to estimate the friction parameter (Piecewize constant velocity).

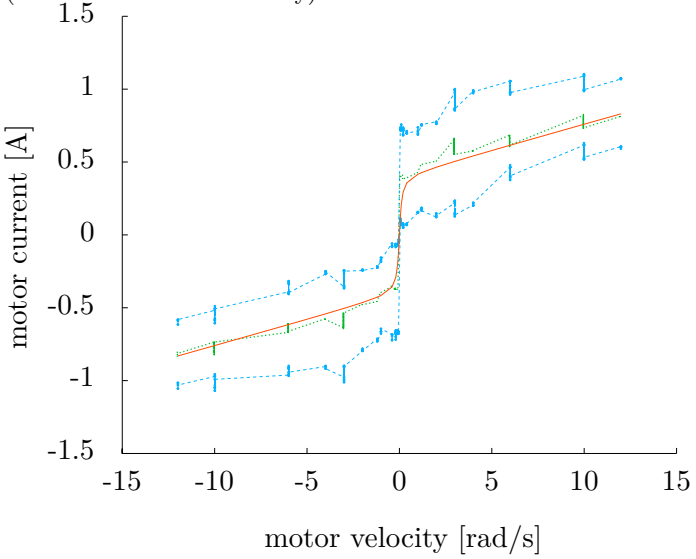

(b) Friction curve. The green (dotted center) is the average, the light blue lines are minimum and maximum (dashed top/bottom) and the red curve is the curve of the selected friction model (solid)

Figure 3.3: Experiment and results for the motor friction estimation

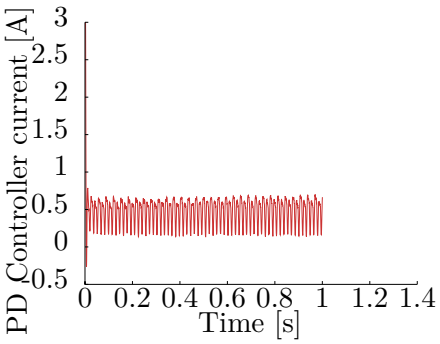

(a) Measured motor torque at a fixed velocity (using a simple PD controller)

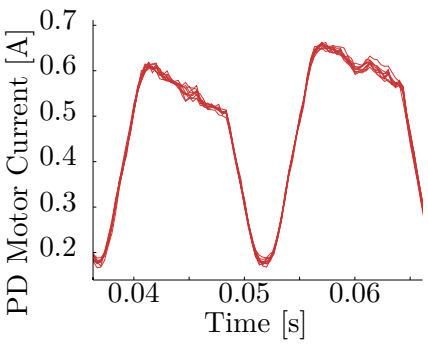

(b) Close view on 10 measures of the motor torque at a fixed velocity (using a simple PD controller)

Figure 3.4: Experiment: commanded torque for constant velocity motions

In Figure 3.5a, two measurements with the different desired velocities $\dot{\theta} = 1$ rad/s and $\dot{\theta} = 0.5$ rad/s are depicted and confirm that the disturbance is position dependent.

In order to assess the performance of the compensation is it necessary to quantify the disturbance. Due to its periodicity, a frequency analysis seems appropriate to analyze the motor recordings. Figure 3.5b shows the initial frequency distribution of the perturbation for the two desired velocities $\dot{\theta} = 1$[rad/s] and $\dot{\theta} = 0.5$[rad/s]. As expected the main frequency of the perturbation is equal to the motor rotation frequency, and the frequencies are clearly identifiable.

From those experiments, it can be concluded that the repeatability of the disturbance is excellent and its phase only depends on the motor position. Moreover, the reduction of the amplitude of the disturbance at the motor rotation frequency is selected to quantify the results (first harmonic removal/attenuation).

To compensate for disturbances, a feedforward term can be added to the controller action. The frequency and phase are directly given by the motor velocity but the amplitude is not known. As mentioned previously, the amplitude estimation must be conservative to avoid introducing potentially destabilizing energy.

3.3 Conclusion

Fig. 3.6b and Fig. 3.6a show the reduction of the torque disturbance amplitude in the frequency and in the time domains. Although hard to perceive in time domain, the attenuation is clearly visible in the frequency domain (as well as simply hearing the motor noise).

The small size of the motor and gear boxes inevitably introduce large

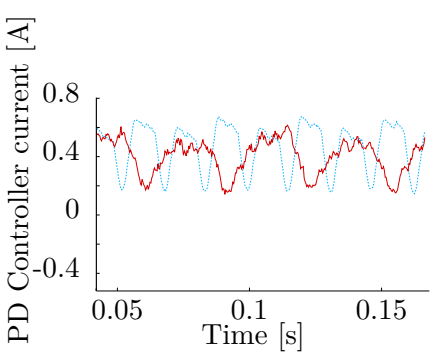

(a) Motor torque measured at two different constant speeds. The light blue dashed curved is obtained with a higher velocity as the red solid curve.

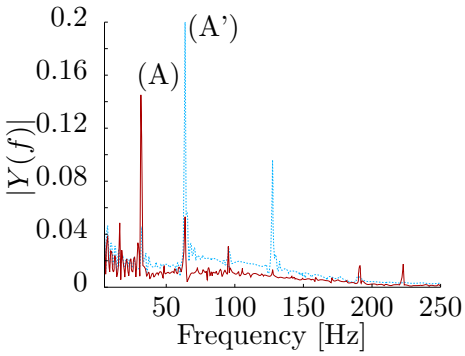

(b) Frequency decomposition at two different constant speeds. The light blue dashed curved is obtained with a higher velocity as the red solid curve. The main disturbance peak (A) is clearly shifted to the right (A').

Figure 3.5: Experiment: commanded torque for a constant velocity motion (time and frequency domains)

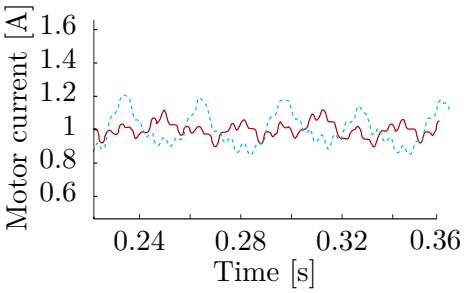

(a) PD controller desired torque (before compensator) without (light blue dashed) and with (red solid) the friction compensator

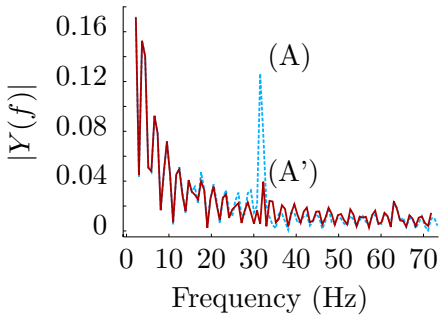

(b) Frequency decomposition without (light blue, dashed, above) and with (red, solid, below) the friction compensator

Figure 3.6: Experiment: resulting controller torque command in time and frequency domains after compensation

friction effects w. r. t. to their output torques (compared to a kW sized motor). However, different compensation mechanisms can benefit from the repeatability of the disturbances. A simple feedforward term can suppress, if not attenuate, most of the disturbances. Based on a rich literature of industrial applications, a compensation mechanism has been successfully designed and applied to the motors. Several experiments and analyses confirmed the benefit of the approach.

Despite the success of the method, some limitations must be stated; thanks to the high control frequency of 3kHz as well as the high quality of the motors and sensors, very high position controller gains can be used thus the benefit of the compensation is limited when the motor is used in position mode. Moreover, it must be noted that the compensation might lead to some noise or instability if the compensation is excessive (and consequently injecting more energy than the mechanism and the controller can dissipate). Nonetheless, the gain is appreciable when the motor is used as a torque source since the produced torque is closer to the desired one (reduced dead zone). It allows to reduce the controller effort (in tendon force control mode) since the forward model is more accurate and thus, indirectly, increases the system accuracy.

4 Tendon model

Several adjustable stiffness mechanisms are reported in [116]. In the hand of the Hand Arm System, tendons are used to carry the motor torque to the joint torque. But, because tendons can only pull and never push, they are used in an antagonistic configuration as depicted in Figure 4.1.

Besides the benefit of looking strongly anthropomorphic, the antagonistic tendon actuation allows to circumvent the issues of tendon slackening, change of tendon path length and routing complexity. Moreover, the use of nonlinear spring mechanism offers the possibility to adjust the joint stiffness (cf. Fig. 4.2). Although several methods can be used to control the system, they all require position or force control of the tendons (at least indirectly, e. g. to limit the tendon forces).

The beginning of this section describes the variable stiffness mechanisms, derives a mathematical model and verifies the model with a calibration experiment. Once the variable mechanism is modeled, the tendon is mounted in conditions similar to the final assembly (i. e. same number of pulleys) to estimate the quality of control that could be achieved. The experiment allows to measure the friction of the guidings and latter estimate the joint friction. The friction behavior with different mounting conditions is studied because a proper tendon force control is paramount to the successful operation of most of the controllers.

4.1 Mechanical design

This section is based on the sensor design by Werner Friedl that has been presented in [3]. The selection process of a tendon material is explained, followed by the geometrical description of the adjustable stiffness mechanism.

Tendon material selection The choice of the tendon material is critical for the design, since it imposes pulley geometries and radii, as well as the type of sliding surfaces that can be used. In the case of the Hand Arm System, a polymer fiber known commercially as Dyneema®[1] is selected over steel or vectran[2]. The main reason is its durability even for small pulley radii(cf. Fig. 4.3). Moreover it offers a termination technique called splicing (cf. Fig. 4.4) allowing to perform on site terminations. Although apparently accessory, this is extremely relevant when considering the time needed to assemble, maintain, and repair the system.

[1] Dyneema®is the commercial name of a strand of Ultra-high-molecular-weight polyethylene fibers.

[2] Vectran is a manufactured fiber of aromatic polyester.

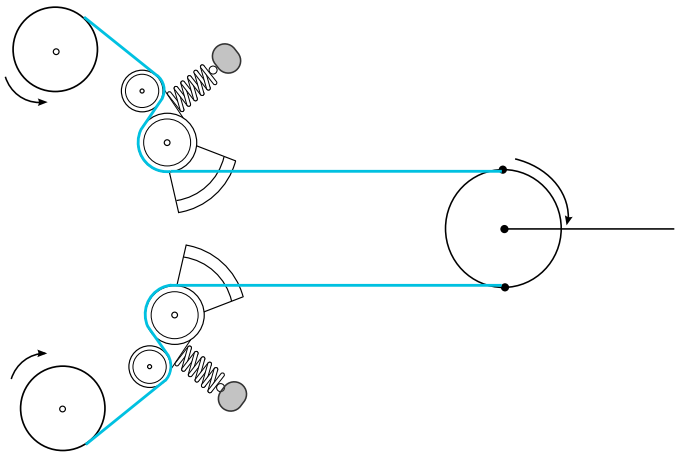

Figure 4.1: Antagonistic arrangement of the tendons allowing to move the joint and adjust its stiffness

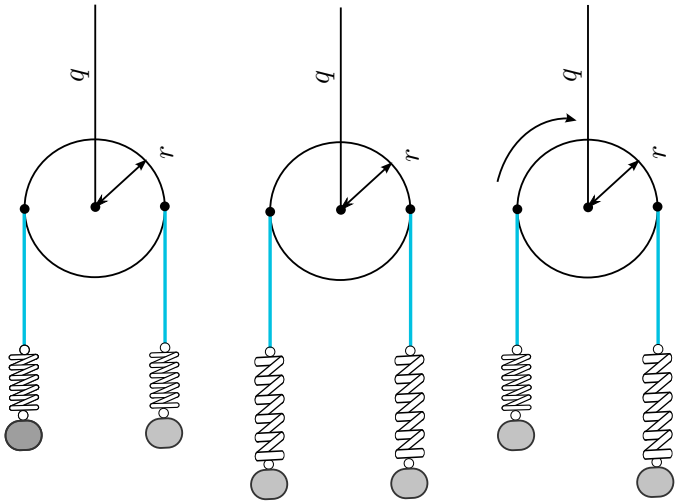

(a) (b) (c)

Figure 4.2: (a) A balanced set of forces is creating no joint torque. (b) Increasing the co-contraction of the tendons increases the link joint stiffness. (c) An unbalanced set of forces creates a torque

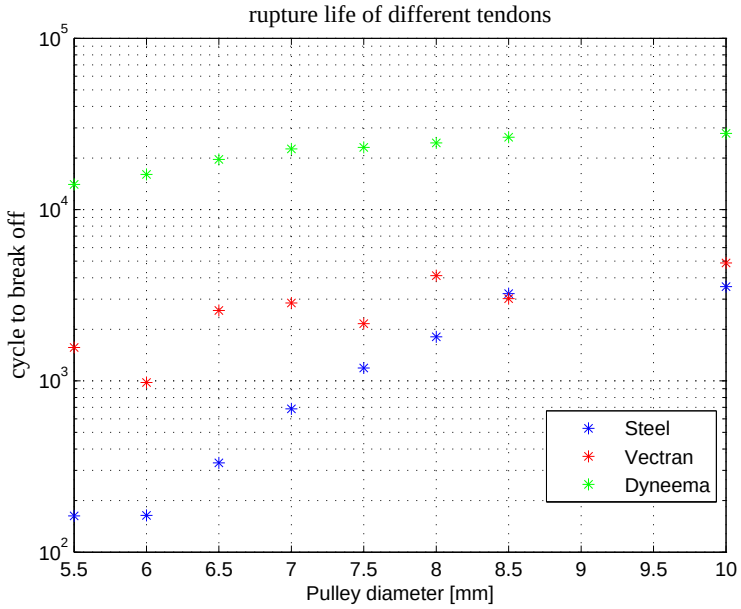

Figure 4.3: Durability test of different tendon material depending on the pulley radius

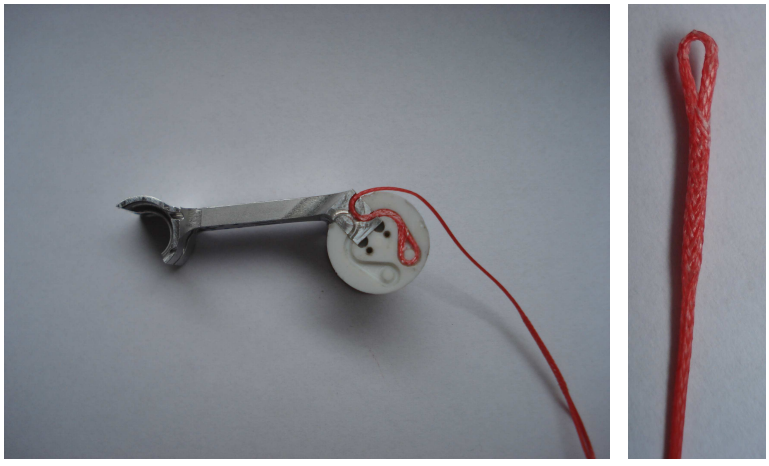

(a) Mounting of a tendon

(b) Splice of a tendon)

Figure 4.4: Splicing technique used to terminate the tendons

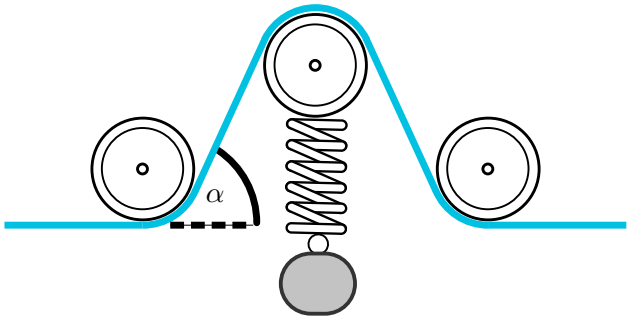

Figure 4.5: Original concept: tangent α mechanism

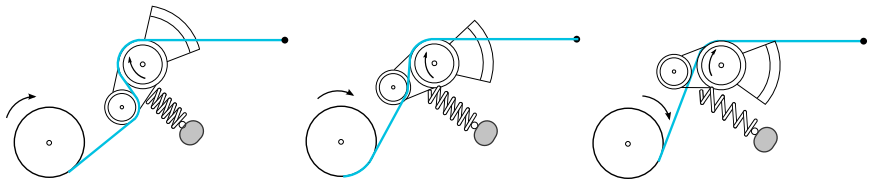

Figure 4.6: Geometry of the tendon force sensor: the stiffness is increasing from left to right

Geometrical Design The variable stiffness spring mechanism is based on the *tangent* α mechanism (cf. Fig. 4.5). The genuine design has been modified to minimize the number of pulleys and to replace the linear guiding by a rotational guiding. The resulting design is depicted in Fig. 4.6. The variables used through the modeling are reported in Table 4.1.

The length of the tendon in the mechanism (referred to as dL) is given with respect to the lever angle (referred to as θ_{lever}). The force characteristic and the tendon stiffness of one tendon are reported in Figure 4.7 (other tendons have different curves but the shape is imposed by the mechanism geometry).

Sensor Design To obtain a compact design a commercial Hall effect sensor is used off-axis (see Fig. 4.8a). The magnet attached to the lever sweeps over the hall effect sensor [117] and creates a magnetic field variation that is the measured quantity. The sensor provides a resolution of 12 bits at a frequency of 3 kHz. The sensor has a filter algorithm included which can be adjusted to reduce the noise level (at the cost of an increased hysteresis).

Calibration The tendon mechanisms must be calibrated because of the mounting variability, the variations in the sensor's sensitivity and the tolerances of the spring constant. The setup depicted in Fig. 4.8a is used to calibrate the sensors in place, therefore including the stiffness of the tendon material in the measurement.

Description	Symbol
θ_{lever}	Angle of the lever
$dL(\theta_{lever})$	Length of tendon from the motor pulley to the fixed pulley
$[x_{motor}, y_{motor}]$	Coordinates of the motor pulley center
$[x_{fixed,pulley}, y_{fixed,pulley}]$	Coordinates of the fixed pulley center
$[x_{lever}, y_{lever}]$	Coordinates of the lever pulley center
$[x_{spring}, y_{spring}]$	Coordinates of the spring fixed
K	Spring constant
R_{motor}	Radius of the motor pulley
R_{lever}	Radius of the lever pulley
$R_{fixed,pulley}$	Radius of the fixed pulley
K	Spring constant

Table 4.1: Parametrization of the spring mechanism

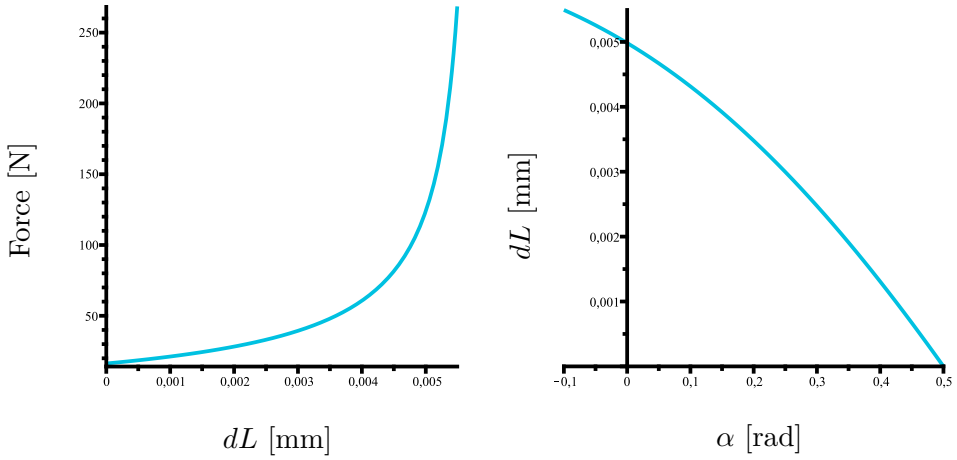

Figure 4.7: Model based mechanism characteristics

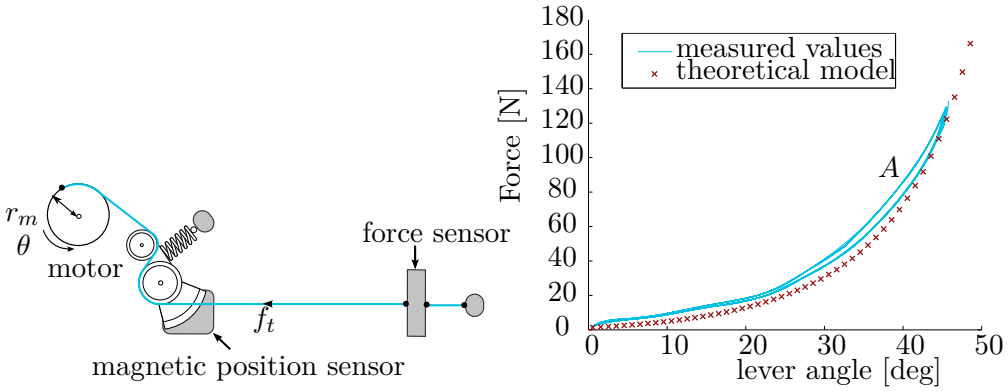

(a) Setup used for the tendon calibration

(b) Measured and model characteristic (position/force) of a tendon. (A) denotes a point where the hysteresis is about 10 N

Figure 4.8: Tendon force/stiffness calibration

The raw measurement of Figure 4.8b exhibits a good similarity with the model. The offset between the model and the measurement can be attributed to the spring constant mismatch and the friction in the lever mechanism. A more accurate fit can be obtained by adjusting the uncertain parameters (e. g. spring constant). Each individual sensor is calibrated after mounting to verify the magnetic sensor and the tendon mounting. Adjusted models are then approximated by polynomials that are used to transform the magnetic sensor output (increments) to the tendon force f_t[N], the tendon stiffness k_t[N/m] and the tendon length in the mechanism dL[m]. The polynomials are required to minimize the computation costs for the real-time implementation. One important element to note is the hysteresis cycle that reaches $10N - 20N$ at a force of about 70N (cf. Fig. 4.8b point (A)).

4.2 Guiding friction estimation

Through the measurement campaign, it appeared that the pulley guidings in the wrist and the palm are introducing a large static friction when used with the Dyneema®tendons. In order to qualify, quantify, and propose a model, a new set of experiments (depicted in Fig. 4.9) was conducted with different pulley radii and tendon diameters and materials. Figure 4.10 show that bending the dyneema fibers around the pulley requires a larger force than for the steel cables. Moreover, the friction is increasing when the bending diameters are diminishing. The friction behavior shows an independence with respect to the tendon speed (in the range of the expected tendon velocities).

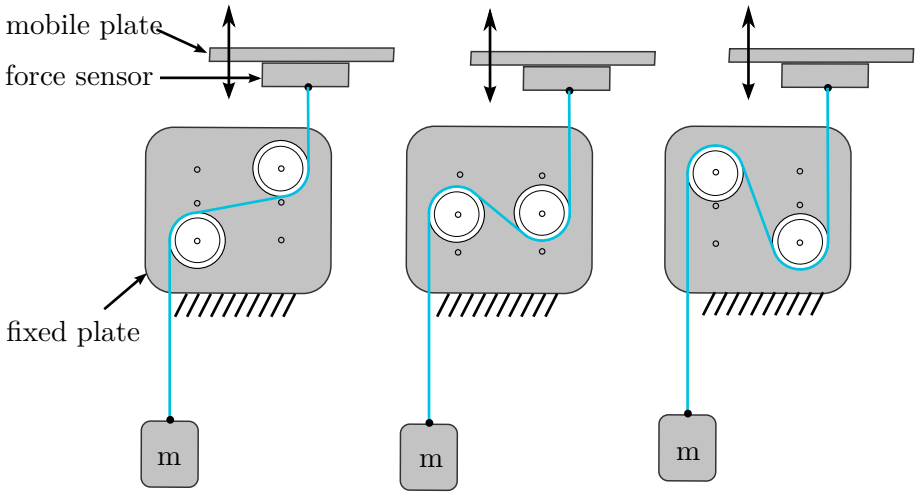

Figure 4.9: Experiment for guiding friction estimation

It appears that the tendon friction force $F_{friction} \in \mathbb{R}^+$ can be approximated by equation,

$$F_{friction} = C_0(1 - e^{-C_1\alpha}), \tag{4.1}$$

where $\alpha \in \mathbb{R}^+$ is the total bending angle and $(C_0, C_1) \in \mathbb{R}^2$ are calibration constants.

The measurements have been performed with a special tendon pulling machine [118] that offers controlled displacements and accurate force measurements. In all tests the friction force is estimated to be the steady-state pulling force during a saw shaped motion. Other experiments have been performed to compare the sliding friction to the pulley friction so as to give all needed information to the mechanical designers. The tables are available to the mechanical teams in order to decide when to use pulleys (that requires space) or sliding surfaces (more compact but limited to small bending angles). Figure 4.10 and 4.11 are the graphs of such tables.

4.3 Conclusion

This section has presented the tendon stiffness mechanism used for each of the 38 tendons of the forearm. The mechanical construction is an improvement over the original tangent α mechanism in terms of size and complexity. The tendon material has been selected to provide a long lifetime as well as to cope with the small bending radii. It has been experimentally verified that the model based stiffness curve of the mechanism exhibits a good match with the measures. The discrepancies between the theoretical model and the measure are related to the imprecision of the spring constant (given by the manufacturer). The stiffness of the tendon material contributes to the over-

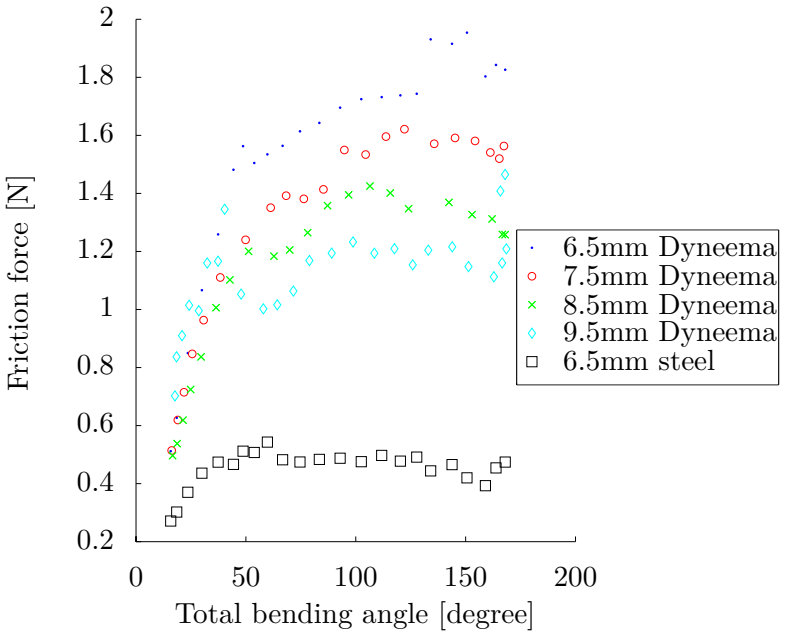

Figure 4.10: Friction force for a single tendon depending on the total bending angle. Pulley diameters and several sliding materials are compared

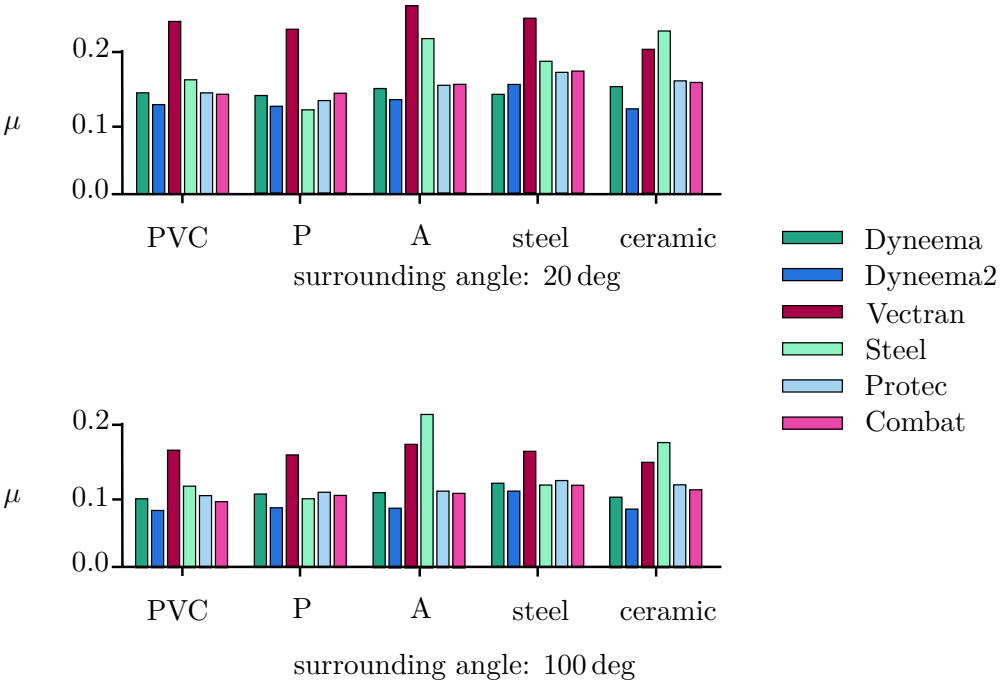

Figure 4.11: Friction coefficient in a sliding experiment for a single tendon depending on the material combinations. P (resp. A) stands for a low friction polymer similar to the one used for the joints (resp. an aluminium alloy).

all stiffness of the mechanism. Therefore, the calibration is performed on the mounted tendon. The real-time implementation uses calibration polynomials to improve the measurement accuracy. A set of characterization experiments has been conducted in order to provide a clear overview of the friction properties of the tendon and the experimental results have been used to establish a model of the tendon friction in the case of rolling and sliding. The model is available to the mechanical engineers. So they have the information needed to decide between the different guiding options.

5 Finger model

In this chapter the mechanical modeling of the fingers is described. First, the homogeneous transformation matrices are derived from the CAD (Computer Aided Design) data. The dynamic model is easily obtained from a symbolic calculation tool, either from the energy expression and the Lagrange method or from the Newton-Euler method. The tendon coupling is presented in detail and is one major novelty of the design. Each of the five fingers has a specific design, but their types can be grouped as follows (cf. Fig. 5.1):

- Base of the thumb (MC: Metacarpal joint, also called TMC: trapezoid metacarpal joint).
- Base of the index, middle, ring, and fifth fingers(MC: Metacarpal joint).
- Medial and distal joints of the thumb, index, middle fingers (PIP: proximal inter-phalangeal and DIP: distal inter-phalangeal joint).
- Medial and distal joints of the ring and fifth fingers (PIP: proximal inter-phalangeal and DIP: distal inter-phalangeal joint).
- Hematometacarpal joint of the fifth finger (HMC: hematometacarpal joint).

Several joint types are used for the fingers. The base joint is a hyperboloid joint (cf. Fig. 5.2) and the PIP and DIP joints are hinges joints (cf. Fig. 5.3).

Those mechanisms have been carefully designed to ensure a maximal robustness while satisfying the functional requirements [98]. The base of the thumb is special since it is using a tensegrity[1] structure to provide an increased torque. The Hematometacarpal joint (HMC) is also very particular since it is realized by a four bar linkage to emulate the anatomical motion. In order to reduce the number of actuators and fit in the forearm, the PIP and DIP joints of the ring and fifth fingers are coupled. Despite the tendon routing differences, the kinematic structures of each finger are identical. Only the bones are different in size and shape.

[1]Tensegrity, tensional integrity or floating compression, is a structural principle based on the use of isolated components in compression inside a net of continuous tension, in such a way that the compressed members (usually bars or struts) do not touch each other and the prestressed tensioned members (usually cables or tendons) delineate the system spatially.

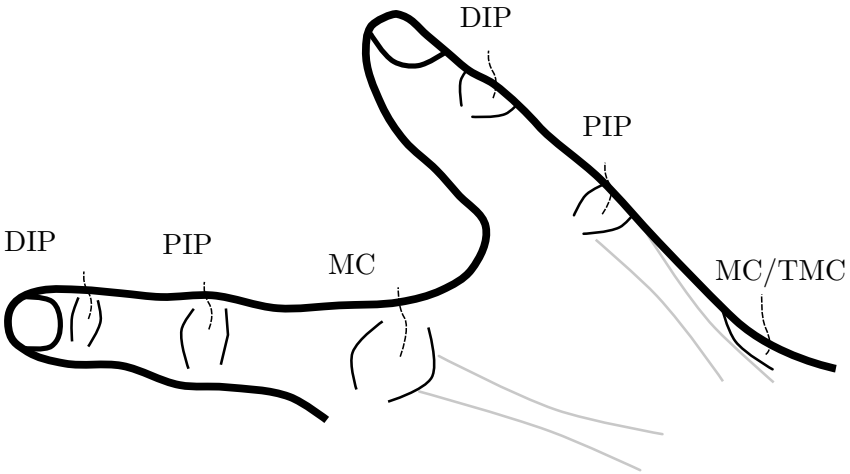

Figure 5.1: Joint names

Figure 5.2: Hyperboloid joint of the finger base

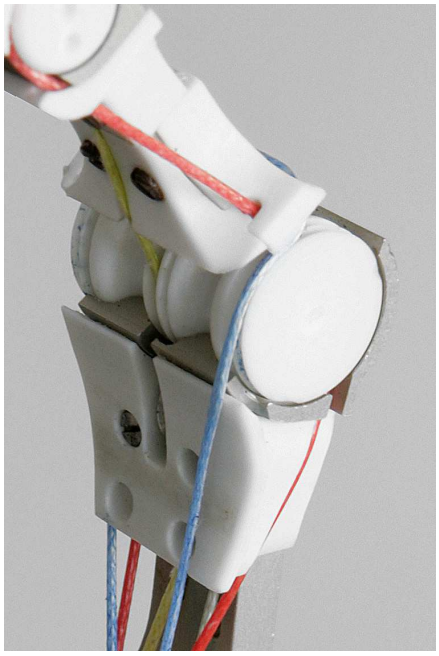

Figure 5.3: Dislocatable hinge joint for the PIP and DIP joints

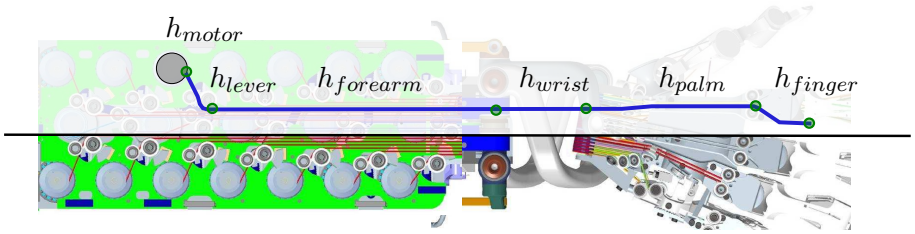

Figure 5.4: Tendon routing of the index finger through the complete forearm

5.1 Tendon routing

The fingers of the hand of the Hand Arm System are actuated by tendons. The tendons are pulled by electromotors that are placed in the forearm. Therefore, the tendons are running in the forearm, crossing the wrist, guided into the palm and finally routed in the finger. The tendons are transmitting the forces of the motors to the joints, thus being one of the most critical component. In order to control the joint torques the transmission chain must be analyzed and modeled. The tendon paths can be divided into six sections (cf. Fig. 5.4).

From figure 5.4 the length of tendon h^i ($i \in [1 \dots 38]$) is

$$h^i = h^i_{motor} + h^i_{lever} + h^i_{forearm} + h^i_{wrist} + h^i_{palm} + h^i_{finger}, \forall i \in [1 \dots 38] \quad (5.1)$$

where:

- h^i_{motor} represents the length of tendon i in the forearm (constant w. r. t. the robot configuration)(cf. Fig. 5.4).
- $h^i_{forearm}$ represents the length of tendon i in the forearm (constant w. r. t. the robot configuration)(cf. Fig. 5.4).
- h^i_{lever} represents the length of tendon h^i in the lever mechanism (depending on the tendon force of the finger)(cf. Fig. 5.4).
- h^i_{wrist} represents the length of tendon h^i in the wrist (depending on the joint angle of the wrist)(cf. Fig. 5.4).
- h^i_{palm} represents the length of tendon h^i in the palm (constant w. r. t. the robot configuration)(cf. Fig. 5.4).
- h^i_{finger} represents the length of tendon h^i in the finger (depending on the joint angle of the finger)(cf. Fig. 5.4, cf. Fig. 5.5).

The length of tendon in the forearm and the palm are independent of the robot configuration and will consequently be *neglected/hidden* in the rest of the thesis. It is interesting to note that, although those sections are of constant length, they depend on the tendon considered. The default length induces a serial stiffness that results in a softer tendon if it is longer. If $E_{dyneema}$[N/m] denotes the Young's modulus of the Dyneema®and $l^i_0, \forall i \in [1 \dots 38]$ is the default length of tendon, the tendon stiffness is given by $k^i_t = E_{dyneema} S / l^i_0, \forall i \in [1 \dots 38]$, where S is the cross-sectional area. It should be noted that the stiffness of the tendon is naturally included in the calibration process since it is performed once the tendon is mounted in the forearm.

5.2 Index, middle, and ring fingers

In this section the modeling of the index, middle, and ring fingers is presented. Due to their specificity, the modeling of the thumb and the fifth finger are deferred and are treated in separate sections.

5.2.1 Kinematic model

The index finger is modeled as a serial kinematic robot. The frames and the joint angle labels relevant for the model are depicted in Fig. 5.6. Table 5.1 reports the numerical values obtained from the CAD. $c_{xi} \in \mathbb{R}, i \in [0..3], x \in [1..5]$ (resp. $s_{xi} \in \mathbb{R}$) is the cosine (resp. the sine) of the joint angle i of finger x. Using some linear algebra, the partial and complete homogeneous transformations are obtained as:

$$ {}^j_i\boldsymbol{T}_x = \prod_{k=i}^{k=j-1} ({}^{k+1}_{k}\boldsymbol{M}_x), \forall (i,j) \in \mathbb{N}^2, \tag{5.2} $$

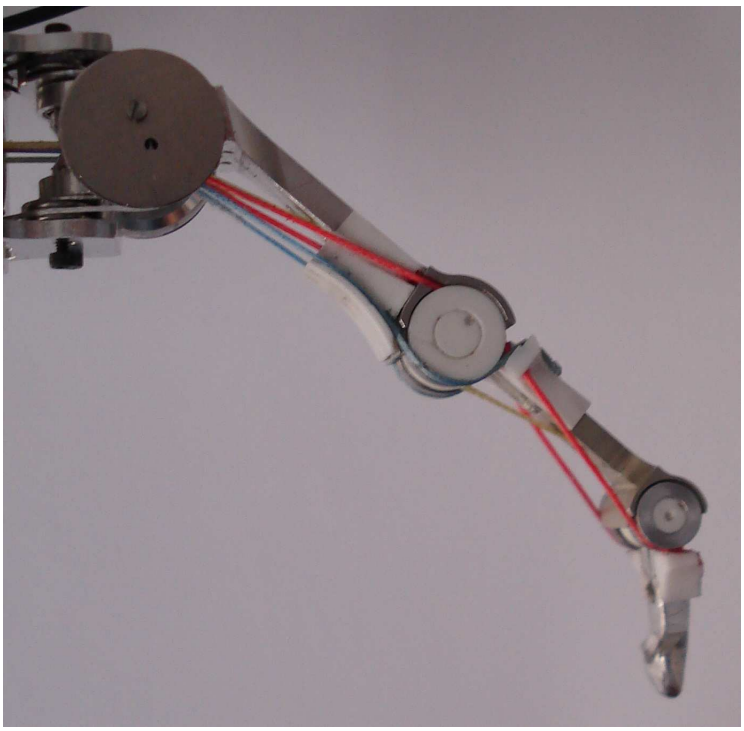

Figure 5.5: Index finger of the Hand Arm System

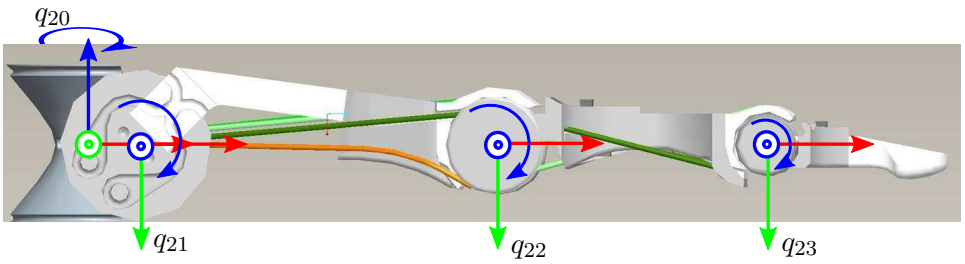

Figure 5.6: Frame definition of the index finger of the Hand Arm System (side view)

$$
{}^{1}_{0}\boldsymbol{M}_{index} = \begin{bmatrix} c20 & -s20 & 0 & 0 \\ s20 & c20 & 0 & 0 \\ 0 & 0 & 1 & 0 \\ 0 & 0 & 0 & 1 \end{bmatrix}
{}^{2}_{1}\boldsymbol{M}_{index} = \begin{bmatrix} 1 & 0 & 0 & 0 \\ 0 & 0 & -1 & 0 \\ 0 & 1 & 0 & 0 \\ 0 & 0 & 0 & 1 \end{bmatrix}
{}^{3}_{2}\boldsymbol{M}_{index} = \begin{bmatrix} 1 & 0 & 0 & 0.006 \\ 0 & 1 & 0 & 0 \\ 0 & 0 & 1 & 0 \\ 0 & 0 & 0 & 0 \end{bmatrix}
$$

$$
{}^{4}_{3}\boldsymbol{M}_{index} = \begin{bmatrix} c21 & -s21 & 0 & 0 \\ s21 & c21 & 0 & 0 \\ 0 & 0 & 1 & 0 \\ 0 & 0 & 0 & 1 \end{bmatrix}
{}^{5}_{4}\boldsymbol{M}_{index} = \begin{bmatrix} 1 & 0 & 0 & 0.04038 \\ 0 & 1 & 0 & 0 \\ 0 & 0 & 1 & 0 \\ 0 & 0 & 0 & 1 \end{bmatrix}
$$

$$
{}^{6}_{5}\boldsymbol{M}_{index} = \begin{bmatrix} c22 & -s22 & 0 & 0 \\ s22 & c22 & 0 & 0 \\ 0 & 0 & 1 & 0 \\ 0 & 0 & 0 & 1 \end{bmatrix}
{}^{7}_{6}\boldsymbol{M}_{index} = \begin{bmatrix} 1 & 0 & 0 & 0.0298 \\ 0 & 1 & 0 & 0 \\ 0 & 0 & 1 & -0.005 \\ 0 & 0 & 0 & 1 \end{bmatrix}
$$

$$
{}^{8}_{7}\boldsymbol{M}_{index} = \begin{bmatrix} c23 & -s23 & 0 & 0 \\ s23 & c23 & 0 & 0 \\ 0 & 0 & 1 & 0 \\ 0 & 0 & 0 & 1 \end{bmatrix}
{}^{9}_{8}\boldsymbol{M}_{index} = \begin{bmatrix} 1 & 0 & 0 & 0.00201 \\ 0 & 1 & 0 & 0 \\ 0 & 0 & 1 & -0.0007 \\ 0 & 0 & 0 & 1 \end{bmatrix}
$$

Table 5.1: Transformations from index base to index fingertip

where i, j are the indices of the frames between which the transformation is calculated. ${}^{j}_{i}\boldsymbol{T}_{x} \in \mathbb{R}^{4\times4}$ is the homogeneous transformation between the frames of index $i \in \mathbb{N}$ and $j \in \mathbb{N}$ of finger x. The matrices ${}^{k+1}_{k}\boldsymbol{M}_{x} \in \mathbb{R}^{4\times4}$ are the partial transformations of the bones or of the joints (in homogeneous coordinates) of the finger x at index k. For example, the transformation from the index base ($x =$ index and $i = 1$) to the index tip ($x =$ index and $j = 9$) is obtained as:

$$
{}^{9}_{0}\boldsymbol{T}_{index} = \prod_{k=0}^{8} ({}^{k+1}_{k}\boldsymbol{M}_{index}) \tag{5.3}
$$

5.2.2 Dynamic model

The Lagrangian L is obtained as $\mathcal{L} = \mathcal{T} - \mathcal{V}$, where $\mathcal{T}$ is the kinetic energy and $\mathcal{V}$ the potential energy due to the gravity. Considering that the forearm is fixed in space, the energy of the motor is reduced to the kinetic energy due to the rotor inertia. The Lagrangian is

$$\mathcal{T} = \frac{1}{2}\sum_{i=1}^{n} M_i v_i(q)^2 + \frac{1}{2}\sum_{i=1}^{n} B_i \dot{\theta}_i^2 + \mathcal{T}_g + \mathcal{T}_e, \tag{5.4}$$

where $n \in \mathbb{N}$ is the number of links, $M_i \in \mathbb{R}$ (resp. $B_i \in \mathbb{R}$) is the mass of the link $i \in \mathbb{N}$ (resp. the inertia of link $i \in \mathbb{N}$ expressed at the center of mass of the link). $v_i \in \mathbb{R}$ (resp. $\dot{\theta}_i \in \mathbb{R}$) is the velocity of the center of mass of link $i \in \mathbb{N}$ expressed in the world coordinates (resp. the rotational velocity of the link $i \in \mathbb{N}$ expressed in the world coordinates). $\mathcal{T}_g$ and $\mathcal{T}_e$ are the potential energy due to gravity and the potential energy due to the elastic storage. The elastic potential has the form $\mathcal{T}_e(\theta, q) = \frac{1}{2}\int k_t(h)h dh$, where $k_t(h)$ is the stiffness of the tendon and $h(\theta, q)$ is the elongation of the tendon.

The Coriolis and centrifugal terms are commonly neglected in hand modeling. This is mostly justified by the short length of the fingers and their small mass. However, in order to verify the assumption, several trajectories with or without the Coriolis and centrifugal terms have been simulated. The motor positions are fixed and the finger is initially deflected 0.1 rad in the second joint (flexion) and it is released at time t=0 s. As expected the finger oscillates and the inertial couplings are generating a motion of the distal links. The first joint is not influenced by the motion and therefore, is remaining at position $q_0 = 0$ rad. A damping of 0.1% was included in the joints. The curves reported in Fig. 5.7 are representing the differences of position in radians for each joint with and without accounting for the Coriolis and centrifugal terms. It can be seen that the simulation error is small compared to the accuracy of the sensors. Therefore, in this thesis, the Coriolis and centrifugal torque covectors are neglected. Similarily, the influence of gravity can be neglected w. r. t. the torques created by the tendons. Indeed, the complete finger mass is about 0.02 kg, with a center at about 0.01 m, which gives a torque of approximatively τ_q =0.02 kg×9.81 N×0.01 m = 0.002 Nm. It represents only 0.3 N to be shared on the base tendon forces.

5.2.3 Tendon coupling

Coupling matrices

The joints are driven by an antagonistic arrangment of tendons (cf. Fig. 5.9). Therefore, in absence of joint friction, the joint can be moved by placing the motors at the proper position (within the joint limits). However,

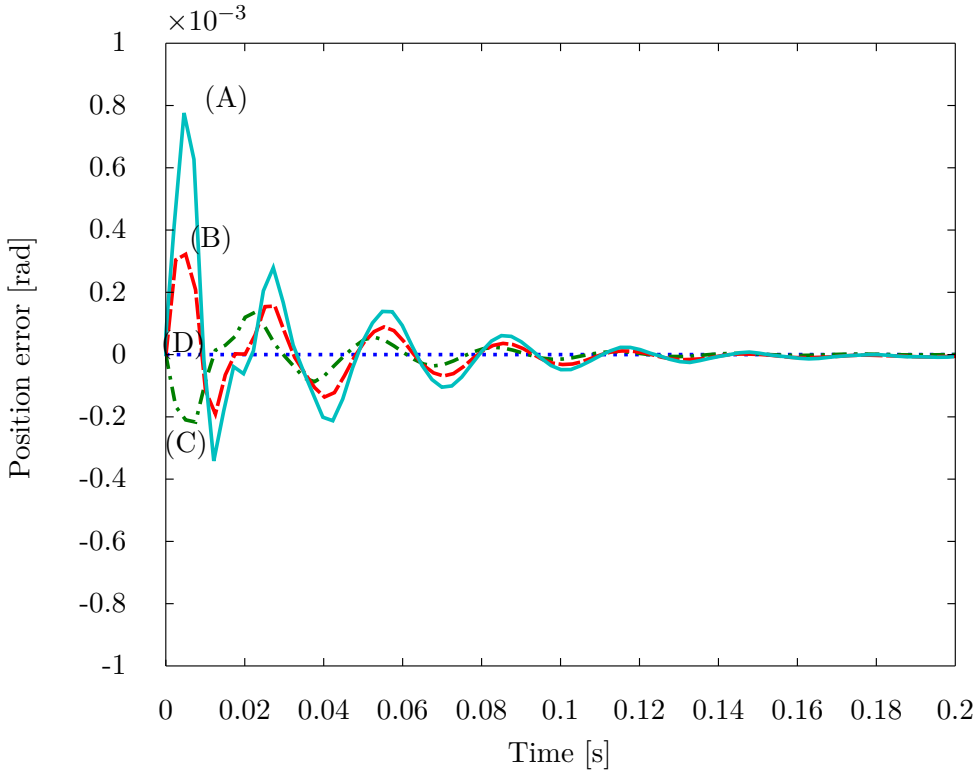

Figure 5.7: Simulation: influence of the Coriolis and centrifugal terms on the link trajectory. The curves illustrate the error between the full model and the simplified model. The base flexion (resp. PIP flexion, DIP flexion and base abduction/adduction) is the light light blue (A) curve (resp. red (B), green (C) and blue (D))

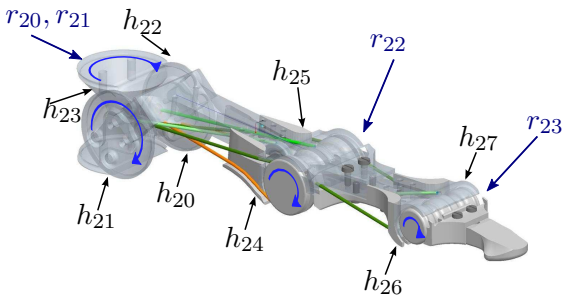

Figure 5.8: Names of the tendons and radii of the pullies of the index finger used to establish eq. (5.22).

without control, a motion of the PIP joint creates a motion of the DIP joint because the DIP tendons are rolling around the PIP joint (cf. Fig. 5.10). The tendon lengths in the finger h_{finger} are obtained from the joint pulley radii:

$$\begin{aligned}
h_{index,1}(\boldsymbol{q}) &= h_{0,index,0} + r_{20}q_{20} + r_{21}q_{21} \\
h_{index,2}(\boldsymbol{q}) &= h_{0,index,1} + r_{20}q_{20} - r_{21}q_{21} \\
h_{index,3}(\boldsymbol{q}) &= h_{0,index,2} - r_{20}q_{20} + r_{21}q_{21} \\
h_{index,4}(\boldsymbol{q}) &= h_{0,index,3} - r_{20}q_{20} - r_{21}q_{21} \\
h_{index,5}(\boldsymbol{q}) &= h_{0,index,4} + r_{22}q_{22} \\
h_{index,6}(\boldsymbol{q}) &= h_{0,index,5} - r_{22}q_{22} \\
h_{index,7}(\boldsymbol{q}) &= h_{0,index,6} + r_{22}q_{22} - r_{23}q_{23} \\
h_{index,8}(\boldsymbol{q}) &= h_{0,index,7} - r_{22}q_{22} + r_{23}q_{23}
\end{aligned} \tag{5.5}$$

where $h_{0,x,i}$, with $i \in [1 \dots 8]$ denotes the initial (arbitrary reference) tendon length in the finger x. $q_i \in \mathbb{R}, i \in [0 \dots 3]$ are the joint angles. $r_{ij} \in \mathbb{R}, (i,j) \in ([1 \dots 5] \times [0 \dots 3])$ are the pulley radii of finger i at joint j (cf. Fig. 5.8).

From the expression of the tendon lengths given in Eq. (5.22), the coupling matrix $\boldsymbol{P}(\boldsymbol{q}) \in \mathbb{R}^{m \times n}$ (for a finger with $n \in \mathbb{N}$ joints driven by $m \in \mathbb{N}$ tendons) is defined as

$$\boldsymbol{P}(\boldsymbol{q}) = \frac{\partial \boldsymbol{h}(\boldsymbol{q})}{\partial \boldsymbol{q}}. \tag{5.6}$$

Equation (5.6) also expresses the relationship between the tendons velocities and the joint velocities:

$$\dot{\boldsymbol{h}} = \boldsymbol{P}(\boldsymbol{q})\dot{\boldsymbol{q}} \tag{5.7}$$

The relation between the motor torques $\boldsymbol{\tau}_\theta \in \mathbb{R}^m$ and the joint torques $\boldsymbol{\tau}_q \in \mathbb{R}^n$ is simply obtained by expressing the work produced by the motors and the work produced by the joints and substituting eq. (5.7).

$$\boldsymbol{\tau}_q = \boldsymbol{P}(\boldsymbol{q})^T \boldsymbol{\tau}_\theta, \tag{5.8}$$

where $\boldsymbol{P}(\boldsymbol{q}) \in \mathbb{R}^{n \times m}$ is the coupling matrix, $\boldsymbol{q} \in \mathbb{R}^n$ is the joint position. $\boldsymbol{\tau}_q \in \mathbb{R}^n$ (resp. $\boldsymbol{\tau}_\theta \in \mathbb{R}^m$) is the joint torque covector (resp. the motor torque covector).

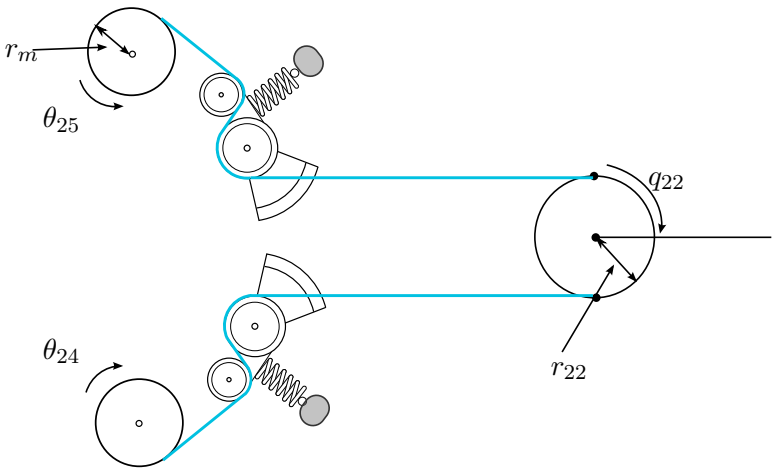

Figure 5.9: Antagonistic model of a joint. Two motors are pulling two tendons guided through the stiffness elements and drive the joint (courtesy of Jens Reinecke).

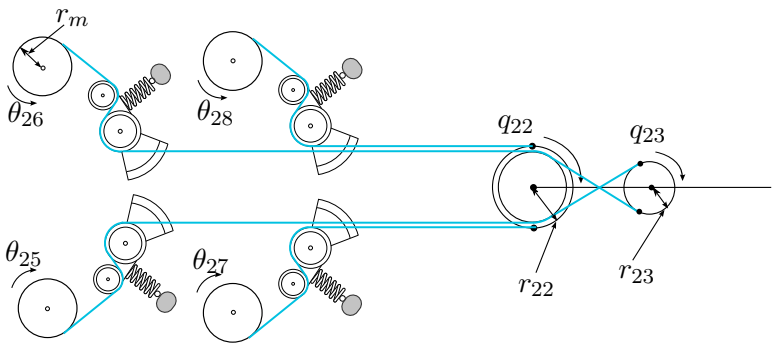

Figure 5.10: Example of the tendon guiding in the PIP and DIP. The total lengths of the tendons are simply obtained because the tendons are rolling on the pulleys.

Applied to the index finger, the coupling matrix is

$$\boldsymbol{P}_{index} = \begin{bmatrix} r_{20} & -r_{21} & 0 & 0 \\ -r_{20} & -r_{21} & 0 & 0 \\ r_{20} & r_{21} & 0 & 0 \\ -r_{20} & r_{21} & 0 & 0 \\ 0 & 0 & -r_{22} & 0 \\ 0 & 0 & r_{22} & 0 \\ 0 & 0 & r_{22} & -r_{23} \\ 0 & 0 & -r_{22} & r_{23} \end{bmatrix}, \tag{5.9}$$

where $(r_{20}, r_{21}, r_{22}, r_{23}) \in (\mathbb{R}^+)^4$ are the radii of the joint pulleys.

Stiffness transformation

The modification of the tendon stiffness modifies the joint stiffness. The joint stiffness matrix $\boldsymbol{K}_q(\boldsymbol{q}) \in \mathbb{R}^{n \times n}$ is by definition:

$$\boldsymbol{K}_q(\boldsymbol{q}) = \frac{\partial \boldsymbol{\tau}_q}{\partial \boldsymbol{q}}. \tag{5.10}$$

The joint torque is obtained from the tendon forces by $\boldsymbol{\tau}_q = \boldsymbol{P}(\boldsymbol{q})\boldsymbol{f}_t$, where $\boldsymbol{P}^T = \frac{\partial \boldsymbol{h}(\boldsymbol{q})}{\partial \boldsymbol{q}}$ leading to

$$\boldsymbol{K}_q(\boldsymbol{q}) = \frac{\partial \boldsymbol{P}(\boldsymbol{q})^T}{\partial \boldsymbol{q}}\boldsymbol{f}_t + \boldsymbol{P}(\boldsymbol{q})^T \frac{\partial \boldsymbol{f}_t^T}{\partial \boldsymbol{q}} \boldsymbol{K}_q(\boldsymbol{q}) = \frac{\partial \boldsymbol{P}(\boldsymbol{q})^T}{\partial \boldsymbol{q}}\boldsymbol{f}_t + \boldsymbol{P}(\boldsymbol{q})^T \frac{\partial \boldsymbol{f}_t^T}{\partial \boldsymbol{h}} \frac{\partial \boldsymbol{h}^T}{\partial \boldsymbol{q}}. \tag{5.11}$$

By definition of the coupling matrix and defining $\boldsymbol{K}_t \in \mathbb{R}^{m \times m}$ ($\boldsymbol{K}_t(i,i) = k_{t_i}$, 0 otherwise, where $k_{t_i} \in \mathbb{R}^+, \forall i \in [0 \dots m-1]$ is the individual tendon stiffness), the stiffness transformation from tendon to link is

$$\boldsymbol{K}_q = \frac{\partial \boldsymbol{P}(\boldsymbol{q})^T}{\partial \boldsymbol{q}}\boldsymbol{f}_t + \boldsymbol{P}(\boldsymbol{q})^T \boldsymbol{K}_t \boldsymbol{P}(\boldsymbol{q}). \tag{5.12}$$

In a case of a position independent coupling matrix, i. e. constant pulley radii, the equation simplifies to

$$\boldsymbol{K}_q = \boldsymbol{P}^T \boldsymbol{K}_t \boldsymbol{P}. \tag{5.13}$$

Link side position

The joints of the fingers do not have a position sensor. On the one hand this provides a high robustness but on the other hand it implies that the link position must be estimated from the tendon displacements. As presented in the spring mechanism section, the change of length of tendon due to the spring mechanism is measured with the magnetic sensor. The displacement

of the tendon due to the motor is easily obtained with the motor position and the pulley radius. Therefore, the tendon displacement at the finger base is measured. The problem is mathematically formulated as

$$\min_{\boldsymbol{q}_x} \left(\sum_{i=1}^{8} \left(h_{xi}^{meas} - h_{xi}(\boldsymbol{q}) \right)^2 \right), \tag{5.14}$$

where $\boldsymbol{q}_x \in \mathbb{R}^4$ are the joint angles of finger x. h_{xi}, with $i \in [0 \dots 7]$, are the model-based lengths of the tendons and h_{xi}^{meas}, with $i \in [0 \dots 7]$, are the measured tendon lengths.

The solution $\boldsymbol{q}_x^* \in \mathbb{R}^n$ to the problem of eq.(5.14) is known to be obtained from the pseudo inverse of $\boldsymbol{P}_x \in \mathbb{R}^{n \times m}$,

$$\boldsymbol{q}_x^* = \boldsymbol{P}_x^+ \boldsymbol{h}^{meas} + \boldsymbol{q0}_x, \tag{5.15}$$

where $\boldsymbol{P}_x^+ = \boldsymbol{P}_x(\boldsymbol{P}_x \boldsymbol{P}_x^T)^{-1}$ is the Moore-Penrose pseudo inverse of the coupling matrix $\boldsymbol{P}_x$ of finger x. $\boldsymbol{h}_x^{meas} \in \mathbb{R}^m$ is the vector of the measured tendon lengths and $\boldsymbol{q0}_x \in \mathbb{R}^n$ is some arbitrary reference position of the joints. It is important to note that the pseudo inverse is always well defined since $\boldsymbol{P}_x$ is constant and matrix has full column rank.

5.3 Ring and fifth fingers

In this section, the specificity of the ring and fifth finger couplings are discussed. The kinematic and dynamic modeling only need minor modifications. Similarily, the tendon couplings need to be modified to account for the reduced count of tendons.

5.3.1 Kinematic model

The kinematic models are derived using homogeneous transformation matrices. The only required modification is to replace the joint angles q_{43} (resp. q_{53}) by its expression in terms of q_{42} (resp. q_{52}). The needed relationships, obtained from the pulley radii, are reported in Equation (5.17).

$$q_{43} = \frac{r_{43}}{r_{42}} q_{42} \tag{5.16}$$

$$q_{53} = \frac{r_{53}}{r_{52}} q_{52} \tag{5.17}$$

5.3.2 Dynamic model

In order to establish the dynamic equations, two methods are available. A first method consists in replacing the relationship of (5.17), the bone transformations, and the inertias in the dynamic model of the index finger.

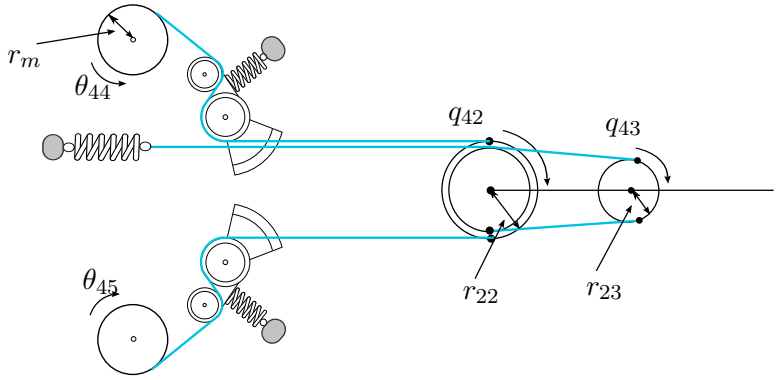

Figure 5.11: Mechanical realization of the PIP/DIP coupling of the ring and fifth fingers (case of the ring finger)

The second method consists in modifying the expression of the kinetic energy and the potential energy in the Lagrangian. Both methods are leading to the same results. However, the second method leads to a more efficient formulation of the dynamics.

5.3.3 Tendon coupling

As mentioned above, the ring and fifth fingers have a mechanical coupling between the PIP and DIP joints. In other words, the two joints are actuated by only 2 motors. Figure 5.11 depicts the mechanical realization of the underactuated joint. The coupling matrix $\boldsymbol{P}_4 \in \mathbb{R}^{6\times 3}$ is obtained by expressing the tendon lengths of the ring, $h_{4i}(\boldsymbol{q})$, with $i \in [0 \dots 5]$, and deriving them with respect to the joint positions $\boldsymbol{q}_{4i}$ ($i \in [0 \dots 3]$). According to the notations of Figure 5.11, the coupled tendon lengths are

$$\begin{array}{rcl} h_{44}(\boldsymbol{q}) & = & h0_{44} + r_{42}q_{42} \\ h_{45}(\boldsymbol{q}) & = & h0_{45} - r_{42}q_{42} \\ h_{46}(\boldsymbol{q}) & = & h0_{46} + (r_{42} + r_{43})q_{42} \\ h_{47}(\boldsymbol{q}) & = & h0_{47} - (r_{42} + r_{43})q_{42}, \end{array} \tag{5.18}$$

where $h0_{4i}$, with $i \in [0 \dots 7]$ denotes the initial (arbitrary reference) tendon length in the ring finger. $q_{4i} \in \mathbb{R}, i \in [0 \dots 3]$ are the joint angles. $r_{4j} \in \mathbb{R}$, with $j \in [1 \dots 5]$ are the pulley radii of the ring finger at joint j (the case of the fifth finger is obtained by replacing 4 by 5 in the previous expressions).

5.4 Thumb

According to numerous biomechanical authors [119–121] the hand would not be more than a spatula if it were not for the thumb. Anthropologists, like Kuczynski, have assumed that the thumb is what makes the human brain so

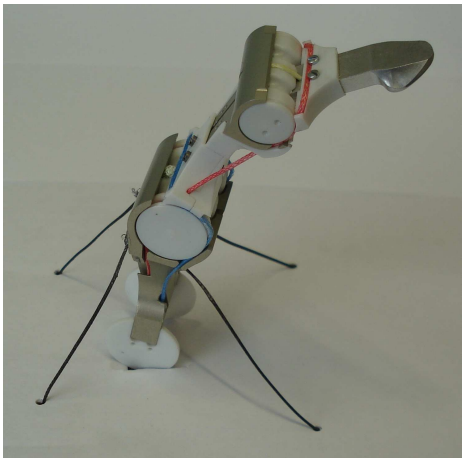

Figure 5.12: Thumb of the Hand Arm System

different from the monkeys. Intuitively, it is obvious that a poorly designed (or poorly controlled) thumb jeopardizes most of the hand functionality. Therefore, the modeling and control of the thumb of the Hand Arm System is one of the focus of this section.

The thumb has been carefully designed and several guidelines have been published in [122]. Very recent work also demonstrated the grasping capabilities of the hand [123]. The thumb PIP and DIP joints are similar to the other fingers but is using larger pulley radii to increase the maximum torques. The base, however, has a different structure. As depicted in Figure 5.12, the joint is driven by four tendons that are emerging from the palm and directly connected below the PIP joint. This structure, called a tensegrity structure, provides an increased maximum joint torque (through the increased moment arm).

The structure creates a nonlinear relationship between the base joint positions $(q_{11}, q_{12}) \in \mathbb{R}^2$ and the tendon lengths $h_{1i} \in \mathbb{R}, i \in [0 \dots 3]$.

5.4.1 Kinematic model

The kinematics of the thumb is computed from the homogeneous transformations of the joints and the bones. The difference with the index finger is that the partial transformation to the base of the PIP (${}^0_4\boldsymbol{T}_{thumb}$) will be used to compute the tendon coupling.

5.4.2 Dynamics model

The dynamical equations of the thumb are obtained from the kinematic equations and the inertia properties of each link. Since the inertia of the tendon is neglectable, there is no difference with the case of the index finger.

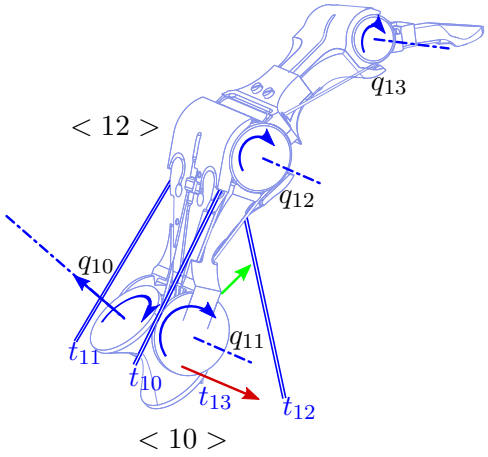

Figure 5.13: Joint axis and tendon names of the thumb of the Hand Arm System

5.4.3 Tendon coupling

Contrarily to the other fingers, the coupling of the thumb is nonlinear and position dependent.

The base joints (q_{10}, q_{11}) are driven by a set of four tendons that are directly inserted below the PIP joint (cf. Fig. 5.14). In order to express the lengths (or the change of lengths) of the base tendons, the coordinates of the tendon insertions points must be expressed in the same coordinate system. To this end the following steps are performed:

- the transformation from the thumb base coordinate system (cf. Fig. 5.13, frame $\{10\}$) to the coordinate system of the PIP base is extracted from the forward kinematics.

- the tendon insertion coordinates $[{}^{12}\boldsymbol{p}_{1i}, 1] \in \mathbb{R}^4, \quad i \in [0 \dots 3]$ (expressed in $\{12\}$) are transformed to the base frame $\{10\}$ with,

$$[{}^{10}\boldsymbol{p}_{1i}, 1] = {}^{12}_{10}\boldsymbol{T}[{}^{12}\boldsymbol{p}_{1i}, 1], \quad \forall i \in [0 \dots 3] \tag{5.19}$$

  where ${}^{12}_{10}\boldsymbol{T} \in \mathbb{R}^{4\times4}$ is the homogeneous transformation from $\{12\}$ to $\{10\}$.

The coordinates of the distal (resp. palmar) insertion of the tendons are more conveniently denoted A, B, C and D (resp. A_0, B_0, C_0 and D_0, cf. Fig. 5.14). The coordinates are reported in Table 5.2. The tendon lengths

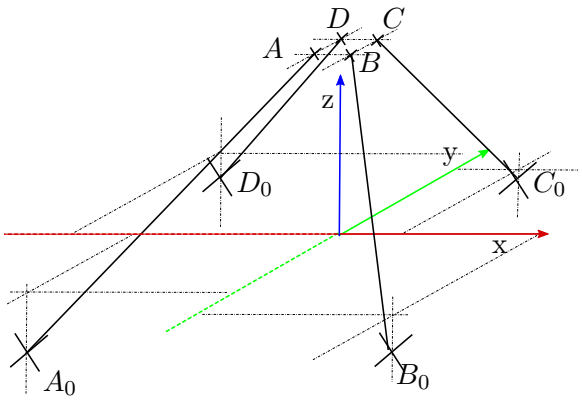

Figure 5.14: Thumb of the Hand arm system

Table 5.2: Coordinates of the bone insertion points for the tendons

Point	Coordinates [m]
A_0	$[0.002, 0.030, -0.025]$
B_0	$[0.002, 0.030, 0.025]$
C_0	$[0.002, -0.030, -0.025]$
D_0	$[0.002, -0.030, 0.025]$
A	$[0.002, 0.030, -0.025]$
B	$[0.002, 0.030, 0.025]$
C	$[0.002, -0.030, -0.025]$
D	$[0.002, -0.030, 0.025]$

$h_{1i}(\boldsymbol{q}) \in \mathbb{R}, \quad i \in [0 \dots 3]$ of the thumb base are obtained as

$$\begin{aligned} h_{thumb,0} &= |A(q_{10}, q_{11}) - A_0| \\ h_{thumb,1} &= |B(q_{10}, q_{11}) - B_0| \\ h_{thumb,2} &= |C(q_{10}, q_{11}) - C_0| \\ h_{thumb,3} &= |D(q_{10}, q_{11}) - D_0|. \end{aligned} \tag{5.20}$$

The PIP and DIP tendons are going through the base and rolling on the PIP and DIP joints. Therefore, their length is linearly dependent on the finger position.

Applied to the thumb finger, the coupling matrix has a block diagonal shape (cf. Fig. 5.15). The lower right part (i. e. the PIP and DIP couplings) is

$$\boldsymbol{P}_{thumb}([3:4],[5:8]) = \begin{bmatrix} -r_{12} & 0 \\ r_{12} & 0 \\ r_{12} & -r_{13} \\ -r_{12} & r_{13} \end{bmatrix}, \tag{5.21}$$

The submatrix selection is following MATLAB®convention[2]. The complete tendon lengths are

$$\begin{aligned} h_{thumb,0} &= h0_{thumb,0} + |A(q_{10}, q_{11}) - A_0| \\ h_{thumb,1} &= h0_{thumb,1} + |B(q_{10}, q_{11}) - B_0| \\ h_{thumb,2} &= h0_{thumb,2} + |C(q_{10}, q_{11}) - C_0| \\ h_{thumb,3} &= h0_{thumb,3} + |D(q_{10}, q_{11}) - D_0| \\ h_{thumb,4} &= h0_{thumb,4} + r_{12}q_{12} \\ h_{thumb,5} &= h0_{thumb,5} - r_{12}q_{12} \\ h_{thumb,6} &= h0_{thumb,6} - r_{12}q_{12} + r_{13}q_{13} \\ h_{thumb,7} &= h0_{thumb,7} + r_{12}q_{12} - r_{13}q_{13}. \end{aligned} \tag{5.22}$$

where $h0_{thumb,i}$ with $i \in [0..7]$ is the initial tendon length when the finger is at its reference position (i. e. $\boldsymbol{q} = \boldsymbol{q0}$), (r_{12}, r_{13}) are the radii of the joint pulleys. The coupling matrix $\boldsymbol{P}_{thumb} \in \mathbb{R}^{4\times 8}$ is obtained by taking the partial derivative of the tendon length $h_{thumb,i}$ with $i \in [0..7]$ w. r. t. the joint position q_{1j} with $j \in [0..3]$.

Stiffness transformation

The equation for the stiffness transformation from tendon stiffness to joint stiffness is identical to the ones of the index finger. However, since the

[2]Indexing is one based, in (5.21) the selection consists of the two last columns and the four last lines

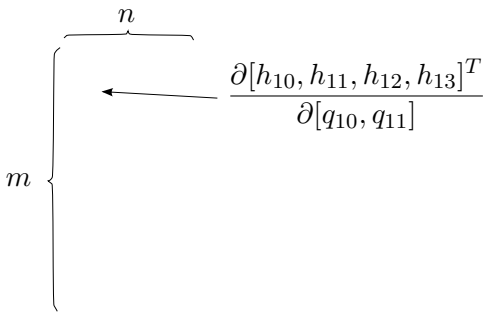

Figure 5.15: Structure of the coupling matrix

coupling matrix is depending on the base position, the generic form must be used,

$$\boldsymbol{K}_q = \frac{\partial \boldsymbol{P}(\boldsymbol{q})^T}{\partial \boldsymbol{q}} \boldsymbol{f} + \boldsymbol{P}(\boldsymbol{q})^T \boldsymbol{K}_t \boldsymbol{P}(\boldsymbol{q}), \tag{5.23}$$

where $q \in \mathbb{R}^n$ is the vector of joint position. $\boldsymbol{K}_q \in \mathbb{R}^{n \times n}$ (resp. $\boldsymbol{K}_t \in \mathbb{R}^{m \times m}$) is the joint stiffness matrix (resp. the diagonal stiffness matrix of the tendons). $\boldsymbol{P}(\boldsymbol{q}) \in \mathbb{R}^{m \times n}$ is the position dependent coupling matrix. $\boldsymbol{f} \in \mathbb{R}^m$ is the vector of tendon forces.

Link position estimation

As in the case of the fingers, the thumb does not have a position sensor. But the pseudo inversion that was used for the linear couplings can not be used for the thumb. Indeed, the coupling matrix is position dependent and the solution to the least square problem is not anymore a simple pseudo inversion. The problem is mathematically formulated as

$$\min_{\boldsymbol{q}} \left(\sum_{i=1}^{7} \left(\hat{h}_{1i} - h_{1i}(\boldsymbol{q}) \right)^2 \right), \tag{5.24}$$

where $q_{1i} \in \mathbb{R}$ with $i \in [0 \dots 3]$ are the base joint angles, h_{1i} with $i \in [0 \dots 7]$ (resp. $\hat{h}_{1i}$) are the analytic length of the tendon i of the thumb (resp. the measured tendon lengths). However, the structure of the thumb implies that only the four base tendons are involved in the nonlinear, position dependant coupling. Therefore, the link side position estimation for the PIP and DIP joints of the thumb are similar to the one of the index finger.

The position estimation for the base must be realized online and therefore has been implemented as a fixed step gradient search. The algorithm is reported in the pseudo code Algorithm 1.

In order to evaluate the algorithm, a grid of tendon position vectors is generated from the kinematic model. The algorithm is evaluated on this vector grid and the resulting joint positions are compared to the ground

Algorithm 1 Pseudo Code of the gradient search algorithm use to estimate the link side position

$B \Leftarrow \ker P$
$\alpha \Leftarrow \alpha_0$
$grad \Leftarrow grad_0$
$step \Leftarrow step_0$
$C_{best} \Leftarrow +\inf$
for $i = 1$ to 50 **do**
  $C, grad \Leftarrow cost_\alpha(\alpha - grad.step)$
  if $C < C_{best}$ **then**
    $\alpha \Leftarrow \alpha - grad.step$
  else
    $step \Leftarrow \frac{step}{2}$
  end if
end for

truth. Fig. 5.16 depicts the results obtained with 30 steps. The two axes are representing the joint angles for the flexion/extension q_{10} and abduction/adduction q_{11} motions. The red circles are the original points and the blue crosses are the estimated coordinates.

In order to check the robustness for the real implementation, a set of vectors with a noise (the amplitude of the noise was 0 [mm], 0.5[mm] and 1[mm]) to simulate the measurement inaccuracy is evaluated. The number of steps is also modified in order to select the optimal value for the real time code. Unlike the implemented code, the search is always started from $(q_{10}, q_{11}) = [0, 0]$, which explains the incorrect results far from the origin. The results are reported in Fig. 5.17. The required number of iterations is easily achieved in real time. Moreover when using the previous solution as a starting point the search always reaches the minimum step size after only a few iterations.

5.5 Hematometacarpal joint

Because the design of a robotic hand is challenging, most of the designs are not spending as much effort in designing the fifth finger as for the other fingers. In the hand of the Hand Arm System the fifth finger base joint received a particular attention. The hematometacarpal joint, i. e. the joint between the fifth finger metacarpal and the palm, has been designed as a four bars linkage mechanism. This allows to mimic the human metacarpal motion and especially provides a locking motion towards the palm center when the joint limits are reached.

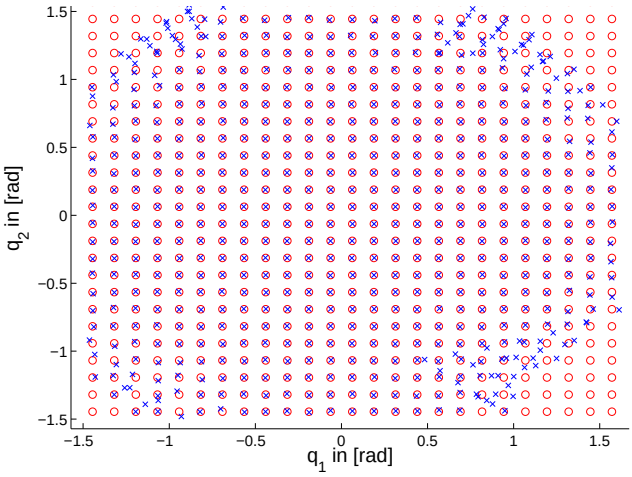

Figure 5.16: Link position estimation : gradient search results with 30 iterations. The red circles are the original points and the blue crosses are the estimated coordinates. The search was always started from (0,0) which explains the errors in the corners. In practice the last value is used as a starting point.

5.6 Conclusion

This chapter presented the modeling of the fingers. The kinematics are obtained from the bone transformations and homogenous transformations. The dynamics are obtained from the systematic Newton-Euler method. The tendon path through the forearm, the wrist, the palm and the fingers is used to derived the coupling matrices. The coupling matrices are further used to estimate the joint positions. However, the special actuation of the thumb by a tensegrity structure creates a nonlinear problem that has been solved with a realtime projected gradient algoritm.

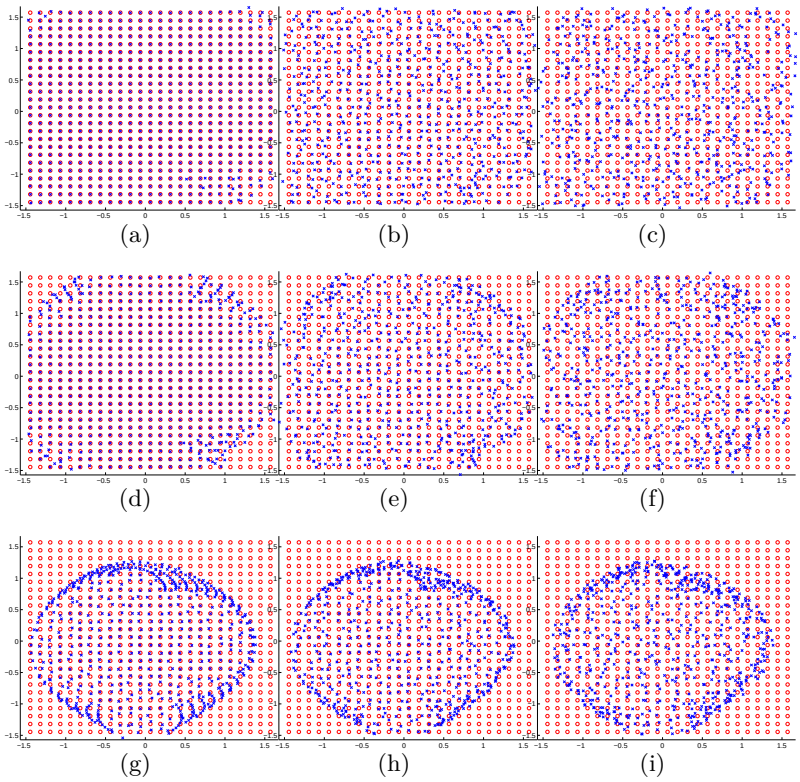

Figure 5.17: Results of the link position estimation with different step size and step count. In each plot, the x and y axis are representing the base joint angle q_{10} and q_{11}. The red circles denote the coordinates used for generation of the tendon length set. The blue crosses depict the result. Ideally, the crosses and circles should match. 5.17a : 50 iterations, 0mm noise. 5.17b : 50 iterations, 0.5mm noise. 5.17c : 50 iterations, 1mm noise. 5.17a : 30 iterations, 0mm noise. 5.17b : 30 iterations, 0.5mm noise. 5.17c : 30 iterations, 1mm noise. 5.17a : 15 iterations, 0mm noise. 5.17b : 15 iterations, 0.5mm noise. 5.17c : 15 iterations, 1mm noise.

6 Wrist Model

The arm and the hand are connected with a wrist, which is actuated with an helping antagonistic concept [2]. Since the motors are located in the forearm all the tendons are guided from the motors to the fingers through the wrist. Therefore, the wrist must withstand the combined load of all the tendons and has been designed to support up to $8000N$ (the weight of a small car). Desirably, all the tendons would go through a unique point and no coupling would be introduced by the wrist motion. However, it is mechanically not possible to let 38 tendons cross at a unique point in space (the tendon would be damaged by the contact to other tendons). Consequently, the wrist is using two layers of 19 tendons that are spaced along the width of the wrist (see Fig. 6.1). Since the wrist can bend along two directions, each tendon should be guided by two pullies in each side of the wrist. The required total of 76 pulleys as well as the space required for their mounting did not allow for this optimal solution (in terms of friction and guiding). The selected solution guides the tendons only along the flexion extension axis of the wrist. The missing lateral guiding is ensured by the flanges of the pulleys and some mechanical grid that ensures that the tendons are not jumping to a different tendon path. Although the solution is suboptimal in terms of tendon guiding, it provides a compact wrist. Moreover, when limited to small abduction/adduction angles (which is the normal case), no significant friction is added. The tendons are not going through the center of rotation of the wrist (which is, as established below, moving over time), thus a motion of the wrist, if not compensated by the controller, creates a motion of the fingers. The change of length of tendon in the wrist must be calculated to have the possibility to compensate this effect using, for example, a feedforward term.

6.1 Kinematic model

This section concentrates on the kinematic modeling of the wrist. The method is explained step by step to tackle the overall complexity of the calculations. The wrist structure can be seen as a double inverted parallelogram. The frames and the angle labels relevant for the model are depicted in Fig. 6.2 and Fig. 6.3. The numerical values and symbols used for the wrist modeling are reported in Table 6.1.

The method can be decomposed as follows:

- Solving a single parallelogram problem in a plane defined by the wrist flexion/adduction axis (calculating t_C).
- Creating a temporary frame.

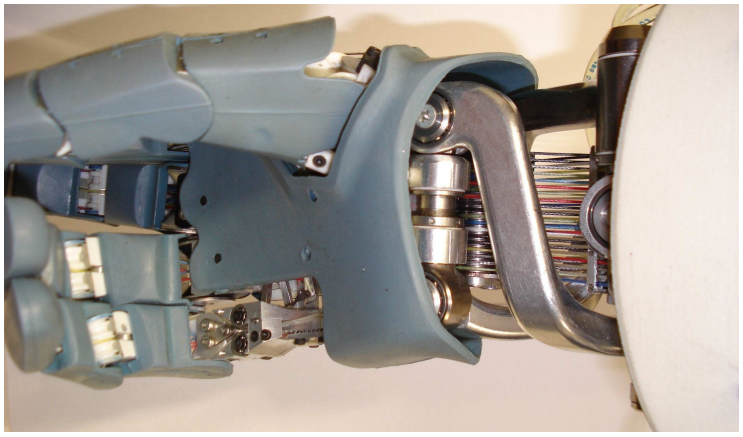

Figure 6.1: Wrist of the hand arm system. The two groups of 19 tendons are going through the wrist

Table 6.1: Wrist symbol definitions, units and values

Symbol	Description	Unit	Value
a	wrist length	$[m]$	0.050
b	wrist width	$[m]$	0.042
c	wrist thickness	$[m]$	0.036

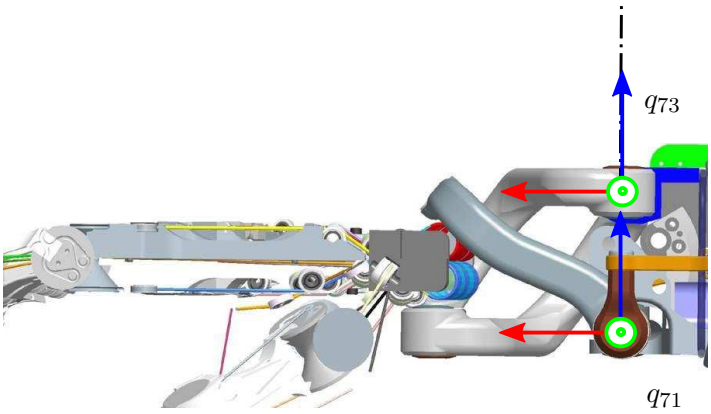

Figure 6.2: Side view of the wrist (CAD)

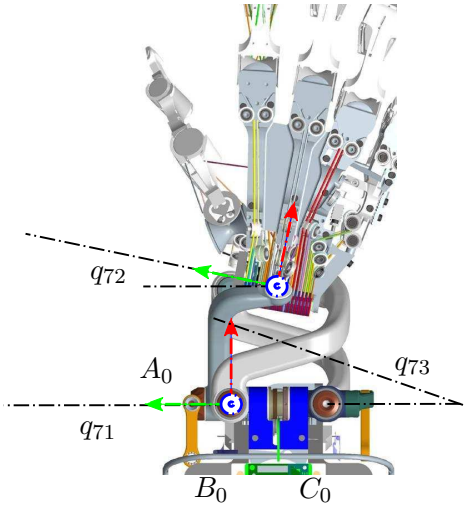

Figure 6.3: Top view of the wrist (CAD)

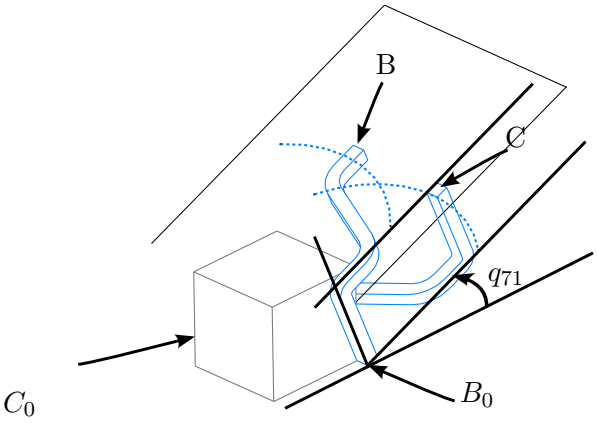

Figure 6.4: BC plane transformation (CAD)

- Expressing the distance constraint between two points in the coordinate system of the temporary frame (The point $\boldsymbol{A}$ in the palm and $\boldsymbol{A}_0$ in the forearm).
- Solving the distance constraint and transforming the coordinates of the solution into the forearm frame $\{0\}$.
- Building a frame $\{ABC\}$ from the coordinates of the 3 points of the palm $(\boldsymbol{A}, \boldsymbol{B}, \boldsymbol{C})$.

6.1.1 Calculation of angle t_C

The first step consists in solving the parallelogram problem defined in the upper plane of the wrist (cf. Fig. 6.4). As depicted in Fig. 6.5, the

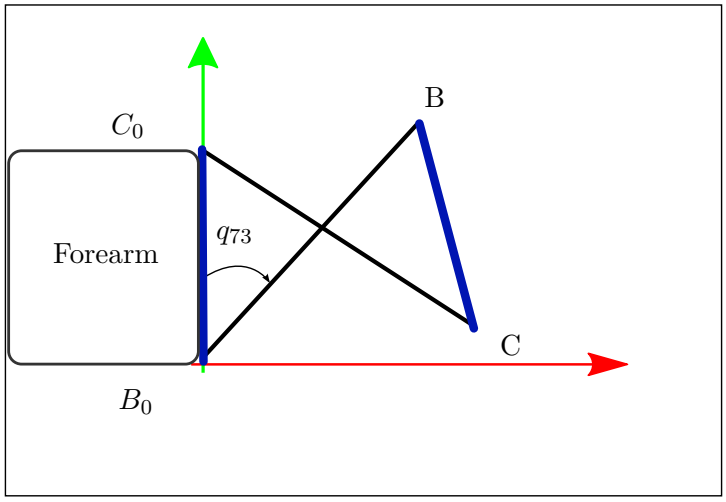

Figure 6.5: Distance constraints between $\boldsymbol{B}$ and $\boldsymbol{C}$ in the plane

coordinates of $\boldsymbol{B}$ and $\boldsymbol{C}$ can be expressed as

$$\boldsymbol{B} : \begin{cases} R_{BB_0} cos(t_B) \\ R_{BB_0} sin(t_B) \end{cases} \quad \text{and} \quad \boldsymbol{C} : \begin{cases} R_{CC_0} cos(t_C) \\ R_{CC_0} sin(t_C) \end{cases} \tag{6.1}$$

where $t_B = \frac{\Pi}{2} - q_{73}$ is the measure of the internal wrist angle obtained with a potentiometer. $t_C \in \mathbb{R}$ (resp. $t_B \in \mathbb{R}$) is an arbitrary parametrization of the circle of center $\boldsymbol{C}$ (resp. $\boldsymbol{B}$), $R_{BB_0} \in \mathbb{R}$ (resp. $R_{CC_0} \in \mathbb{R}$) is the radius of the circle of center $\boldsymbol{B}$ (resp. of center $\boldsymbol{C}$). But $\boldsymbol{B}$ and $\boldsymbol{C}$ are rigidly linked at a constant distance $D_{BC} \in \mathbb{R}$. Mathematically, the constraint on the length BC is:

$$\|BC\|^2 = (R_{BB_0} sin(q_3) - R_{CC_0} cos(t_C))^2 + (R_{BB_0} cos(q_3) - R_{CC_0} sin(t_C))^2 = D_{BC}^2. \tag{6.2}$$

Solving eq. (6.2) for q_3 gives two solutions,

$$\begin{aligned} t_C &= \arctan(\sin(t_B), \cos(t_B)), \\ t_C &= \arctan\left(\frac{(BC^2 + BB_0^2)\sin(t_B) - 2BB_0BC}{(BB_0^2 - BC^2)\cos(t_B)}\right). \end{aligned} \tag{6.3}$$

The first solution is the symmetric from $\boldsymbol{B}$ and therefore should be discarded. The second solution, once injected in the Equation of C (eq. (6.1)), yields

$$\boldsymbol{C} : \begin{cases} \dfrac{BB_0(BB_0^2 - BC^2)cos(t_B)}{-2BB_0BC\sin(t_B) + BC^2 + BB_0^2} \\ \dfrac{(BB_0^2 - BC^2)(BB_0 sin(t_B) - BC)}{-2BB_0BC\sin(t_B) + BC^2 + BB_0^2} \end{cases}. \tag{6.4}$$

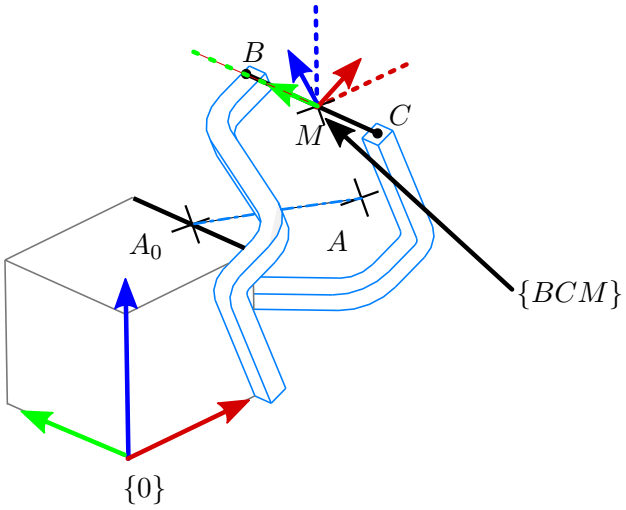

Figure 6.6: BC plane transformation with $\alpha = 0$ (CAD). A is located on a circle defined by $\|AB\| = \|AC\|$

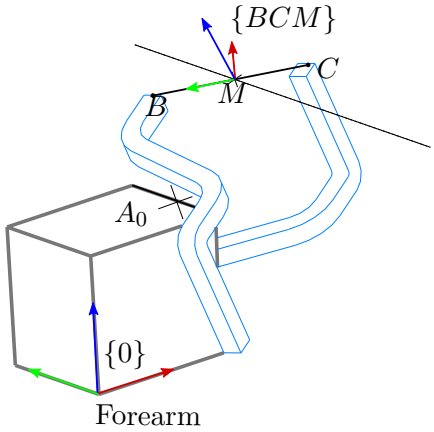

Figure 6.7: BC plane transformation with $\alpha = 30\,\text{deg}$ (CAD)

6.1.2 Calculation of angle t_A

The coordinates of the points $\boldsymbol{B}$ and $\boldsymbol{C}$ are known in the world coordinate system. Three distances constraints are left in order to determine the position of the last point of the palm $\boldsymbol{A}$: $\|AA_0\|$, $\|AB\|$, $\|AC\|$. However, a direct attempt to express and solve the constraints with a symbolic calculation tool failed. As depicted in Fig. 6.7 a coordinate system $\{BCM\}$ can be constructed. $\boldsymbol{M}$ is the middle of BC. $\boldsymbol{x}$ is aligned with MC, $\boldsymbol{z}$ is normal to the plane rotated around $\boldsymbol{x}$ (the original wrist frame) by an amount of q_{71}. $\boldsymbol{y} = \boldsymbol{z} \times \boldsymbol{x}$ simply completes the frame. It is interesting to remark that the distance constraints $\|AB\|$ and $\|AC\|$ are geometrically equivalent to saying that $\boldsymbol{A}$ is located on a circle (cf. Fig. 6.6, non degenerated intersection of two spheres), centered in M and in the plane orthogonal to BC containing $\boldsymbol{M}$ (because $\|AB\| = \|AC\|$). Based on this interpretation, the coordinates of $\boldsymbol{A}$ in $\{BCM\}$ have the simple form:

$$ {}^{BCM}\boldsymbol{A} : \begin{cases} x = 0 \\ y = R_{AA_0} cos(t_A) \\ z = R_{AA_0} sin(t_A) \end{cases} \tag{6.5} $$

The coordinates of $\boldsymbol{A}_0$ (in the coordinate system $\{BCM\}$), ${}^{BCM}\boldsymbol{A}_0$ are obtained with the transformation:

$$ [{}^{BCM}\boldsymbol{A}_0, 1] = {}^{BCM}_{0}\boldsymbol{T}[{}^{0}\boldsymbol{A}_0, 1] \tag{6.6} $$

where ${}^{0}\boldsymbol{A}_0$ (resp. ${}^{BCM}\boldsymbol{A}_0$) are the coordinates of A_0 in the frame $\{0\}$ (resp. $\{BCM\}$) and ${}^{BCM}_{0}\boldsymbol{T}$ is the homogeneous transformation matrix from the coordinate system $\{0\}$ to the coordinate system $\{BCM\}$.

$$ (A_{0x})^2 + (A_{0y} - R_{AA_0} cos(t_A))^2 + (A_{0z} - R_{AA_0} sin(t_A))^2 = d^2_{AA_0} \tag{6.7} $$

It remains to solve a distance constraint equation given by Eq. (6.7)) between $\boldsymbol{A}_0$ and A, both expressed in $< BCM >$. The equation is solved for t_A and re-injected in the coordinates of $\boldsymbol{A}$. The coordinates of A in $\{BCM\}$ are transformed back into $\{0\}$ with Eq. (6.8).

$$ [{}^{0}\boldsymbol{A}, 1] = {}_{BCM}{}^{0}\boldsymbol{T}[{}^{BCM}\boldsymbol{A}, 1] \tag{6.8} $$

where ${}^{0}\boldsymbol{A}$ (resp. ${}^{BCM}\boldsymbol{A}$) are the coordinates of A in the frame $\{0\}$ (resp. $\{BCM\}$) and ${}_{BCM}{}^{0}\boldsymbol{T}$ is the homogeneous transformation matrix from the coordinate system $\{BCM\}$ to the coordinate system $\{0\}$.

Finally, $\boldsymbol{A}$, $\boldsymbol{B}$ and $\boldsymbol{C}$ are used to build the palm base frame $\{ABC\}$, as depicted in Fig. 6.8. The lengths of the different tendons through the wrist are easily expressed from the frames $\{ABC\}$ and $\{A_0B_0C_0\}$.

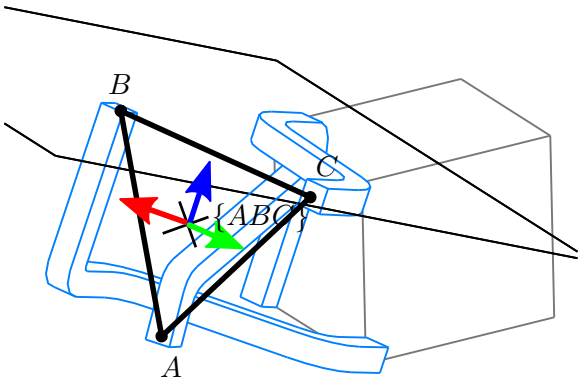

Figure 6.8: Palm frame ABC

Each tendon i with $i \in [1 \dots 38]$ is going through a fixed point in the palm ${}^{ABC}h_{palm,offset,i} \in \mathbb{R}^3$ and a fixed point in the forearm ${}^{0}h_{forearm,offset,i} \in \mathbb{R}^3$. Expressing the coordinates of the palm point ${}^{ABC}h_{palm,offset,i} \in \mathbb{R}^3$ in the forearm coordinate system $\{0\}$ allows to express the tendon lengths in the wrist

$$h_{wrist,i} = \left\| [{}^{0}h_{forearm,offset,i}, 1] - {}^{0}_{ABC}T[{}^{ABC}h_{palm,offset,i}, 1] \right\|, \qquad (6.9)$$

where ${}^{0}h_{forearm,offset,i}, i \in [1 \dots 38]$ and ${}^{ABC}h_{palm,offset,i}, i \in [1 \dots 38]$ are defined in the Table 6.2. As usual, the form $[x, y, z, 1]$ is used to perform homogeneous operations.

6.2 Kinematic verification

A first simulation consists in a flexion/extension motion of 30 degrees followed by an abduction/adduction of 20 degrees. It allows to verify that the modeling of the wrist kinematics and the tendon coupling is globally correct. Figure 6.9 shows that the errors in the constraints are limited to numerical inaccuracies.

The tendon displacements resulting from the wrist motion are depicted in Figure 6.10 and give an insight in the way the wrist interacts with the fingers. According to the designer of the wrist, the coupling with the finger during the flexion/extension should be minimal. This is confirmed by the first part of the plot where the motion is only performed in the flexion/extension direction. Moreover, the shape of the elongation confirms that the coupling is nonlinearly related to the wrist flexion angle. The abduction/adduction motion has a large influence on the tendon lengths. The perturbation is directly proportional to the distance to the median axis of the wrist (i. e. the tendons in the center of the wrist are barely moving while the side ones are undergoing the largest motions). Similar to the flexion/extension

Table 6.2: Tendon offset in the forearm frame and in the palm frame

Tendon	Forearm	Palm
1	[0.004, 0.007, 0.008]	[-0.004, -0.011, 0.010]
2	[0.004, 0.008, 0.008]	[-0.004, -0.010, 0.010]
3	[0.004, 0.010, 0.008]	[-0.004, -0.008, 0.010]
4	[0.004, 0.011, 0.008]	[-0.004, -0.006, 0.010]
5	[0.004, 0.013, 0.008]	[-0.004, -0.005, 0.010]
6	[0.004, 0.015, 0.008]	[-0.004, -0.003, 0.010]
7	[0.004, 0.016, 0.008]	[-0.004, -0.002, 0.010]
8	[0.004, 0.018, 0.008]	[-0.004, 0.000, 0.010]
9	[0.004, 0.019, 0.008]	[-0.004, 0.002, 0.010]
10	[0.004, 0.021, 0.008]	[-0.004, 0.003, 0.010]
11	[0.004, 0.023, 0.008]	[-0.004, 0.005, 0.010]
12	[0.004, 0.024, 0.008]	[-0.004, 0.006, 0.010]
13	[0.004, 0.026, 0.008]	[-0.004, 0.008, 0.010]
14	[0.004, 0.027, 0.008]	[-0.004, 0.010, 0.010]
15	[0.004, 0.029, 0.008]	[-0.004, 0.011, 0.010]
16	[0.004, 0.031, 0.008]	[-0.004, 0.013, 0.010]
17	[0.004, 0.032, 0.008]	[-0.004, 0.014, 0.010]
18	[0.004, 0.034, 0.008]	[-0.004, 0.016, 0.010]
19	[0.004, 0.035, 0.008]	[-0.004, 0.018, 0.010]
20	[0.004, 0.006, 0.028]	[-0.004, -0.013, -0.010]
21	[0.004, 0.007, 0.028]	[-0.004, -0.011, -0.010]
22	[0.004, 0.009, 0.028]	[-0.004, -0.010, -0.010]
23	[0.004, 0.011, 0.028]	[-0.004, -0.008, -0.010]
24	[0.004, 0.012, 0.028]	[-0.004, -0.006, -0.010]
25	[0.004, 0.014, 0.028]	[-0.004, -0.005, -0.010]
26	[0.004, 0.015, 0.028]	[-0.004, -0.003, -0.010]
27	[0.004, 0.017, 0.028]	[-0.004, -0.002, -0.010]
28	[0.004, 0.019, 0.028]	[-0.004, 0.000, -0.010]
29	[0.004, 0.020, 0.028]	[-0.004, 0.002, -0.010]
30	[0.004, 0.022, 0.028]	[-0.004, 0.003, -0.010]
31	[0.004, 0.023, 0.028]	[-0.004, 0.005, -0.010]
32	[0.004, 0.025, 0.028]	[-0.004, 0.006, -0.010]
33	[0.004, 0.027, 0.028]	[-0.004, 0.008, -0.010]
34	[0.004, 0.028, 0.028]	[-0.004, 0.010, -0.010]
35	[0.004, 0.030, 0.028]	[-0.004, 0.011, -0.010]
36	[0.004, 0.031, 0.028]	[-0.004, 0.013, -0.010]
37	[0.004, 0.033, 0.028]	[-0.004, 0.014, -0.010]
38	[0.004, 0.035, 0.028]	[-0.004, 0.016, -0.010]

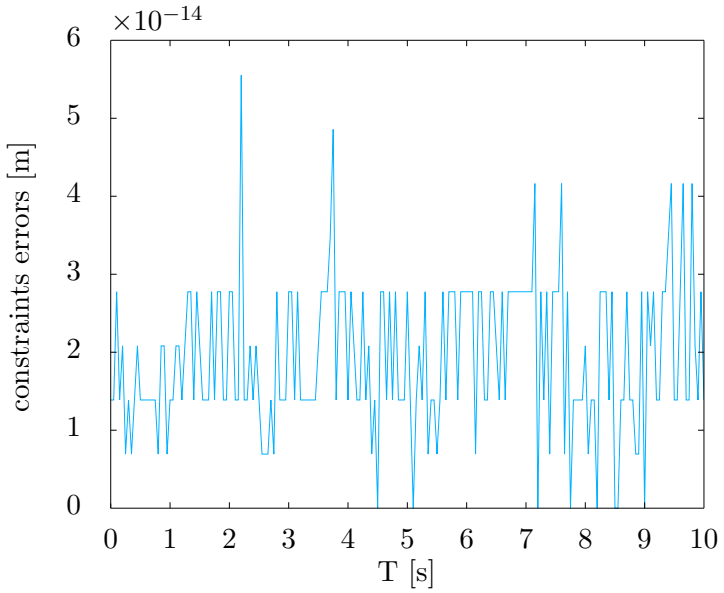

Figure 6.9: Simulation: maximum error on the distance constraints between the points, that is $\max(\|AA_0\|, \|BB_0\|, \|CC_0\|, \|AB\|, \|AC\|, \|BC\|)$

case, the relationship between the displacements and the input angle are nonlinear.

During the experiments, the tendons are controlled by a force controller such that the motors are simply following the tendon displacement imposed by the wrist coupling. Figure 6.11 shows how the tendons are moving according to the imposed wrist motion.

To verify more precisely the model, a simulation and the corresponding experiment are compared in order to verify that the wrist frame calculation and the tendon length calculations are correct. In the experiments, the wrist is driven manually while the fingers are fixed to a reference plate. Figure 6.10 reports the calculated tendon displacement due to the wrist motion. Figure 6.12 (resp. Figure 6.13) reports the measured tendon displacement due to the wrist abduction/adduction (resp. flexion/extension) motion. The identical patterns indicate that the modeled lengths are matching the real tendon displacements.

The discrepancies between the plots can be explained by the steady-state error of the tendon force controller added to the approximated contact model between the tendon and the pulleys (they are considered fixed points in the wrist although the contact points are changing slightly due to the approach angle).

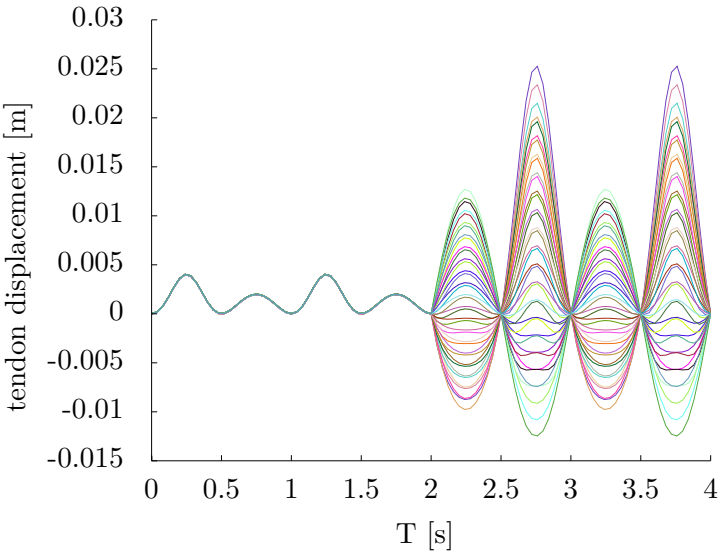

Figure 6.10: Simulation: calculated tendon displacement resulting from a wrist motion

6.3 Conclusion

The wrist has a double inverted parallelogram structure. This allows all tendons to be guided through the wrist while providing a large range of motion. However, because the tendons cannot all go through a unique point, a motion of the wrist modifies the tendon path which results in a motion in the fingers. Forwarding the tendon length of the wrist prevents the finger position deviations. Therefore, the homogeneous transformation between the forearm frame and the palm frame has been derived. It should be noted that the wrist position modifies the mechanical stiffness of the tendons since the wrist is also actuated with a stiffness-adjustable mechanism. The exact expression of the mechanical stiffness of the fingers, including the wrist contribution, is however not treated in this thesis. Simulations and experiments confirm the behavior announced by the designers. The good match between the simulated and the measured the tendon displacements validate the wrist kinematic model.

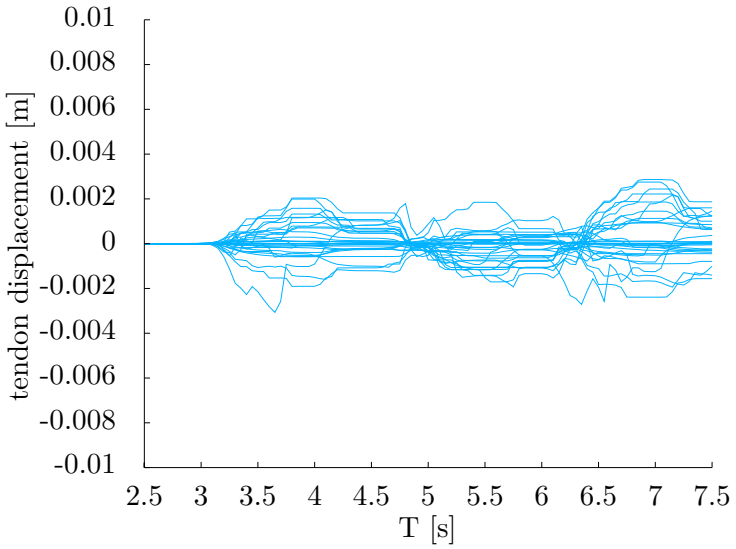

Figure 6.11: Experiment: measured tendon displacement resulting from the recorded wrist motion

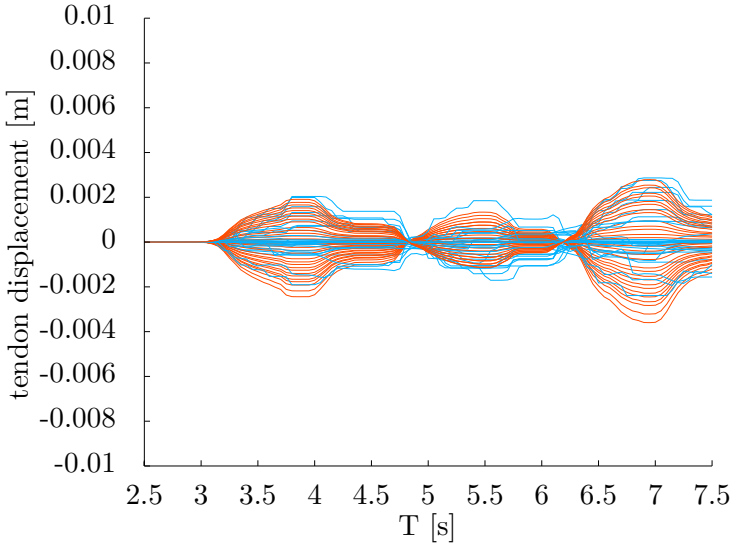

Figure 6.12: Experiment: simulated tendon displacement resulting from the recorded wrist flexion/extension motion

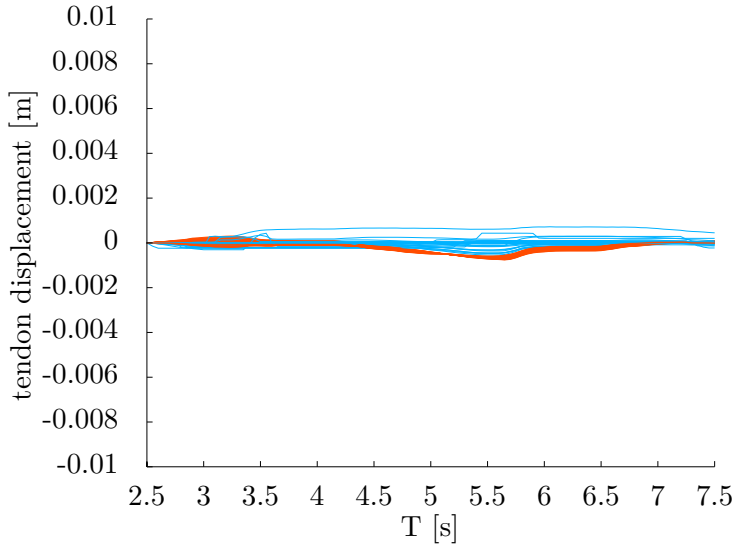

Figure 6.13: Experiment: measured tendon displacement resulting from the recorded wrist abduction/adduction

Part II

Control

The first objective in the control of a highly complex hand system is the robustness w. r. t. unmodeled dynamics and unexpected disturbances, as well as the protection of the system. The secondary objective is to change the finger configurations within a reasonable time and precision since the execution time is not critical, especially when compared to the case of pick and place machines. The third objective is to be able to adjust the mechanical stiffness and thereby adapt the finger to the environment. The use of a hand in an unstructured environment implies a large number of expected contacts, e. g. during grasping, or unexpected contacts (if not impacts), e. g. during exploration. The flexible tendons provide a natural robustness against impact by the mean of a mechanical low-pass filter. This mechanical protection, while clearly outperforming any controller in terms of response time, is limited in amplitude and a suitable controller action must take place to offer a larger range of deflection. Indeed, for example, the mechanical filter does not prevent tendon slackening. Therefore, the control architecture must actively maintain the system into its operational space. Namely, the controller must keep the tendon forces in a specified range, and if possible, prevent the subluxation of the fingers. Meanwhile, the controller should allow the user to modify the effective stiffness and the finger configuration.

In the case of flexible-tendon driven systems it is usually argued that the stiffness and the position can be adjusted independently, however in practice the tendon force range creates some coupling in the workspace [41]. Indeed, intuitively, once the tendon forces are close to the tendon force limits the stiffness cannot anymore be adjusted. Similarily, holding a heavy load requires a given amount of tendon force, thereby imposing a minimum stiffness. The mechanical stiffness does not usually correspond to the user's needs. Therefore, a compliant behavior is introduced by an admittance or impedance controller. As a result, the effective finger stiffness depends on the controller loop stiffness as well as on the mechanical stiffness. The serial/parallel connection of the impedances creates some dependencies between the values. For example, it is impossible to create a finger stiffer than its mechanical stiffness (which is not totally exact; a negative feedback can achieve the desired behavior, however the stability is very difficult to obtain).

This second part of the thesis concentrates on the control of an antagonistically driven joint with nonlinear, flexible tendons. However, as the complexity of systems is increasing it becomes an increasingly difficult task to define control objectives. In many cases, a step response behavior is the reference (analyzed as a second order linear system, i. e. pulsation and damping). In the case of a multifingered hand where nonlinear couplings are present, the individual joint behavior might not be a good/fair comparison. The question is simplified when considering only one joint and comparing the control approaches in simulation and experiments. It should be noted that the standardized comparisons, i. e. step response, tracking accuracy,

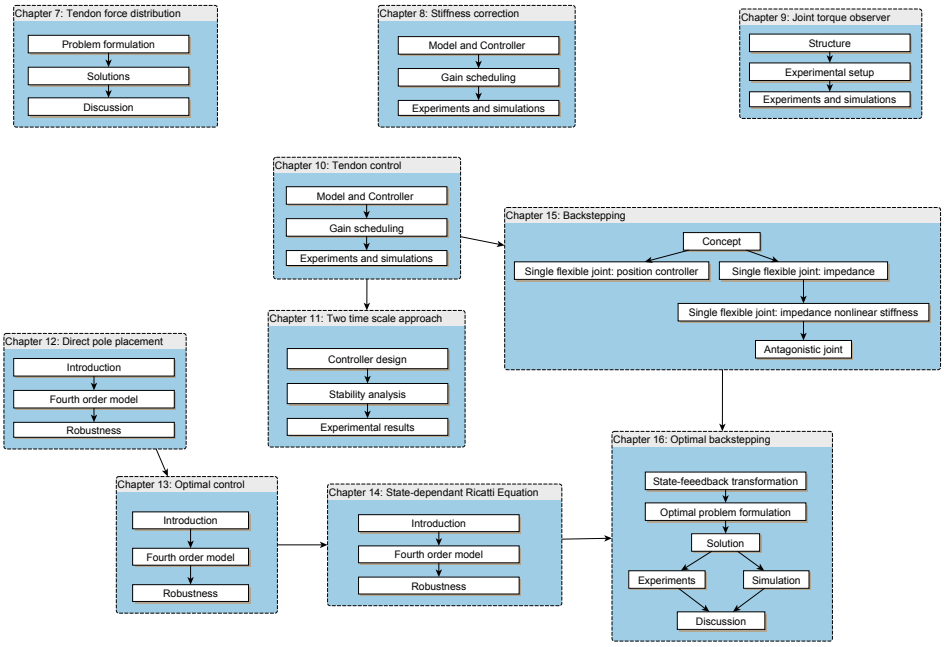

Figure 6.14: Overview of the structure of the control part

must be considered with respect to some *non standard* elements. Elements such as noise, power consumption, behavior in case of sensor failure or tendon failure must be included in the choice of a controller. The first three chapters present the problems specific to the tendon actuation but not directly related to the control of flexible joints. The followings chapters derive controllers for a single joint with increasing complexity. All approaches are evaluated and compared in simulations and experiments. Finally, because of its success, the backstepping approach is selected and the novel question of automatically selecting gains is analysed. The logical links between the different chapters of this part are depicted in Fig. 6.14. The first chapter describes the tendon force distribution and the internal force selection problems. It proposes some algorithms that have been successfully implemented.

The second chapter focuses on the correction of the controller stiffness. Indeed, by structure, the effective stiffness at the fingertip is the combination of the controller stiffness (active) and the mechanical stiffness (passive). However, during interactions the mechanical stiffness is modified nonlinearly, resulting in a modified effective tip stiffness. A control scheme that adapts the controller stiffness online is described. Its effectiveness is demonstrated by simulation and experiments. However, ensuring stability remains an open question.

In the third chapter, strain gauges are integrated in the link side of the finger to highlight the possible improvements in terms of accuracy. Despite

the excellent results, the concept is not further used since it involves a redesign of the electronic hardware and severely impairs the finger robustness (e. g. reliability of cables).

The fourth chapter presents the results obtained with the tendon force controller. A gain scheduling approach confirms that the performance can be improved in the whole workspace.

In the fifth chapter, a simple controller is implemented under the hypothesis of a complete decoupling of the motors and link dynamics.

The sixth chapter uses a direct pole placement approach.

Chapter seven continues the pole placement approach and proposes an optimal control approach to select the gains.

Chapter eight applies a backstepping approach on the system. The method is applied on problems of increasing complexity. The method will prove to be very successful. However, its main limitation lies in the delicate choice of the feedback gains.

Finally, Chapter nine considers the problem of locally selecting optimal gains for the backstepping. It aims at combining the advantages of the backstepping structure and the automatic choice of gains of the optimal control.

7 Tendon force distribution

A key characteristic of tendon-driven systems is the necessity of maintaining positive tendon forces. Indeed, the model is invalid if the tendon tension falls to zero. In such a case, the system does not any longer comply with the equations of motion and may become uncontrollable[1]. Depending on the mechanical design, it might even get damaged. In the Awiwi Hand , the antagonistic configuration and the use of nonlinear springs[2] allows to adjust the joint stiffness by modifying the pretension of the tendons. Therefore, the question arises: How should one select the tendon forces to generate the desired joint torque in real time and realize the desired mechanical stiffness while preventing slackening or overload of the tendons? In the modeling part, it has been shown that the joint torque can be obtained from the tendon forces and the coupling matrix. Therefore, an algorithm that inverses the mapping is needed. However, neither a pseudo-inversion of the coupling matrix nor a projection can guarantee that the desired tendon forces will be restricted to a given range. In the following chapter, the objective is to build an algorithm to set the pretension forces to approximate the user-required mechanical stiffness. Because of the constraints, this is not possible in general and only an approximative solution can be found. First, a formal description of the problem is given. The second section presents several solutions to the problem and discusses the advantages and drawbacks of each method. A pseudo-code that corresponds to the current implementation is reported.

7.1 Problem formulation

As presented in the modeling part, as well as in several works [18, 41], the joint stiffness matrix is obtained by the following transformation

$$\begin{aligned} \boldsymbol{K}_{\mathrm{q}}(\boldsymbol{q}, \boldsymbol{f}_{\mathrm{t}})|_{\boldsymbol{q}=\boldsymbol{q}_0, \boldsymbol{f}_{\mathrm{t}}=\boldsymbol{f}_{\mathrm{t},0}} &= \frac{\partial \boldsymbol{\tau}(\boldsymbol{f}_{\mathrm{t}})}{\partial \boldsymbol{q}}|_{\boldsymbol{q}=\boldsymbol{q}_0, \boldsymbol{f}_{\mathrm{t}}=\boldsymbol{f}_{\mathrm{t},0}} \\ &= \boldsymbol{P}^T(\boldsymbol{q})\frac{\partial \boldsymbol{f}_{\mathrm{t}}}{\partial \boldsymbol{q}} + \frac{\partial \boldsymbol{P}(\boldsymbol{q})^T}{\partial \boldsymbol{q}}|_{\boldsymbol{q}=\boldsymbol{q}_0}\boldsymbol{f}_{\mathrm{t}} \\ &= \boldsymbol{P}^T(\boldsymbol{q})\frac{\partial \boldsymbol{f}_{\mathrm{t}}}{\partial \boldsymbol{h}}\frac{\partial \boldsymbol{h}}{\partial \boldsymbol{q}} + \frac{\partial \boldsymbol{P}(\boldsymbol{q})^T}{\partial \boldsymbol{q}}|_{\boldsymbol{q}=\boldsymbol{q}_0}\boldsymbol{f}_{\mathrm{t}} \\ &= \boldsymbol{P}^T(\boldsymbol{q})\boldsymbol{K}_{\mathrm{t}}(\boldsymbol{f}_{\mathrm{t}})\boldsymbol{P}(\boldsymbol{q}) + \frac{\partial \boldsymbol{P}(\boldsymbol{q})^T}{\partial \boldsymbol{q}}|_{\boldsymbol{q}=\boldsymbol{q}_0}\boldsymbol{f}_{\mathrm{t}} \end{aligned} \quad , \quad (7.1)$$

where $\boldsymbol{P}(\boldsymbol{q}) \in \mathbb{R}^{n\times m}$ is the coupling matrix defined as $\boldsymbol{P}(\boldsymbol{q}) = \partial \boldsymbol{h}(\boldsymbol{q})/\partial \boldsymbol{q}$. $\boldsymbol{q} \in \mathbb{R}^n$ and $\boldsymbol{f}_{\mathrm{t}} \in \mathbb{R}^m$ are the vector of joint angles and the vector of tendon

[1] e. g. due to the change of coupling

[2] The springs themselves are linear but they are used in a mechanism that exhibits a nonlinear stiffness behavior [3].

forces. $\boldsymbol{K}_{\mathrm{t}} = \partial \boldsymbol{f}_{\mathrm{t}} / \partial \boldsymbol{h} \in \mathbb{R}^{m \times m}$ is the tendon stiffness matrix. However, in the Hand Arm System the tendon stiffnesses are independent, thus it is a diagonal matrix. $\boldsymbol{K}_{\mathrm{q}} \in \mathbb{R}^{n \times n}$ is the joint stiffness matrix (positive definite). Classically, $\boldsymbol{q} = \boldsymbol{q}_0, \boldsymbol{f}_{\mathrm{t}} = \boldsymbol{f}_{\mathrm{t},0}$ denote the reference around which the stiffness is calculated. The application that transforms the tendon forces into joint torques and derives the joint stiffness matrix can be defined from (7.1) by

$$\begin{aligned} \Psi: \quad & [f_{\mathrm{t,min}}, f_{\mathrm{t,max}}]^m \mapsto \mathbb{R}^n \times \mathbb{R}^{n \times n} \\ & \boldsymbol{f}_{\mathrm{t}} \to \begin{bmatrix} \boldsymbol{P}(\boldsymbol{q})^T \boldsymbol{f}_{\mathrm{t}} \\ \dfrac{\partial \boldsymbol{P}(\boldsymbol{q})^T}{\partial \boldsymbol{q}} \boldsymbol{f}_{\mathrm{t}} + \boldsymbol{P}^T \boldsymbol{K}_{\mathrm{t}}(\boldsymbol{f}_{\mathrm{t}}) \boldsymbol{P} \end{bmatrix} = \begin{bmatrix} \boldsymbol{\tau} \\ \boldsymbol{K}_{\mathrm{q}} \end{bmatrix} . \end{aligned} \tag{7.2}$$

Therefore, the problem consists in solving the equation

$$\Psi(\boldsymbol{f}_{\mathrm{t}}) = [\boldsymbol{\tau}_{\mathrm{des}}, \boldsymbol{K}_{\mathrm{q,des}}]^T , \quad \text{with} \quad \boldsymbol{f}_{\mathrm{t}} \in [f_{\mathrm{t,min}}, f_{\mathrm{t,max}}]^m , \tag{7.3}$$

where $\boldsymbol{\tau}_{\mathrm{des}} \in \mathbb{R}^4$ is the user-desired torque. The question is to select the tendon forces given a desired joint torque $\boldsymbol{\tau}_{\mathrm{des}}$ and a desired joint stiffness matrix $\boldsymbol{K}_{\mathrm{q,des}}$. The problem is overconstrained since the torque requires four parameters and the symmetric stiffness matrix requires ten parameters, while only eight tendon forces are available.

7.2 Solutions

The problem (7.3) might not accept any solution because of the force range limits. A simple saturation of the solutions to the feasible tendon forces does not ensure that the joint torque is achieved, thus possibly destabilizing the system (the stability proofs are usually not including the nonlinear effects of the force saturation). The desired joint torque must be achieved as closely as possible, possibly even increasing the stiffness error. In order to circumvent this issue the problem is transformed into a quadratic optimization problem under linear constraints.

$$\begin{aligned} & \min_{\boldsymbol{f}_{\mathrm{t}}} (\| \boldsymbol{K}_{\mathrm{q,des}} - \boldsymbol{K}_{\mathrm{q}} \|) \\ & \boldsymbol{\tau}_{\mathrm{des}} = \boldsymbol{P}^T \boldsymbol{f}_{\mathrm{t}} \end{aligned} \quad \text{with} \quad \boldsymbol{f}_{\mathrm{t}} \in [f_{\mathrm{t,min}}, f_{\mathrm{t,max}}]^m , \tag{7.4}$$

where the desired (resp. achieved) joint stiffness matrix is denoted $\boldsymbol{K}_{\mathrm{q,des}} \in \mathbb{R}^{n \times n}$ (resp. $\boldsymbol{K}_{\mathrm{q}} \in \mathbb{R}^{n \times n}$). The norm is the $\mathcal{L}_2$ norm. Because the problem is nonlinear (loosely said: $k_{\mathrm{t}}(\alpha f_{\mathrm{t}}) \neq \alpha k_{\mathrm{t}}(f_{\mathrm{t}})$), it is not possible to separate the selection of the internal tendon forces and the tendon forces that generate a link torque. The non-superposability distinguishes the problem from most of the cases discussed in the literature [53,124]. The transformation that maps the tendon forces in the joint torques and derives the joint stiffness is not bijective in general (but is certainly injective from $[f_{\mathrm{t,min}}, f_{\mathrm{t,max}}]^m$ to $\mathbb{R}^n \times \mathbb{R}^{n \times n}$). Thus, for a given choice of joint stiffness matrix and torque, no exact

solution exists. Moreover, as presented in the tendon modeling chapter, the tendon characteristics are approximated by polynomials or lookup tables. Therefore, it is not possible to explicitly find the inverse function Ψ^{-1} that maps the desired joint torques and stiffness to the tendon forces. It should be noted that the inversion can be reduced to a simple matrix inversion and allows an easier analysis if a suitable tendon stiffness model can be used [54]. A first possible approach to this problem is to perform a nonlinear optimization with constraints defined as,

$$\begin{cases} \min\limits_{\boldsymbol{f}_\mathrm{t}}(\beta_1 \left\|\boldsymbol{K}_\mathrm{q} - \boldsymbol{K}_\mathrm{q,des}\right\| + \beta_2 \left\|\boldsymbol{\tau} - \boldsymbol{\tau}_\mathrm{des}\right\|) \\ \boldsymbol{f}_\mathrm{t} \in [f_\mathrm{t,min} \dots f_\mathrm{t,max}]^m \end{cases}, \tag{7.5}$$

where $(\beta_1, \beta_2) \in \mathbb{R}^2$ are weights to be selected depending on the desired behavior. Unfortunately, this optimization does not ensure that the desired torques are achieved. The stiffness can potentially lead to an incorrect torque and destabilize the system. Due to this stability issue, the torque is more important than the mechanical stiffness. A constraint can be added in the problem to solve the issue,

$$\begin{cases} \min\limits_{\boldsymbol{f}_\mathrm{t}}(\boldsymbol{\beta}_1 \left\|\boldsymbol{K}_\mathrm{q} - \boldsymbol{K}_\mathrm{q,des}\right\|) \\ \boldsymbol{f}_\mathrm{t} \in [f_\mathrm{t,min} \dots f_\mathrm{t,max}]^m \\ \boldsymbol{P}\boldsymbol{f}_\mathrm{t} = \boldsymbol{\tau}_\mathrm{des} \end{cases}, \tag{7.6}$$

where $\boldsymbol{\beta}_1 \in \mathbb{R}^{n\times n}$ is a weight matrix to be selected depending on the relative importance of the joints. This latter formulation revealed to be complex to implement efficiently on the real-time machine, mainly due to the constraints. As a results the solver is not suitable for a real-time use. A reformulation of the problem (inspired by [18]) ensures that the desired torques are achieved if it is possible given the limits of the tendon forces. The problem is given by

$$\min_{\boldsymbol{\alpha}} \left(\gamma_1 \|\boldsymbol{K}_\mathrm{q,des} - \boldsymbol{K}_\mathrm{q}\| + \gamma_2 \Psi(\boldsymbol{f}_\mathrm{t}, \boldsymbol{f}_\mathrm{t,min}) + \gamma_3 \Psi(\boldsymbol{f}_\mathrm{t}, \boldsymbol{f}_\mathrm{t,max})\right), \tag{7.7}$$

where $\boldsymbol{f}_\mathrm{t} = (\boldsymbol{P}^T)^+ \boldsymbol{\tau}_\mathrm{des} + \ker(\boldsymbol{P}^T)\boldsymbol{\alpha}$. The desired joint stiffness matrix (resp. the achieved joint stiffness matrix) is $\boldsymbol{K}_\mathrm{q,des} \in \mathbb{R}^{n\times n}$ (resp. $\boldsymbol{K}_\mathrm{q} \in \mathbb{R}^{n\times n}$). The tendon force limits are $(\boldsymbol{f}_\mathrm{t,min}, \boldsymbol{f}_\mathrm{t,max}) \in \mathbb{R}^2$. The term $\ker(\boldsymbol{P}^T)\boldsymbol{\alpha}$ operates in the null space of the coupling, and therefore, it does not generate any joint torque. The weighting factors γ_1, γ_2, and γ_3 are used to balance the relative importance of the boundary potentials and the error. The boundary function Ψ implements a repulsive potential to repel the solution from the tendon force limits. It is important to note that, in contrast to (7.6) where the search is performed on $\boldsymbol{f}_\mathrm{t} \in \mathbb{R}^m$, in (7.6) the search is performed only on $\boldsymbol{\alpha} \in \mathbb{R}^n$. This reduction of the search space provides a valuable run-time speed-up. Using this formulation, the particular shape of the nullspace of

the coupling matrix is used advantageously to improve the search speed. The pseudo-code corresponding to the search is reported in Alg. 2. The key feature of the algorithm is to ensure that the desired torque is exactly achieved. Although it does not strictly enforce that the force constraints are satisfied, they are in practice achieved since the boundary gains, i. e. γ_2 and γ_3, can be large to prevent the search from exceeding the limits. In particular, this algorithm is extremely efficient with constant coupling matrices (i. e. all fingers but the thumb of the hand of Awiwi Hand). Indeed, if $\boldsymbol{P}$ is constant, a base $\boldsymbol{W}$ of the kernel of $\boldsymbol{P}^T$ can be computed offline. In case of a position-varying coupling matrix, this algorithm needs to compute a singular value decomposition (or a pseudo-inverse) online thus severely impairing its execution time. Nonetheless, in the case of the thumb, despite its position dependance, the special shape of the coupling matrix (block diagonal) allows efficient implementation techniques.

7.3 Discussion

In this chapter, the problem of selecting the internal tendon forces has been described. Since the tendon forces modify the joint stiffness, it is not possible to independently set the stiffness and the torque. Several formulations of the problem are proposed and discussed. Unless assumptions are made on the stiffness function of the tendons, numerical search algorithms are the only available tool to optimally select the tendon forces. Although, initially, the search problem is of dimension equal to the number of tendons, it is possible to restrict the search to a base of the kernel of the coupling matrix. It ensures that the search algorithm satisfies the desired torque and reduces the dimension of the problem. Experimental results have been presented in [41].

Norms In this chapter, the notion of norm is required to define the optimization goals/costs. For real vectors, the norm operation from $\mathbb{R}^n$ to $\mathbb{R}$ defined by (7.8) will be used unless otherwise specified.

$$\|\boldsymbol{x}\| = \sqrt{\sum_{i=0}^{n} x_i^2} \tag{7.8}$$

where $\boldsymbol{x} \in \mathbb{R}^n$ is a real vector of dimension $n \in \mathbb{N}$. $i \in [1 \dots n]$ is a generic summation symbol. For real matrices, the definition is less natural and multiple norms have been proposed (max norm, entrywise norm, Schatten norm, Frobenius norm, [125]). In this chapter, either the norm defined by (7.9) or by (7.10) will be used.

$$\|\boldsymbol{A}\| = \sqrt{\sum_{i=0}^{n} a_i^2} \tag{7.9}$$

or

$$\|\boldsymbol{A}\| = \max a_{i,j} \tag{7.10}$$

where $\boldsymbol{A} \in \mathbb{R}^{n \times n}$ is a real square matrix of dimension $n \in \mathbb{N}$. $(i, j) \in [1 \dots n]^2$ are a generic summation symbols. In most cases, the norms can easily be changed since they are not needed to establish the properties.

Algorithm 2 The projected gradient search algorithm.

% $\boldsymbol{W}$: null space of $\boldsymbol{P}^T$
% s: step size
% $\boldsymbol{g}$: gradient
% ∇: gradient operator
% C: cost at the current point

$\boldsymbol{W} \leftarrow \ker(\boldsymbol{P}^T)$
$\boldsymbol{\alpha} \leftarrow \boldsymbol{\alpha}_0$
$s \leftarrow s_0$
$\boldsymbol{g} \leftarrow 0$
$C_{\text{best}} \leftarrow +\inf$
for $i = 0$ to $\text{N} - 1$ **do**
    $C, \boldsymbol{g} \leftarrow cost_{\boldsymbol{\alpha}}(\boldsymbol{\alpha} - s \cdot \boldsymbol{g})$
    if $C < C_{\text{best}}$ **then**
        $C_{\text{best}} \leftarrow C$
        $\boldsymbol{\alpha} \leftarrow \boldsymbol{\alpha} - s \cdot \boldsymbol{g}$
    else
        $s \leftarrow s/2$
    end if
end for

---

function $cost_{\boldsymbol{\alpha}}(\boldsymbol{\alpha})$
    $\boldsymbol{f}_{\text{t}} \leftarrow (\boldsymbol{P}^T)^{+}\boldsymbol{\tau}_{\text{des}} + \boldsymbol{W}\boldsymbol{\alpha}$
    $C \leftarrow \gamma_1 \|\boldsymbol{K}_{\text{q,des}} - \boldsymbol{K}_{\text{q}}(\boldsymbol{f}_{\text{t}})\| + \gamma_2 \Psi(\boldsymbol{f}_{\text{t}}, \boldsymbol{f}_{\text{t,min}}) +$
        $\gamma_3 \Psi(\boldsymbol{f}_{\text{t}}, \boldsymbol{f}_{\text{t,max}})$
    $\boldsymbol{g} \leftarrow \nabla C$
    return C, $\boldsymbol{g}$
end function

8 Stiffness correction

The fingers of the Awiwi Hand are driven by flexible tendons. As a result of this design, the stiffness obtained at a joint is a combination of the mechanical stiffness and the controller stiffness. In this chapter, two problems are presented. The first problem is the computation of the effective stiffness, that is the stiffness that the user feels. The second problem is the question of generating the controller parameters in order to achieve a given effective stiffness. In the first section, the serial interconnexion of the stiffnesses is modeled. The second section presents a controller that adjusts the stiffness online, in order to yield the user desired stiffness. Several challenges associated with the problem are highlighted. Finally, experiments and simulations confirm the effectiveness of the approach.

8.1 Problem formulation

For a given joint torque, the deflection observed at the joint is generated by three contributions. First, the springs of the tendons are elongated. Then, the motor controller moves the motors according to the impedance control law. In the Awiwi Hand , the motor control is similar to a simple PD controller, therefore the motors do not exactly reach their final position because of the external disturbance. The general case is discussed in [54], however, in the case of the Awiwi Hand , the high position gains of the motors allow to neglect the motor contribution. An alternative consists in adding an integral term to supress the steady-state error. The effective stiffness at the finger joints results from the controller stiffness and the mechanical stiffness. This serial interconnection is expressed by

$$\boldsymbol{K}_{\text{eff}}^{-1} = \boldsymbol{K}_{\text{imp}}^{-1} + \boldsymbol{K}_{\text{mech}}^{-1}, \tag{8.1}$$

where $\boldsymbol{K}_{\text{eff}} \in \mathbb{R}^{n\times n}$(resp. $\boldsymbol{K}_{\text{imp}}^{-1} \in \mathbb{R}^{n\times n}$ and $\boldsymbol{K}_{\text{mech}} \in \mathbb{R}^{n\times n}$) is the effective joint stiffness matrix (resp. the stiffness matrix of the impedance joint controller and the mechanical joint stiffness due to the tendons). This serial interconnection is represented in Figure 8.1. From Equation (8.1) it becomes obvious that by fixing two of the stiffness matrices, it is at least conceptually possible to generate any third matrix.

8.2 Adaptive Controller

The user most likely wants to specify the effective stiffness and does not want to interfere with the rest of the matrices. Therefore, the main concept of this design is to let the user specify an effective link stiffness $\boldsymbol{K}_{\text{eff}}$. Then compute automatically the optimal mechanical stiffness $\boldsymbol{K}_{\text{mech}}$ with respect

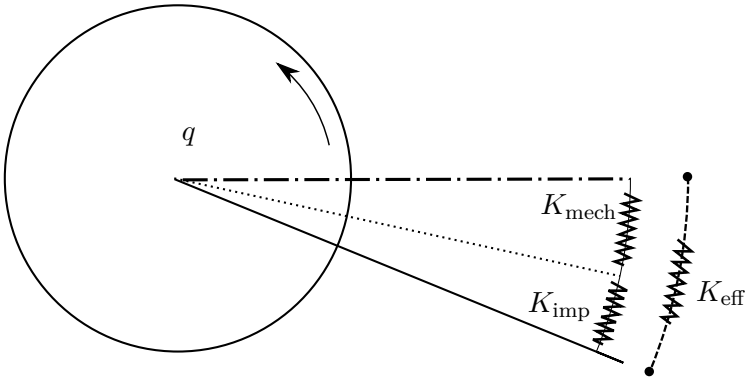

Figure 8.1: Serial interconnexion of the controller stiffness and the mechanical stiffness

to some criteria, such as the maximum robustness or minimum control effort. Finally, the controller impedance gain $\boldsymbol{K}_{\text{imp}}$ is selected to obtain, if possible, the proper effective stiffness. Theoretically, if the adjustment of $\boldsymbol{K}_{\text{imp}}$ is quasi-static, the stability only depends on $\boldsymbol{K}_{\text{eff}}$ being positive definite. It implies that the mechanical stiffness can be arbitrarily selected (but positive definite by nature) and the effective stiffness $\boldsymbol{K}_{\text{eff}}$ can always be achieved. However, it should be noted that non-positive definite gain matrices $\boldsymbol{K}_{\text{imp}}$ are practically often unstable. A non-positive definite matrix corresponds to a *negative* feedback, that is the controller pushes against the disturbance instead of releasing. For the implementation, it is needed to ensure that the gains of the controller remain positive definite, possibly, at the cost of not reaching the desired effective stiffness. The control scheme used to implement this correction is depicted in Fig. 8.2.

8.3 Challenges

In this control scheme, several challenges appear. First, the overall stability of the plant is not guaranteed due to the online adjustment of the impedance gain matrix. Second, if the mechanical stiffness selection algorithm selects a stiffness close to the user-desired effective stiffness, the impedance gains can become infinite ($\boldsymbol{K}_{\text{eff}}^{-1} = \boldsymbol{K}_{\text{mech}}^{-1} \rightarrow \boldsymbol{K}_{\text{imp}}^{-1} = \boldsymbol{0}$). Therefore, the implementation must prevent such a case and rules should be devised for the mechanical stiffness selection to circumvent this issue.

The stability question is challenging, involving a nonlinear adaptive controller for a nonlinear plant. A possible solution consists in building a controller that ensures that the plant remains passive [126]. It is an approach mostly used in telemanipulation scenarios. Despite its implementation simplicity, the method requires to estimate the energy dissipation in the system which is a delicate task.

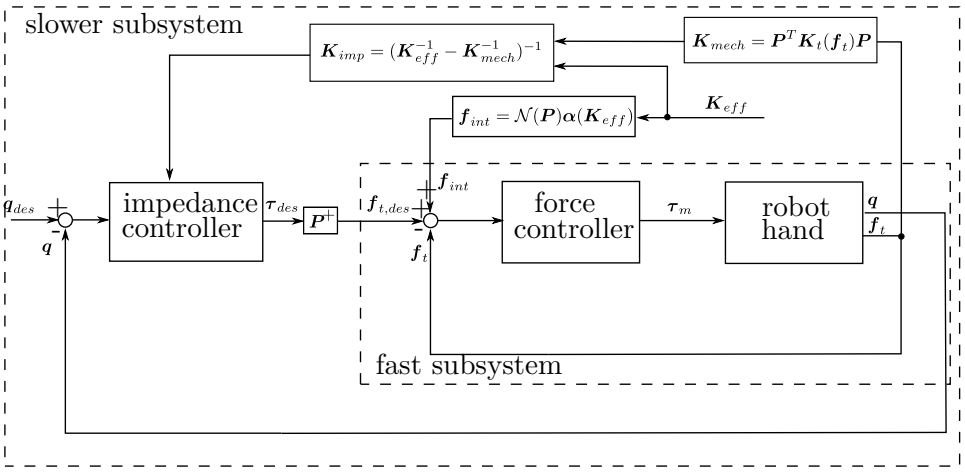

Figure 8.2: Control structure used for adjusting online the impedance gain to obtain the desired effective impedance.

The second question, that is the selection of the controller parameters to achieve the user-desired effective stiffness, can be answered in several ways. A simple and practical solution consists in selecting a mechanical stiffness always higher than the desired, therefore avoiding the asymptotic cases. Such a selection can be,

$$\boldsymbol{K}_{\text{mech,des}} = \epsilon \boldsymbol{K}_{\text{eff,des}}, \tag{8.2}$$

where $\epsilon > 1 \in \mathbb{R}$ is a positive constant used to avoid the singular cases (practically 2 or 3 are good values). The desired mechanical stiffness matrix (resp. the desired effective stiffness matrix) is denoted $\boldsymbol{K}_{\text{mech,des}} \in \mathbb{R}^{n \times n}$ (resp. $\boldsymbol{K}_{\text{eff,des}} \in \mathbb{R}^{n \times n}$). A more involved answer consists in designing both gains $(\boldsymbol{K}_{\text{imp}}, \boldsymbol{K}_{\text{mech}})$ in an optimal manner with respect to a cost function that integrates the asymptotic issue. For example, the gains could be selected according to some weights on the robustness and the accuracy. An open research problem is the question of the choice of the mechanical stiffness that would minimize the controller action. Indeed, selecting the closest mechanical stiffnesses for some joints, is not necessarily minimizing the effort needed to achieve the other directions. Moreover, recent work on the arm control showed that it is possible to achieve limit cycles if the joint stiffness is selected properly. The stability of a grasp can also be improved by choosing suitable joint stiffnesses such that the internal forces are primarily maintained by the springs thus easing the controller task.

8.4 Simulation and experiments

Selecting the target mechanical stiffness 1.5 times the value of the effective stiffness shows acceptable results. The measurements reported in Figure

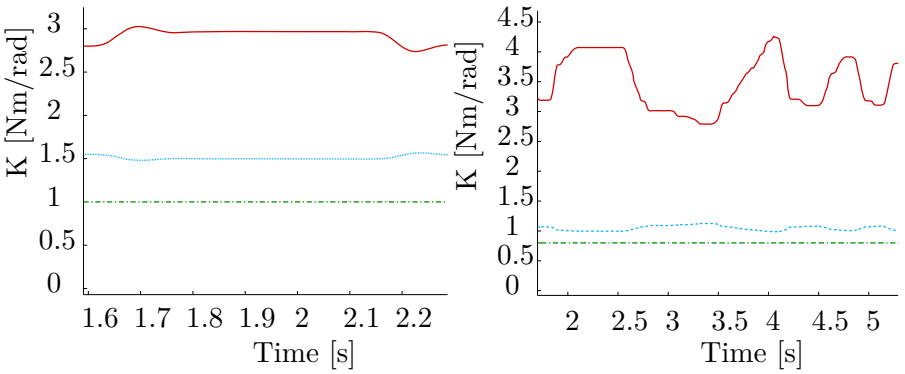

(a) Simulation (b) Experiment

Figure 8.3: Effective stiffness using the active correction. The red/solid curve depicts the impedance controller stiffness. The blue/dotted curve represents the mechanical stiffness. The green/dashed dotted curve depicts the resulting, nearly constant, stiffness.

8.3a are obtained on a single joint using a simulation model that includes the calibration curve and a structure identical to the control model (only the hardware block is replaced by a plant model). Figure 8.3b reports the real system measurements. In both cases the green/dashed-dotted line depicts the effective stiffness $\boldsymbol{K}_{\text{eff}}$ computed according to (8.1). The red/solid curve shows the impedance gain $\boldsymbol{K}_{\text{imp}}$ and the light blue/dotted curve represents the mechanical stiffness $\boldsymbol{K}_{\text{mech}}$ (estimated from the desired tendon forces to limit the noise). The perturbations in the simulation and the experiment are generated by applying a disturbance to the link. It can be seen that the effective stiffness is regulated around its desired value (1 Nm/rad and 0.7Nm/rad) although the external disturbances modify the mechanical stiffness.

8.5 Discussion

The method performs as expected but its effect is not noticeable during the experiments. Indeed, it is very difficult for a human user to evaluate the stiffness of a fingertip mainly due to other effects such as the joint friction. Therefore, this stiffness compensation scheme is not used in the following work since its advantages are limited and it lacks a stability proof. More experimental results and details are presented in [55]. Nonetheless, the method shows that it is possible to select the stiffness matrices in order to generate a constant effective stiffness. There might exist a choice of stiffness that optimizes the robustness (the spring storage is fully available) or the precision since the sensitivity to disturbances decreases with the stiffness.

However, the joint friction increases with the stiffness, therefore it seems intuitive that there exists an optimal choice of the mechanical stiffness, e. g. to maximize robustness. It is part of future works to study the trade-off between robustness and accuracy. Eventually, the robot could modulate the internal forces to adapt to its task, such as precision manipulation or tactile exploration.

9 Joint torque observer

As presented in the tendon modeling chapter, the tendon friction due to the pulleys and the sliding surfaces creates a substantial error in the tendon force estimation. Depending on the mounting condition and the routing path, the tendon friction reaches 10 % to 50 %. That is for a measured force of 20 N the effective pulling force is between 10 N and 30 N. Consequently, even an ideal control scheme cannot produce the desired behavior (a deflection of the link is not corrected even without any external disturbance because the estimated joint torque is biased). For the mechanical designers it is important to understand the influence of the tendon friction. According to the desired performance, the materials or the routing might be revised possibly at the expense of reduced maximum torque. To bring more sensitivity to the finger, an external force sensor can be used to circumvent the tendon friction error. Similar to other hands developed at the institute, some strain gauges have been placed on the bone of the finger. This has been done mostly for testing purposes since the introduction of sensors and cables in the fingers jeopardizes the robustness of the complete system. Indeed, if applied to the complete system, around 100 tiny cables would be required between the strain gauges and the analog converters. Therefore, the work of this chapter is carried out to obtain an idea of the system capabilities, if the measurements of the tendon forces perfectly represented the joint torques.

The first section briefly describes the structure of the controller and explains the main ideas. The details about the stability and the passivity aspects of the controller are found in [58]. The second section presents simulations, the implementation and experimental results.

9.1 Structure

The friction compensation mechanism is based on the idea of estimating the external joint torque by comparing the model dynamics and the observed dynamics. It is similar to the collision detection algorithm presented in [127]. The observer compares the applied torque and the measured acceleration and identifies the missing part to the friction. The actuator dynamics is

$$u = B\ddot{\theta} + \tau + \tau_{\text{fric}}\,, \tag{9.1}$$

where $u \in \mathbb{R}$ is the applied motor torque, $\ddot{\theta} \in \mathbb{R}$ is the motor acceleration. $B \in \mathbb{R}$ is the motor inertia around the rotation axis and $\tau \in \mathbb{R}$ (resp. $\tau_{\text{fric}} \in \mathbb{R}$) is the joint torque (resp. the friction torque). As depicted in Fig. 9.1, the observer equations are

$$\begin{aligned} u = &\quad B\ddot{\hat{\theta}} + \tau_a + \hat{\tau}_{\text{fric}} \\ \hat{\tau}_{\text{fric}} = &\quad -LB(\dot{\theta} - \dot{\hat{\theta}}) \end{aligned}\,, \tag{9.2}$$

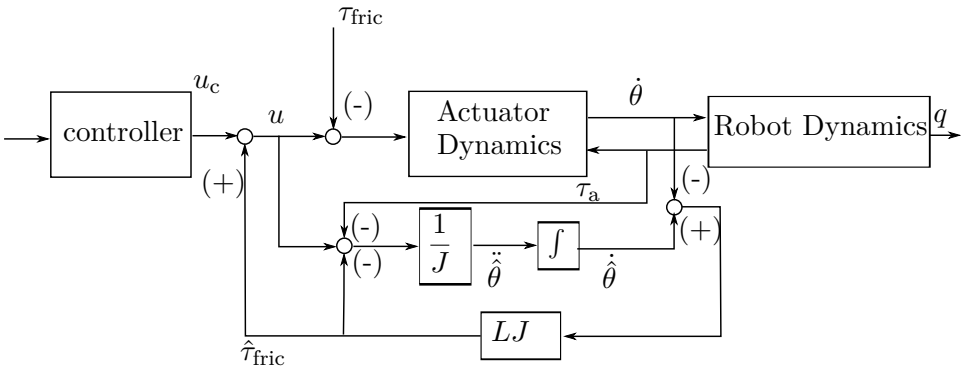

Figure 9.1: Structure of the link side friction observer

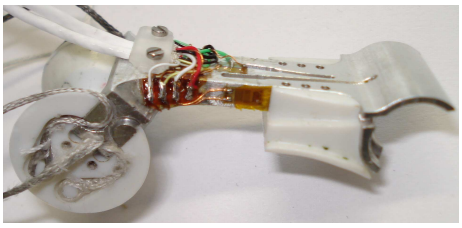

(a) Picture of the real strain gauges in the finger base

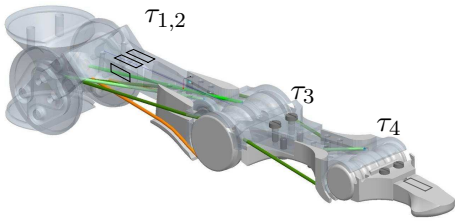

(b) Placement of the strain gauges (in hatched black)

Figure 9.2: Placement of the stain gauges in the index finger

where $L \in \mathbb{R}^+$ is an observer gain to be selected. The structure of (9.2) is the one of a Luenberger observer [128]. Finally, the control input is modified as $u = u_c + \hat{\tau}_{\text{fric}}$, which effectively compensates for the estimated friction torque. As mentioned in [58], the friction observer results in a filtered version of the real friction. Thus, the design is not always passive and might, at least for a short period of time, input more energy than needed. The analysis provided in [58] shows that the passivity mainly depends on the friction model.

9.2 Experimental setup

The experiments are conducted on the index finger of the right hand. In order to implement the controller described above, a direct access to the joint torque is required. To that end, eight strain gauges are applied directly to the structure of the finger (namely the bones). A total of four degrees of freedom are measured, two for the base (cf. Fig. 9.2a), one for the PIP and one for the DIP (cf. Fig. 9.2b). The observer is implemented for the complete finger but only the PIP results are presented for brevity.

9.3 Simulation and experiments

A slow sinusoidal motion profile for the link side is used for the evaluation of the observer. Four cases are studied:

1. Simulation without compensation (cf. Fig. 9.3a).
2. Simulation with compensation (cf. Fig. 9.3b).
3. Experiment without compensation (cf. Fig. 9.3c).
4. Experiment with compensation (cf. Fig. 9.3d).

The improvements, due to the use of the link side measurement, that are visible in the simulations (cf. Fig. 9.3a and Fig. 9.3b) are clearly visible in the experiments (cf. Fig. 9.3c and Fig. 9.3d). The simulations are performed with low stiffness and link damping to highlight the improvements.

9.4 Discussion

The joint friction observer presented in this section proved that a reduction of the joint friction significantly improves the tracking performance. However, it is important to mention that the compensation leads to a violent reaction of motors. Indeed, around a given position, the estimation of the stick slip results in a bang bang style estimation. Moreover, around the equilibrium the stiffness is minimal, emphasizing the required motion of the motors (for the same change of torque the motion of the motors is inversely proportional to the stiffness). More results on the fingers are reported in [129] as well as tests with different tendon materials and different finger configurations. To obtain long term results, the joint friction should be reduced mechanically. Indeed, a reduction of the mechanical friction is expected to lead to a positioning accuracy similar to the one obtained with the joint torque observer but without the chattering effect.

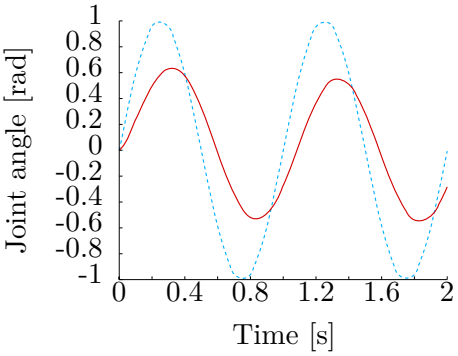

(a) Simulation: Joint position without compensation

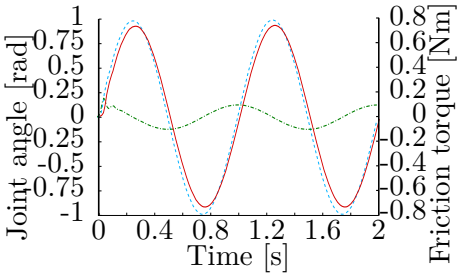

(b) Simulation: Joint position with compensation

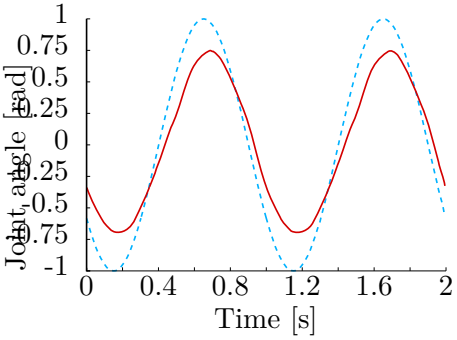

(c) Experiment: Joint position without compensation

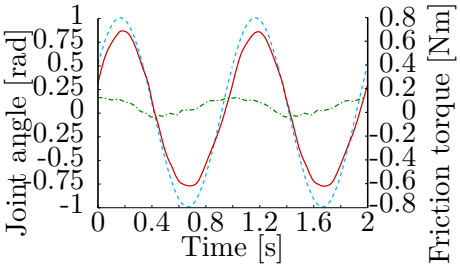

(d) Experiment: Joint position with compensation

Figure 9.3: Joint tracking performance in simulation (top) and in experiments (bottom). A sinusoidal trajectory, represented in light blue/dotted is used as reference joint trajectory. The effective joint motion is represented in red/solid. The estimated joint friction torque is depicted by the green/dashed-dotted curve.

10 Tendon control

This chapter describes the control of the tendon forces. The control of the tendon forces is needed to implement the cascaded control and its performance gives a good insight in the best performance that could be achieved. It also helps to understand the effect of the nonlinear springs and to verify the validity of the modeling. First, a tendon force dynamic model is described that consists of a motor, a spring element, and a tendon. In the second section a force controller is designed. The feedforward term is added to significantly reduce the steady-state error. However, because the controller gains are selected for a specific working point, the controller is not adapted to the complete workspace. Therefore, in the third section, a gain scheduling controller is derived in order to deal with the changing stiffness. It is simulated on a plant similar to the real one in terms of noise and quantization and exhibits the desired behavior. Finally, experiments are performed to verify the applicability of the method on the real system.

10.1 Control model

According to the modeling part, the motor/tendon subsystem is modeled as a second order system. The equation of dynamics, reported for ease of reference, is

$$B\ddot{\theta} = \tau_{\text{fric}}(\theta, \dot{\theta}) + \tau_{\text{m}} + \tau_{\text{f}_\text{t}} \ , \tag{10.1}$$

where $B \in \mathbb{R}$ is the motor inertia, $\theta \in \mathbb{R}$ (resp. $\dot{\theta} \in \mathbb{R}, \ddot{\theta} \in \mathbb{R}$) is the motor position (resp. velocity, acceleration). The torque resulting for the viscous and static friction is denoted $\tau_{\text{fric}}(\theta, \dot{\theta}) \in \mathbb{R}$. The motor torque is denoted $\tau_{\text{m}} \in \mathbb{R}$. The torque generated by the tendon force is denoted by $\tau_{\text{f}_\text{t}} = r f_{\text{t}}(\theta)$, where $r \in \mathbb{R}$ and $f_{\text{t}} \in \mathbb{R}$ are the motor pulley radius and the tendon force. The dynamics are nonlinear because the function $f_{\text{t}}(\theta)$ is not linear in its arguments. This nonlinear behavior is the very reason why it is not possible to directly use linear design methods.

10.2 Controller design

A PD controller is used for the tendon force control. The control law is

$$\boldsymbol{\tau}_{\text{m}} = K_{\text{p}}(f_{\text{t,des}} - f_{\text{t}}) + K_{\text{d}}(\dot{f}_{\text{t,des}} - \dot{f}_{\text{t}}) + \hat{\tau}_{\text{fric}}(\theta, \dot{\theta}) + \hat{\tau}_{\text{f}_\text{t}} \ , \tag{10.2}$$

where $(K_{\text{p}}, K_{\text{d}}) \in \mathbb{R}^2$ are positive gains and $\hat{(\cdot)}$ denotes an estimated quantity. The desired tendon force and the velocity of the desired tendon force are denoted $f_{\text{t,des}} \in \mathbb{R}$ and $\dot{f}_{\text{t,des}} \in \mathbb{R}$. A friction compensation and a torque feedback term are used in order to shorten the rise time and reduce the

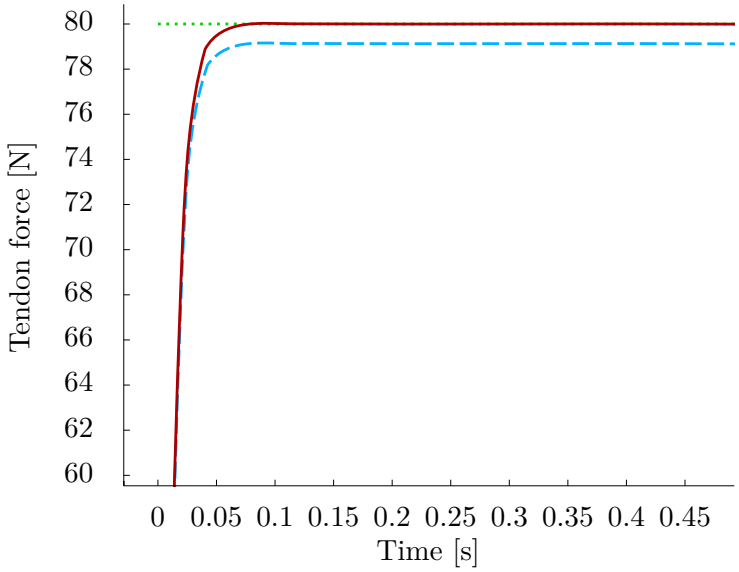

Figure 10.1: Simulation: force step response of the plant with and without feedforward terms. The dotted/green curve denotes the desired force. The blue/dashed curve represents the force without feedforward term. The solid/red curve represents the force with feedforward term.

steady-state error. Figure 10.1 depicts that the steady-state error is reduced by the feedforward terms. It is important to note that the improvements visible in the experiments are smaller than in simulations because of the imprecision of the models and the impossibility to achieve perfect measurements. The steady-state error is obtained by setting all time derivatives to zero in Eq. (10.2). Without feedforward term, the error is

$$f_{\mathrm{t,des}} - f_{\mathrm{t}} = -\frac{1}{K_{\mathrm{p}}}\left(\tau_{\mathrm{fric}}(\theta,\dot{\theta}) + \tau_{\mathrm{f_t}}\right) \ , \tag{10.3}$$

whereas, with compensation, the error is

$$f_{\mathrm{t,des}} - f_{\mathrm{t}} = \frac{1}{K_p}\left(\tau_{\mathrm{fric}}(\theta,\dot{\theta}) - \hat{\tau}_{\mathrm{fric}}(\theta,\dot{\theta}) + \tau_{\mathrm{f_t}} - \hat{\tau}_{\mathrm{f_t}}\right) \ , \tag{10.4}$$

which, if the observer is properly designed, is smaller since $\|\tau_{\mathrm{fric}}(\theta,\dot{\theta}) + \tau_{\mathrm{f_t}} - \hat{\tau}_{\mathrm{fric}}(\theta,\dot{\theta}) - \hat{\tau}_{\mathrm{f_t}}\| < \|\tau_{\mathrm{fric}}(\theta,\dot{\theta}) + \tau_{\mathrm{f_t}}\|$. If the observer of the estimates is asymptotically stable (that is $\lim_{t\to\mathrm{inf}}(\hat{\tau}_{\mathrm{fric}}(\theta,\dot{\theta})) = \tau_{\mathrm{fric}}(\theta,\dot{\theta})$ and $\lim_{t\to\mathrm{inf}}(\hat{\tau}_{\mathrm{f_t}}) = \tau_{\mathrm{f_t}}$), the regulation is perfectly achieved with respect to the modeling assumptions. Under the assumption that the estimation errors are negligible the closed-loop equation, obtained by combining Eq. (10.1) and Eq. (10.2), is

$$B\ddot{\theta} = K_{\mathrm{p}}(f_{\mathrm{t,des}} - f_{\mathrm{t}}) + K_{\mathrm{d}}(\dot{f}_{\mathrm{t,des}} - \dot{f}_{\mathrm{t}}) \ . \tag{10.5}$$

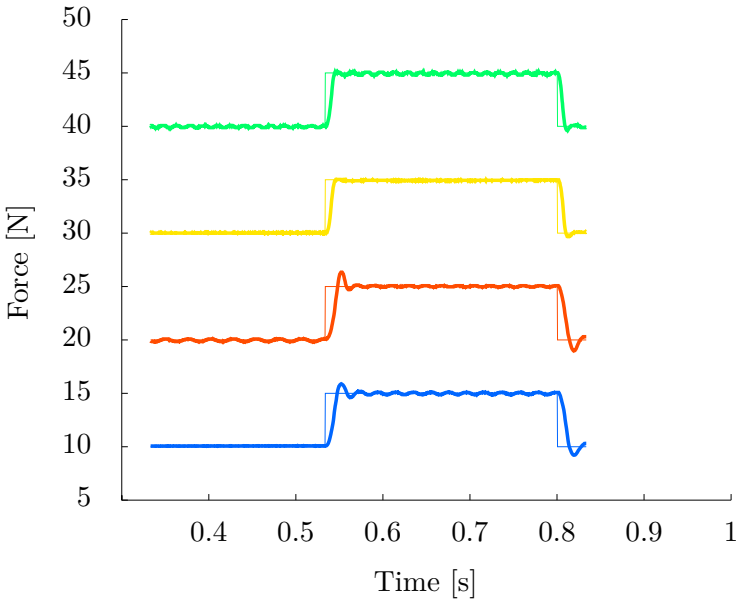

Figure 10.2: Force step response of the controller whose gains are tuned for 30 N. The gains are tuned to obtain the fastest settling time without overshoot. In each experiment, only the initial tendon force and the target tendon force are modified. It can be observed that the response is ideal for 30 N but underdamped for 10 N and 20 N.

It is possible to adjust the controller gains manually to obtain a satisfying behavior since there are only two parameters to tune. However, since θ and f_t are not linearly dependent, the closed loop equation is neither linear in the motor position nor in the tendon force. Therefore, a fixed gain tuning is limited to the vicinity of a force reference. In Figure 10.2, several step responses for a controller tuned for critical damping at 30 N are reported. As expected, it is not well adapted for the other working points. The controller is underdamped if the tendon stiffness is lower than expected (e. g. 20 N). If the stiffness is higher than expected, the controller is underdamped and its rise time could be reduced (up to the saturation of the motor torque). The steady state is obtained by setting all time derivatives to zero in (10.5). If $f_\mathrm{t}(\theta)$ is bijective, the equilibrium is unique and given by $\theta_\mathrm{eq} = f_\mathrm{t}^{-1}(f_\mathrm{t,des})$. Practically, the function f is continuous and strictly increasing on the interval $[f_\mathrm{t,min}, f_\mathrm{t,max}]$ and therefore is a bijection. Although the steady-state force is the desired one, it is important to note that the gains of the system cannot be directly selected by identification to a second order system since the closed-loop equation is not linear in the controlled variable f_t. The objective is to regulate the tendon force to a reference and specify the transient behavior of the tendon force (or the motor position) and not to deal with a combination of both variables. Therefore, in the following sections, this

simple controller is improved to fit the different working points and to allow to specify the transient behavior in terms of f_t or θ.

10.3 Gains scheduling design

The basic concept of the gain scheduling method consists in selecting the gains adapted to each working point, in order to improve the performance of the controller described by (10.2). The first step of the method requires to express the dynamics in terms of a scheduling variable. Then, the controller gains are selected under the assumption that the scheduling variable is frozen and a table of parameters is constructed (or an analytic expression when possible). Finally, for the current scheduling variable, the controller gains are extracted from the table (or evaluated from the analytic expression). Numerous methods to *interpolate* the gains have been proposed that fit the specific meaning of the scheduling variable (e. g. piecewise continuous, linear interpolation). In the tendon control case, the regularity of the stiffness function leads to the choice of a simple linear interpolation. The gain scheduling method is very powerful in the sense that it can be applied to a very large variety of nonlinear problems by linearization. However, it is not generally ensuring the global asymptotic stability.

10.3.1 Linearized form

The first step needed to apply the gain scheduling method consists in writing the dynamics to make the scheduling variable appear. The scheduled form is obtained by linearizing the dynamics around a working point but the choice of the linearization variable is free. In the present case, the linearization is done w. r. t. the tendon force or the motor position which are the most natural coordinates of the problem. It should be noted that in general, a partial feedback linearization does not enforce a particular choice of coordinates. It allows to work with the coordinates that are the most explicit to the designer, at the expense of a feedback to cancel the extra terms. The case of linearization w. r. t. the motor position θ is reported here, the case of the tendon force can be derived in a similar way. The tendon force function is assumed to be sufficiently smooth. Around a point $\theta_\mathrm{des} \in \mathbb{R}$ selected such that $f_\mathrm{t}(\theta_\mathrm{des}) = f_\mathrm{des}$, the force and the time derivate of the force are expressed by

$$f_\mathrm{t}(\theta_\mathrm{des} + \delta\theta) = f_\mathrm{t}(\theta_\mathrm{des}) + \frac{\partial f_\mathrm{t}}{\partial \theta}|_{\theta_\mathrm{des}} \delta\theta, \tag{10.6}$$

$$\dot{f}_\mathrm{t}(\theta_\mathrm{des}+\delta\theta, \dot{\theta}_\mathrm{des}+\delta\dot{\theta}) = \dot{f}_\mathrm{t}(\theta_\mathrm{des}, \dot{\theta}_\mathrm{des}) + \frac{\partial \dot{f}_\mathrm{t}}{\partial \theta}|_{\theta_\mathrm{des},\dot{\theta}_\mathrm{des}} \delta\theta + \frac{\partial \dot{f}_\mathrm{t}}{\partial \dot{\theta}}|_{\theta_\mathrm{des},\dot{\theta}_\mathrm{des}} \delta\dot{\theta}\ , \tag{10.7}$$

where $\delta\theta \in \mathbb{R}$ represents an infinitesimal change of the motor position θ. Defining $\alpha = \partial f_\mathrm{t}/\partial\theta|_{\theta_\mathrm{des}}$, $\beta = \partial \dot{f}_\mathrm{t}/\partial\theta|_{\theta_\mathrm{des},\dot{\theta}_\mathrm{des}}$ and $\gamma = \partial \dot{f}_\mathrm{t}/\partial\dot{\theta}|_{\theta_\mathrm{des},\dot{\theta}_\mathrm{des}}$ yields

$$B(\ddot{\theta}_\mathrm{des} + \ddot{\delta}\theta) = K_\mathrm{p}(f_\mathrm{t,des} - (f_\mathrm{t}(\theta_\mathrm{des}) + \alpha\delta\theta)) + K_\mathrm{d}(\dot{f}_\mathrm{t,des} - (\dot{f}_\mathrm{t}(\theta_\mathrm{des}) + \beta\dot{\delta\theta}))) \ , \tag{10.8}$$

which is a linear differential equation in $\delta\theta$ with the scheduling variables α and β.

10.3.2 Fixed gain controller design

Using the linearized closed-loop defined by (10.8), the gains $(K_\mathrm{p}, K_\mathrm{d}) \in \mathbb{R}^2$ can be selected to obtain the desired behavior. Since, by definition, $f_\mathrm{t}(\theta_\mathrm{des}) = f_\mathrm{t,des}$, (10.12) can be simplified to

$$\ddot{\delta}\theta + \frac{K_\mathrm{d}}{B}\beta\dot{\delta\theta} + \frac{K_\mathrm{p}}{B}\alpha\delta\theta = \frac{1}{B}(\ddot{\theta}_\mathrm{des} + K_\mathrm{d}(\dot{f}_\mathrm{t,des} - \dot{f}_\mathrm{t}(\theta_\mathrm{des}))) \ . \tag{10.9}$$

The gains are selected by identification to obtain the target closed-loop dynamics that is a damped second order system for the error dynamics $\delta\theta$. The right hand side of Eq. (10.9) is independent of time, thus it is possible to identify the desired gains, which yields the system

$$\begin{aligned} \omega^2 &= \frac{K_\mathrm{p}}{B}\beta \\ 2\xi\omega &= \frac{K_\mathrm{d}}{B}\alpha \end{aligned} \ , \tag{10.10}$$

where $\omega \in \mathbb{R}$ is the desired angular frequency and $\xi \in \mathbb{R}$ the desired damping ratio. Solving the system of (10.10), leads to

$$\begin{aligned} K_\mathrm{p} &= \frac{\omega^2 B}{\beta} \\ K_\mathrm{d} &= \frac{2\xi\omega B}{\alpha} \end{aligned} \ . \tag{10.11}$$

As one might expect, the gains are properly defined only if $\alpha > 0$ and $\beta > 0$. This condition expresses that the system should not be degenerated in order to place the poles. Indeed, it is not possible to place the poles of a system where the stiffness vanishes since, in such a case, the tendon force and the motor are not related anymore. The issue is well known by the mechanical designers and the stiffness in the Awiwi Hand is never equal to zero. The case of a vanishing stiffness involves, for example, the use of hysteresis or dead-zone functions but is not treated in the work.

10.3.3 Gain scheduled controller

As pointed out in [84, p.488], the model resulting from the linearization of the system with the fixed gain controller and the model resulting from the linearization of the system with scheduled gains are not equal. In both cases, the desired steady state is the equilibrium, however, the transfer functions are different. Depending on the control objective, the controller design can be acceptable or can be modified to yield the desired transfer function. It is considered acceptable for the Hand Arm System to have a different transfer function since, experimentally, the transfer function is qualitatively close enough to the desired one. The linearized closed-loop equation under the action of the fixed gain controller is obtained by substituting the gains of (10.11) into (10.5) and gives

$$\ddot{\delta\theta} + 2\xi\omega\dot{\delta\theta} + \omega^2\delta\theta = \frac{1}{B}(\ddot{\theta}_0 + K_{\mathrm{d}}(\dot{f}_{\mathrm{t,des}} - \dot{f}_{\mathrm{t}}(\theta_0))). \tag{10.12}$$

Around any constant desired working point (i. e. in the regulation case), the right hand side vanishes and the error dynamics is indeed the one of a linear second order differential equation with the selected poles.

10.4 Experimental and simulation results

The gain scheduling method proposed in the previous section is simulated on a single tendon. The model uses the friction and ripple models developed in the Chapter 3. The stiffness characteristics of a calibrated tendon are used to provide a realistic force/stiffness displacement curve. Noise of an amplitude similar to the one observed on the real system is added through a sensor model (quantization and white noise). The test pattern consists of a force step from 10N (resp. 20N, 30N and 40N) to a force of 20N (resp. 30N, 40N and 50N) and is repeated several times. The test pattern is used in four different cases:

1. Simulation with fixed gains (cf. 10.3a).
2. Simulation with scheduled gains (cf. 10.3b).
3. Experiment with fixed gains (cf. 10.4a).
4. Experiment with scheduled gains (cf. 10.4b).

The simulations and the experiments both confirm that the method is successful. The transient behavior of the force, that was underdamped or overdamped under the fixed gain controller, is always well damped under the scheduled gain controller. Although only approximative (the partial derivative of the gains modifies the pole locations), the method is intuitive and relatively easy to implement. A more detailed experimental work which

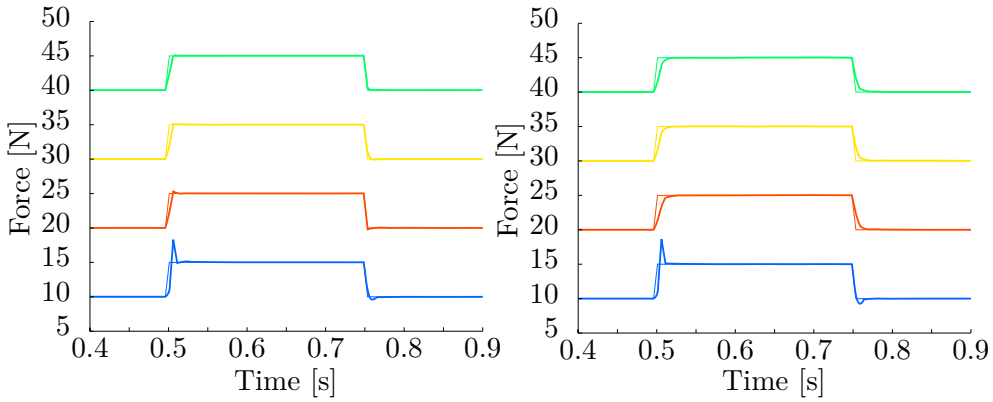

(a) Simulation: Fixed gains (b) Simulation: Adaptive gains

Figure 10.3: Simulations: Tendon force control with/without adaptive gains. In both figures, the measured and desired tendon force is depicted. A step of 5N is commanded from different initial states. The adaptive controller is superior to the fixed gain controller except for the lowest force which is due to the saturation of the control input. The fixed gain controller is tuned for 30N.

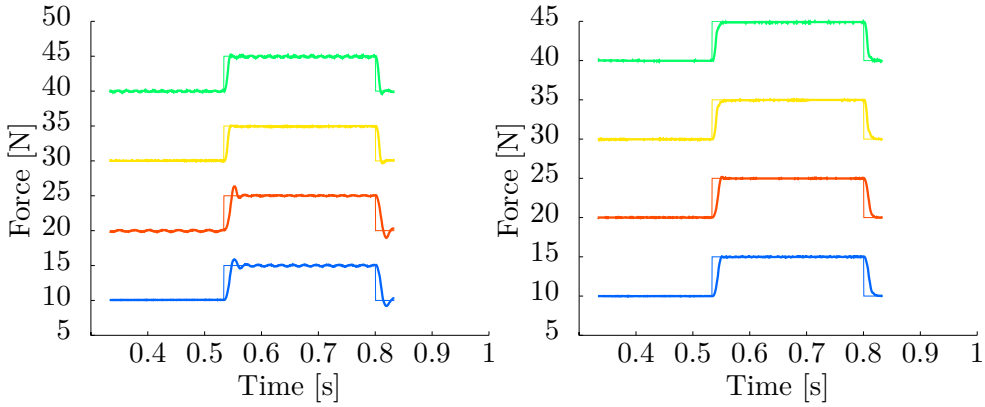

(a) Experiments: Fixed gains (b) Experiments: Adaptive gains

Figure 10.4: Experiments: Tendon force control with/without adaptive gains. In both figures, the measured and desired tendon force is depicted. A step of 5N is commanded from different initial states. The adaptive controller is superior to the fixed gain controller for all the cases. The fixed gain controller is tuned for 30N.

is not reported here, shows that the scheduling in β can be neglected and only α has a noticeable influence. Unsurprisingly, α is nothing else but the tendon stiffness (up to a multiplicative constant) at each working point.

10.5 Discussion

In this chapter, a tendon force controller is presented. A proportional derivative controller for the tendon force using fixed gains is implemented and experiments have been conducted. However, since the system is nonlinear, the controller gains can only be tuned for a specific working point and the controller is underdamped or overdamped around the nominal point. The experimental results and the simulations both confirm it. The linearization of the state dynamics allows to use a gain scheduling method that adapts the gains at each working point. The use of state dependent gains enables to design the gains by identification and to set directly the poles of a linear differential equation of the motor position error. The method only requires the derivative of the stiffness curve. Experiments and simulations confirm that the controller is indeed well damped for all the working points. It should be noted, however, that vibrations appear at higher stiffness mostly due to the noise introduced by the high derivatives. A limitation of the gain design is the fact that it does not account for the control input magnitude (as with all linearization or pole placement methods). Therefore, the controller should be tested on the complete working range to ensure that nonlinear effects of an input saturation are not destabilizing the plant. Indeed, at low stiffness, the control effort is not very effective and a large motor displacement is needed for a small force adjustment.

11 Two time scale approach

In this chapter, a joint impedance controller is designed by building a joint controller upon the tendon force controller. Two different designs are presented: the first one is using the singular perturbation approach and the second one is using the cascaded approach.

The singular perturbation approach relies upon the time scale difference between the tendon force controller and the link side dynamics. This assumption is similar to the one made when considering the motors as torque sources while commanding currents or voltages. In the Awiwi Hand the stiffness is modified by the internal pretension, thus modifying the time scale differences. Moreover, the assumption is only partially valid in the case of fingers since the links have a low inertia and the motors, together with the gear boxes, have larger inertias. It can be expected, and it is experimentally verified that the validity of the singular perturbation assumption depends on the mechanical stiffness. In the first case, the outer loop is considered as constant for the inner loop. The inner loop error is neglected arguing that, because of its speed, the inner loop is stabilized before the outer loop is *disturbed*. Despites its limitations it remains a good technique to approach the problem thanks to its intuitive structure.

In the second case, namely the cascaded approach, the system is brought into a cascaded form, that is, a triangular system. The stability is obtained by explicitly considering the inner loop tracking error as a forcing term for the outer loop. However, the analysis is more complex than in the singular perturbation case.

This chapter applies both methods to the case of a flexible joint, the difference being essentially visible in the stability proofs. In the first section the dynamic model is transformed into a cascaded form. Then, the tendon force controller designed in the previous chapter is augmented with some feedforward terms and their influence is experimentally verified. Next, the equations of a joint impedance controller are established by considering that a torque source is available at the joint. The next sections are establishing stability in the case of the singular perturbation approach and the cascaded approach. Finally, experimental results are presented. They highlight that increasing the internal pretension reduces the validity the singular perturbation approach.

11.1 Model

Under the assumption that the tendon force controller and the link impedance controller are working in two *independent* frequency domains the dynamic

equations of a finger can be written as

$$\boldsymbol{B}\ddot{\boldsymbol{\theta}} = -\boldsymbol{E}^T \boldsymbol{f}_{\mathrm{t}}(\boldsymbol{\theta} - \boldsymbol{q}_0) + \boldsymbol{\tau}_{\mathrm{m}} + \boldsymbol{b}(\boldsymbol{\theta}, \dot{\boldsymbol{\theta}}) \ , \tag{11.1}$$

where the link position $\boldsymbol{q}_0$ is considered to be constant w. r. t. the scale of the motor dynamics. When considering m tendons, $\boldsymbol{B} \in \mathbb{R}^{m \times m}$ is a diagonal motor inertia matrix, $\boldsymbol{\theta} \in \mathbb{R}^m$ is the vector of the motor positions, $\boldsymbol{E} \in \mathbb{R}^{m \times m}$ is a diagonal matrix of the pulley radius, $\boldsymbol{f}_{\mathrm{t}} \in \mathbb{R}^m$ is the vector of the tendon forces. The electromagnetic torque is denoted $\boldsymbol{\tau}_{\mathrm{m}} \in \mathbb{R}^m$. Following the same approach, the link side equations are modified to integrate the fact that the tendon forces are the input variables.

$$\boldsymbol{M}(\boldsymbol{q})\ddot{\boldsymbol{q}} + \boldsymbol{C}(\boldsymbol{q}, \dot{\boldsymbol{q}})\dot{\boldsymbol{q}} + \boldsymbol{g}(\boldsymbol{q}) + \boldsymbol{b}(\boldsymbol{q}, \dot{\boldsymbol{q}}) = \boldsymbol{P}^T \boldsymbol{f}_{\mathrm{t}} + \boldsymbol{\tau}_{\mathrm{ext}} \ . \tag{11.2}$$

When considering n links, $\boldsymbol{M}(\boldsymbol{q}) \in \mathbb{R}^{n \times n}$ is the link inertia matrix, $\boldsymbol{q} \in \mathbb{R}^n$ is the vector of the joint positions, $\boldsymbol{C}(\boldsymbol{q}, \dot{\boldsymbol{q}})\dot{\boldsymbol{q}} \in \mathbb{R}^n$ is the vector of the Coriolis and centrifugal terms, $\boldsymbol{P} \in \mathbb{R}^{n \times m}$ is the coupling matrix, $\boldsymbol{f}_{\mathrm{t}} \in \mathbb{R}^m$ is the vector of the tendon forces. The external torques and the vector of joint frictional torques are represented by $\boldsymbol{\tau}_{\mathrm{ext}} \in \mathbb{R}^n$ and $\boldsymbol{b}(\boldsymbol{q}, \dot{\boldsymbol{q}}) \in \mathbb{R}^n$.

11.2 Tendon Controller Design

The control of the tendon force is realized by a PD controller with a feedforward term for the expected torque generated by the tendon force. A friction compensation term, $\hat{\boldsymbol{b}}(\boldsymbol{\theta}, \dot{\boldsymbol{\theta}})$, is added to further improve the transient response. It is structurally similar to the tendon controller with gain scheduling but the gains are constant in order to facilitate the analysis.

$$\boldsymbol{\tau}_{\mathrm{m}} = \boldsymbol{E}^T \left(\boldsymbol{f}_{\mathrm{t}} + \boldsymbol{K}_{\mathrm{p}}(\boldsymbol{\theta}_{\mathrm{des}} - \boldsymbol{\theta}) - \boldsymbol{K}_{\mathrm{d}}\dot{\boldsymbol{\theta}} + \hat{\boldsymbol{b}}(\boldsymbol{\theta}, \dot{\boldsymbol{\theta}}) \right) \ , \tag{11.3}$$

where $\boldsymbol{\theta}_{\mathrm{des}} \in \mathbb{R}^m$ is the motor position vector that would generate the desired force vector. The friction model identified in the modeling chapter is represented by $\hat{\boldsymbol{b}}(\boldsymbol{\theta}, \dot{\boldsymbol{\theta}})$. The force tracking and motor damping gain matrices are diagonal and positive definite. They are denoted $\boldsymbol{K}_{\mathrm{p}} \in \mathbb{R}^{m \times m}$ and $\boldsymbol{K}_{\mathrm{d}} \in \mathbb{R}^{m \times m}$. Figure 11.1a shows the simulation results obtained with and without a feedforward force component. Fig. 11.1b shows the influence of the friction compensation on the rise time of the force step response. The improvements in settling time are limited by the saturation of the control and the control delay ($333\mu s$).

11.3 Link Controller Design

The link side dynamics are designed as a regular impedance controller [78]. The link side torque input is,

$$\boldsymbol{\tau}_{\mathrm{des}} = \boldsymbol{M}(\hat{\boldsymbol{q}})\ddot{\boldsymbol{q}}_{\mathrm{des}} + \boldsymbol{C}(\hat{\boldsymbol{q}}, \dot{\hat{\boldsymbol{q}}})\dot{\boldsymbol{q}}_{\mathrm{des}} + \boldsymbol{K}_{\mathrm{p,imp}}(\boldsymbol{q}_{\mathrm{des}} - \hat{\boldsymbol{q}}) + \boldsymbol{K}_{\mathrm{d,imp}}(\dot{\boldsymbol{q}}_{\mathrm{des}} - \dot{\hat{\boldsymbol{q}}}) + \hat{\boldsymbol{b}}(\hat{\boldsymbol{q}}, \dot{\hat{\boldsymbol{q}}}) + \boldsymbol{g}(\hat{\boldsymbol{q}}) \ , \tag{11.4}$$

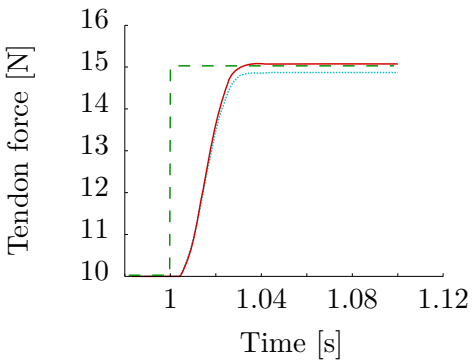

(a) Tendon force step response, without desired force feedforward and with force feedforward

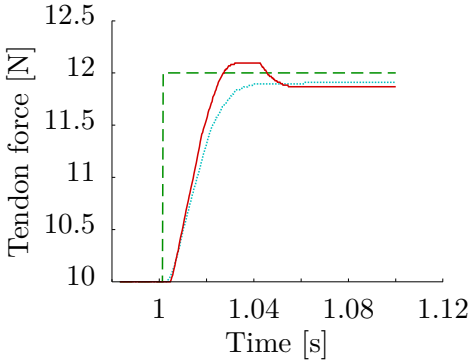

(b) Tendon force step response, with and without friction compensation

Figure 11.1: Tendon force controller experiments. The green/dashed line depicts the desired tendon force. The measured tendon force is represented in red/solid (resp. in light blue/dotted) for the case with feedforward term (resp. without).

where $\hat{.}$ denotes an estimated quantity, obtained by a linear observer or a filtering process (e. g. using a low pass or a Kalman filter). The joint position vector (resp. the desired joint position vector) is denoted $\boldsymbol{q} \in \mathbb{R}^n$ (resp. $\boldsymbol{q}_{\text{des}} \in \mathbb{R}^n$). The terms $\boldsymbol{M}(\boldsymbol{q}) \in \mathbb{R}^{n \times n}$, $\boldsymbol{C}(\boldsymbol{q}, \dot{\boldsymbol{q}}) \in \mathbb{R}^{n \times n}$ and $\boldsymbol{g}(\boldsymbol{q}) \in \mathbb{R}^n$ are the link inertia matrix, the vector of the Coriolis torques and the vector of gravity torques. The vector of frictional torques identified in the modeling section is represented by $\boldsymbol{b}(\boldsymbol{\theta}, \dot{\boldsymbol{\theta}})$. The impedance and damping matrices (positive definite) are denoted $\boldsymbol{K}_{\text{p,imp}} \in \mathbb{R}^{m \times m}$ and $\boldsymbol{K}_{\text{d,imp}} \in \mathbb{R}^{m \times m}$. The term $\boldsymbol{M}(\hat{\boldsymbol{q}})\ddot{\boldsymbol{q}}_{\text{des}}$ is traditionally used to improve the tracking performance but has only little influence in the case of fingers. The desired tendon forces that are required to generate the joint torque for the impedance controller are obtained with the help of the coupling matrix pseudo-inverse.

11.4 Stability Conditions: The singular perturbation case

In this section, the stability conditions are derived for the link controller and the tendon controller. Finally the stability of the closed-loop system is concluded, under the singular perturbation hypothesis.

Tendon force controller

In order to establish the stability conditions, the Lyapunov method is used. All tendons are assumed to be independent and therefore all matrices are simply diagonal. For the tendon force controller, the Lyapunov candidate

function is defined as

$$V(\boldsymbol{\theta}) = \frac{1}{2}\dot{\boldsymbol{\theta}}^T \boldsymbol{B}\dot{\boldsymbol{\theta}} + V_{\mathrm{k}}(\boldsymbol{\theta}) - V_{\mathrm{k}}(\boldsymbol{\theta}_{\mathrm{des}}) + \left.\frac{\partial V_{\mathrm{k}}}{\partial \boldsymbol{\theta}}\right|_{\boldsymbol{\theta}_{\mathrm{des}}} (\boldsymbol{\theta}_{\mathrm{des}} - \boldsymbol{\theta})^T + \frac{1}{2}(\boldsymbol{\theta} - \boldsymbol{\theta}_{\mathrm{des}})^T \boldsymbol{K}_{\mathrm{p}}(\boldsymbol{\theta} - \boldsymbol{\theta}_{\mathrm{des}}) \,, \tag{11.5}$$

where $\boldsymbol{\theta}_{\mathrm{des}} = \phi^{-1}(\boldsymbol{f}_{\mathrm{t,des}})$ is the motor position that would result in the desired tendon force. The storage function of the spring is denoted $V_{\mathrm{k}}(\theta) = \int_0^{\theta} f(x)dx$. The Lyapunov function is composed of the kinetic energy, the spring elastic energy, and the expected energy at the equilibrium point. The time derivative is

$$\dot{V}(\boldsymbol{\theta}) = \dot{\boldsymbol{\theta}}^T \boldsymbol{B}\ddot{\boldsymbol{\theta}} + \dot{\boldsymbol{\theta}}^T \frac{\partial V_{\mathrm{k}}}{\partial \boldsymbol{\theta}} - \left.\frac{\partial V_{\mathrm{k}}}{\partial \boldsymbol{\theta}}\right|_{\boldsymbol{\theta}_{\mathrm{des}}} \dot{\boldsymbol{\theta}}^T - \dot{\boldsymbol{\theta}}^T \boldsymbol{K}_{\mathrm{p}}(\boldsymbol{\theta}_{\mathrm{des}} - \boldsymbol{\theta}) \,. \tag{11.6}$$

Replacing the expression of V_{k}, as well as the controller equations yields

$$\dot{V}(\boldsymbol{\theta}) = \dot{\boldsymbol{\theta}}^T (\boldsymbol{f}_{\mathrm{t,des}} - \boldsymbol{K}_{\mathrm{p}}(\boldsymbol{\theta}_{\mathrm{des}} - \boldsymbol{\theta}) - \boldsymbol{K}_{\mathrm{d}}\dot{\boldsymbol{\theta}} + \hat{\boldsymbol{b}} - \boldsymbol{b} + \boldsymbol{f}_{\mathrm{t}}) + \dot{\boldsymbol{\theta}}^T \boldsymbol{f}_{\mathrm{t}} - \dot{\boldsymbol{\theta}}^T \boldsymbol{\phi}(\boldsymbol{\theta}_{\mathrm{des}}) - \dot{\boldsymbol{\theta}}^T \boldsymbol{K}_{\mathrm{p}}(\boldsymbol{\theta}_{\mathrm{des}} - \boldsymbol{\theta}) \,. \tag{11.7}$$

Since $\boldsymbol{f}_{\mathrm{des}} = \boldsymbol{\phi}(\boldsymbol{\theta}_{\mathrm{des}})$:

$$\dot{V}(\boldsymbol{\theta}) = -\dot{\boldsymbol{\theta}}^T (\boldsymbol{K}_{\mathrm{d}}\dot{\boldsymbol{\theta}} + \hat{\boldsymbol{b}} - \boldsymbol{b}) \,. \tag{11.8}$$

As long as the viscous friction is not overestimated or at least less than the damping injected by the controller, the term $(\boldsymbol{K}_{\mathrm{d}}\dot{\boldsymbol{\theta}} + \hat{\boldsymbol{b}} - \boldsymbol{b})$ is positive, thereby ensuring that the derivative of the Lyapunov function is negative semi-definite. Finally, the global asymptotic stability is obtained by invoking the LaSalle theorem.

Positive definiteness of V The terms $\dot{\boldsymbol{\theta}}^T \boldsymbol{B}\dot{\boldsymbol{\theta}}$ and $(\boldsymbol{\theta} - \boldsymbol{\theta}_{\mathrm{des}})^T \boldsymbol{K}_p(\boldsymbol{\theta} - \boldsymbol{\theta}_{\mathrm{des}})$ are positive definite due to the fact that $\boldsymbol{B} > 0$ and $\boldsymbol{K}_{\mathrm{p}} > 0$. It remains to prove that $\Gamma(\boldsymbol{\theta}) = V_{\mathrm{k}}(\boldsymbol{\theta}) - V_{\mathrm{k}}(\boldsymbol{\theta}_{\mathrm{des}}) + \frac{\partial V_{\mathrm{k}}}{\partial \boldsymbol{\theta}}|_{\boldsymbol{\theta}_{\mathrm{des}}}(\boldsymbol{\theta}_{\mathrm{des}} - \boldsymbol{\theta})^T$ is positive definite. Trivially, $\Gamma(\boldsymbol{\theta}_{\mathrm{des}}) = \boldsymbol{0}$. Γ has an extremum in $\boldsymbol{\theta}_{\mathrm{des}}$ since $\frac{\partial \Gamma}{\partial \boldsymbol{\theta}}(\boldsymbol{\theta}_{\mathrm{des}}) = \frac{\partial V_{\mathrm{k}}}{\partial \boldsymbol{\theta}}(\boldsymbol{\theta}_{\mathrm{des}}) - \frac{\partial V_{\mathrm{k}}}{\partial \boldsymbol{\theta}}|_{\boldsymbol{\theta}_{\mathrm{des}}} = \boldsymbol{0}$. It is a minimum because $\frac{\partial^2 \Gamma}{\partial \boldsymbol{\theta}^2} = \frac{\partial \phi(\boldsymbol{\theta})}{\partial \boldsymbol{\theta}} > 0$ because $\boldsymbol{f}_{\mathrm{t}} = \boldsymbol{\phi}(\boldsymbol{\theta})$ is strictly increasing, which completes the proof.

Link side controller

The equations for the link side dynamics and the link side controller are

$$\boldsymbol{M}(\boldsymbol{q})\ddot{\boldsymbol{q}} + \boldsymbol{C}(\dot{\boldsymbol{q}}, \boldsymbol{q})\dot{\boldsymbol{q}} + \boldsymbol{g}(\boldsymbol{q}) = \boldsymbol{\tau}_{\mathrm{ext}} + \boldsymbol{\tau} \tag{11.9}$$

and

$$\boldsymbol{\tau} = -\boldsymbol{K}_{\mathrm{p,imp}}(\boldsymbol{q} - \boldsymbol{q}_{\mathrm{des}}) - \boldsymbol{K}_{\mathrm{d,imp}}(\boldsymbol{q} - \boldsymbol{q}_{\mathrm{des}}) + \boldsymbol{g}(\boldsymbol{q}) + \boldsymbol{C}(\dot{\boldsymbol{q}}, \boldsymbol{q})\dot{\boldsymbol{q}}_{\mathrm{des}} + \boldsymbol{M}(\boldsymbol{q})\ddot{\boldsymbol{q}}_{\mathrm{des}}. \tag{11.10}$$

The regulation problem is used to prove stability, that is, $\boldsymbol{q}_{\mathrm{des}} = \dot{\boldsymbol{q}}_{\mathrm{des}} = \ddot{\boldsymbol{q}}_{\mathrm{des}} = \boldsymbol{0}$. The two following paragraphs present two alternative proofs.

Lyapunov Approach Consider the Lyapunov function

$$V(\boldsymbol{q}, \dot{\boldsymbol{q}}) = \frac{1}{2}\dot{\boldsymbol{q}}^T \boldsymbol{M}(\boldsymbol{q})\dot{\boldsymbol{q}} + \frac{1}{2}\boldsymbol{q}^T \boldsymbol{K}_{\mathrm{p,imp}}\boldsymbol{q} \ . \tag{11.11}$$

Its derivative along the solutions is

$$\dot{V}(\boldsymbol{q}, \dot{\boldsymbol{q}}) = \dot{\boldsymbol{q}}^T \boldsymbol{M}(\boldsymbol{q})\ddot{\boldsymbol{q}} + \frac{1}{2}\dot{\boldsymbol{q}}^T \dot{\boldsymbol{M}}(\boldsymbol{q})\dot{\boldsymbol{q}} + \dot{\boldsymbol{q}}^T \boldsymbol{K}_{\mathrm{p,imp}}\boldsymbol{q} \ . \tag{11.12}$$

Replacing the controller equation in free environment leads to

$$\dot{V}(\boldsymbol{q}, \dot{\boldsymbol{q}}) = \dot{\boldsymbol{q}}^T(\boldsymbol{\tau} - \boldsymbol{C}(\dot{\boldsymbol{q}}, \boldsymbol{q}) + \boldsymbol{g}(\boldsymbol{q})) + \frac{1}{2}\dot{\boldsymbol{q}}^T \dot{\boldsymbol{M}}(\boldsymbol{q})\dot{\boldsymbol{q}} + \dot{\boldsymbol{q}}^T \boldsymbol{K}_{\mathrm{p,imp}}\boldsymbol{q} \ , \tag{11.13}$$

which is further simplified to

$$\dot{V}(\boldsymbol{q}, \dot{\boldsymbol{q}}) = -\dot{\boldsymbol{q}}^T \boldsymbol{K}_{\mathrm{d,imp}}\dot{\boldsymbol{q}} \ . \tag{11.14}$$

Since $\boldsymbol{K}_{\mathrm{d,imp}}$ is positive definite, the Lyapunov derivative is negative semi-definite. The global asymptotic stability is concluded by invoking the LaSalle theorem.

Alternative proof By design the closed-loop dynamics of the error $\boldsymbol{e} = \boldsymbol{q}_{\mathrm{des}} - \boldsymbol{q}$ is

$$\boldsymbol{M}(\boldsymbol{q})\ddot{\boldsymbol{e}} + \boldsymbol{K}_{\mathrm{d,imp}}\dot{\boldsymbol{e}} + \boldsymbol{K}_{\mathrm{p,imp}}\boldsymbol{e} = 0. \tag{11.15}$$

The stability is ensured by the choice of the stiffness and the damping matrices (which ought to be positive definite).

11.5 Stability Conditions : The cascaded case

The previous section neglected the influence of the force controller error and established the closed-loop stability under the singular perturbation hypothesis. It is possible to explicitly take into account the tendon force error if the system is considered as a cascaded system. However, because the systems must depend on the same set of variables, the linearizing tendon force controller is used instead of the motor position controller. As a result, a differential system of equations in the variable θ is considered. The initial system, under the action of the controller is given by:

$$\begin{aligned} \boldsymbol{B}_{\mathrm{f}}\ddot{\boldsymbol{e}}_{\mathrm{f}} + \boldsymbol{K}_{\mathrm{p}}\dot{\boldsymbol{e}}_{\mathrm{f}} + \boldsymbol{K}_{\mathrm{p}}\boldsymbol{e}_{\mathrm{f}} = 0 \\ \boldsymbol{M}\ddot{\boldsymbol{q}} + \boldsymbol{K}_{\mathrm{d,imp}}(\dot{\boldsymbol{q}} - \dot{\boldsymbol{q}}_{\mathrm{des}}) + \boldsymbol{K}_{\mathrm{p,imp}}(\boldsymbol{q} - \boldsymbol{q}_{\mathrm{des}}) = \boldsymbol{P}^T\boldsymbol{e}_{\mathrm{f}} \ . \end{aligned} \tag{11.16}$$

where $\boldsymbol{e}_{\mathrm{f}} = \boldsymbol{f}_{\mathrm{t,des}} - \boldsymbol{f}_{\mathrm{t}}$ is the tendon force error. To establish stability, the two decoupled system must be asymptotically stable. Moreover, the coupled system must be proved to be stable. Then, the global system is asymptotically stable. The construction of the proof is inspired by Ott [130]. The first

conditions are trivially obtained given that the gain matrices are positive definite. Even exponential stability is possible. The second condition, however, is more subtle. The solution consists in building a quadratic Lyapunov function for which it is possible to show that there always exists a choice of gains that ensures stability. A candidate Lyapunov function is given by

$$V(\boldsymbol{q}, \dot{\boldsymbol{q}}, \boldsymbol{e}) = \frac{1}{2}\dot{\boldsymbol{q}}^T \boldsymbol{M}\dot{\boldsymbol{q}} + \frac{1}{2}\boldsymbol{q}^T \boldsymbol{K}_{\mathrm{p,imp}}\boldsymbol{q} + \boldsymbol{e}^T \boldsymbol{G}\boldsymbol{e} \ , \tag{11.17}$$

where all matrices are positive definite, thus being a quadratic Lyapunov function. The derivative of the candidate along the solution of the system is

$$\begin{aligned}\dot{V}(\boldsymbol{q}, \dot{\boldsymbol{q}}, \boldsymbol{e}) = \dot{\boldsymbol{q}}^T(-\boldsymbol{K}_{\mathrm{d,imp}}(\dot{\boldsymbol{q}} - \boldsymbol{q}_{\mathrm{des}}) - \boldsymbol{K}_{\mathrm{p,imp}}(\boldsymbol{q} - \boldsymbol{q}_{\mathrm{des}}) + \boldsymbol{P}^T\boldsymbol{e}_{\mathrm{f}}) \\ +\boldsymbol{q}^T\boldsymbol{K}_{\mathrm{p,imp}}\dot{\boldsymbol{q}} + \tfrac{1}{2}\dot{\boldsymbol{e}}^T\boldsymbol{G}\boldsymbol{e} + \tfrac{1}{2}\boldsymbol{e}^T\boldsymbol{G}\dot{\boldsymbol{e}}\end{aligned} \ . \tag{11.18}$$

In the regulation case, it simplifies to

$$\dot{V}(\boldsymbol{q}, \dot{\boldsymbol{q}}, \boldsymbol{e}) = -\dot{\boldsymbol{q}}^T\boldsymbol{K}_{\mathrm{d,imp}}\dot{\boldsymbol{q}} - \dot{\boldsymbol{q}}^T\boldsymbol{P}^T\boldsymbol{e}_{\mathrm{f}} + \dot{\boldsymbol{e}}^T\boldsymbol{G}\boldsymbol{e} \ , \tag{11.19}$$

which can be rewritten in the following matrix form by defining a state vector $w = [\dot{\boldsymbol{q}}, \boldsymbol{e}, \dot{\boldsymbol{e}}]$.

$$\dot{V}(\boldsymbol{w}) = -\boldsymbol{w}^T\boldsymbol{W}\boldsymbol{w}. \tag{11.20}$$

The matrix $\boldsymbol{W}$ is given by

$$\boldsymbol{W} = \begin{bmatrix} \boldsymbol{K}_{\mathrm{d,imp}} & \boldsymbol{P}^T/2 \\ \boldsymbol{P}/2 & -\boldsymbol{G} \end{bmatrix} \ . \tag{11.21}$$

According to Schur's Lemma the matrix is positive definite if $\boldsymbol{K}_{\mathrm{d,imp}} > \boldsymbol{0}$ and $\boldsymbol{K}_{\mathrm{d,imp}} - \frac{1}{4}\boldsymbol{P}^T\boldsymbol{G}^{-1}\boldsymbol{P} > \boldsymbol{0}$. The first condition is trivially fulfilled while the second one can always be satisfied by a good choice of a positive definite $\boldsymbol{G}$. Since $\boldsymbol{G}$ can be selected freely as being one solution of the Riccati equation, the system is globally stable. Together with the exponential stability of the subsystems, the cascaded system is globally asymptotically stable.

11.6 Experimental Results

The performance of the singular perturbation and the cascaded approaches would optimally be analyzed in three separated setups: a single tendon motor unit with motor torque input, a finger with a *direct* joint torque input and the combination of a tendon force controller and the joint torque impedance controller. However, it is not possible to create a direct joint torque controller, since the hardware can not be adapted for it. Nonetheless, previous experiments with the DLR Hand II, where the motors are directly located in the joints, confirmed the validity of the design. The experimental results of the tendon controller have been reported in the previous chapter.

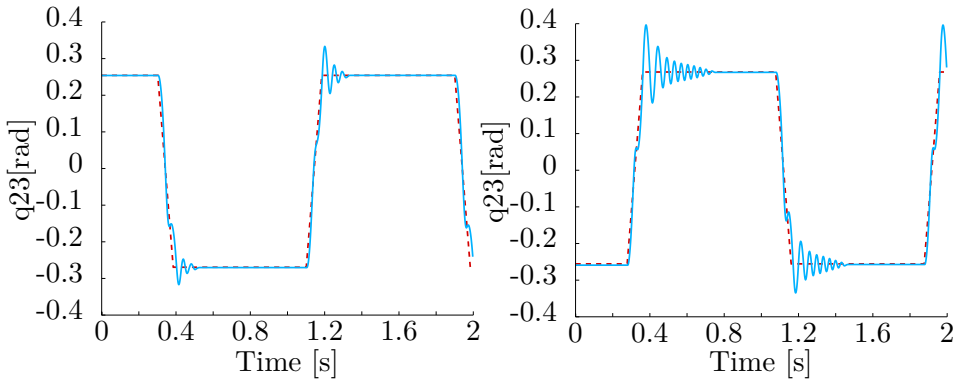

(a) Low impedance stiffness

(b) High impedance stiffness

Figure 11.2: Experiment: step response for two impedance controller stiffness

Therefore, this chapter reports only the controller results corresponding to the complete system.

A simple experiment allows to verify the basic functionality of the link side controller. A desired position change of the link is commanded with two different impedance stiffness. Because the low damping of the impedance is left unchanged, as well as the other controller parameters, the oscillations should be increasing. In Figure 11.2, the desired link position is depicted in dashed/red and the measured link position is represented in light blue/solid. The plots are complying with the expected increase of the oscillations. A second experiment is performed with different initial mechanical stiffness while all other parameters are constant. The results reported in Fig. 11.3 show the trajectory of the link depending on the mechanical stiffness. Unlike the first experiment, the oscillation are expected to be reduced when the mechanical stiffness is increased. Indeed, a stiff mechanism minimizes the error between the desired and the achieved torque since the system requires less motion for the same change of torque. Moreover, increasing the initial pretension increases the friction in the tendon guiding and leads to a higher damping ratio. It should be noted that in the high mechanical stiffness case, the initial tendon load is so high that the stick-slip effects in the joint are preventing the link to reach the desired joint position

Remarks about the singular perturbation approach In the case of the singular perturbation approach, the controller design is based on the assumption that the two controllers are independent. Several experiments confirmed that oscillations can appear when the desired joint stiffness is modified. Fig. 11.4 shows that the resonance frequency is shifted if the mechanical stiffness is modified, thus confirming that the singular perturbation approach may only be valid across a restricted frequency range.

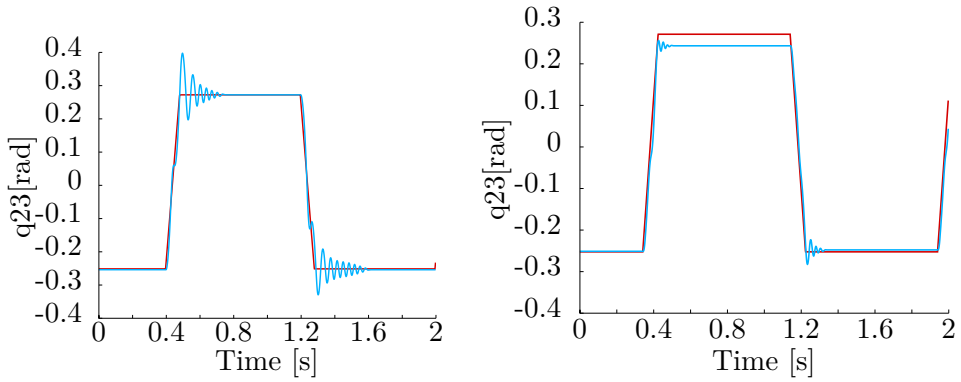

(a) Low mechanical stiffness (b) High mechanical stiffness

Figure 11.3: Experiment: step response for two different mechanical stiffness

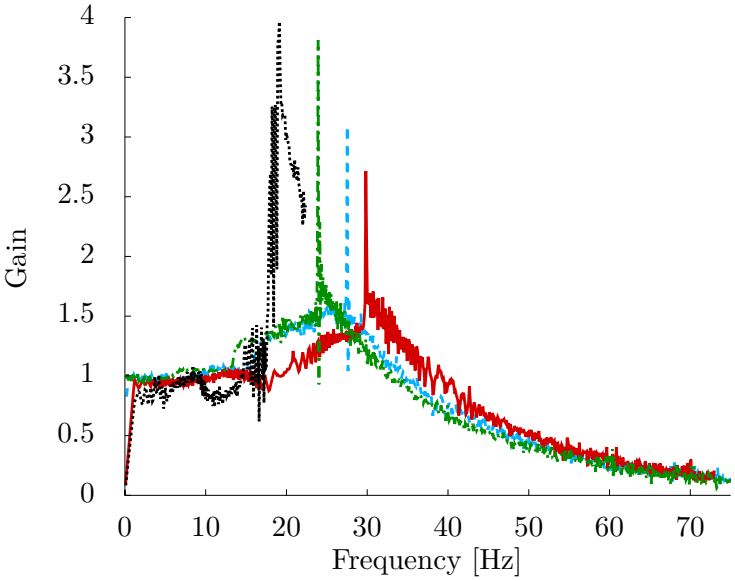

Figure 11.4: Experiments: gain diagram of the output link position across a frequency range and for different stiffness. The responses are obtained by a sinusoidal sweep input for the desired link. It can be observed that the resonance frequency is shifted when the mechanical stiffness is modified.

11.7 Discussion

This chapter presented two approaches for the control of a flexible joint: the singular perturbation approach and the cascaded approach. In both cases the stability can be established by the use of the Lyapunov stability theorems. The singular perturbation case simply neglects the influence of the force tracking error. However, it was experimentally verified that the validity of the time scale separation assumption depends on the mechanical stiffness settings. The cascaded stability analysis is more involved but explicitly includes the tendon force error, thus is independent of the mechanical stiffness. It is important to note that the tendon controller used for the proof must depend on $\boldsymbol{f}_{\mathrm{t}}$ and not on $\boldsymbol{\theta}$ in order to obtain a cascaded form. The controller was experimentally tested and demonstrated a basic performance.

12 Direct pole placement

The singular perturbation method is restricted to the domains where the two subsystems, that is the link side impedance controller and the tendon force controller, do not interact. The cascaded method does not require such a restriction at the cost of a more complex choice of the gains. In order to improve the controller, in the sense that the time scale hypothesis is not required anymore, it is necessary to use a more global approach. The concept of direct pole placement using a feedback controller is, historically, one of the first methods applied to control multi-DOF systems. It is described by a slightly different form in nearly all control books, for example in [131, p. 176]. The method consists in computing the closed-loop poles of the system and designing the feedback such that the poles are placed as desired. The very notion of poles being restricted to linear system (there exist some extensions work for nonlinear systems, e. g. [132] for an introduction or [133] for an application to discrete systems). The proposed approaches in the literature are mostly focusing on two aspects: whether the closed-loop system reaches the targeted behavior (locally) and, since the controllers are by construction locally stable, how large is the actual region of stability and how to enlarge it.

This chapter focuses on the placement of the poles of the system and the sensitivity of the poles around the nominal model. One important question is how sensitive is the controller w. r. t. the plant modeling errors. A more practical question is the choice of the poles. Indeed, whereas selecting a negative real part for the poles is trivially ensuring stability, it is challenging to *imagine* which poles should be used for a fourth order system that will result in a *good* behavior.

The chapter is organized as follows. First, a simple example is proposed to illustrate the method. It is shown that the identification of the closed-loop poles to the poles of a well-known system is an intuitive method. Then, the method is applied to a linear flexible joint model which is a fourth order system. The closed-loop solutions are given and, by identification, the poles are placed. Finally, a robustness analysis is proposed. The sensitivity of the poles w. r. t. the modeling errors is studied. To this end, modeling errors are introduced and the poles of the system under the nominal controller are calculated. It is shown that the method is highly sensitive to the system stiffness. Since the method is not robust to modeling errors, even in the linear case, the method is not applied to the nonlinear case. However, the nonlinear case is handled in a later chapter with the help of the state dependent Riccati equations.

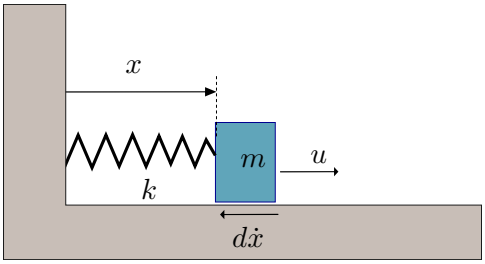

Figure 12.1: Simple mass spring damper system. The viscous friction generated by the ground is denoted $d\dot{x}$.

12.1 Introductory example

This section is an introduction example to the pole placement method. The reader familiar with linear control theory can safely skip this section. The equation of a simple spring-mass-damper system (cf. Fig. 12.1) is

$$m\ddot{x} = -d\dot{x} - kx + u \ , \tag{12.1}$$

where $m \in \mathbb{R}$ is the mass of the solid, $(x, \dot{x}) \in \mathbb{R}^2$ are the position and velocity of the mass, $(k, d) \in \mathbb{R}^2$ are spring constant and damping coefficient. The system input is denoted $u \in \mathbb{R}$. Assuming that the complete state is available (at least through some observer), the controller equation can take the general form of a static (i. e. the coefficient are constant w. r. t. time) state feedback

$$u = -\beta\dot{x} - \alpha x \ , \tag{12.2}$$

where $(\alpha, \beta) \in \mathbb{R}^2$ are time invariant gains. Under the action of the controller the normalized closed-loop equation is

$$\ddot{x} + \frac{(d+\beta)}{m}\dot{x} + \frac{(k+\alpha)}{m}x = 0 \ . \tag{12.3}$$

Equation (12.3) is nothing else than a linear, second order differential equation in x with constant coefficients. Trivially, the solutions of this second order equation are

$$\begin{array}{l} \gamma_1 = \frac{-(d+\beta)-\sqrt{(d+\beta)^2-4m(k+\alpha)}}{2m} \\ \gamma_2 = \frac{-(d+\beta)+\sqrt{(d+\beta)^2-4m(k+\alpha)}}{2m} \end{array} \ . \tag{12.4}$$

Transformed into the time domain, the solution is,

$$x(t) = Ae^{-\gamma_1 t} + Be^{-\gamma_2 t}, t > 0, \tag{12.5}$$

where $(A, B) \in \mathbb{R}^2$ are constants depending on the initial conditions. The solution might oscillate or not and converge or not, depending on whether

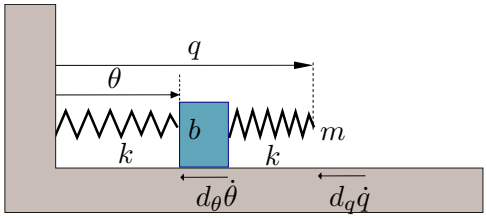

Figure 12.2: Double spring mass damper system in the case of a flexible joint model

γ_1, γ_2 are complex or not and whether their real part is positive or negative. Therefore, directly selecting the poles γ_1, γ_2 such that they have a negative real part ensures stability. However, it does not allow an easy design of the system behavior since the combination of the contributions of the poles is not intuitive. It is easier to identify the system to a well-known system, such as a harmonic oscillator, and select the parameters accordingly. Identifying the coefficients of the normalized equation to the coefficients of a damped harmonic oscillator gives the following equation to be solved:

$$\ddot{x} + \frac{(d+\beta)}{m}\dot{x} + \frac{(k+\alpha)}{m}x = \ddot{x} + 2\xi\omega_0\dot{x} + \omega_0^2 x \ , \tag{12.6}$$

where $\omega_0 \in \mathbb{R}$ and $\xi \in \mathbb{R}$ are the undamped angular frequency and the damping ratio of the harmonic oscillator. For a given choice of ω_0 and ξ, one obtains the controller gains $(\alpha, \beta) \in \mathbb{R}^2$ that result in the desired behavior. The gains are given by

$$\begin{array}{rcl} \alpha & = & m\omega_0^2 - k \\ \beta & = & 2m\xi\omega_0 - d \end{array} . \tag{12.7}$$

The method is simple and can be applied to many linear systems. It is important to note that, although the method does not enforce it, selecting poles that are far from the natural behavior might practically lead to instabilities.[1]

12.2 Fourth order model

The most simple model for a flexible joint system is a fourth order system. Therefore, in this section, the pole placement method is applied on the joint model depicted in Fig. 12.2. Referring to the modeling of Chapter 5, the joint equations are given by

$$\begin{array}{rcl} m\ddot{q} & = & -d_{\mathrm{q}}\dot{q} + k(\theta - q) \\ b\ddot{\theta} & = & -d_\theta\dot{\theta} - k(\theta - q) + u \end{array} , \tag{12.8}$$

[1] unmodeled dynamics or actuator saturation invalidate the stability proof.

where $(m, b) \in \mathbb{R}^2$ are the masses, $(q, \dot{q}, \theta, \dot{\theta}) \in \mathbb{R}^4$ are the link position, the link velocity, the motor position and the motor velocity. The damping coefficients and the spring constant are represented by $(d_\mathrm{q}, d_\theta, k) \in \mathbb{R}^3$. The actuator torque is represented by $u \in \mathbb{R}$. Defining the state vector $\boldsymbol{x} = [q, \dot{q}, \theta, \dot{\theta}]^T$, the dynamics can be written in matrix form

$$\dot{\boldsymbol{x}} = \boldsymbol{A}\boldsymbol{x} + \boldsymbol{K}\boldsymbol{B}u, \tag{12.9}$$

where $\boldsymbol{A} \in \mathbb{R}^{4\times4}$, $\boldsymbol{B} \in \mathbb{R}^{4\times1}$ are called the dynamic matrix and the input matrix. $\boldsymbol{K} \in \mathbb{R}^4$ is the feedback gain vector. Following (12.8) the matrices are given by

$$\boldsymbol{A} = \begin{bmatrix} 0 & 1 & 0 & 0 \\ -\frac{k}{m} & -\frac{d_\mathrm{q}}{m} & \frac{k}{m} & 0 \\ 0 & 0 & 0 & 1 \\ \frac{k}{b} & 0 & -\frac{k}{b} & -\frac{d_\theta}{b} \end{bmatrix} \tag{12.10}$$

and

$$\boldsymbol{K} = \begin{bmatrix} \alpha_1 & \alpha_2 & \alpha_3 & \alpha_4 \end{bmatrix}^T . \tag{12.11}$$

With the help of a symbolic calculation software, the coefficients of the characteristic polynomial of the closed-loop system are

$$\begin{bmatrix} -\frac{k}{mb}(\alpha_1 + \alpha_3) \\ \frac{-d_\mathrm{q}\alpha_3 - k(\alpha_2 + \alpha_4 - d_\mathrm{q} - d_\theta)}{mb} \quad \frac{d_\mathrm{q}d_\theta - m\alpha_3 + k(m+b) - d_\mathrm{q}\alpha_4}{mb} \\ \frac{md_\theta - m\alpha_4 + d_\mathrm{q}b}{mb} \\ 1 \end{bmatrix} . \tag{12.12}$$

To guarantee exponential stability it is necessary that the roots of the polynomial have negative real parts. However, it is neither easy to select the gains $\boldsymbol{\alpha}$ nor intuitive to choose the amplitude of the real part. Indeed, it is important to remember that although the theory guarantees exponential stability, it is practically impossible to use arbitrarily large gains. Similar to the case of the mass spring damper, if the coefficients of a well-known fourth order system are available it is possible to proceed by identification. Motivated by the mechanical structure of the system, one choice consists in taking the dynamics of a double harmonic oscillators as a target.

$$(s^2 + 2s\xi_1\omega_1 + \omega_1^2)(s^2 + 2s\xi_2\omega_2 + \omega_2^2) = 0 \ , \tag{12.13}$$

where s is the Laplace transform of x and $(\xi_1, \xi_2, \omega_1, \omega_2) \in \mathbb{R}^4$ are the damping ratios and the undamped angular frequencies of the harmonic oscillators.

By identification of the coefficients, one obtains a set of equations

$$\begin{array}{c} -\dfrac{k}{mb}(\alpha_1+\alpha_3)=\omega_1^2\omega_2^2 \\ \dfrac{-d_{\mathrm{q}}\alpha_3-k(\alpha_2+\alpha_4-d_{\mathrm{q}}-d_\theta)}{mb}=2(\xi_2\omega_1^2\omega_2+\xi_2\omega_1\omega_2^2) \\ \dfrac{d_{\mathrm{q}}d_\theta-m\alpha_3+k(m+b)-d_{\mathrm{q}}\alpha_4}{mb}=\omega_1^2+4\xi_1\xi_2\omega_1\omega_2+\omega_2^2 \\ \dfrac{md_\theta-m\alpha_4+d_{\mathrm{q}}b}{mb}=2(\xi_1\omega_1+\xi_2\omega_2) \end{array}, \tag{12.14}$$

where the unknowns are $(\alpha_1, \alpha_2, \alpha_3, \alpha_4) \in \mathbb{R}^4$. The system of equations can be written as

$$\boldsymbol{J}\boldsymbol{\gamma} = \boldsymbol{\mu}, \tag{12.15}$$

where $\boldsymbol{\gamma} = [\alpha_1, \alpha_2, \alpha_3, \alpha_4]^T$ is the vector of unknowns, $\boldsymbol{\mu} \in \mathbb{R}^4$ is the vector of desired values and $\boldsymbol{J}$ is the Jacobian matrix given by,

$$\boldsymbol{J} = \frac{k}{bm}\begin{bmatrix} -1 & 0 & -1 & 0 \\ 0 & -1 & -\frac{d_{\mathrm{q}}}{k} & -1 \\ 0 & 0 & -\frac{m}{k} & -\frac{d_{\mathrm{q}}}{k} \\ 0 & 0 & 0 & -\frac{m}{k} \end{bmatrix}. \tag{12.16}$$

The system has solutions as long as $\boldsymbol{J}$ is invertible, that is if the determinant is not 0. The determinant of $\boldsymbol{J}$ is $\det(()\boldsymbol{J}) = \frac{k^2}{m^2b^4} > 0$. Therefore, a unique solution for the selection of the gains always exists.

12.3 Robustness analysis

The controller gains obtained in the last section are, by construction, leading to a system whose characteristic equation is given by (12.13) Using the numerical values reported in Table 12.1, the associated poles are

$$\begin{array}{c} -100+0.66i \\ -100-0.66i \\ -10+0.38i \\ -10-0.38i \end{array} \tag{12.17}$$

showing that the nominal system under the pole placement controller is exponentially stable. The corresponding gains for the state feedback are (numerical values from Table 12.1)

$$\begin{array}{c} \alpha_1 = 4395 \\ \alpha_2 = 6.177 \\ \alpha_3 = -4395 \\ \alpha_4 = 288.99 \end{array} \tag{12.18}$$

Table 12.1: Numerical values used to evaluate the poles

Symbol	Value	Units
b	$2e-3$	$kg\,m^2$
m	$4e-7$	$kg\,m^2$
k	0.605	Nm/rad
d_{q}	0.0012	$Nm/(rad/s)$
d_θ	0.0012	$Nm/(rad/s)$
ω_1	100	rad/s
ω_2	30	rad/s
ξ_1	0.7	
ξ_2	0.7	

It is interesting to note that the damping coefficient for the link is positive. It implies that the controller is trying to reduce the link friction by *pushing* the link. Although the closed-loop system is stable, this type of feedback is not recommended in practice. As with all model-based designs, the exact plant parameters are not perfectly known and it is important to study the influence of the plant model errors on the overall stability. Modifying the real plant parameters from $k = 0.605Nm/rad$ to $k = 0.600Nm/rad$ and recomputing the poles yields

$$\begin{matrix} -318.78 \\ 53.27 + 225.14i \\ 53.27 - 225.14i \\ -0.058 \end{matrix} \tag{12.19}$$

The modified plant under the nominal pole placement controller has a positive real part leading to an unstable system. It indicates that the pole placement method is very sensitive to the plant modeling errors, at least around the selected target dynamics. A more accurate sensitivity analysis is obtained by a parametric analysis. All quantities are fixed (to the nominal parameters of Table 12.1) but one that is varied across an uncertainty range. The root locus plots are then used to evaluate the sensitivity to each parameter. Fig. 12.3 depicts the sensitivity of open loop the poles w. r. t. to the spring stiffness and the link damping. Fig. 12.4 depict the sensitivity of the closed-loop poles w. r. t. to the link stiffness. It can be seen that the poles of the closed-loop plant are very sensitive to the link stiffness. The range of stiffness that is tested is a realistic range of adjustability of the stiffness. The simulation highlights the limited robustness of the controller, even though this particular choice of feedback gains does not lead to an unstable system.

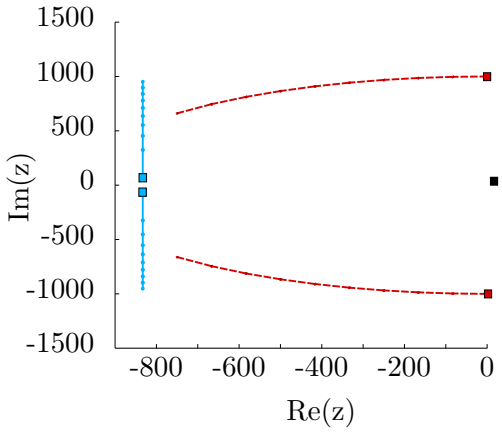

Figure 12.3: Open loop poles depending on the stiffness and the link damping. The influence of the link stiffness $K = [0.43, 1.15]$ is depicted in light blue/solid. The influence of the link damping $D_\mathrm{q} = [0.43, 1.15]$ is depicted in red/dashed. In both cases the square indicates the start values. The third and fourth poles are depicted in black and do not change significantly.

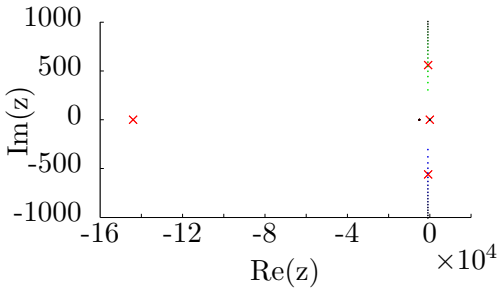

Figure 12.4: Closed-loop poles depending on the stiffness $K = [0.43, 1.15]$. The nominal poles are indicated by squares. It can be seen that the poles are sensitive to the link stiffness.

12.4 Discussion

As highlighted in the previous section, the robustness of the method is very limited for the selected target dynamics. Because of the sensitivity, it is not guaranteed that the overall system will be robust enough to cope with the modeling errors unless a very conservative performance is selected. Indeed, despite the extensive modeling, the stiffness of the Awiwi Hand is not precisely known. Moreover, the method is only local thus the stiffness change around the nominal position is only treated as a disturbance. The modeling errors, the calibration errors, the unmodeled dynamics, and the linearization approximations would practically lead to a marginally stable system. One major concern is that, if the target dynamics is far from the natural behavior, the magnitude of the control input might be extremely large. If the controller action is too large, the nonlinearities associated with the actuator saturation might introduce, as well, instabilities. Therefore, the idea of using a full state feedback controller around each linearization point, as reported in [77] is not applied. Their approach is successful mainly because the range of stiffness they considered is higher and their link inertia much larger. As a result their system is less sensitive to the modeling errors.

13 Optimal control

The direct pole assignment method did not account for the magnitude of the control input, resulting in an unpractical command law. Although theoretically very capable, its robustness revealed to be practically limited for the selected choice of target dynamics. In this chapter the focus lies on finding a method that mitigates the costs of the error and the magnitude of the input, thus implicitly selects good target dynamics. A possible way to express the objective mathematically is to formulate an optimization problem in the form

$$\min_{u(t)} \int_0^t (\boldsymbol{x}(t)^T \boldsymbol{Q} \boldsymbol{x}(t) + u(t)^T R u(t)) dt \ , \tag{13.1}$$

where $\boldsymbol{x}(t) \in \mathbb{R}^2$ and $u(t) \in \mathbb{R}$ are the state vector and the input vector. $\boldsymbol{Q} \in \mathbb{R}^{2\times 2}$ and $R \in \mathbb{R}$ are a positive definite matrix and a scalar that represent sthe cost of the error and the cost of the input. In this chapter, a linear quadratic regulator (LQR) is analyzed. It serves as an introduction to the SDRE method presented in the next chapter. The chapter is organized as follows. First, a simple example is proposed to illustrate the method. In the second section, the method is applied to the linear flexible joint model, which is a Linear Time Invariant system (LTI). Finally, simulations are performed to evaluate the results.

13.1 Introduction example

Similar to the previous chapters, a single spring mass damper is used to introduce the method. The equation of a simple single spring mass system (Fig. 13.1) is

$$m\ddot{x} = -d\dot{x} - kx + u \ , \tag{13.2}$$

where $m \in \mathbb{R}$ is the mass of the solid, $(x, \dot{x}) \in \mathbb{R}^2$ are the mass position and velocity, and $(k, d) \in \mathbb{R}^2$ are some positive spring constant and damping coefficients. The system input, an external force, is denoted $u \in \mathbb{R}$. The

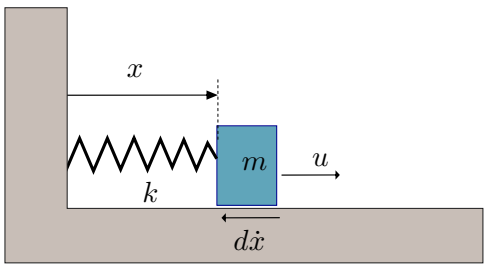

Figure 13.1: Single mass-spring-damper.

regulator feedback has the form

$$u(t) = -\boldsymbol{K}(t)^T \boldsymbol{x}(t) \ , \tag{13.3}$$

where $\boldsymbol{x}(t) \in \mathbb{R}^2$ is the state vector and $\boldsymbol{K}(t) = R^{-1}\boldsymbol{B}^T\boldsymbol{S}(t)$ is the vector of the state feedback gains. $\boldsymbol{S}(t)$ is the solution of the differential Riccati equation

$$\frac{d\boldsymbol{S}(t)}{dt} = -\boldsymbol{S}(t)\boldsymbol{A} - \boldsymbol{A}^T\boldsymbol{S}(t) + \boldsymbol{S}(t)\boldsymbol{B}R^{-1}\boldsymbol{B}^T\boldsymbol{S}(t) - \boldsymbol{Q} \ , \tag{13.4}$$

where $\boldsymbol{A} \in \mathbb{R}^{2\times 2}$ denotes the dynamic matrix. For an infinite time horizon, the equation is the algebraic Riccati equation (ARE) given by

$$\boldsymbol{S}\boldsymbol{A} + \boldsymbol{A}^T\boldsymbol{S} - \boldsymbol{S}\boldsymbol{B}R^{-1}\boldsymbol{B}^T\boldsymbol{S} + \boldsymbol{Q} = 0 \ . \tag{13.5}$$

In such a case, all matrices are constant and solving the ARE given by (13.5) for $\boldsymbol{S}$ yields the optimal linear regulator gains. Solving the ARE is not critical since it can be performed offline and several solvers are available.

13.2 Fourth order system

According to the previous chapter, a double mass spring damper system is described by

$$\dot{\boldsymbol{X}} = \boldsymbol{A}\boldsymbol{X} + \boldsymbol{B}u \ , \tag{13.6}$$

where the state matrix $\boldsymbol{A} \in \mathbb{R}^{4\times 4}$ and the input matrix $\boldsymbol{B} \in \mathbb{R}^{4\times 1}$ are given by

$$\boldsymbol{A} = \begin{bmatrix} 0 & 1 & 0 & 0 \\ -\frac{k}{m} & -\frac{d_q}{m} & \frac{k}{m} & 0 \\ 0 & 0 & 0 & 1 \\ \frac{k}{b} & 0 & -\frac{k}{b} & -\frac{d_\theta}{b} \end{bmatrix} \tag{13.7}$$

and

$$\boldsymbol{B} = \begin{bmatrix} 0 \\ 0 \\ 0 \\ 1/b \end{bmatrix} \ . \tag{13.8}$$

The optimal feedback gains are obtained by solving the ARE equation. Defining the state cost matrix $\boldsymbol{Q} \in \mathbb{R}^{4\times 4}$ and the input cost $R \in \mathbb{R}$ by

$$\boldsymbol{Q} = \begin{bmatrix} 10 & 0 & 0 & 0 \\ 0 & 0.01 & 0 & 0 \\ 0 & 0 & 1 & 0 \\ 0 & 0 & 0 & 0.01 \end{bmatrix} \ , \tag{13.9}$$

and

$$R = 0.01 \ , \tag{13.10}$$

Table 13.1: Parameters used for the simulation of the optimal state feedback

Symbol	Value	Units
B	$2e-3$	$kg.m^2$
M	$4e-7$	$kg.m^2$
k	0.605	Nm/rad
Q	$\begin{bmatrix} 10 & 0 & 0 & 0 \\ 0 & 0.01 & 0 & 0 \\ 0 & 0 & 1 & 0 \\ 0 & 0 & 0 & 0.01 \end{bmatrix}$	
R	$\in [0.0001, 0.01, 1]$	

MATLAB® gives the following solution

$$u = -\left[-126.21, -0.11, 159.37, 1.52\right]^T \boldsymbol{x} \ . \tag{13.11}$$

.

13.3 Simulation

The simulations are performed using the numerical solver from MATLAB®, with the parameters of Table 13.1. The link and motor positions obtained for different input costs are reported in Figure 13.2. The corresponding inputs are reported in Figure 13.3. As desired, the amplitude of the input command can be controlled by the cost matrices R and $\boldsymbol{Q}$. It should be noted that the simulations are performed with costs matrices that are not directly suitable for the real implementation. In practice, the gain matrices must be selected according to the expected performance, the noise of the sensors and the computation delays.

13.4 Discussion

The optimal control method has been applied to a linear fourth order system. In the case of such a system, the optimality problem can be reduced to the problem of solving the ARE. The method allows to specify the relative cost of the input amplitude w. r. t. the state errors. Therefore, it is possible to moderate the controller action by setting a high cost on the input. However, a limited command also results in a degraded feedback effect in terms of settling time. The plant under such a controller is guaranteed to be exponentially stable by construction. However, the method is not suitable for nonlinear plants since the problems must be written in a linear form. Moreover, solving directly the corresponding nonlinear, optimal control problem online is practically intractable.

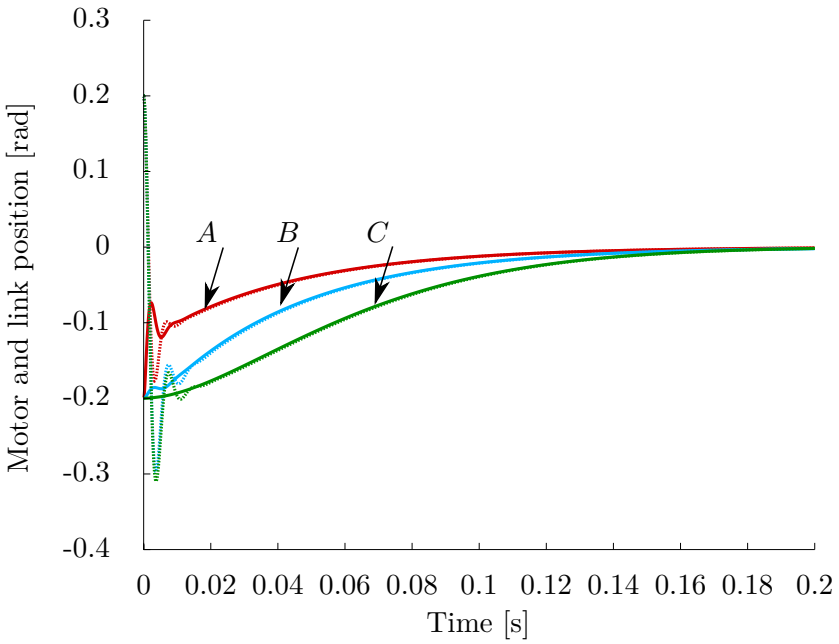

Figure 13.2: Simulation: link and motor trajectories of the plant under an optimal state feedback controller. The simulations performed with $R = 0.0001$ (resp. 0.01 and 1 are denoted by A/red (resp. B/light blue, C/green). The solid line represents the motor position whereas the dotted line represents the link position.

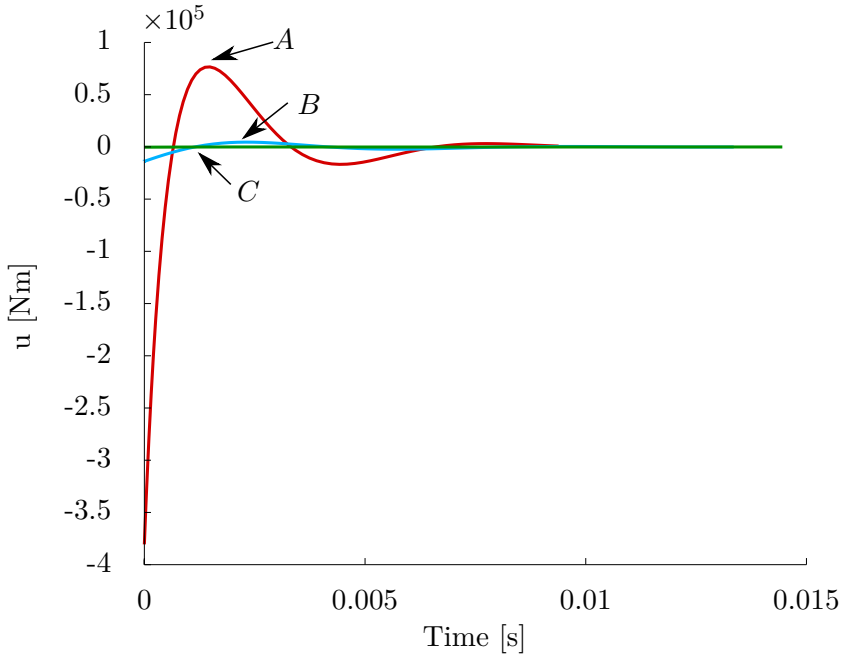

Figure 13.3: Simulation: input command of the plant under an optimal state feedback controller. The curves A/red (resp. B/light blue, C/green) are corresponding to the simulations of Figure 13.2.

14 State-Dependent Riccati Equation

The 19 joints of the hand are driven by 38 tendons that have a nonlinear stiffness characteristic. It means that the motor displacement required to adjust the tendon force depends on the current force. As demonstrated previously, the gain scheduling method is effective to assign the poles (of the pointwise linear system) but does not account for the input command magnitude. The optimal control method, that leads to the ARE in the case of a linear system, is able to account for the cost of the state error and the input amplitude. However, its genuine form is limited to linear problems. The optimization problem, that is solved relatively easily in the case of a linear system, is not anymore trivial to solve in the presence of nonlinearities. The exact solution of an optimal control problem is obtained by solving the Hamilton-Jacobi-Bell (HJB) equation given by

$$V(u(t)) = \int_0^T C(\boldsymbol{x}(t), u(t))dt + D(\boldsymbol{x}(T)), \tag{14.1}$$

where $\boldsymbol{x} \in \mathbb{R}^n, n \in \mathbb{N}$ is the state vector. The running state cost and the terminal state cost are denoted $C \in \mathbb{R}$ (resp. $D \in \mathbb{R}$). The functional to be minimized by the choice of the input function $u(t) \in \mathbb{R}, t \in [0, T], T > 0$ is represented by $V(u(t) \in \mathbb{R}$. Direct methods to solve the optimal control problems are reported as early as in 1959, in [87]. It has been applied to solve offline optimization problem such as space shuttle trajectory, ship maneuver or, more recently, throwing problem [88]. A result of optimal control due to Pontryagrin [86] is that in many cases bang-bang control is the solution (saturated maximum/minimum control input). However only a limited number of forms can be solved analytically. One must resort to numerical methods for the other cases, nonetheless their form can give further insights on the most efficient numerical techniques to be employed. Unfortunately, they require forward and backward integrations and, in general, are extremely expensive to compute. Especially, they are generally for real-time or online application.

An intermediate way between the linear optimal control, with the ARE, and the optimal nonlinear control, with the HBJ equation, has been proposed around 1962 by Pearson under the name of State Dependent Riccati Equation (SDRE) [89]. It has been expended by Wernly [90] and popularized by Cloutier [91–95]. The method is an intuitive extension of the ARE, applied to a pointwize linearized system. The existence of a SDRE stabilizing feedback is discussed in [96]. The method offers only limited theoretical results for global stability but proved to be effective in practice. More details can be found in the extensive survey [97].

In a first section the method is presented with a generic example based on [91]. The second section applies the method to two problems: the control

of the tendon force, similar to the gain scheduling example, and the control of a single joint with one motor and a nonlinear spring. The third section evaluates the controller with the help of simulations. Finally, section four discusses the results.

14.1 State Dependant Riccati Equations

Considering a nonlinear multi-variable system,

$$\dot{\boldsymbol{x}} = \boldsymbol{f}(\boldsymbol{x}) + \boldsymbol{u} \ , \tag{14.2}$$

where the state dimension is $n \in \mathbb{N}$ and $\boldsymbol{x} \in \mathbb{R}^n$ is the state vector. A nonlinear function of the state variables, that is assumed to be sufficiently smooth, is denoted $\boldsymbol{f}(\boldsymbol{x}) \in \mathbb{R}^n$. The control input is $\boldsymbol{u} \in \mathbb{R}^n$. It is possible to write (14.2) in a pseudo-linear form, also referred to as the pointwise linear form, as

$$\dot{\boldsymbol{x}} = \boldsymbol{A}_{\mathrm{k}}\boldsymbol{x} + \boldsymbol{B}_{\mathrm{k}}\boldsymbol{u} \ , \tag{14.3}$$

One pointwise linearized form and the associated input for a given factorization $\Xi_{\mathrm{k}}, \mathrm{k} \in \mathbb{N}$ are denoted $\boldsymbol{A}_{\mathrm{k}} \in \mathbb{R}^{n\times n}$ and $\boldsymbol{B}_{\mathrm{k}} \in \mathbb{R}^{n\times m}$. It should be noted that, excepted the case $n = 1$, there exists an infinite number of factorization Ξ_{k} and its associated matrices $(\boldsymbol{A}_{\mathrm{k}}, \boldsymbol{B}_{\mathrm{k}})$. Once a factorization has been selected, the ARE can be used to select the optimal gains. According to Chapter 13, the state feedback gains are selected as

$$\boldsymbol{K} = \boldsymbol{R}^{-1}\boldsymbol{B}_{\mathrm{k}}^T\boldsymbol{S} \ , \tag{14.4}$$

where $\boldsymbol{R}(t) \in \mathbb{R}^{m\times m}$ is a positive definite cost matrix for the input, $\boldsymbol{B}_{\mathrm{k}}$ is the input matrix and $\boldsymbol{S}(t)$ is one solution of the Riccati equation defined by

$$\boldsymbol{S}\boldsymbol{A}_{\mathrm{k}} + \boldsymbol{A}_{\mathrm{k}}^T\boldsymbol{S} + \boldsymbol{S}\boldsymbol{B}_{\mathrm{k}}\boldsymbol{R}^{-1}\boldsymbol{B}_{\mathrm{k}}^T\boldsymbol{S} - \boldsymbol{Q} = 0 \ , \tag{14.5}$$

where $\boldsymbol{Q} \in \mathbb{R}^{n\times n}$ (resp. $\boldsymbol{R} \in \mathbb{R}^{m\times m}$) is the state error cost (resp. the control input cost) both positive definite. The closed-loop system is

$$\dot{\boldsymbol{x}} = \boldsymbol{A}_{\mathrm{k}}\boldsymbol{x} + \boldsymbol{B}_{\mathrm{k}}^T\boldsymbol{R}^{-1}\boldsymbol{B}_{\mathrm{k}}^T\boldsymbol{S}\boldsymbol{x} \ . \tag{14.6}$$

Under the assumption that all quantities are continuous and continuously differentiable (C^1), and by construction of $\boldsymbol{S}$, the closed-loop system of (14.6) is Hurwitz, therefore locally asymptotically stable.

14.2 Applications

In this section the state-dependent Riccati equation (SDRE) is derived for two particular cases. First, the force regulation of the tendon forces when

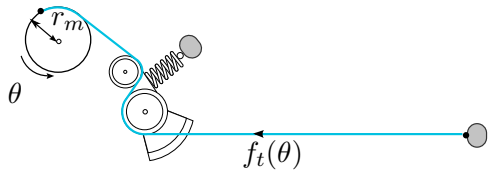

Figure 14.1: Model for the tendon force controller. The link is assumed to be fixed, thus the tendon force only depends on the motor position.

considering the joint fixed is studied. It is the problem that was motivating the gain scheduling method of Chapter 10. Second, a single nonlinear flexible joint model driven by a single motor is proposed. The second problem is a simplification of the real case problem that allows to understand the effect of the control.

14.2.1 Tendon force controller

The model comprises a motor, a spring element and a tendon (cf. Fig. 16.1). The tendon is attached to a fixed reference (grounded). The control objective is to regulate the tendon force ($f_\mathrm{t} \in \mathbb{R}$), measured by the spring lever, by adjusting the position $\theta \in \mathbb{R}$ of the motor with the torque input $u \in \mathbb{R}$. The dynamic equation of the system is

$$B_\theta \ddot{\theta} = -f_\mathrm{t}(\theta) + u \ , \tag{14.7}$$

where $B_\theta \in \mathbb{R}$ is the motor inertia (w. r. t. the motor acceleration), $\theta \in \mathbb{R}$ and $u \in \mathbb{R}$ are classically the motor position and the torque input. The tendon force depending on the motor position is denoted $f_\mathrm{t}(\theta) = \varphi(\theta)$. It is important to note that for the following analysis, the function $\varphi(\theta)$ is required to be at least C^2 w. r. t. θ. To apply the SDRE method it is first necessary to establish the pointwise linear form. One possible solution is given by equation (14.8). The linearization w. r. t. to θ is

$$B_\theta \ddot{\theta} = -f_\mathrm{t}(\theta_0) - \frac{\partial f_\mathrm{t}(\theta)}{\partial \theta}|_{\theta_0}(\theta - \theta_0) + u \ , \tag{14.8}$$

where θ_0 is the linearization point. Adding a feedforward term to the command $u = f_\mathrm{t}(\theta_0) + v$ shifts the equilibrium to the origin. Introducing the error $\xi = \theta - \theta_0$ leads to the matrix form,

$$\dot{\boldsymbol{x}} = \boldsymbol{A}(\boldsymbol{x})\boldsymbol{x} + \boldsymbol{B}v = \begin{bmatrix} 0 & 1 \\ \frac{1}{B_\theta}\frac{\partial f_\mathrm{t}}{\partial \theta}|_{f_0} & 0 \end{bmatrix} \boldsymbol{x} + \begin{bmatrix} 0 \\ \frac{1}{B_\theta} \end{bmatrix} v \ , \tag{14.9}$$

where $\boldsymbol{x} = [\xi, \dot{\xi}]$. It is also possible to linearize w. r. t. to the tendon forces.

14.2.2 Flexible joint model

A generic flexible joint model is depicted in Fig. 14.2. As mentioned previously, there exists an infinite number of factorizations but the method used to establish the dynamic equations naturally leads to a factorization by the stiffness of the tendons.

$$\boldsymbol{A}(\boldsymbol{x}) = \begin{bmatrix} 0 & 1 & 0 & 0 \\ -\frac{k(x_1-x_3)}{m} & -\frac{d_q}{m} & \frac{k(x_1-x_3)}{m} & 0 \\ 0 & 0 & 0 & 1 \\ \frac{k(x_1-x_3)}{b} & 0 & -\frac{k(x_1-x_3)}{b} & -\frac{d_\theta}{b} \end{bmatrix}, \tag{14.10}$$

where $n \in \mathbb{N}$ is the state dimension, $\boldsymbol{x} \in \mathbb{R}^n$ is the state vector defined as $\boldsymbol{x} = [q, \dot{q}, \theta, \dot{\theta}]$. The control input is denoted $u \in \mathbb{R}$. The joint stiffness is represented by $k(x_1 - x_3) \in \mathbb{R}$. The viscous frictional torque of the joint (resp. motor) are denoted d_q (resp. d_θ). Finally, the inertias of the link and the motor are $m \in \mathbb{R}$ and $b \in \mathbb{R}$. One pointwise linear form is given by

$$\dot{\boldsymbol{x}} = \boldsymbol{A}(\boldsymbol{x})\boldsymbol{x} + \boldsymbol{B}u \ , \tag{14.11}$$

with

$$\boldsymbol{A}(\boldsymbol{x}) = \begin{bmatrix} 0 & 1 & 0 & 0 \\ -\frac{k(x_1-x_3)}{m} & -\frac{d_\mathrm{q}}{m} & \frac{k(x_1-x_3)}{m} & 0 \\ 0 & 0 & 0 & 1 \\ \frac{k(x_1-x_3)}{b} & 0 & -\frac{k(x_1-x_3)}{b} & -\frac{d_\theta}{b} \end{bmatrix}$$

and

$$\boldsymbol{B}(\boldsymbol{x}) = \begin{bmatrix} 0 \\ 0 \\ 0 \\ \frac{1}{b} \end{bmatrix} \ .$$

The control input is a state feedback defined by

$$u = -\boldsymbol{K}^T\boldsymbol{x} \ , \tag{14.12}$$

where the gain vector $\boldsymbol{K} \in \mathbb{R}^m$ is given by the SDRE method, ie. $\boldsymbol{K} = \boldsymbol{R}^{-1}\boldsymbol{B}^T\boldsymbol{P}$. The matrix $\boldsymbol{P} \in \mathbb{R}^{4\times4}$ being the solution of the Riccati equation (14.5).

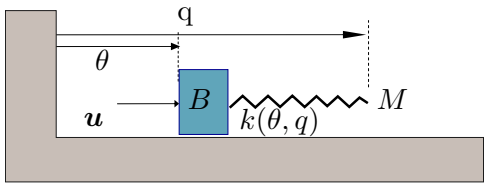

Figure 14.2: Mass spring damper system in the case of a flexible joint model

14.3 Simulation and experiments

The two cases derived above are verified by simulations. First, the tendon force controller (as depicted in Fig. 16.1) is evaluated. The flexible joint model (cf. Fig. 14.2) is verified in a second step.

14.3.1 Application to a tendon force controller

The simulations are performed using the numerical solver ode23t from MATLAB®, with the parameters of Table 14.1.

Table 14.1: Simulation parameters for the tendon controller

Symbol	Value	Units
B_θ	$2e-3$	$kg.m^2$
Q	$\begin{bmatrix} 1 & 0 \\ 0 & 0.0001 \end{bmatrix}$	
R	0.000001	

The simulation results are depicted in Fig. 14.3. First an initial desired force step from 0 N to 40 N is commanded. Then, a smaller adjustment is made to reach 45 N. The differences between the two controllers are hardly visible. The main reason is that the plant equations are not changing as much as one might expect. The change in stiffness of the real mechanism during the experiment only results in a minimal change of the optimal gains.

14.3.2 Application to a joint controller

The parameters of Table 14.2 are used for the joint simulation. The resulting

Table 14.2: Simulation parameters for the joint controller

Symbol	Value	Units
B_θ	$2e-3$	$kg.m^2$
M	$7.2e-7$	$kg.m^2$
Q	$\begin{bmatrix} 10 & 0 & 0 & 0 \\ 0 & 0.01 & 0 & 0 \\ 0 & 0 & 0.1 & 0 \\ 0 & 0 & 0 & 0.01 \end{bmatrix}$	$N.A$
R	0.0001	$N.A$

link trajectories are reported in Fig. 14.4. The improvement is not noticeable in the case of a free motion. Indeed, the low link inertia does not create a significant dynamic load, thus the stiffness change is extremely small.

However, when a load is applied externally, the stiffness change is visible, as depicted in Fig. 14.5. In such a case, the SDRE method is able to modify the gains to account for the modified plant equations.

14.4 Discussion

This chapter has presented an extension of the optimal linear control method of the previous chapter. The method, called the SDRE method, has been appreciated in the optimal control research groups because of its good practical results. The first section described the general idea of the method on an abstract example. Since the method is based on the pointwise linear form of a system, the second section transformed the system dynamics into the proper form. The third section applied the method to two different systems and proposed several simulations. It was shown that for the tendon control problem, the method only marginally contributes to improve the behavior mainly because the optimal gains do not change significantly. On the contrary, the improvements were visible in the case of a flexible joint. Nonetheless, the gain designed for the nominal load were also satisfying, especially in case of free motion. Nonetheless, the method is relatively easy to use and the optimal control community is very active in developing the supporting theory. From the implementation point of view it is very similar to the gain scheduling method. Some first analysis and simulations[1] are showing that the ARE gains can be computed at a lower rate than the control loop without significant effect on the resulting behavior. Practically, a rate of about 200Hz is sufficient. The method is theoretically limited to a local analysis. Thus, the following chapters are focusing on using global, nonlinear controller designs. The ARE and SDRE method are reused in the last chapters as a mean to select the best, optimal in a sense, gains for the backstepping controller.

[1] not reported in this thesis

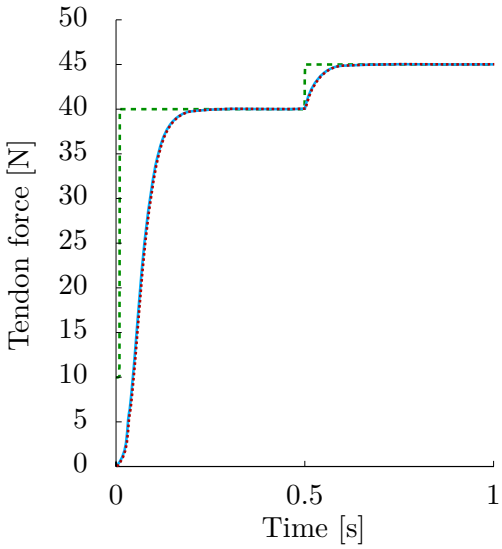

Figure 14.3: Simulation: Comparison between the SDRE controller and the fixed gains controller for a tendon force control problem. The green/dashed line is the desired tendon force. The light blue/solid and red/dotted lines represent the tendon forces.

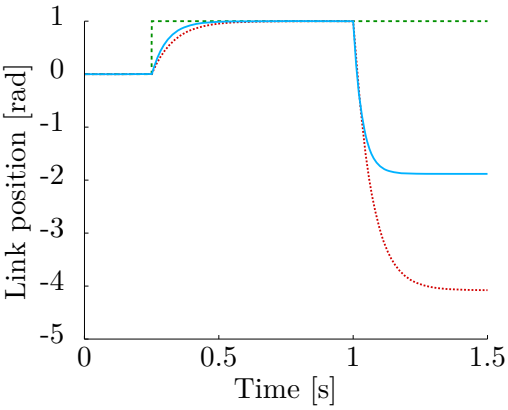

Figure 14.4: Simulation: Comparison between the SDRE controller and the fixed gains controller for a link positioning task. The green/dashed line is the desired link position. The light blue/solid and red/dotted lines depict the link position with the SDRE controller and the fixed gains controller.

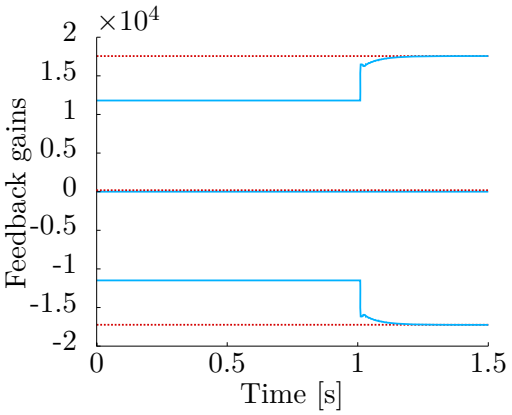

Figure 14.5: Simulation: Comparison between the SDRE controller and the fixed gains controller for a link positioning task. The light blue/solid lines depict the gains with the SDRE controller. The gains of the fixed gains controller are represented in red/dotted lines.

15 Backstepping

The backstepping design procedure is a design method for nonlinear controllers by Kokotovic in the 90's. It is a recursive method for strict feedback system. In each step, the derivative of the previous error is compensated and well known stabilizing reference is applied to the system. Then, the error introduced is propagated to the next level and the method is applied again. The backstepping procedure has been described in [68, 85, 134] and applied to a large variety of problems. Only little work deals with the practical implementation of the backstepping method and most of the papers are only presenting simulation results. Its main limitations are the need for high order derivatives and the fast growth of the expression, known as the *complexity due explosion of terms* which is a direct consequence of the recursivity of the method. Althought the procedure only requires positive definiteness of the gain matrices, it should also be noted that they do not always have an intuitive interpretation and the manual tuning of the numerous gains can be tedious for complex systems.

Nonetheless, it is a purely nonlinear method that does not require the previous assumptions on the system (eg. cascaded system). Moreover, the designed controller is stable by design as long as the gain matrices are positive definite. This allows a great freedom in the choice of the gains. The main contribution of this chapter is to provide experimental validation of the controllers, derive the backstepping equation in the case of a nonlinear flexible joint and extend the single motor controller to an antagonistic controller.

In the first section, an example of the backstepping method, inspired by [84, p.489] is proposed. The reader familiar with the backstepping method can safely skip the section. The second section applies the backstepping control method to two cases that have a structure similar to the one of the real system. More precisely, a backstepping controller in the case of a constant stiffness (resp. variable stiffness) single flexible joint is derived. Simulations are performed to evaluate the results. The controllers are state controllers and are not suitable for interaction with the grasped object. A *soft* controller is needed to perform stable grasps in the presence of inaccuracies. Therefore, in the third section, the control law for an impedance controller is derived. Because of its importance, simulations and experimental results are presented on a single joint actuated by one motor with a linear spring. It is verified numerically and experimentally that the controller is behaving like an impedance controller. The fourth section extends the single joint controller to the nonlinear case. Unsurprisingly, one of the main condition for the existence of the control law is to have a strictly convex force/displacement characteristic of the spring. The fifth section extends the single joint/single motor controller to an antagonistic joint actuation.

Finally, the backstepping method is applied to the equations of the real system. Simulation and experimental results are reported.

15.1 Concept

This section presents the concept of the integrator backstepping method. In the first section the equation of control are derived on a simple example. In a second part, some simulation results are reported to help the reader to understand the behavior of the controller. It is a very basic introduction to the backstepping concept and can safely be skipped.

15.1.1 Controller design

Consider the dynamic system described by Eq. (15.1), where $(x_1, x_2) \in \mathbb{R}^2$ are the state variables and $u \in \mathbb{R}$ is the control input. It is assumed that all quantities are directly measurable and that all functions are sufficiently smooth.

$$\begin{cases} \dot{x}_1 &= -{x_1}^3 + {x_1}^2 + x_2 \\ \dot{x}_2 &= u \end{cases} \tag{15.1}$$

If $\bar{x}_2 = x_2$ is considered as a virtual input for the (15.1), an exponentially stabilizing control input is

$$\bar{x}_2 = -{x_1}^2 - k_1 x_1 \ , \tag{15.2}$$

where $k_1 \in \mathbb{R}^+$ is a gain used to accelerate the convergence and $\bar{x}_2$ is the reference input. It is proved using the Lyapunov function $V_1(x_1) = \frac{1}{2}x_1^2$. Taking the time derivative of V_1 along the solutions of the first equation of (15.1) one obtains

$$\dot{V}_1(x_1) \ = \ x_1(-{x_1}^3 - k_1 x_1) = -{x_1}^4 - k_1 x_1^2 \ . \tag{15.3}$$

However, it is not possible to track exactly the reference input $\bar{x}_2$. Defining $z_2 = x_2 - \bar{x}_2$, the system (15.1), is transformed in

$$\dot{x}_1 \ = \ -{x_1}^3 - k_1 x_1 - x_1 \tag{15.4}$$

$$\dot{z}_2 \ = \ u - \dot{\bar{x}}_2 \tag{15.5}$$

The second equation is stabilized by $u = \dot{\bar{x}}_2 - k_2 z_2$, where $k_2 \in \mathbb{R}^+$ is a feedback gain used to accelerate the convergence of the system. The global asymptotic stability is demonstrated using the Lyapunov function $V_2(x_1, z_1) = \frac{1}{2}x_1^2 + \frac{1}{2}z_2^2$ along the trajectories. From Equation (15.6), simply replacing the expressions gives

$$\dot{V}_2(x_1, z_2) = x_1\dot{x}_1 + z_2\dot{z}_2 \ , \tag{15.6}$$

simplifying and grouping the terms leads to

$$\dot{V}_2(z_1, z_2) = x_1(-{x_1}^3 - k_1 x_1 - x_1) + z_2(u - \dot{\bar{x}}_2) \ , \tag{15.7}$$

and

$$\dot{V}_2(x_1, z_2) = (-{x_1}^4 - k_1 {x_1}^2 - {x_1}^2) + z_2(-k_2 z_2) \ . \tag{15.8}$$

Finally, one obtains

$$\dot{V}_2(x_1, z_2) = -{x_1}^4 - k_1 {x_1}^2 - {x_1}^2 - k_2 {z_2}^2 \ . \tag{15.9}$$

The final expression of u is obtained by going back to the original coordinates and is reported in (15.10).

$$u = \dot{\bar{x}}_2 - k_2 z_2 = (-2x_1\dot{x_1} - k_1\dot{x_1}) - k_2(x_2 + {x_1}^2 + k_1 x_1) \ , \tag{15.10}$$

where $(k_1, k_2) \in (\mathbb{R}^+ \times \mathbb{R}^+)$ are two feedback gains used to accelerate the convergence of the system.

It should be noted that the presence of the derivative of the reference control signal is the main caracteristic of the backstepping methodology. In each step of the method, the derivative of the reference control is derived once more. This leads to the phenomenon refered to as the *complexity due to the explosion of terms*. Consequently, the backstepping method, although very sound mathematically, can be delicate to apply to high order systems (unless the derivatives of all quantities are available). An interesting property of the backstepping method is that it is not necessary to cancel the *good* nonlinearities (such as $-x_1^2$ in the example). It allows to reduce the control effort w. r. t. the feedback linearization method that systematically cancels the nonlinearities.

15.1.2 Simulations

To analyze the behavior of the controller derived in the previous section several simulations are performed. The system defined by (15.1) together with the control law of (15.10) is simulated using MATLAB®. The feedback gains (k_1, k_2) are modified and the resulting trajectories are reported. In Figure 15.1 the feedback gains are modified and the resulting trajectory for $x_1(t), t \in [1 \dots 10]$ are plotted. As expected, the trajectory are converging to the origin for any combination of $(k_1, k_2) \in (\mathbb{R}^+)^2$. The higher the gains are, the faster the system is converging. Figure 15.2, 15.3 and 15.4 report the phase diagram of x_1 for three different gain combinations and varying initial conditions. All combinations are converging toward the origin, thus confirming that the controller is effective. The convergence trajectory is changing according to the choice of the feedback gains. However, increasing the gains of the outmost layer does not ensure that the convergence will be

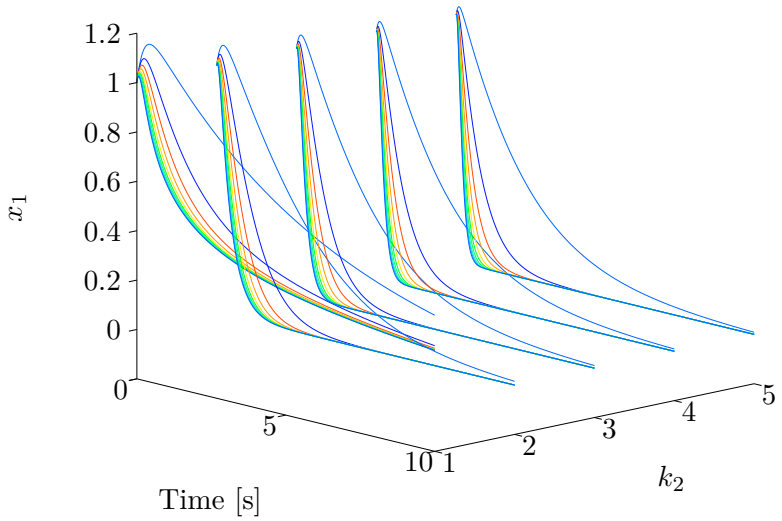

Figure 15.1: Simulation results: x_1 trajectories obtained for different values of k_1 and k_2. Slice are for $k_1 \in [0.01, 2.0, 5.0, 7.5, 10.0]$. Colors are for $k_2 \in [0.5, 1.55, 2.61, 3.67, 4.72, 5.78, 6.83, 7.89, 8.94, 10.0]$. Initial conditions are $x_1 = 1, x_2 = 1$.

faster. Indeed, if x_2 is not regulated to the desired value, no value of x_1 can improve the convergence rate. Moreover, the measurement noise of the low layers $x_2, x_3, \ldots$ is likely to be increasingly large, thought limiting the gains in the real implementation.

15.1.3 Conclusion

This section explained how the backstepping method works on a two degrees of freedom example. The stability of the close loop system was numerically demonstrated through a combination of numerical simulations (different initial conditions and different gains).

15.2 Single flexible joint: position controller

In this section, the backstepping methodology is applied to a single joint driven by one motor with a linear spring (i. e. the spring elongation has no influence on its stiffness). The spring stiffness is given by $K = \frac{\partial f(x)}{\partial x}$, where $f \in \mathbb{R}$ and $x \in \mathbb{R}$ are the spring force and the spring elongation (w. r. t. its default length). For a linear spring, the stiffness is constant i. e. $\frac{\partial K}{\partial x} = 0$.

15.2.1 Model

The mechanical model of the flexible joint is depicted in Figure 15.5 and the corresponding differential equations are reported in (15.11) and (15.12).

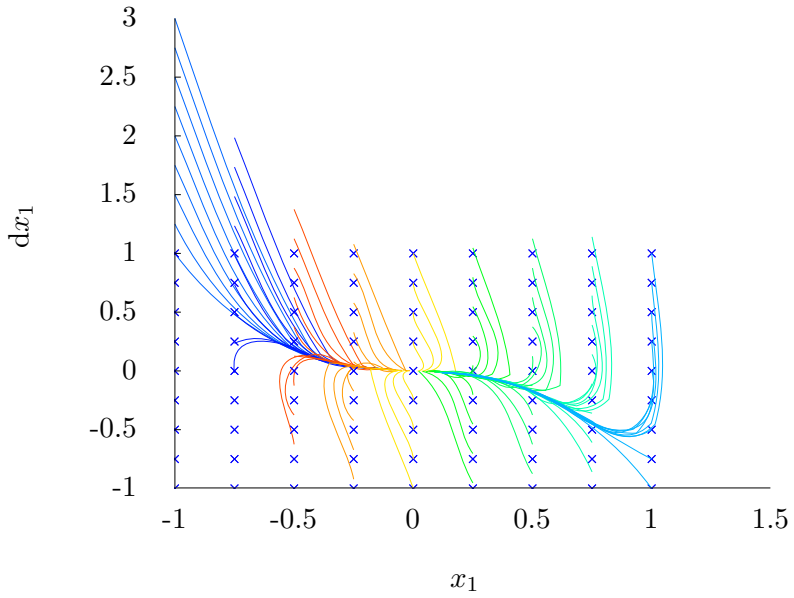

Figure 15.2: Simulation results: solution trajectories for different initial conditions represented in a phase diagram of $\dot{x}_1(x_1)$. Feedback gains are $k_1 = 0.1, k_2 = 5$. Initial conditions are marked by a cross symbol.

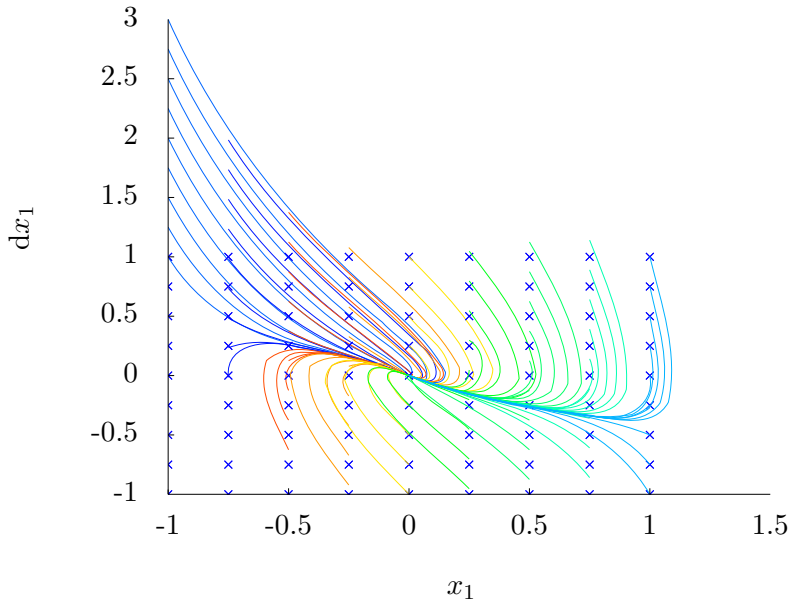

Figure 15.3: Simulation results: solution trajectories for different initial conditions represented in a phase diagram of $\dot{x}_1(x_1)$. Feedback gains are $k_1 = 1, k_2 = 1$. Initial conditions are marked by a cross symbol.

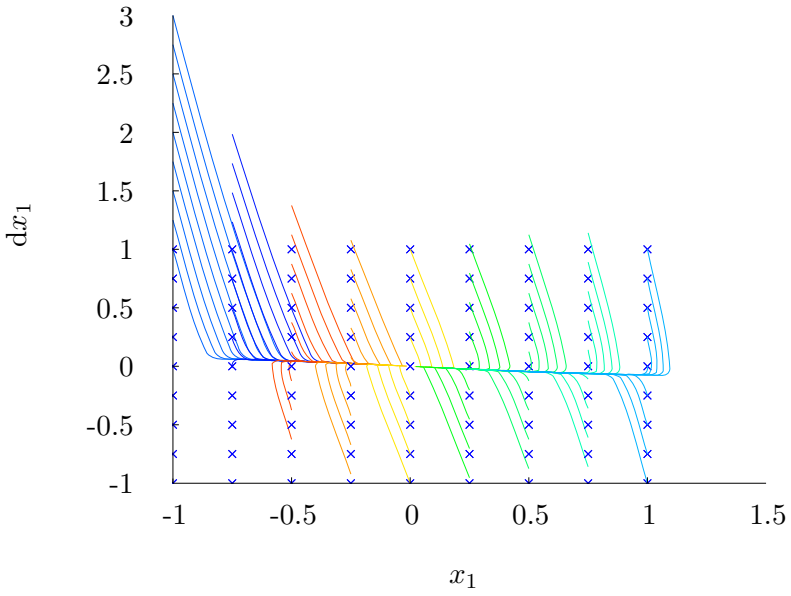

Figure 15.4: Simulation results: solution trajectories for different initial conditions represented in a phase diagram of $\dot{x}_1(x_1)$. Feedback gains are $k_1 = 5, k_2 = 0.1$. Initial conditions are marked by a cross symbol.

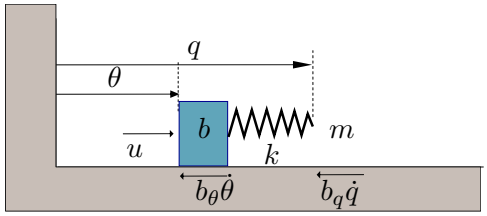

Figure 15.5: Double spring mass damper system in the case of a flexible joint model.

$$m\ddot{q} + b_q\dot{q} = -f(\theta, q) \tag{15.11}$$

$$b\ddot{\theta} + b_\theta\dot{\theta} = f(\theta, q) + u \tag{15.12}$$

$\theta \in \mathbb{R}, q \in \mathbb{R}$ are the motor position and link position. The link mass and the motor mass are denoted $m(q) \in \mathbb{R}, b \in \mathbb{R}$. The force generated by the elastic element is represented by $f(\theta, q) \in \mathbb{R}$. The input vector, that is, the motor force, is denoted $u \in \mathbb{R}$. Finally, b_q (resp. b_θ) is the friction force vector associated to the link (resp. motor). Neglecting the frictional terms to simplify the expression, the system described by (15.11) and (15.12) is written in a vector form as

$$\dot{\boldsymbol{x}} = \boldsymbol{f}(\boldsymbol{x}) + \boldsymbol{g}(u) \ , \tag{15.13}$$

where the state vector $\boldsymbol{x} \in \mathbb{R}^4$ is defined as

$$\boldsymbol{x} = \begin{bmatrix} q \\ \dot{q} \\ \theta \\ \dot{\theta} \end{bmatrix} \quad . \tag{15.14}$$

The vector-valued functions $\boldsymbol{f} : \mathbb{R}^4 \mapsto \mathbb{R}^4$ and $\boldsymbol{g} : \mathbb{R} \mapsto \mathbb{R}^4$ are

$$\boldsymbol{f} = \begin{bmatrix} x_2 \\ -\dfrac{f(x_1 - x_3)}{m} \\ x_4 \\ \dfrac{f(x_1 - x_3)}{m} \end{bmatrix} \quad \text{and} \quad \boldsymbol{B} = \begin{bmatrix} 0 \\ 0 \\ 0 \\ \dfrac{1}{b} \end{bmatrix} \quad . \tag{15.15}$$

15.2.2 Strict Feedback Form

In order to apply the integrator backstepping methodology it is required to transform the system into a strict feedback form. That is, the i^{th} differential equation (corresponding to the i^{th} state variable) is only allowed to depend on the variables up to $i-1$. Indeed, one variable must disappear after each backstepping step otherwise the method would not converge to an expression for u. Graphically, the arguments of state function $\boldsymbol{f}$ must be located in a triangle with a line above the diagonal, as depicted in Fig. 15.6. Similarily, the arguments of the input function $\boldsymbol{g}$ should be non zero on the last line.

$$\begin{matrix} \neq 0 & 0 & 0 \\ & \neq 0 & 0 \\ & & \neq 0 \\ & & \end{matrix} \quad + \quad \begin{matrix} \\ \\ \\ \neq 0 \end{matrix} \quad u$$

Figure 15.6: Graphical representation of the state transition matrix of a system in strict feedback form.

This section constructs a new coordinate system in which the equations are in strict feedback form. In the case of a constant stiffness spring the spring torque is simply

$$\tau(\theta, q) = k(\theta - q), \tag{15.16}$$

where $K \in \mathbb{R}^{*+}$ is the spring stiffness. Therefore, it is possible to remove one variable (q or θ). Using θ from (15.12) and replacing it in (15.11) yields a fourth order differential equation on q

$$\frac{bm}{k} q^{(4)}(t) + (b+m) q^{(2)}(t) = u(t) \ , \tag{15.17}$$

where all quantities are defined as previously done. The system can even be written in the linear form $\dot{\boldsymbol{X}} = \boldsymbol{A}(\boldsymbol{X})\boldsymbol{X} + \boldsymbol{B}u$ where the state vector $\boldsymbol{X} \in \mathbb{R}^4$ is defined as

$$\boldsymbol{X} = \begin{bmatrix} q \\ \dot{q} \\ \ddot{q} \\ q^{(3)} \end{bmatrix}. \tag{15.18}$$

The state transition matrix $\boldsymbol{A} \in \mathbb{R}^{4\times 4}$ and the input vector are

$$\boldsymbol{A} = \begin{bmatrix} 0 & 1 & 0 & 0 \\ 0 & 0 & 1 & 0 \\ 0 & 0 & 0 & 1 \\ 0 & 0 & -\dfrac{(b+m)k}{bm} & 0 \end{bmatrix} \quad \text{and} \quad \boldsymbol{B} = \begin{bmatrix} 0 \\ 0 \\ 0 \\ \dfrac{k}{bm} \end{bmatrix}. \tag{15.19}$$

The system is written in a strict feedback form and is ready for the application of the backstepping method.

15.2.3 Controller design

According to (15.19), defining the state vector $\boldsymbol{x} \in \mathbb{R}^4$ as $[x_1, x_2, x_3, x_4] = [q, \dot{q}, \ddot{q}, \dddot{q}]$ allows to write the system in the strict feedback form

$$\begin{cases} \dot{x}_1 &= & f_1(x_1) + g_1(x_1)x_2 \\ \dot{x}_2 &= & f_2(x_1, x_2) + g_2(x_1, x_2)x_3 \\ \dot{x}_3 &= & f_3(x_1, x_2, x_3) + g_3(x_1, x_2, x_3)x_4 \\ \dot{x}_4 &= & f_4(x_1, x_2, x_3, x_4) + g_4(x_1, x_2, x_3, x_4)u \end{cases}, \tag{15.20}$$

with

$$\begin{cases} f_1(x_1) &= & 0 \\ g_1(x_1) &= & 1 \\ f_2(x_1, x_2) &= & 0 \\ g_2(x_1, x_2) &= & 1 \\ f_3(x_1, x_2, x_3) &= & 0 \\ g_3(x_1, x_2, x_3) &= & 1 \\ f_4(x_1, x_2, x_3, x_4) &= & -\dfrac{k(b+m)}{bm}x_3 \\ g_4(x_1, x_2, x_3, x_4) &= & \dfrac{k}{bm} \end{cases}. \tag{15.21}$$

Remark : The choice of f_4 and g_4 could be changed to $f_4 = 0$ and $g_4 = 1$ by feedback linearization in a strict integrator form by $u = \dfrac{bm}{k}(\dfrac{k(b+m)}{bm}\ddot{q} + v)$. The new system could be $\dot{\boldsymbol{X}}\boldsymbol{A}_v\boldsymbol{X} + \boldsymbol{B}_v v$, with the state transition matrix

$\boldsymbol{A_v} \in \mathbb{R}^{4\times4}$ and the input vector defined as

$$\boldsymbol{A_v} = \begin{bmatrix} 0 & 1 & 0 & 0 \\ 0 & 0 & 1 & 0 \\ 0 & 0 & 0 & 1 \\ 0 & 0 & 0 & 0 \end{bmatrix} \quad \text{and} \quad \boldsymbol{B_v} = \begin{bmatrix} 0 \\ 0 \\ 0 \\ 1 \end{bmatrix} . \tag{15.22}$$

However, the backstepping procedure naturally includes the feedback cancellation of f_4 and the scaling g_4 so it is not needed to perform the feedback linearization before designing the controller. The system is of order four and consequently four steps are needed to complete the integrator backstepping procedure. The following sections report the steps along with the stability proofs which helps understanding the procedure.

First equation The arguments of the functions are removed for clarity. According to the state matrix defined (15.19), the system is given by

$$\dot{x}_1 = x_2 \tag{15.23}$$
$$\dot{x}_2 = x_3 \tag{15.24}$$
$$\dot{x}_3 = x_4 \tag{15.25}$$
$$\dot{x}_4 = f_4 + g_4 u \tag{15.26}$$

Considering only (15.23) and taking $\bar{x}_2 = x_2$ as a virtual input, the scalar system is stabilized by

$$\bar{x}_2 = -k_1 x_1, \tag{15.27}$$

where $k_1 \in \mathbb{R}^{*+}$. The stability is proved using the Lyapunov function $V(x_1) = \frac{1}{2}x_1^2$. The time derivative of V_1 along the solution is,

$$\dot{V}(x_1) = x_1\dot{x}_1 = -k_1 x_1^2 \tag{15.28}$$

which, after invoking the LaSalle theorem, concludes the proof.

Second equation The ideal control input of the first equation cannot be exactly tracked because the system has internal dynamics (the input goes through several integrators). Therefore, a tracking error z_2 is defined as $z_2 = x_2 - \bar{x}_2$ and propagated in the system. Eliminating x_2 in the original system leads to

$$\begin{cases} \dot{x}_1 = (\bar{x}_2 + z_2) \\ \dot{z}_2 = x_3 - \dot{\bar{x}}_2 \\ \dot{x}_3 = x_4 \\ \dot{x}_4 = f_4 + g_4 u \end{cases} . \tag{15.29}$$

Replacing $\bar{x}_2$ and $\dot{\bar{x}}_2$ by their expressions gives

$$\begin{cases} \dot{x}_1 = -k_1 x_1 + z_2 \\ \dot{z}_2 = x_3 - \dot{\bar{x}}_2 \\ \dot{x}_3 = x_4 \\ \dot{x}_4 = f_4 + g_4 u \end{cases} . \tag{15.30}$$

Considering only the two first equations of Eq. (15.30) and taking $\bar{x}_3 = x_3$ as a virtual input, it can be stabilized by,

$$\bar{x}_3 = -x_1 + \dot{\bar{x}}_2 - k_2 z_2 \ , \tag{15.31}$$

where $k_2 \in \mathbb{R}^{*+}$. The stability is proved using the Lyapunov function $V(x_1, z_2) = \frac{1}{2}(x_1^2 + z_2^2)$. The time derivative of V_1 along the solution is,

$$\dot{V}(x_1, z_2) = x_1\dot{x}_1 + z_2\dot{z}_2 = x_1(-k_1 x_1 + z_2) + z_2(x_3 - \dot{\bar{x}}_2) \ . \tag{15.32}$$

After simplification, it results in

$$\dot{V}(x_1, z_2) = -k_1 x_1^2 + z_2(x_1 + x_3 - \dot{\bar{x}}_2) \ . \tag{15.33}$$

Replacing the expression of x_3 gives

$$\dot{V}(x_1, z_2) = -k_1 x_1^2 - k_2 z_2^2 \ , \tag{15.34}$$

which concludes the proof.

Third equation Similarly to the the second step, the control input of the second equation cannot be exactly tracked and therefore z_3 is defined as $z_3 = x_3 - \bar{x}_3$. The system is

$$\begin{cases} \dot{x}_1 &= & -k_1 x_1 + z_2 \\ \dot{z}_2 &= & -k_2 z_2 + z_3 - x_1 \\ \dot{x}_3 &= & x_4 \\ \dot{x}_4 &= & f_4 + g_4 u \end{cases} . \tag{15.35}$$

Eliminating x_3 leads to

$$\begin{cases} \dot{x}_1 &= & -k_1 x_1 + z_2 \\ \dot{z}_2 &= & -k_2 z_2 + z_3 - x_1 \\ \dot{z}_3 &= & x_4 - \dot{\bar{x}}_3 \\ \dot{x}_4 &= & f_4 + g_4 u \end{cases} . \tag{15.36}$$

Using x_4 as a virtual input, the system is be stabilized by

$$\bar{x}_4 = -z_2 + \dot{\bar{x}}_3 - k_3 z_3 \ , \tag{15.37}$$

where $k_3 \in \mathbb{R}^{*+}$. The stability is proved using the Lyapunov function $V(x_1, z_2, z_3) = \frac{1}{2}(x_1^2 + z_2^2 + z_3^2)$. The time derivative of V_1 along the solution is,

$$\begin{array}{rcl} \dot{V}(x_1, z_2, z_3) &= & x_1\dot{x}_1 + z_2\dot{z}_2 + z_3\dot{z}_3 \\ &= & x_1(-k_1 x_1 + z_2) + z_2(-k_2 z_2 + z_3 - x_1) + z_3(x_4 - \dot{\bar{x}}_3) \end{array} . \tag{15.38}$$

After simplification

$$\dot{V}(x_1, z_2, z_3) = -k_1 x_1^2 - k_2 z_2^2 + z_3(x_4 + z_2 - \dot{\bar{x}}_3) \ . \tag{15.39}$$

Replacing the expression of x_4 gives

$$\dot{V}(x_1, z_2, z_3) = -k_1 x_1^2 - k_2 z_2^2 - k_3 z_3^2 \ , \tag{15.40}$$

which concludes the proof.

Fourth equation The control input of the third equation cannot be exactly tracked and therefore z_4 is defined as $z_4 = x_4 - \bar{x}_4$ The system is now

$$\begin{cases} \dot{x}_1 &= -k_1 x_1 + z_2 \\ \dot{z}_2 &= -k_2 z_2 + z_3 - x_1 \\ \dot{z}_3 &= -k_3 z_3 + z_4 - z_2 \\ \dot{x}_4 &= f_4 + g_4 u \end{cases} . \tag{15.41}$$

Eliminating x_4 leads to

$$\begin{cases} \dot{x}_1 &= -k_1 x_1 + z_2 \\ \dot{z}_2 &= -k_2 z_2 + z_3 - x_1 \\ \dot{z}_3 &= -k_3 z_3 + z_4 - z_2 \\ \dot{z}_4 &= f_4 + g_4 u - \dot{\bar{x}}_4 \end{cases} . \tag{15.42}$$

The **real**, as opposed to virtual, control input u is selected as

$$u = \frac{1}{g_4}(-f_4 - z_3 + \dot{\bar{x}}_4 - k_4 z_4) , \tag{15.43}$$

where $k_4 \in \mathbb{R}^{*+}$. The stability is proved using the Lyapunov function $V_4(x_1, z_2, z_3, z_4) = \frac{1}{2}(x_1^2 + z_2^2 + z_3^2 + z_4^2)$. The time derivative of V_4 along the solution is,

$$\begin{aligned} \dot{V}_4(x_1, z_2, z_3, z_4) &= x_1\dot{x}_1 + z_2\dot{z}_2 + z_3\dot{z}_3 + z_4\dot{z}_4 \\ &= x_1(-k_1 x_1 + z_2) + z_2(-k_2 z_2 + z_3 - x_1) \\ &+ z_3(-k_3 z_3 + z_4 - z_2) + z_4(x_4 - \dot{\bar{x}}_4). \end{aligned} . \tag{15.44}$$

After simplification

$$\dot{V}_4(x_1, z_2, z_3, z_4) = -k_1 x_1^2 - k_2 z_2^2 - k_3 z_3^2 + z_4(z_3 + f_4 + g_4 u - \dot{\bar{x}}_4) . \tag{15.45}$$

Replacing the expression of u gives

$$\dot{V}_4(x_1, z_2, z_3, z_4) = -k_1 x_1^2 - k_2 z_2^2 - k_3 z_3^2 - k_4 z_4^2 , \tag{15.46}$$

which concludes the proof.

Input equation The input signal is obtained by recursively replacing the expression in terms of x_1, x_2, x_3 and x_4.

$$g_4 u = (-f_4 - z_3 + \dot{\bar{x}}_4 - k_4 z_4) \tag{15.47}$$

Starting with z_4, the input expression is

$$g_4 u = -f_4 - z_3 + \dot{\bar{x}}_4 - k_4(x_4 - \bar{x}_4) . \tag{15.48}$$

Then the $\bar{x}_4$ virtual input is expanded.

$$
\begin{aligned}
g_4 u &= -f_4 - z_3 + \frac{d}{dt}(-z_2 + \dot{\bar{x}}_3 - k_3 z_3) - k_4(x_4 - (-z_2 + \dot{\bar{x}}_3 - k_3 z_3))) \\
&= -f_4 - z_3 + \frac{d}{dt}(-z_2 + \dot{\bar{x}}_3 - k_3 z_3) - k_4 x_4 + k_4(-z_2 + \dot{\bar{x}}_3 - k_3 z_3)) \\
&= -f_4 - z_3 - k_4 x_4 + \frac{d}{dt}(-z_2 + \dot{\bar{x}}_3 - k_3 z_3) + k_4(-z_2 + \dot{\bar{x}}_3 - k_3 z_3)
\end{aligned}
\tag{15.49}
$$

The procedure is continued by removing $z_3 = x_3 - \bar{x}_3$ and results in the input expression

$$
\begin{aligned}
g_4 u &= -f_4 - (x_3 - \bar{x}_3) - k_4 x_4 + \frac{d}{dt}(-z_2 + \dot{\bar{x}}_3 - k_3(x_3 - \bar{x}_3)) + k_4(-z_2 + \dot{\bar{x}}_3 - k_3(x_3 - \bar{x}_3)) \\
&= -f_4 - x_3 + \bar{x}_3 - k_4 x_4 + \frac{d}{dt}(-z_2 + \dot{\bar{x}}_3 - k_3 x_3 + k_3 \bar{x}_3) + k_4(-z_2 + \dot{\bar{x}}_3 - k_3 x_3 + k_3 \bar{x}_3) \\
&= -f_4 - x_3 - k_4 x_4 - k_3 x_4 - k_4 k_3 x_3 + \bar{x}_3 + \frac{d}{dt}(-z_2 + \dot{\bar{x}}_3 + k_3 \bar{x}_3) + k_4(-z_2 + \dot{\bar{x}}_3 + k_3 \bar{x}_3)
\end{aligned}
\tag{15.50}
$$

15.2.4 Simulations

Although the theory guarantees that the control law results in an asymptotically stable system, the analysis does not include errors such as noise, unmodeled dynamics, unmodeled nonlinearities, saturations, or delays. This section presents several numerical simulations that evaluate the backstepping controller under the presence of such errors. The controller will eventually be implemented on a real-time system where sampling, communication and computation delays are unavoidably introduced. Similarly, the maximal motor torque is limited by nature and creates a saturation of the command. The feedback gains are influencing the convergence rate and the simulations can be used to get an order of magnitude of some practical values. The following simulations are performed in order to qualitatively evaluate the different effects.

- several controller gains K_1 and K_2.
- several saturation values for the motor input.
- several time delays in the control loop.

It is important to keep in mind that the simulations must be carefully designed to avoid issues related to the numerical inaccuracies or numerical solvers. For example, using a variable step solver with a continuous derivative block and a continuous integration block creates a convergence issue. Solutions for this issue are:

- use a fixed step solver.

symbol	description	value	units
$gearratio$	gear ratio	100	N.A
m	link side inertia	7.2×10^{-7}	$[kgm^2]$
b	motor inertia	2×10^{-4}	$[kgm^2]$
b_θ	motor damping	10^{-2}	$[Nm/(rad/s)]$
b_q	link damping	10^{-3}	$[Nm/(rad/s)]$
K	joint stiffness	20	$[Nm/rad]$
K_3	controller gain 3	100	N.A
K_4	controller gain 4	100	N.A

Table 15.1: Simulation parameters for a single joint and single motor with linear stiffness

- use a discrete integration or derivative.
- compute symbolically the derivatives (preferred solution).

It is a good practice to slightly modify the sampling time or the error tolerance and check that the results of the simulation are not changed significantly. It is advisable to verifiy the results in the case where the results are very sensitive to the solver parameters. Either by performing some experiments or running some reference simulation. Table 15.1 reports the important simulation parameters and their values. The simulations are performed using a variable step solver and use symbollic derivatives (*ode23t* of Matlab).

In the Figures 15.7 and 15.8, the influence of the two first feedback gains is investigated. In Fig. 15.7, the first gain is increased and consequently, the stiffness of the link is increased. Oscillations are appearing if the value is increased too much. Fig. 15.8 shows that the second feedback gain behaves mainly as a damping coefficient. Increasing the value of K_2 slows down the response of the link.

An electrical motor has a limited torque capability. This limitation is either due to the maximum torque the structure can support or the maximum current that can flow through the coils. In practice, to avoid any damages, the motor maximum desired torque is limited by firmware or software. In the case of the motors of the hand arm system, a first limitation is implemented in the system driver and a hard limit is implemented in the motor controller FPGA. The saturation introduces a nonlinearity that can destabilize the system. Although some theories (such as the sliding mode control [135]) are able to explicitly deal with saturation effects, this remains an open field of research. In this work, the influence of the saturation is evaluated by simulation. The diagram corresponding to the simulation is reported in Fig. 15.9. In a first step the simulation is performed without saturation (cf. Fig. 15.11 red/solid). A second simulation with the same

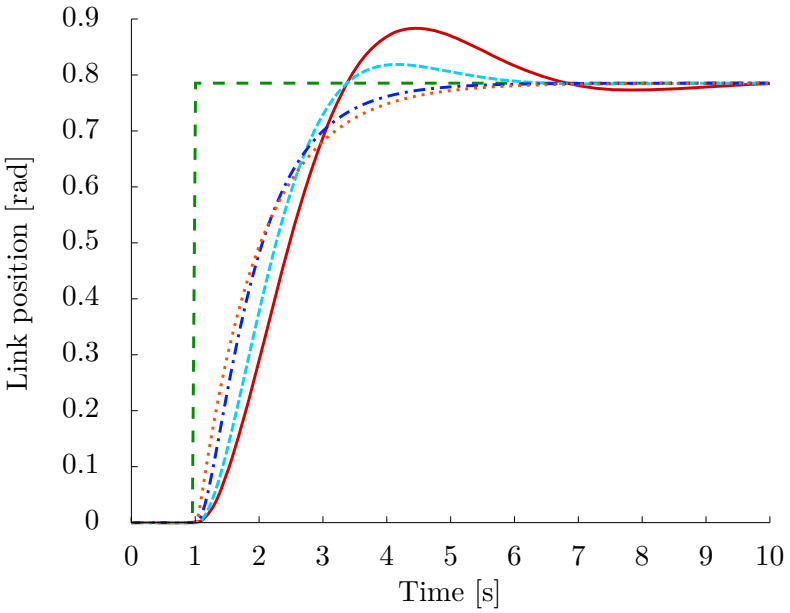

Figure 15.7: Simulations, influence of K_1: link position after a commanded step of 0.8 rad. The red/solid, light blue/dashed, blue/dot dashed and orange/dotted lines depict the responses obtained for a gain K_1 of 0.2, 1, 5 and 50 (the K_2 coefficient being set to $K_2 = 1$). The coefficient K_1 has a strong influence on the stiffness of the link.

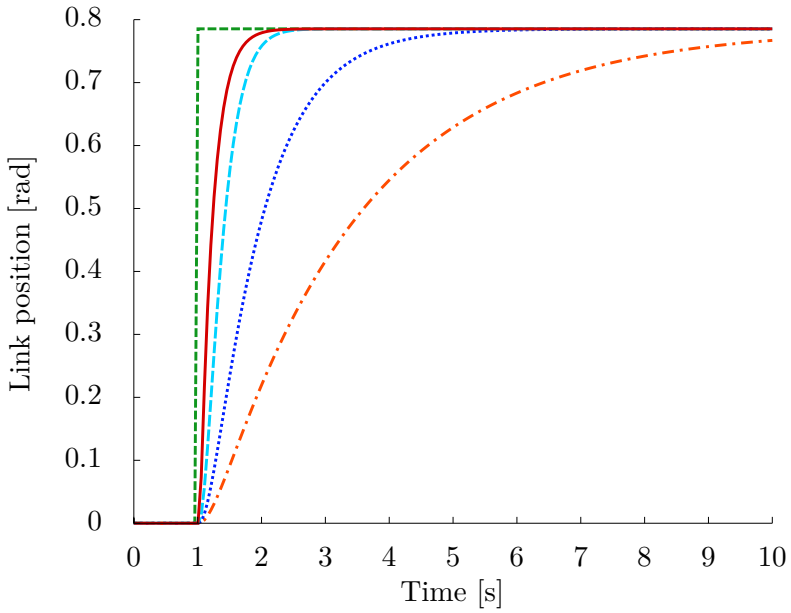

Figure 15.8: Simulations, influence of K_2: link position after a commanded step of 0.8 rad. The red/solid, light blue/dashed, blue/dot dashed and orange/dotted lines are representing the link position obtained for a K_2 coefficient of 0.2, 1, 5 and 50 (the K_1 coefficient being set to $K_1 = 5$). The coefficient K_2 has a strong influence on the damping of the link.

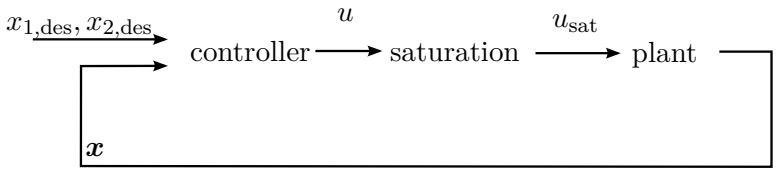

Figure 15.9: Diagram of the simulation used for the evaluation of the influence of input saturation. A saturation block is placed between the controller output and the plant.

ïĄą

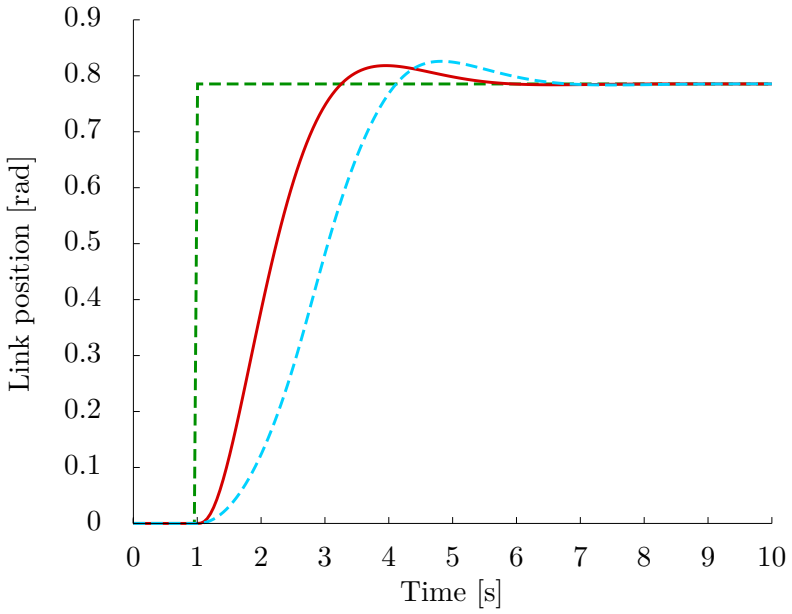

Figure 15.10: Simulations, influence of a saturation of the control input u: link position after a commanded step of 0.8 rad. The red/solid and light blue/dashed curves are the responses obtained without and with a saturation of $|u| < 0.0005$ (the coefficients are set to $K_1 = 1$, $K_2 = 1$, $K_3 = 100$ and $K_4 = 100$).

parameters and the same initial conditions is conducted with the saturation (cf. Fig.15.11 light blue/dashed). The plots are showing that the controller remains stable in the two cases, despite the strong saturation visible in the command (cf. Fig. 15.11).

A last simulation on the single joint driven by a single motor and with a linear stiffness is performed to analyze the influence of delays. Based on the experience of the previous robots developed in the institute, it is known that delays can have very deleterious effects on the stability. The analysis of such system delays, together with nonlinear dynamics, is still a research topic and is out of the scope of the present work. The interested reader can consult [136–138] for work, mainly oriented towards the issues of time varying delays in telemanipulation scenario, on the modeling and the control of system with delays. In this work, the influence of time delay in the control loop is evaluated by adding a constant time delay between the command and the plant as well as between the measurements and the controller. The diagram corresponding to the simulation is reported in Fig. 15.12. Increasing the delay from 0ms to 1ms confirms that they have a strong influence on the control performance. As described in the modeling part, the delay for a complete round trip of the signals, i. e. from measure to actuation, is 333μs. Therefore, according to the simulations, the system

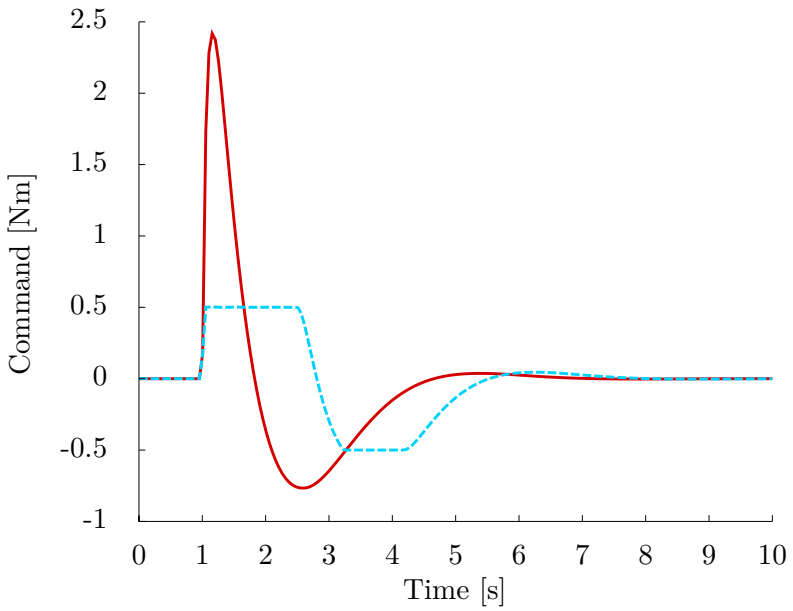

Figure 15.11: Simulations, influence of a saturation of the control input u: input command after a commanded step of 0.8 rad. The light blue(solid) and blue (dashed) lines are the responses obtained without and with a saturation of $|u| < 0.0005$ (the coefficients are set to $K_1 = 1$, $K_2 = 1$, $K_3 = 100$ and $K_4 = 100$).

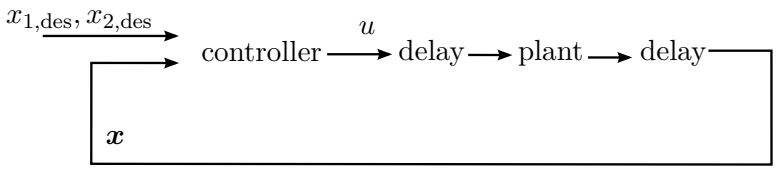

Figure 15.12: Diagram of the simulation used for the evaluation of the influence of time delays. A fixed delay is placed between the command and the actuator as well as between the measurements and the controller.

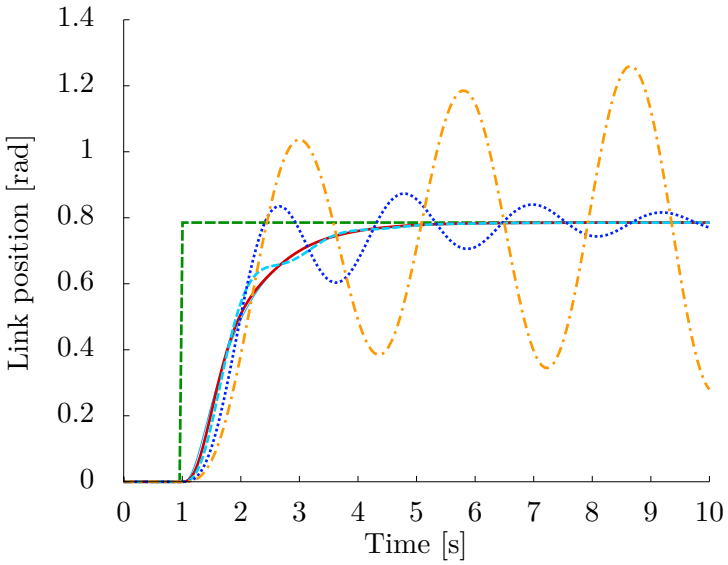

Figure 15.13: Simulations, influence of a delay in the control input u: link position after a commanded step of 0.8 rad. The red/solid (resp. light blue/dashed, blue/dotted, orange/dot dashed) line is the response obtained with a 0ms delay (resp. 0.1, 0.2, 0.5 and 1ms) (the coefficients are set to $K_1 = 5$, $K_2 = 1$, $K_3 = 100$ and $K_4 = 100$).

should be non oscillating even with the large gains that were selected for this simulation.

15.2.5 Experiments

The controller derived and simulated in the previous sections is implemented on a test setup described in Fig. 15.14. A motor, similar to the one of the modeling section, is connected to a low inertia link with two elastic tendons. The stiffness of the tendons is linear (i. e. the force is proportional to the elongation). An internal pretension is required in order to avoid slack in the tendons during motion. However, because of the linearity of the springs it is not influencing the dynamic equations (as long as slackening or breaking is not happening). Table 15.2 reports the values used for the controller and the parameters corresponding to the physical setup. The stiffness of the springs has been obtained by direct measurement and the inertia of the link has been estimated from the CAD data. Figure 15.15 depicts the measured link position obtained after a commanded step in the case of the backstepping controller and a PD controller (for reference). It is clearly visible that the backstepping controller manages to control the link without generating oscillations. The motor trajectory denoted by $\boldsymbol{A}$ in Fig. 15.15 is a characteristic of the flexible joint systems.

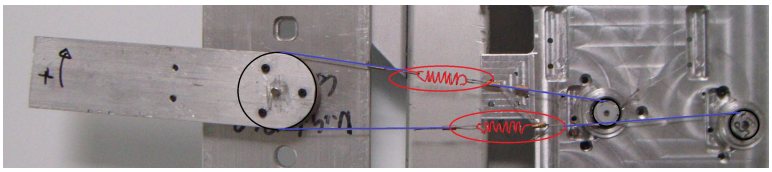

Figure 15.14: Experimental setup used for the verification of the backstepping controller

symbol	description	value	units
$gearratio$	gear ratio	100	N.A
M	link side inertia	7.2×10^{-7}	$[kgm^2]$
B	motor inertia (output inertia)	2×10^{-4}	$[kgm^2]$
b_θ	motor damping	10^{-2}	$[Nm/(rad/s)]$
b_q	link damping	10^{-3}	$[Nm/(rad/s)]$
K	joint stiffness	20	$[Nm/rad]$
K_3	controller gain 3	100	N.A
K_4	controller gain 4	100	N.A

Table 15.2: Experimental parameters and controller parameters for a single joint and single motor with linear stiffness

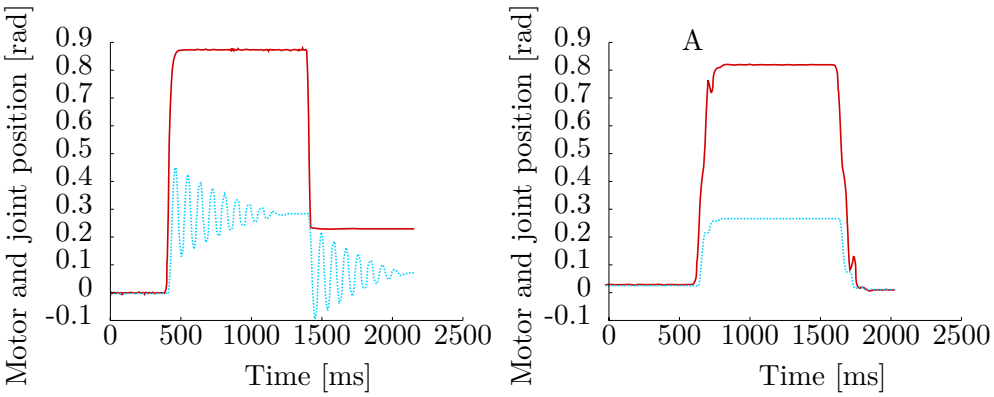

Figure 15.15: Experiment: measured motor position red/solid and link position light blue/dotted after a commanded position step. The pulley ratio between the motor and the link is about 3. Left: a PD controller on the motor position is used. Right: the backstepping controller is used.

15.2.6 Conclusion

A nonlinear control law for a a single flexible joint driven by a single motor and a linear stiffness has been derived. Despite the simplicity of the plant, the controller has a rather complex expression. It highlights the main drawback of the backstepping method. Although, by construction, the controller ought to be stable, several simulations were performed to evaluate the sensitivity to implementation conditions such as delays and saturations. Finally, the controller was implemented on a test setup and the measurements confirmed the simulations.

15.3 Single flexible joint: impedance

During grasping tasks it is more advantageous to use a joint impedance controller than a joint position controller. Indeed, because the models of the objects are inaccurate, a position controller can lead to large interaction forces. Large forces can damage the fingers or the objects. Consequently, a force control loop is required to *softly* interact with the environment. Several control schemes have been developed that allow to moderate the forces, such as hybrid force control, admittance control or torque control. Based on the practical experience in manipulation of the DLR, a joint impedance controller is selected to provide the compliant behavior. Similar work is proposed in [68], however with experimental results on a very different system (an arm with comparatively large stiffness) as well as limited to the case of a constant stiffness.[1]

In this section, the backstepping design method is applied to a single joint driven by a single motor. Unlike the previous section, the behavior of an impedance controller is targeted. First, the coordinates of the joint model are transformed in order to apply the desired link side control law. The internal dynamics of the motor results in a tracking error of the desired link torque, therefore, the backstepping procedure is applied to ensure that the system is regulated to the desired state while remaining globally stable. In the third section, several simulations are presented in order to obtain a first selection of gains for the experiments. The practical implementation is presented in the last section. A test setup with a single flexible joint and adjustable parameters, such as link mass and joint stiffness, is designed and built for those specify tests.

[1] in [68] the joint stiffness results from the structure stiffness.

15.3.1 Model

Similar to the previous sections, the equations of the simplified system are :

$$\begin{cases} m\ddot{q} &= k(\theta - q) + \tau_{\text{ext}} \\ b\ddot{\theta} &= -k(\theta - q) + \tau_{\text{m}} \end{cases} , \tag{15.51}$$

where $\theta \in \mathbb{R}, q \in \mathbb{R}$ are the motor position and link position. The link inertia and the motor inertia (along the rotation axis) are denoted $m \in \mathbb{R}, b \in \mathbb{R}$. In the linear case, defining $\tau = k(\theta - q)$, and using both equation leads to

$$\ddot{\tau} = -\frac{k(m+b)}{mb}\tau + \frac{k}{b}\tau_{\text{m}} - \frac{k}{m}\tau_{\text{ext}} \ . \tag{15.52}$$

Therefore, θ can be removed from (15.51). Defining the state vector $\boldsymbol{x} \in \mathbb{R}^4$ as $\boldsymbol{x} = [x_1, x_2, x_3, x_4]^T = [q, \dot{q}, \tau, \dot{\tau}]^T$, results in a strict feedback form description

$$\begin{cases} \dot{x}_1 = & x_2 \\ \dot{x}_2 = & m^{-1}(x_3 + \tau_{\text{ext}}) \\ \dot{x}_3 = & x_4 \\ \dot{x}_4 = & \frac{k}{m}\left(-\frac{(m+b)}{m}x_3 + \tau_{\text{m}} - \frac{b}{m}\tau_{\text{ext}}\right) \end{cases} . \tag{15.53}$$

Similar to the example of the previous section, a feedback can be used to cancel most of the terms of the last equation of (15.53).

15.3.2 Controller

The backstepping methodology can be applied in the similar way as in the section 15.2. However, the method does not enforce that the steps are performed one by one if, of course, stability can be established at the end of the step. In the case of an impedance controller, the desired torque is a function of the position and the velocity errors. Recalling that $\bar{x}_3 = x_3 = \tau_{\text{q,des}}$ and using it as a virtual input, the link side controller is designed by selecting $\bar{x}_3$ as

$$\begin{array}{ccc} \tau_{\text{q,des}} & = -K_{\text{p,imp}}q - K_{\text{d,imp}}\dot{q} \\ \Updownarrow & & , \\ \bar{x}_3 & = -K_{\text{p,imp}}x_1 - K_{\text{d,imp}}x_2 \end{array} \tag{15.54}$$

where $(K_{\text{p,imp}}, K_{\text{d,imp}}) \in (\mathbb{R}^{*+})^2$ are the impedance stiffness and damping. The case of a regulation controller to the origin is presented, but the regulation to any other point is obtained by a change of variable. Assuming $\tau_{q,des} = x_3$ can be perfectly generated, the stability is proved using the Lyapunov function, $V_1(q) = \frac{1}{2}\dot{q}^T m\dot{q} + \frac{1}{2}q^T K_{p,imp}q = \frac{1}{2}\dot{x_1}^T m\dot{x_1} + \frac{1}{2}x_1^T K_{p,imp}x_1$. The time derivative of V_1 along the solutions is

$$\begin{aligned} \dot{V}_1(x_1) &= \dot{x}_1^T m\ddot{x}_1 + \dot{x}_1^T K_{\text{p,imp}}x_1 \\ &= x_2^T(-K_{\text{p,imp}}x_1 - K_{\text{d,imp}}x_2 + \tau_{\text{ext}}) + x_2^T K_{\text{p,imp}}x_1 + x_2^T\tau_{\text{ext}} \ , \\ &= -K_{\text{d,imp}}x_2^2 + x_2^T\tau_{\text{ext}} \end{aligned} \tag{15.55}$$

which completes the proof since, in the absence of disturbances $\tau_{\text{ext}} = 0$, thus $\dot{V}_1(x_1) \leq 0$ and $\dot{V}_1(x_1) = 0 \implies x_1 = 0$.

First backstep Since τ_{ext} can not be exactly generated, the error $z_3 = x_3 - \bar{x}_3$ between the reference input and the realized input is introduced. It is interesting to note that the error z_3 is equivalent to the error $\boldsymbol{P}^T \boldsymbol{e}_{\text{f}}$ that was introduced in the cascaded case. The system is expressed in terms of this error as

$$\begin{array}{rcc} \dot{x}_1 = & x_2 & \\ \dot{x}_2 = & m^{-1}(-K_{\text{p,imp}}x_1 - K_{\text{d,imp}}x_2 + z_3 + \tau_{\text{ext}}) & \\ \dot{z}_3 = & x_4 - \dot{\bar{x}}_3 & . \\ \dot{x}_4 = & kb^{-1}(-\dfrac{(m+b)}{m}x_3 + \tau_{\text{m}} - \frac{b}{m}\tau_{\text{ext}}) & \end{array} \tag{15.56}$$

Using $\bar{x}_4 = x_4$ as a virtual input, it is possible to design the link side controller by selecting $\bar{x}_4$ as

$$\bar{x}_4 = -K_3 z_3 + \dot{\bar{x}}_3 - x_2 \ , \tag{15.57}$$

where $K_3 \in \mathbb{R}^{*+}$ is a design parameter. Let $V_2(x_1, x_2, z_3)$ be the Lyapunov function

$$V_2(x_1, x_2, z_3) = \frac{1}{2}\dot{x}_1^T m \dot{x}_1 + \frac{1}{2}x_1^T K_{p,imp} x_1 + \frac{1}{2}z_3^T C_t z_3 \ . \tag{15.58}$$

Thanks to the symmetry of m and $K_{\text{p,imp}}$, the time derivative of V_2 is given by,

$$\dot{V}_2(x_1, x_2, z_3) = \dot{x}_1^T m \dot{x}_2 + x_1 K_{\text{p,imp}} \dot{x}_1 + z_3^T \dot{z}_3 \ . \tag{15.59}$$

Injecting $\dot{x}_2$ and $\dot{z}_3$ from the dynamic equation gives

$$\begin{array}{rcc} \dot{V}_2 & = & x_2^T(-K_{p,imp}x_1 - K_{\text{d,imp}}x_2 + z_3 + \tau_{\text{ext}}) + x_1 K_{\text{p,imp}} x_2 + z_3^T(x_4 - \dot{\bar{x}}_3) \\ & = & x_2^T(-K_{p,imp}x_1 - K_{\text{d,imp}}x_2 + z_3 + \tau_{\text{ext}}) + x_1 K_{\text{p,imp}} x_2 \\ & + & z_3^T(-K_3 z_3 + \dot{\bar{x}}_3 - x_2 - \dot{\bar{x}}_3 - \tau_{\text{ext}}) \\ & = & -x_2^T K_{\text{d,imp}} x_2 - z_3^T K_3 z_3 - z_3^T \tau_{\text{ext}} \end{array} \ , \tag{15.60}$$

which, after invocation of the LaSalle theorem, completes the proof.

Second backstep Since x_4 can not be exactly generated, the error $z_4 = x_4 - \bar{x}_4$ between the reference input and the realized input is introduced and the system is expressed in terms of this error. The system is

$$\begin{array}{rcc} \dot{x}_1 = & x_2 & \\ \dot{x}_2 = & m^{-1}(-K_{p,imp}x_1 - K_{\text{d,imp}}x_2 + z_3 + \tau_{\text{ext}}) & \\ \dot{z}_3 = & -K_3 z_3 - x_2 + z_4 & . \\ \dot{z}_4 = & kb^{-1}(-\dfrac{(m+b)}{m}x_3 + \tau_{\text{m}} - \dfrac{b}{m}\tau_{\text{ext}}) - \dot{\bar{x}}_4 & \end{array} \tag{15.61}$$

Finally, since the motor input τ_{m} is appearing in (15.61) the backstepping ends. The control input τ_{m} is selected as

$$\tau_{\mathrm{m}} = \frac{(m+b)}{m} x_3 + bk^{-1}u + \frac{b}{m}\tau_{\mathrm{ext}} \ , \tag{15.62}$$

$$u = -K_4 z_4 + \dot{\bar{x}}_4 - z_3 \ , \tag{15.63}$$

where $K_4 \in \mathbb{R}^{*+}$ is a design parameter. Let $V_3(x_1, x_2, z_3, z_4)$ be the Lyapunov function

$$V_3(x_1, x_2, z_3, z_4) = \frac{1}{2}\dot{x}_1^T m \dot{x}_1 + \frac{1}{2} x_1^T K_{p,imp} x_1 + \frac{1}{2} z_3^T z_3 + \frac{1}{2} z_4^T z_4 \ . \tag{15.64}$$

The time derivative of V_3 is given by (using the symmetry of m and $K_{\mathrm{p,imp}}$)

$$\dot{V}_3(x_1, x_2, z_3, z_4) = \dot{x}_1^T m \dot{x}_2 + x_1 K_{\mathrm{p,imp}} \dot{x}_1 + z_3^T \dot{z}_3 + z_4^T \dot{z}_4. \tag{15.65}$$

Injecting $\dot{x}_2$, $\dot{z}_3$ and $\dot{z}_4$ from the dynamic equation yields

$$\begin{aligned}
\dot{V}_3 = \ & x_2^T(-K_{p,imp}x_1 - K_{\mathrm{d,imp}}x_2 + z_3 + \tau_{\mathrm{ext}}) + x_1 K_{\mathrm{p,imp}} x_2 + z_3^T(-K_3 z_3 - x_2 + z_4) \\
& + z_4^T(-kb^{-1}(\frac{(m+b)}{m}x_3 + \tau_{\mathrm{m}} - \tfrac{b}{m}\tau_{\mathrm{ext}}) - \dot{\bar{x}}_4) \\
= \ & x_2^T(-K_{p,imp}x_1 - K_{\mathrm{d,imp}}x_2 + z_3) + x_1 K_{\mathrm{p,imp}} x_2 + z_3^T(-K_3 z_3 - x_2 - z_4) \\
& + z_4^T(-K_4 z_4 - z_3) \\
= \ & -x_2^T K_{\mathrm{d,imp}} x_2 - z_3^T K_3 z_3 - z_4^T K_4 z_4 + x_2^T \tau_{\mathrm{ext}}
\end{aligned} \ , \tag{15.66}$$

which completes the proof.

Input expression The input expression is obtained by replacing the expressions of $\bar{x}_3$ and $\bar{x}_4$. It is interesting to note that, using the relations $m\ddot{q} = k(\theta - q) + \tau_{\mathrm{ext}}$ and $mq^{(3)} = k(\dot{\theta} - \dot{q}) + \dot{\tau}_{\mathrm{ext}}$, the derivatives must only be available for the link velocity. The original system was

$$\begin{cases}
\dot{x}_1 = & x_2 \\
\dot{x}_2 = & m^{-1}x_3 \\
\dot{x}_3 = & x_4 \\
\dot{x}_4 = & -kb^{-1}\left(m^{-1}(m+b)x_3 + \tau_m\right) \\
\tau_m = & -m^{-1}(m+b)x_3 - bk^{-1}u \\
u = & -K_4 z_4 + \dot{\bar{x}}_4 - z_3
\end{cases} . \tag{15.67}$$

The virtual inputs are defined as

$$\begin{cases}
\bar{x}_3 = & -K_{p,imp}x_1 - K_{\mathrm{d,imp}}x_2 \\
\bar{x}_4 = & -K_3 z_3 + \dot{\bar{x}}_3 - x_2 \\
\tau_m = & bk^{-1}(-k(mb)^{-1}(m+b)x_3 - K_4 z_4 + \dot{\bar{x}}_4 - z_3)
\end{cases} , \tag{15.68}$$

and the error definitions are

$$\begin{cases}
z_3 = & x_3 - \bar{x}_3 \\
z_4 = & x_4 - \bar{x}_4
\end{cases} . \tag{15.69}$$

Finally, the input expression is

$$\begin{array}{rc} u = & -\frac{b}{k}(K_4K_3K_{\mathrm{p,imp}} + K_{\mathrm{p,imp}})x_1 \\ - & \frac{b}{k}(K_3K_{\mathrm{p,imp}} + K_4(K_3K_{\mathrm{d,imp}} + K_{\mathrm{p,imp}} + 1) + K_{\mathrm{d,imp}})x_2 \\ - & \frac{b}{k}((k\frac{(m+b)}{mb} + K_4(K_3 + K_{\mathrm{d,imp}}m^{-1}) + m^{-1}(K_3K_{\mathrm{d,imp}} + K_{\mathrm{p,imp}}) + 1)x_3 \\ - & \frac{b}{k}(K_4 + K_{\mathrm{d,imp}}m^{-1} + K_3)x_4 \end{array} . \tag{15.70}$$

15.3.3 Simulations

In this section numerical simulations are performed to verify that the designed controller is indeed providing the behavior of an joint impedance controller and that it is stable (naturally limited to numerical experiments). Fig. 15.16 and Fig. 15.17 depict the influence of the controller impedance parameters $K_{\mathrm{p,imp}}$ and $K_{\mathrm{d,imp}}$ on the link position after a step command of 45 degrees (at time $t = 0.5$s) and an external disturbance of 1Nm (at time $t = 1.5$s). In Figure 15.16, it can be seen that the selected joint stiffness of

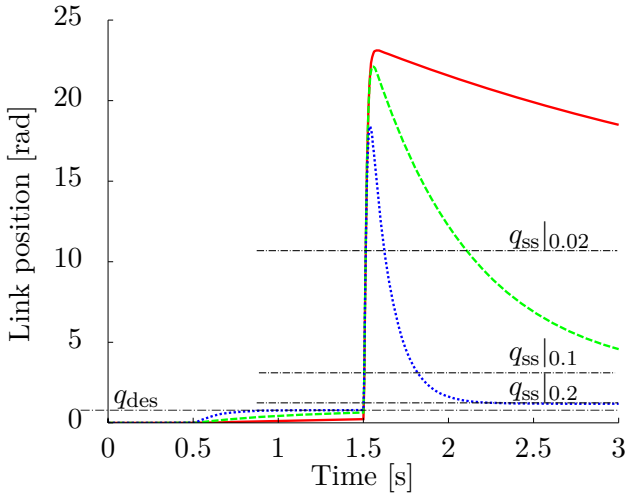

Figure 15.16: Simulation: influence of the stiffness coefficient $K_{\mathrm{p,imp}} \in [0.02, 0.1, 0.5], K_{\mathrm{d,imp}} = 0.05$ on the link side position after a desired position step of 45 degrees (at time $t = 0.5$s) and external disturbance of 0.2Nm (at time $t = 1.5$s).The desired joint position is denoted q_{des} and the steady states are denoted $q_{\mathrm{ss}}|_{0.02}$, $q_{\mathrm{ss}}|_{0.1}$ and $q_{\mathrm{ss}}|_{0.2}$.

the impedance controller leads to the proper steady-state joint deflection. It is interesting to notice that, although the stiffness is modified, the rising times are identical since it is imposed by the motor controller dynamics. In Figure 15.17 the influence of the link damping is noticeable through the increase of the settling time. However, as for the case of the stiffness, the motor dynamics is imposing most of the behavior. Unlike the singular perturbation approach, the system is stable because the motor dynamics are

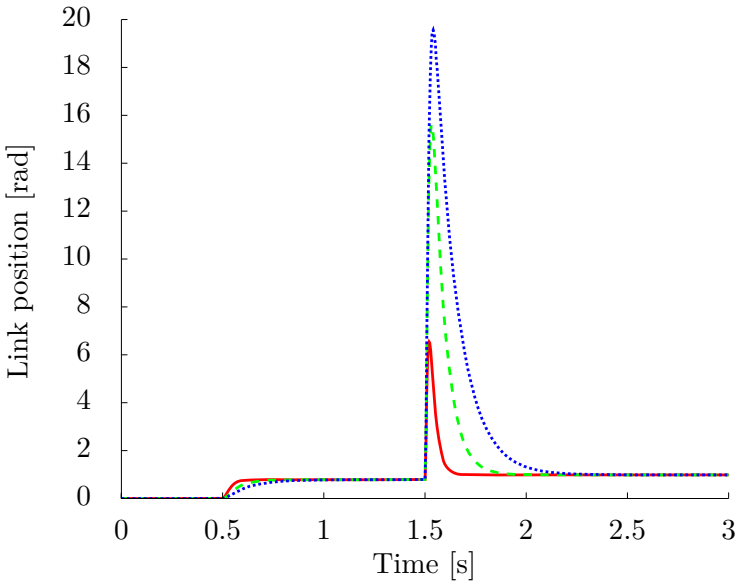

Figure 15.17: Simulation: influence of the damping coefficient $K_{\text{p,imp}} = 1, K_{\text{d,imp}} \in [0.01, 0.05, 0.1]$ on link side position after a desired position step of 45 degrees (at time $t = 0.5$s) and external disturbance of 0.2Nm (at time $t = 1.5$s).

included in the design of the controller and not because of its robustness. In other words, the motor dynamics are not disturbances in the backstepping controller design.

15.3.4 Experiments

Using the same setup as in the previous section, several experiments are performed to verify that the controller behaves as expected with the physical plant. Figure 15.18 shows that the controller successfully moves the link to the desired position and provides an impedance behavior w. r. t. the external load applied (for practical reasons a displacement is imposed to the link and the torque is measured). After applying the displacement to the link, the expected torque should be $\tau = K_{\text{p,imp}}(q - q_0)$ where q (resp. q_0) is the link position (resp. the desired link position). The measured torque is $\tau = 0.579$ Nm for a measured deflection of 0.3 radians and a stiffness of 2 Nm/rad (i. e. an expected torque of $\tau = 0.6$Nm). Although the measured torque is not exactly the expected torque, the behavior is perfectly suited for an interaction between the fingers and the environment.

15.3.5 Conclusion

This section derived an impedance controller for a linear flexible joint driven by a single motor. The controller is designed based on the state controller

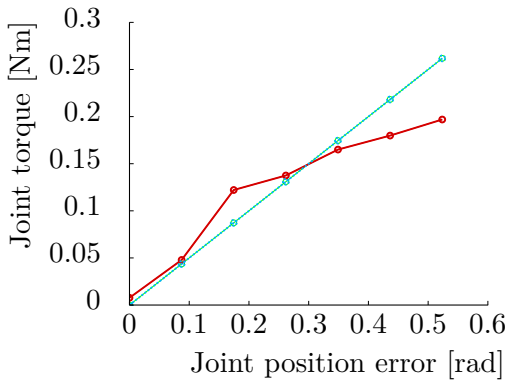

Figure 15.18: Experiment: measured and expected joint torque w. r. t. an increasing joint position error from 0 to 0.5 rad.

of the previous section. It formally requires the measure of the external torque and its derivative. However, it is practically sufficient to neglect the derivative and to estimate the joint torque through the deflection of the spring. Indeed, since the motor position θ and the link position q are measured, the joint torque is obtained as $\tau = k(\theta - q)$ and its derivative $\dot{\tau} = k(\dot{\theta} - \dot{q})$. The usual drawback of the backstepping, that is, the need for high order derivatives, is therefore not a practical issue. Several simulations showed that the controller behaves as an impedance controller. Experiments confirm that the controller performs satisfactorily and reveals to be very robust to disturbances.

15.4 Single flexible joint: impedance non linear stiffness

In the previous sections, the spring stiffness was considered constant. However, in the Hand Arm System, nonlinear springs are used in order to offer the possibility to adjust the joint stiffness. Moreover, the *explosion* of the spring stiffness when reaching its elongation limits creates a natural protection for the end stops of joints. Preliminary experiments on a system with nonlinear springs with the backstepping controller designed for a linear spring showed that the controller is robust to the unmodeled nonlinearities. However, it is possible to include the nonlinear effects directly in the controller to ensure that the stability is achieved without the robustness properties. In this section the backstepping impedance controller for a single flexible joint is modified to include the nonlinear spring characteristic. First, the nonlinearity is introduced in the model. Then, the nonlinear effects are propagated in the controller. The nonlinear effects are only modifying the last backstepping stage. Unsurprisingly, one condition for the stability

proof is that the spring stiffness is strictly positive. Finally, simulations and experiments are performed in order to verify the validity of the controller.

15.4.1 Model

The dynamical model is similar to the previous sections. However, because the spring stiffness is a function of its elongation the system takes the form

$$\begin{array}{ll} m\ddot{q} & = r_q\phi(r_\theta\theta - r_q q) + \tau_{\text{ext}} \\ b\ddot{\theta} & = -r_\theta\phi(r_\theta\theta - r_q q) + \tau_{\text{m}} \end{array} , \tag{15.71}$$

where all quantities are defined as in the linear case. The force generated by the spring is represented by $\phi(r_\theta\theta - r_q q) \in \mathbb{R}$, which is the force depending on the spring elongation. The motor pulley radius and the link pulley radius are denoted $r_\theta \in \mathbb{R}^+$ and $r_q \in \mathbb{R}^+$. In order to simplify the notation, the radii of the motor pulley and the link pulley are considered equal to one. Considering that the spring function is sufficiently smooth on the workspace, defining $\tau = \phi(\theta - q)$ leads to

$$\begin{array}{ll} \dot{\tau} = & \dfrac{\partial\phi}{\partial\theta}(\dot{\theta} - \dot{q}) \\ \ddot{\tau} = & \dfrac{\partial^2\phi}{\partial\theta^2}(\dot{\theta} - \dot{q})^2 + \dfrac{\partial\phi}{\partial\theta}(\ddot{\theta} - \ddot{q}) \end{array} . \tag{15.72}$$

The partial derivative can be taken w. r. t. θ or q because of the symmetry of the function. Using the dynamics to express $\dot{\tau}$ in terms of $q, \dot{q}, \tau$ and $\dot{\tau}$ results in the relation between the spring elongation and the torque, as well as the expression of the torque derivative in terms of the joint torque and the external torque. The expressions are

$$(\dot{\theta} - \dot{q}) = \left(\frac{\partial\phi}{\partial\theta}\right)^{-1}\dot{\tau} , \tag{15.73}$$

and

$$\begin{array}{ll} \ddot{\tau} = & \dfrac{\partial^2\phi}{\partial\theta^2}\left(\left(\dfrac{\partial\phi}{\partial\theta}\right)^{-1}\dot{\tau}\right)^2 + \dfrac{\partial\phi}{\partial\theta}\left(\dfrac{1}{b}\left(-\tau + \tau_{\text{m}}\right) - \dfrac{1}{m}\tau - \dfrac{1}{m}\tau_{\text{ext}}\right) \\ \ddot{\tau} = & \dfrac{\partial^2\phi}{\partial\theta^2}\left(\left(\dfrac{\partial\phi}{\partial\theta}\right)^{-1}\dot{\tau}\right)^2 + \dfrac{\partial\phi}{\partial\theta}\dfrac{1}{b}\left(\tau_{\text{m}} - \dfrac{(b+m)}{m}\tau - \dfrac{b}{m}\tau_{\text{ext}}\right) \end{array} . \tag{15.74}$$

Just as it was done with the linear case, defining the state vector $\boldsymbol{x} \in \mathbb{R}^4$ as $\boldsymbol{x} = [q, \dot{q}, \tau, \dot{\tau}]^T$, results in a strict feedback form description

$$\begin{array}{ll} \dot{x}_1 = & x_2 \\ \dot{x}_2 = & M^{-1}(x_3 + \tau_{\text{ext}}) \\ \dot{x}_3 = & x_4 \\ \dot{x}_4 = & \dfrac{\partial^2\phi}{\partial\theta^2}\left(\left(\dfrac{\partial\phi}{\partial\theta}\right)^{-1}x_4\right)^2 + \dfrac{\partial\phi}{\partial\theta}\dfrac{1}{b}\left(\tau_{\text{m}} - \dfrac{(b+m)}{m}x_3 - \dfrac{b}{m}\tau_{\text{ext}}\right) \end{array} . \tag{15.75}$$

It is important to note that the nonlinear effects are only visible in the last equation of (15.71). None of the partial derivatives is zero since the force characteristic is convex. Therefore, it is possible to feedback linearize the last equation by choosing $\tau_{\mathrm{m}} = \left(\frac{\partial \phi}{\partial \theta}\right)^{-1} b \left(u - \frac{\partial^2 \phi}{\partial \theta^2} \left(\left(\frac{\partial \phi}{\partial \theta}\right)^{-1} x_4 \right)^2 + \frac{(b+m)}{m} x_3 + \frac{b}{m} \tau_{\mathrm{ext}} \right)$.
It yields

$$\begin{array}{rcc} \dot{x}_1 = & x_2 & \\ \dot{x}_2 = & m^{-1} x_3 & \\ \dot{x}_3 = & x_4 & \\ \dot{x}_4 = & u & \end{array} , \tag{15.76}$$

which is similar to the linear case.

15.4.2 Controller

The controller derivation is identical to the case of the linear system until the input expression replacement. The control input u is selected as

$$\tau_{\mathrm{m}} = \left(\frac{\partial \phi}{\partial \theta}\right)^{-1} b \left(u - \frac{\partial^2 \phi}{\partial \theta^2} \left(\left(\frac{\partial \phi}{\partial \theta}\right)^{-1} x_4 \right)^2 \right) + \frac{(b+m)}{bm} x_3 \ , \tag{15.77}$$

with

$$u = -K_4 z_4 + \dot{\bar{x}}_4 - z_3 \ , \tag{15.78}$$

where $K_4 \in \mathbb{R}^{*+}$ is a design parameter. The stability of the plant under the controller is obtained by Lyapunov analysis. Let $V_3(x_1, x_2, z_3, z_4)$ be the Lyapunov function,

$$V_3(x_1, x_2, z_3, z_4) = \frac{1}{2} \dot{x}_1^T m \dot{x}_1 + \frac{1}{2} x_1^T K_{\mathrm{p,imp}} x_1 + \frac{1}{2} z_3^T z_3 + \frac{1}{2} z_4^T z_4 \ . \tag{15.79}$$

The time derivative of V_3 is given by

$$\dot{V}_3(x_1, x_2, z_3, z_4) = \dot{x}_1^T m \dot{x}_2 + x_1 K_{\mathrm{p,imp}} \dot{x}_1 + z_3^T \dot{z}_3 + z_4^T \dot{z}_4 \ . \tag{15.80}$$

Injecting $\dot{x}_2$, $\dot{z}_3$ and $\dot{z}_4$ from the dynamic equation yields

$$\begin{array}{rcc} \dot{V}_3 = & x_2^T(-K_{p,imp} x_1 - K_{d,imp} x_2 + z_3) + x_1 K_{\mathrm{p,imp}} x_2 + z_3^T(-K_3 z_3 - x_2 + z_4) & \\ & + z_4^T((\frac{\partial \phi}{\partial \theta})^{-1} x_4^2 + \frac{\partial^2 \phi}{\partial \theta^2} \frac{1}{b} (\tau_{\mathrm{m}} - \frac{(b+m)}{bm} x_3) - \dot{\bar{x}}_4) & \\ = & x_2^T(-K_{p,imp} x_1 - K_{d,imp} x_2 + z_3) + x_1 K_{\mathrm{p,imp}} x_2 + z_3^T(-K_3 z_3 - x_2 - z_4) & , \\ & + z_4^T(-K_4 z_4 - z_3) & \\ = & -x_2^T K_{d,imp} x_2 - z_3^T K_3 z_3 - z_4^T K_4 z_4 & \end{array} \tag{15.81}$$

which, after invoking LaSalle theorem, completes the proof.

15.4.3 Simulations

In this section numerical simulation are performed to verify that the controller provides an impedance behavior and that it is stable (naturally limited to numerical experiments). For the simulation, a realistic spring characteristic is used and the derivatives are tabulated in a lookup table in order to stay close to the implementation case. Throughout this section, the term *linear* controller refers to the backstepping controller designed for the linear plant, the term *nonlinear* controller refers to the backstepping controller designed for the nonlinear plant. The difference between the linear and the nonlinear controllers is depicted in Figure 15.19. The improvement of the *nonlinear* controller is mainly noticeable in terms of settling time, although a larger overshot is observed. The *nonlinear* components of the controller

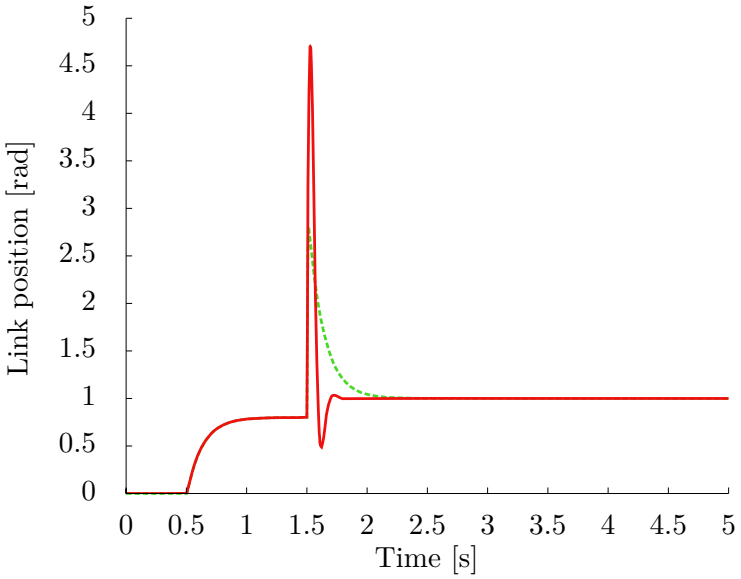

Figure 15.19: Simulation: comparison between the linear backstepping controller and the nonlinear backstepping controller on a nonlinear plant. The solid/red curve depicts the link position under the *nonlinear* controller. The dashed/green curve depicts the link position under the *linear* controller.

have an effect only when the stiffness of the link is far from the nominal stiffness, therefore the difference between the trajectories is not noticeable during the free motion between $t = 0.5s$ and $t = 1.0s$. Indeed, the inertia of the link is low w. r. t. to the joint stiffness thus the link deflection is minimal and the stiffness variation is negligible. A load applied to the link modifies noticeably the stiffness, this effect in depicted in Fig. 15.19 where the stiffness during both experiments is reported. Since a torque peak must be generated to begin the motion, one would expect a change of stiffness at the point denoted by A. However, this change of stiffness is negligible w. r. t.

the change of stiffness imposed by the load. As with most nonlinear control

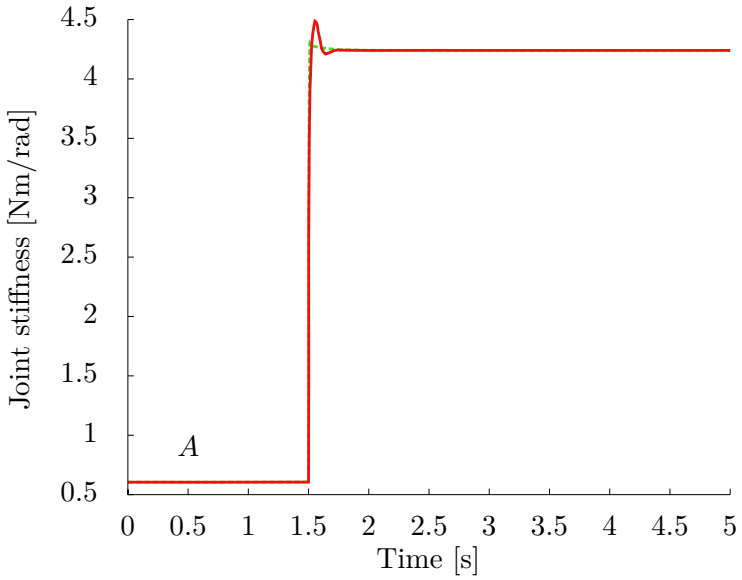

Figure 15.20: Simulation: change of the joint stiffness during the experiment depicted in Fig. 15.19. The solid/red curve depicts the link position under the *nonlinear* controller. The dashed/green curve depicts the link position under the *linear* controller. The stiffness change when accelerating the link (cf. point A, at $t = 0.5s$) is negligible w. r. t. the change of stiffness imposed by the external load (at time $t = 1.5s$).

approaches, the cancellation of the nonlinear terms tends to generate very large control actions. Therefore, a comparison between the *linear* and the *nonlinear* controller, together with an torque input saturation, is reported in Fig. 15.21.

15.4.4 Experiments

Using the same setup as used in the previous section but replacing the linear springs by nonlinear ones, experiments are performed to verify that the controller behaves as expected with the physical plant. Similar to the linear case, the controller successfully moves the link to the desired position and provides an impedance behavior w. r. t. the externally applied load. The link side position and the joint torques trajectories are depicted in Figure 15.22.

15.4.5 Conclusion

This section derived a nonlinear impedance controller for a nonlinear flexible joint driven by a single motor. The equations reveal that the differences between the *linear* backtepping controller and the *nonlinear* backstepping are

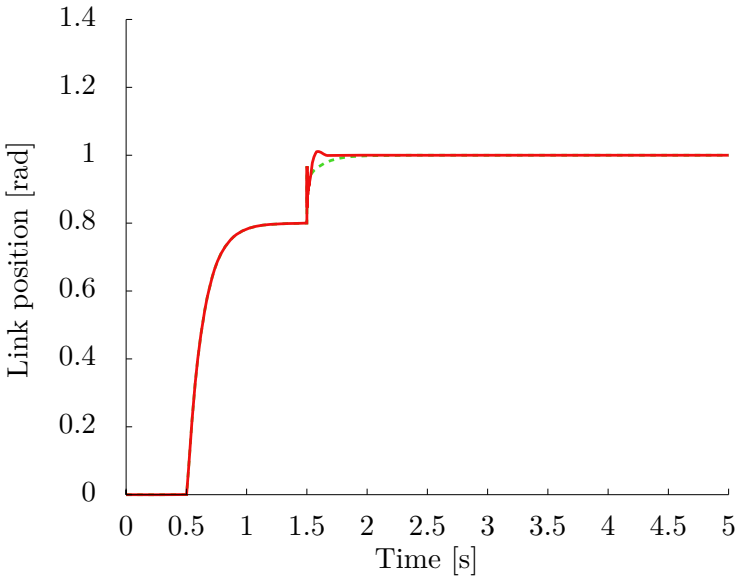

Figure 15.21: Simulation: effect of a motor torque saturation on the controllers. The solid/red curve depicts the link position under the *nonlinear* controller. The dashed/green curve depicts the link position under the *linear* controller. In both cases, a saturation is applied on the motor torque. The difference between the two controller is reduced. Nonetheless, the settling time of the *nonlinear* controller remains shorter.

limited if the input saturation is taken into account. Although the stiffness of the joint is nonlinear, the stiffness of the link only changes significantly when an external load is applied. Simulations and experiments confirm that the controller performs satisfactorily and reveals to be very robust to disturbances. The implementation of this nonlinear backstepping controller requires a stiffness model and its derivatives. It is interesting to note that one condition for the use of the controller is that the stiffness and its first derivative are non zero.

15.5 Antagonistic joint

The previous sections have demonstrated that the backstepping method is able to provide a solid theoretical background as well as excellent practical results. However, the previous cases where limited to the case of a single joint driven by a single motor. As presented in the modeling part, the fingers of the Awiwi Hand are driven by an antagonistic arrangement of tendons thus, it is necessary to extend the backstepping controller to the case of an antagonistic controller.

In this section, the backstepping design method is applied to a single joint driven by a pair of motors. First, the dynamics equations of the system are

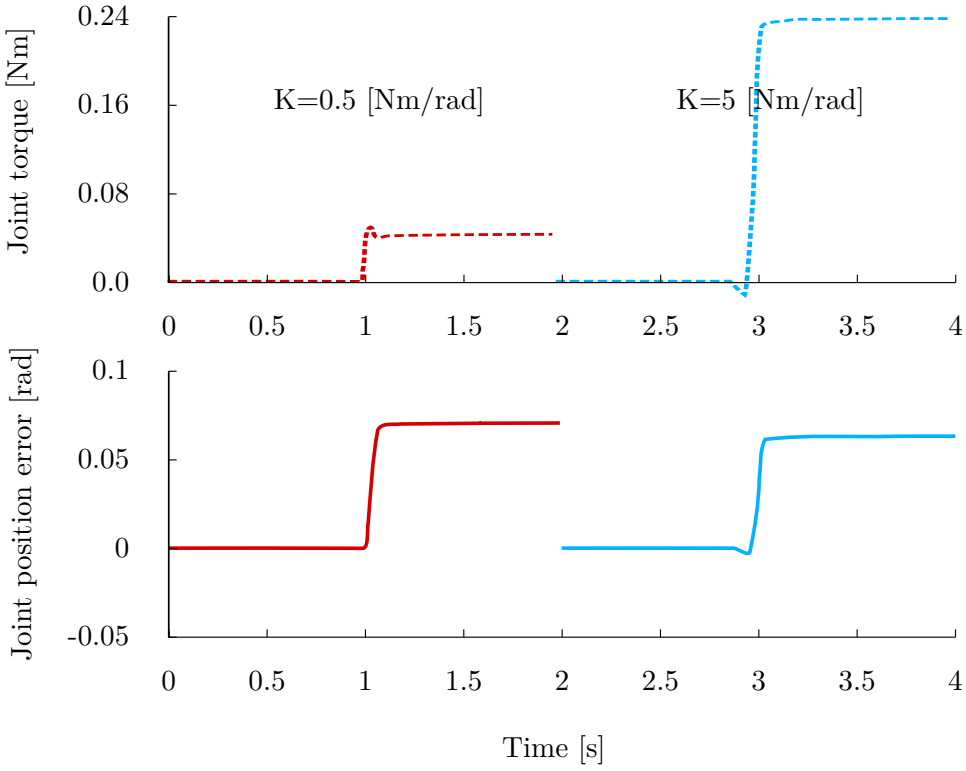

Figure 15.22: Experiment: measured link side position and joint torque after a desired position step of 1.3 rad and external obstacle placed at 0.8 rad. Between 0s and 2s the impedance gain is 0.5Nm/rad (in red). The impedance gain is 5Nm/rad between 2s and 4s (in blue).

derived. The system must be transformed in a strict feedback form to be suited for the backstepping procedure. However, transforming the complete system in such a form would loose the symmetry of the problem. Because it is preferred to keep the system symmetry, it is better to transform it in the strict feedback form by considering that the motors are not *aware* of one another. The desired link torque is shared between the motors and a pretension torque is added in order to maintain the pulling constraints and possibly achieve the desired stiffness. Finally, the backstepping method is applied to the two separated systems with the notations used by [130].

The simulations and experiments are presented in the last part. The main difficulty is to select the numerous gain matrices in order to obtain a satisfactory behavior. The gains have been initially selected to lead to feedback gains for the tendon force error that is close to the cascaded case.

15.5.1 Model

The equations for a linear antagonistic setup are

$$\begin{array}{rcl} m\ddot{q} & = & k(\theta_1 - q) - k(\theta_2 + q) + \tau_{\text{ext}} \\ b_1\ddot{\theta}_1 & = & -k_1(\theta_1 - q) + \tau_{\text{m},1} \\ b_2\ddot{\theta}_2 & = & -k_2(\theta_2 + q) + \tau_{\text{m},2} \end{array}, \tag{15.82}$$

where $(\theta_1, \theta_2) \in \mathbb{R}^2, q \in \mathbb{R}$ are the motor positions and link position. The link inertia and the motor inertia are denoted $m \in \mathbb{R}, b \in \mathbb{R}$. In the following, it is assumed that $b_1 = b_2 = b$ in order to simplify the notations. Defining $\tau_1 = k_1(\theta_1 - q), \tau_2 = k_2(\theta_2 + q)$, and using both equation leads to

$$\begin{array}{rcl} \ddot{\tau}_1 = & \frac{k_1}{m}\left(\frac{(m+b)}{b}\tau_1 + \tau_2 + \frac{m}{b}\tau_{\text{m},1} - \tau_{\text{ext}}\right) \\ \ddot{\tau}_2 = & \frac{k_2}{m}\left(\frac{(m+b)}{b}\tau_2 + \tau_1 + \frac{m}{b}\tau_{\text{m},2} + \tau_{\text{ext}}\right) \end{array}. \tag{15.83}$$

The system (15.83) can be decoupled with

$$\begin{array}{rcl} \tau_{\text{m},1} = & \frac{b}{m}(u - \tau_2) \\ \tau_{\text{m},2} = & \frac{b}{m}(u - \tau_1) \end{array}, \tag{15.84}$$

which yields

$$\begin{array}{rcl} \ddot{\tau}_1 = & \frac{k_1}{m}\left(\frac{(m+b)}{b}\tau_1 + u_1 - \tau_{\text{ext}}\right) \\ \ddot{\tau}_2 = & \frac{k_2}{m}\left(\frac{(m+b)}{b}\tau_2 + u_2 + \tau_{\text{ext}}\right) \end{array}. \tag{15.85}$$

Therefore, both motors can be treated independently. The following treats the case of θ_1. Defining the state vector $\boldsymbol{x} \in \mathbb{R}^4$ as $\boldsymbol{x} = [x_1, x_2, x_3, x_4]^T = [q, \dot{q}, \tau_1, \dot{\tau}_1]^T$, results in a strict feedback form description

$$\begin{array}{rcl} \dot{x}_1 = & x_2 \\ \dot{x}_2 = & m^{-1}(x_3 + \tau_{\text{ext}}) \\ \dot{x}_3 = & x_4 \\ \dot{x}_4 = & \frac{k_1}{m}\left(\frac{(m+b)}{b}x_3 + u_1 - \tau_{\text{ext}}\right) \end{array}. \tag{15.86}$$

Since an impedance behavior of the link side is wished, we have

$$\tau_{\text{q,des}} = \tau_1 - \tau_2 = -K_{\text{p,imp}}q - K_{\text{d,imp}}\dot{q} \tag{15.87}$$

However, because two motors are acting one the joint, they exists many combinations of motor torques that generate the desired joint torque. The choice

$$\begin{array}{rcl} \bar{\tau}_1 = & \tau_{1,\text{offset}} + \frac{1}{2}\tau_{\text{q,des}} \\ \bar{\tau}_2 = & \tau_{2,\text{offset}} - \frac{1}{2}\tau_{\text{q,des}} \end{array}, \tag{15.88}$$

where $\bar{\tau}_1$ and $\bar{\tau}_2$ denote the desired torque to be produced by each motor, is a choice that symmetrically shares the torque.

First backstep

Because the two motors have been decoupled it is possible to treat the problem as a set of independent differential systems. Therefore, all quantities are scalars. Let $V_2(\boldsymbol{x})$, be the Lyapunov function

$$V_2(\boldsymbol{x}) = \frac{1}{2}mx_2^2 + \frac{1}{2}K_{\text{p,imp}}x_1^2 + \frac{1}{2}e_{\text{t}}^T C_{\text{t}} e_{\text{t}} \ , \tag{15.89}$$

where $C_{\text{t}} \in \mathbb{R}$ and $K_{\text{p,imp}} \in \mathbb{R}$ are two positive scalars. The torque tracking error $e_{\text{t}} \in \mathbb{R}$ is defined as

$$e_t = \tau_1 - \bar{\tau}_1 = x_3 - \bar{x}_3 \ . \tag{15.90}$$

The time derivative of V_2 is given by

$$\dot{V}_2(q) = \dot{q}^T M\ddot{q} + qK_{p,imp}\dot{q} + e_t^T C_t \dot{e}_t \ . \tag{15.91}$$

Injecting $\ddot{q}$ from the dynamic equation gives

$$\dot{V}_2(q) = \dot{q}^T(-K_{p,imp}q - K_{d,imp}\dot{q} + e_t) + qK_{p,imp}\dot{q} + e_t^T C_t \dot{e}_t \ , \tag{15.92}$$

further simplified in

$$\dot{V}_2(q) = -\dot{q}^T K_{d,imp}\dot{q} + \dot{q}e_t + e_t^T C_t \dot{e}_t \ . \tag{15.93}$$

It is possible to cancel the positive term $\dot{q}e_t$ by choosing a suitable $\dot{e}_t$, however the cancellation must account for an new tracking error e_s. Inserting the error gives

$$\dot{e}_t = \dot{e}_{t,des} + e_s \tag{15.94}$$

$$\dot{e}_{t,des} = -C_t^{-1}(\dot{q} - K_t e_t) \ , \tag{15.95}$$

and leads to

$$\dot{V}_2(q) = -\dot{q}^T K_{d,imp}\dot{q} - e_t^T K_t e_t + e_t^T C_t e_s \ . \tag{15.96}$$

Second backstep

To eliminate $e_t^T C_t e_s$ from $\dot{V}_2$ one needs to perform a second time the procedure. Let V_3 be a Lyapunov function including the missing term

$$V_3(q) = \frac{1}{2}\dot{q}^T M\dot{q} + \frac{1}{2}q^T K_{p,imp}q + \frac{1}{2}e_t^T C_t e_t + \frac{1}{2}e_s^T C_s e_s \tag{15.97}$$

The time derivative is

$$\dot{V}_3(q) = \dot{q}^T M\ddot{q} + q^T K_{p,imp}\dot{q} + e_t^T C_t \dot{e}_t + e_s^T C_s \dot{e}_s \tag{15.98}$$

Replacing $\ddot{q}$ and $\dot{e}_t$

$$\dot{V}_3(q) = \dot{q}^T(-K_{p,imp}q - K_{d,imp}\dot{q} + e_t) + q^T K_{p,imp}\dot{q} + e_t^T C_t(-C_t^{-1}(\dot{q} - K_t e_t) + e_s) + e_s^T C_s \dot{e}_s \tag{15.99}$$

Simplified in

$$\dot{V}_3(q) = -K_{d,imp}\dot{q}^2 - e_t^T K_t e_t + e_t^T C_t e_s + e_s^T C_s \dot{e}_s \tag{15.100}$$

It is possible to cancel the positive term $e_t^T C_t e_s$ by choosing a suitable $\dot{e}_s$

$$\dot{e}_s = \ddot{\tau} - \ddot{\tau}_d - \ddot{e}_{t,des} \tag{15.101}$$

Once the torque dynamic equations are placed back in the Lyapunov V_3

$$\dot{V}_3(q) = -K_{d,imp}\dot{q}^2 - e_t^T K_t e_t + e_t^T C_t e_s + e_s^T C_s(\ddot{\tau} - \ddot{\tau}_d - \ddot{e}_{t,des}) \tag{15.102}$$

Substituting $\ddot{\tau}$

$$\dot{V}_3(q) = -K_{d,imp}\dot{q}^2 - e_t^T K_t e_t + e_t^T C_t e_s + e_s^T C_s(KB^{-1}(\tau_m - B\ddot{q} - \tau) - \ddot{\tau}_d - \ddot{e}_{t,des}) \tag{15.103}$$

The control law is selected as

$$\tau_m = B\ddot{q} + \tau + BK^{-1}(\ddot{\tau}_d + \ddot{e}_{t,des} - C_s^{-1}C_t e_t - C_s^{-1}K_s e_s) \ , \tag{15.104}$$

which gives the Lyapunov derivative $\dot{V}_3$

$$\dot{V}_3(q) = -\dot{q}^T K_{d,imp}\dot{q} - e_t^T K_t e_t - e_s^T C_s e_s \ . \tag{15.105}$$

Input expression

The input expression is obtained by recursively replacing the expression of the errors. The final expression is given by

$$\tau_m = B\ddot{q} + \tau + BK^{-1}(\ddot{\tau}_d - C_t^{-1}(q^{(3)} - K_t(\ddot{\tau} - \ddot{\tau}_d)) - C_s^{-1}C_t(\tau - \tau_d) - C_s^{-1}K_s(C_t^{-1}\ddot{q} + (1 - C_t^{-1}K_t)(\dot{\tau} - \dot{\tau}_d))) \ . \tag{15.106}$$

15.5.2 Simulations

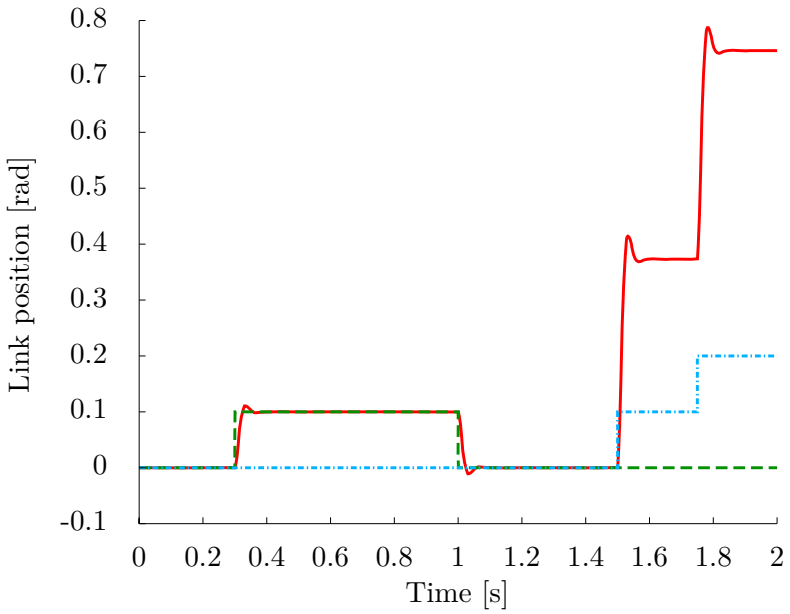

Figure 15.23: The plot depicts the simulated link position, in red/solid and the desired link position, in green/dashed along with the external joint torque, in light blue/dashed-dotted.

In figure 15.23, the results of the backstepping controller simulation are reported. In a first time, a position step is commanded and the link successfully moves to the desired position. In a second time, the desired position is maintained constant and an external torque is applied. As depicted the link is deflected according to the impedance control law.

15.5.3 Experiments

The performance of the backsptepping controller has been tested on a single finger and the results were compared with the ones of the cascaded controller. The finger used is a finger with bearings and steel cables.

Step response and sinus tracking results The figure 15.24 shows the step response for the PIP joint. The step response is an important indicator of the speed and the accuracy of the system which is particularly useful for rapid motions. Figure 15.25 reports the tracking of a sinus, which is a good representation of the motion used in a grasp approach phase.

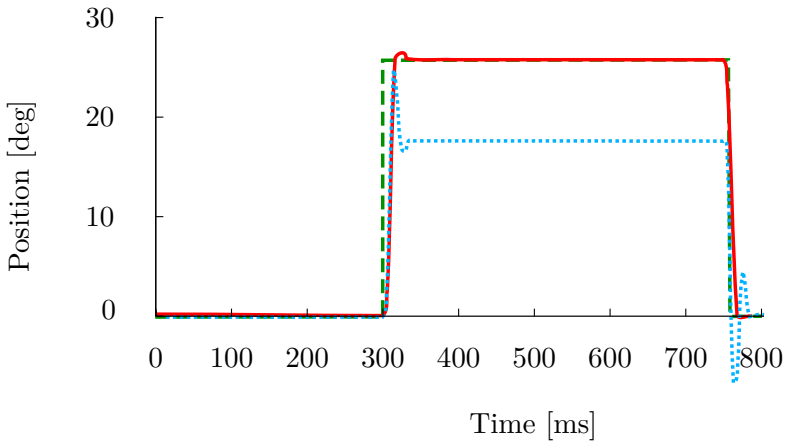

Figure 15.24: Step response for the PIP joint. Pretension forces were set to $f_{int} = 10N$. The green/dashed curve depict the desired position. The solid/red one represents the response with the backstepping controller. The light blue/dotted one shows the response with the cascaded controller.

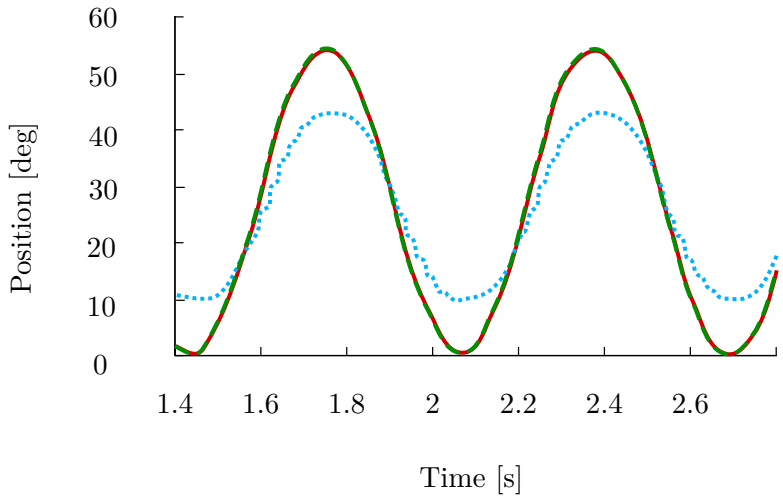

Figure 15.25: Sinus tracking for the PIP joint. The pretension forces are set to $f_{pre} = 15N$. The green/dashed curve depicts the desired position. The red/solid one depicts the response with the backstepping controller. The light blue/dotted one represents the response with the cascaded controller. The vibrations of the light blue/dotted signal are caused by the stick-slip effect.

The backstepping controller shows accuracy and speed that are in the required range for grasping and throwing objects. The cascaded controller is inaccurate because the maximum impedance gain $\boldsymbol{K}_{\mathrm{p,imp}}$ that can be selected without amplifying the sensor noise is significantly lower than in

the case of the backsteppping controller.

Gain diagram A comparison of the gain diagram of the singular perturbation controller of the previous chapter and the antagonistic backstepping is depicted in Fig. 15.26. For each experiment two sets of gains are depicted. One set corresponds to the gain obtained for the positive half sinus and the other one is associated with the negative sinus wave. The backstepping controller results in a unit gain over a longer range of frequency than the singular perturbation controller. It is interesting to note that the singular perturbation controller systematically underestimates the actual link displacement and yields an incorrect sinus amplitude. The singular perturbation controller using the link side position was unable to produce a stiffness comparable to the backstepping controller, therefore, the experiment has been performed with the link position using only the motor positions. It is the reason why the amplitude is incorrect.

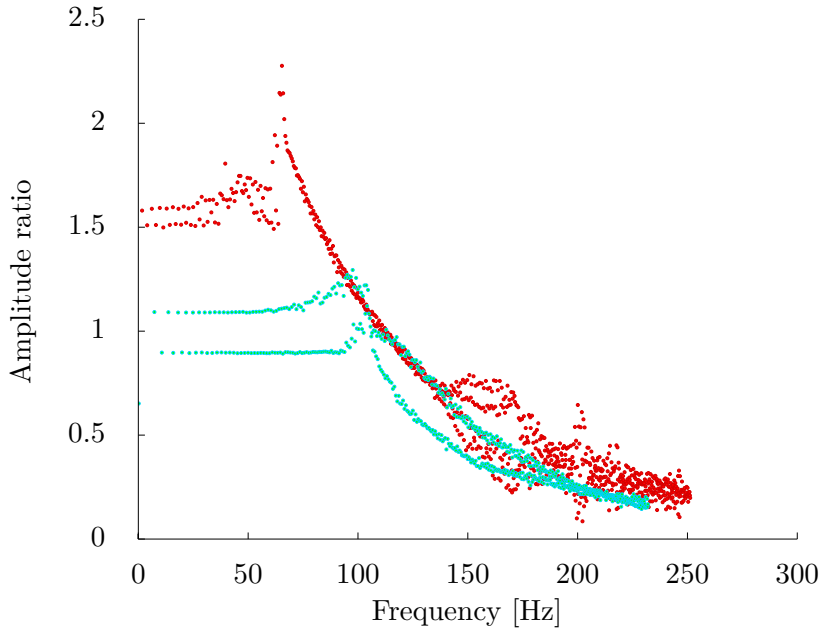

Figure 15.26: Gain diagram for the PIP join controlled by the backstepping controller (indicated by light blue dots) and the singular perturbation controller (red dots). The pretension was set to $f_{pre} = 20N$ for both experiments.

Validation of the impedance behavior The influence of $\boldsymbol{K}_{\mathrm{p,imp}}$ has been tested for the backstepping controller. It is verified experimentally that the antagonistic backstepping controller design is resulting in the expected impedance behavior. More specifically, the stiffness component is verified.

The experiment consists in imposing a joint deflection with a mechanical fixture and compare the torque generated by the measured tendon forces and the desired joint stiffness. The results are reported in Figure 15.27.

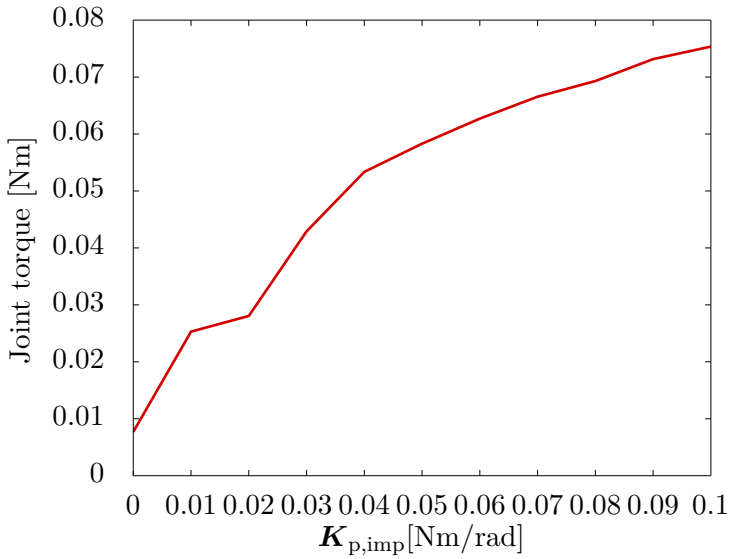

Figure 15.27: The curve depicts the joint torque generated by the tendon forces depending on the desired impedance stiffness. A position error of the joint was imposed externally by a mechanical fixture.

15.5.4 Conclusion

In this section, the backstepping method has been extended to the case of an antagonistic actuation. The extension, based on a very simple sharing of the desired joint torque, allows to derived two symmetric controllers. Dealing with both motor independently allows to avoid dealing with a system of order six. Moreover, because the symmetry is conserved, the pretension of the tendon is naturally introduced as a shifting of the desired working point. The simulations and the experimental results both confirmed that the method sucessfully provides an impedance behavior.

15.6 Conclusion

In this chapter the backstepping method has been applied. It is a nonlinear control method adapted to problems that can be written in a strict feedback form. The chapter first introduced the method on an academic example. Then, the method was applied to a state controller. The state controller was then modified to produce an impedance behavior. Simulations and experiments confirmed the performance of the controller. The controller was

modified to account for the nonlinear spring behavior and it has been shown that only minor modifications are required. The saturation of the motor torque limits the advantage of using a controller that accounts for the plant nonlinearities. Finally, the backstepping controller was extended to the case of the antagonistic actuation. Simulations and experiments confirm that the method is successfully providing a link side impedance behavior. The method is superior to the cascaded case in the sense that it allows to reach higher impedance stiffness and thus better link side positioning accuracy.

It is important to note that the choice of the gains to obtain the desired behavior is a challenge. In the presented experiments and simulations the gains have initially been selected to be close to the gains of the cascaded control. The gains were then tuned manually, which is a slow and imprecise method, until the behavior was satisfactory. This tuning method is very tedious for a full hand. Therefore, a systematic method to select and adjust the gains is investigated in the next chapter.

16 Optimal backstepping

In the previous chapters it has been demonstrated that the backstepping method can be applied to the antagonistic joint of the Awiwi Hand. The backstepping method has many advantages over the linear control methods. It provides a solid theoretical framework that smoothly includes the motor and link dynamics. The usual drawbacks of the method, that are the complexity due to the explosion of terms and the need for high derivatives are manageable in the case of a flexible joint. Nonetheless, the selection of the gains is the next main challenge. Indeed, although the theory guarantees stability for any positive definite gains, it is clear that some limits are imposed by the hardware. Choosing and tuning the gains by hand for the 38 tendons of is possible but tedious. Therefore, in this chapter, a method is developed that allows to automatically select the gains for the two lower levels of the backstepping controller. The two upper gains, namely the stiffness and the damping of the impedance controller are directly specified by the user. It is *reasonable* to imagine that if gains of the backstepping are leading to a state feedback set of gains that are close to the ones of an optimal linear controller, it will itself be close to *optimal*. It is important to note that the purpose of the method is not to reach optimality but rather to propose an automated method to select the gains. The method consists in performing the following steps:

- derive the equation of a backstepping controller
- transform the control law into a state feedback form
- establish and solve a linear optimal problem, e. g. with an ARE solver.
- compute the backstepping gains that minimize the distance between the state feedback gains and the optimal gains (according to some norm).

The chapter is organized as follows. First, the equations of the backstepping controller are expanded into a state feedback by using the dynamic relationship between link acceleration and joint torque. In the second section, the idea of optimality is explained and the resulting nonlinear problem is stated. The third section proposes a numerical method to find a possible solution to the problem. Finally, the fourth section reports the results of several simulations and the experimental results obtained on one finger.

16.1 State-feedback transformation

The backtepping control law u, derived in the section 15.3, can be expressed as a state feedback by

$$u = \boldsymbol{K}_{\text{bs}}\boldsymbol{x} \ , \tag{16.1}$$

where $\boldsymbol{x} \in \mathbb{R}^4$ is a state vector defined by

$$\boldsymbol{x} = \left[q, \dot{q}, \theta, \dot{\theta}\right] \tag{16.2}$$

and $\boldsymbol{K}_{\text{bs}} \in \mathbb{R}^4$ is a gain vector defined by

$$\boldsymbol{K}_{\text{bs}} = \begin{bmatrix} 0.0033K_4K_3K_{\text{p,imp}} + 0.0033K_{\text{p,imp}} \\ 0.0033K_3K_{\text{p,imp}} + 0.0033K_4(K_3K_{\text{d,imp}} + K_{\text{p,imp}} + 1) + 0.0033K_{\text{d,imp}} \\ 7400 + 0.0033K_4(K_3 + 1400000K_{\text{d,imp}}) + 4600K_3K_{\text{d,imp}} + 4600K_{\text{p,imp}} \\ 0.0033K_4 + 4600K_{\text{d,imp}} + 0.0033K_3 \end{bmatrix} . \tag{16.3}$$

The vector defined in (16.3) is made of a nonlinear combination of the backstepping controller gains. Therefore, there exists a selection of the backstepping gains that are resulting in a state-feedback vector close to the one obtained with the optimal approach.

16.2 Optimal problem formulation

Formally, the problem consists in choosing a set of control gains, $\boldsymbol{\Omega} = [K_{\text{p,imp}}, K_{\text{d,imp}}, K_3, K_4]$ that results in state feedback gains close to the gains obtained by an optimal linear approach. That is

$$\min_{\boldsymbol{\Omega}}(\|\boldsymbol{K}_{\text{bs}}(\boldsymbol{\Omega}) - \boldsymbol{K}_{\text{opt}}\|) \quad \text{with} \quad \boldsymbol{\Omega} > \boldsymbol{0} \ , \tag{16.4}$$

where $\boldsymbol{K}_{\text{opt}} \in \mathbb{R}^4$ are the feedback gains obtained by solving the ARE (cf. chapter 13). The condition $\boldsymbol{\Omega} > \boldsymbol{0}$ is required by the backstepping controller in order to guarantee stability.

16.3 Solution

Since the objective is to find initial gains offline, the speed of the method is not an important requirement. Similarly, the convergence of the method, that is whether the algorithm yields an answer or not, does not need to be guaranteed. Consequently, a Monte-Carlo algorithm can be used to find a solution. The code is reported in the pseudo-code 3. The code is not written for efficiency and many refinements are possible such as simulated annealing or particle filtering. Nonetheless, the solution stabilizes if a sufficiently large number of iterations is allowed. For a use online, it is possible to tabulate

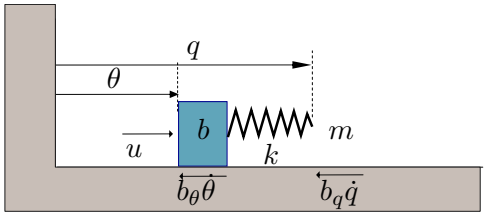

Figure 16.1: Simulation model for a flexible joint with linear springs

the results and use a few iterations of a gradient search algorithm to tune the gains. Alternatively, a closed-form solution may exist and could be used together with an ARE solver to obtain a purely online implementation.

Algorithm 3 Gains selection algorithm

% N: number of samples
% $\boldsymbol{\Omega}_{\text{des}}$: desired gains obtained by the ARE
% C: cost at the current point

$C_{\text{best}} \leftarrow +\inf$
$\boldsymbol{\Omega}_{\text{best}} \leftarrow +\inf$
for $i = 0$ to $\text{N} - 1$ **do**
  $\boldsymbol{\Omega} = \text{rand}(1, 4)$
  $\boldsymbol{K}_{\text{bs}}, C \leftarrow \text{sfkfun}(\boldsymbol{\Omega})$
  if $C < C_{\text{best}}$ **then**
    $C_{\text{best}} \leftarrow C$
    $\boldsymbol{\Omega}_{\text{best}} \leftarrow \boldsymbol{K}_{\text{bs}}$
  end if
end for

---

function sfkfun($\boldsymbol{\Omega}$)
% returns the equivalent state fedback gains and the distance to the desired gains
  return $\boldsymbol{K}_{\text{bs}}$, C
end function

16.4 Simulation

The simulation is performed on a single joint with linear stiffness. The parameters are reported in Table 16.1.

The simulation consists in computing several sets of gains using the algorithm and observing if the resulting behavior is correct. In Figure 16.2, 5 simulations are gathered. For each of the simulation, the same cost matrices

Table 16.1: Numerical values for the simulations

Symbol	Value
M	$7.2 \cdot 10^{-7}$
Bm	$2 \cdot 10^{-7} \cdot ratio \cdot ratio$
K	0.605
K_{des}	$[-7.7018, -3.8384, -3.8384, -0.0100]$
A	$\begin{bmatrix} 0,1,0,0 \\ 0,0,M^{-1},0 \\ 0,0,0,1 \\ 0,0,0,0 \end{bmatrix}$
B	$[0;0;0;K/B_{\text{m}}]$
Q	$\begin{bmatrix} 100 & 0 & 0 & 0 \\ 0 & 0.01 & 0 & 0 \\ 0 & 0 & 0.01 & 0 \\ 0 & 0 & 0 & 0.01 \end{bmatrix}$
R	0.1

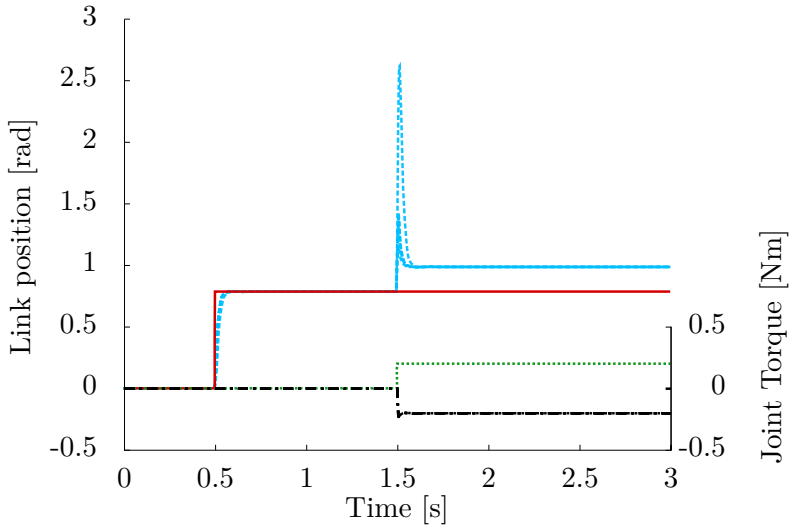

Figure 16.2: Simulations: joint behavior for different samples of gains. The desired link position is depicted in red/solid and the measured joint position in light blue/dashed. The external joint torque is traced in green/dotted and the joint torque is represented in black/dashed-dotted.

are given to the ARE solver. The ARE solver returns a vector of state feedback gains and the Monte-Carlos optimizer computes the best set of backstepping gains. Then, the simulation of the backstepping controller is executed with the gains and the resulting trajectories are stored. Because of its stochastic nature, the gain vectors are always different, nonetheless the behavior of the link is very similar for all generated gain sets. The simulation proves that it is possible to select the gains of the backstepping controller based on the gains given by an optimal control approach.

16.5 Experiments

In order to evaluate the method experimentally two main challenges are to be tackled. First, the ARE solver must be replaced by a SDRE solver, that is the optimal gains must be computed online. Secondly, the Monte-Carlo optimizer must be modified in order to yield the gains online and without any convergence issues. The various approaches to solve the challenges and their in-depth analysis are too long to be reported in this work and only the most simple approach is reported. It is an approximative method that aims at demonstrating the applicability of the method on a real setup.

It has been shown in the SDRE chapter, i. e. in Chapter 14, that the joint stiffness only changes significantly if a load is applied, therefore, the ARE equation can be solved offline if interaction with the finger are prohibited. Moreover, because the backstepping structure does not depend on the linearity of the problem, the optimizer can also be executed offline. The link trajectories obtained for ten distinct experiments are reported in Figure 16.3. The experimental data is reported in Table 16.2. The experiments reveal that the method yields acceptable gains. Small differences can be seen between the trajectories but they are minimal. One of the trajectory is clearly distinct which shows that the optimizer did not find a good solution.

16.6 Discussion

This chapter presented an algorithm used to select the gain matrices of the backstepping controller. The main purpose of the method is not to build an optimal controller but rather to allow for a systematic tuning of the controller. It is shown that the method can be used to automatically select the gains that are leading to a good performance. Further work could consists in evaluating the performance of the resulting controller w. r. t. a nonlinear optimal controller.

Table 16.2: Numerical values for the experiments

Symbol	Value
M	$7.2 \cdot 10^{-7}$
Bm	$2 \cdot 10^{-7} \cdot ratio \cdot ratio$
K	0.605
K_{des}	$[-7.7018, -3.8384, -3.8384, -0.0100]$
A	$\begin{bmatrix} 0,1,0,0 \\ 0,0,M^{-1},0 \\ 0,0,0,1 \\ 0,0,0,0 \end{bmatrix}$
B	$[0;0;0;K/B_{\text{m}}]$
Q	$\begin{bmatrix} 100 & 0 & 0 & 0 \\ 0 & 0.01 & 0 & 0 \\ 0 & 0 & 0.01 & 0 \\ 0 & 0 & 0 & 0.01 \end{bmatrix}$
R	0.1

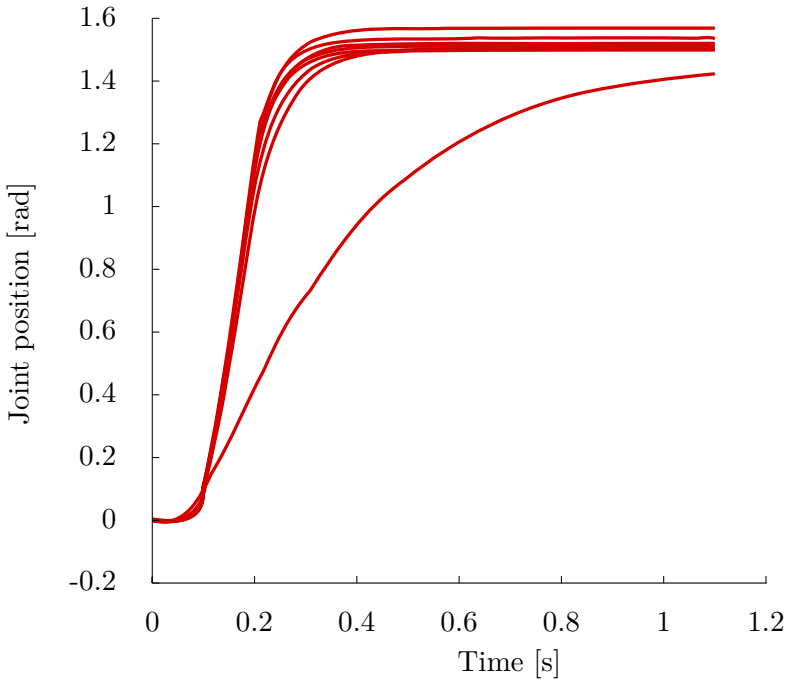

Figure 16.3: Experiments: joint behavior for different samples of gains. The measured joint position are reported.

Part III

Conclusion

Conclusion

In this thesis, the modeling and the control of a complex and novel hand has been presented. The system is unique in terms of complexity as well as in structure. Indeed, the 19 joints of the hand are driven by 38 motors and 38 nonlinearly flexible tendons.

The modeling followed an incremental approach and, starting with the motor modeling, provided a comprehensive and complete model of the system. Each phase of the modeling was verified with simulations and experiments since the models established are the basis for the future work on the system. The specificities of antagonistically tendon driven systems have been presented in details and the required mathematical formalism has been introduced. An important step was the derivation of the coupling matrices, that are a fundamental element of tendon driven system. Indeed, they allow to transform the quantities, such as the stiffness, the torques and the positions, from joint space to tendon space. The knowledge of the link position is paramount to implement most controller. However, in the Awiwi does not provide a link side position sensor, which is one of the key elements for its robustness, thus the finger configuration must be reconstructed from the tendon displacements. The estimation of the link side position in case of the thumb revealled to be particularily challenging and several optimization approaches have been proposed and discussed. An implementation of the link estimation for the thumb has been reported and experimental results confirmed the applicability of the method. The final modeling step consisted in computing a forward kinematic model for the wirst. Indeed, the paths of the tendon are modified by the wrist motions and a compensation scheme is required. The proposed method was verified by comparing simulations and measurements.

The control part aimed at identifying a suitable control approach for the finger. In a first step, a motor controller was designed that improves the velocity tracking performance. Following a bottom-up approach, a tendon

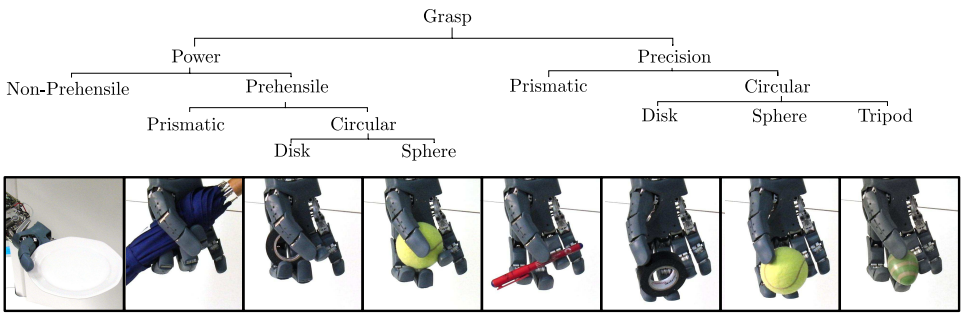

Figure 16.4: Grasp taxonomy

force controller was designed. However, since the plant is nonlinear, a linearization of the system by feedback was proposed and implemented. The improvement of the step response demonstrated the superiority of a nonlinear controller w. r. t. a linear controller. The next logical step consisted in combining two tendon controllers in order to achieve a joint controller. A first analysis, based on the singular perturbation argument, demonstrated that an joint impedance controller could be constructed. However, the time scale argument depends on the joint stiffness and experiments confirmed that the gain tuning was challenging. A cascaded system analysis removed the need for a time scale separation assumption. The tuning of the controller gains is really tedious for a system such as the Awiwi hand since each of the fingers is different. Therefore, an optimal control approach was proposed in order to simplify the choice of the gains. The approach simplifies the choice of the gains and an extension to the case of a nonlinear plant, known as the SDRE, was proposed. Unfortunately, the method did not guarantee global stability. The second half of the control part focuses on nonlinear control methods. There exist a large number of nonlinear control methods but only a subset is applicable case of a flexible joint. This work focused on one specific method: the integrator backstepping approach. The control method had to be modified twice. First, it had to be adapted to the case of an antagonistic actuation. Second, it was adapted in order to yield an impedance control of the joints. The superiority of the method was demonstrated in experimentally and in simulation. The method guarantees global asymptotic stability and was implemented on the complete hand. The performance of the controller is very satisfying and it is used daily on the platform to support research on grasping. Similar to other method, the tuning of such a controller is tedious. Therefore, the last chapter of the control part proposed an automated gain selection method for the backstepping gain design. The method was implemented and its effectiveness was demonstrated. The control part demonstrated that nonlinear control theory can be successfully applied to the Awiwi hand. It results in a high performance control of the hand. The work reported in the thesis focused on a single joint such that the controller could be compared but it has been systematically applied to the 19 joints of the hand. The controllers have been used to verify the capabilities of the hand in terms of grasping as depicted in Fig. 16.4.

The models and controllers developped in this thesis are a very first layer upon which research in grasping and manipulation can be build. The high performance of the control allows to implement new approaches that were not available on other platforms. For example, the influence of the choice of the mechanical stiffness on the grasp stability.

I am proud to say that the complete Hand Arm System, used as a leading research platform for dexterous manipulation is currently using the models and the controllers created in this work.

Bibliography

[1] M. Grebenstein, A. Albu-Schäffer, T. Bahls, M. Chalon, O. Eiberger, W. Friedl, R. Gruber, U. Hagn, R. Haslinger, H. Höppner, S. Jörg, M. Nickl, A. Nothhelfer, F. Petit, J. Reill, N. Seitz, T. Wimböck, S. Wolf, T. Wüsthoff, and G. Hirzinger, "The DLR Hand Arm System," *Robotics and Automation, IEEE International Conference on*, vol. 1, pp. 3175 – 3182, 2011.

[2] F. Petit, M. Chalon, W. Friedl, M. Grebenstein, A. A. Schäffer, and G. Hirzinger, "Bidirectional antagonistic variable stiffness actuation: Analysis, design & implementation," *Robotics and Automation, IEEE International Conference on*, pp. 4189–4196, 2010.

[3] W. Friedl, J. Reinecke, M. Chalon, and G. Hirzinger, "FAS A Flexible Antagonistic Spring element for a high performance tendon driven hand," *Intelligent Robots and Systems, IEEE International Conference on*, vol. 1, pp. 1366 – 1372, 2011.

[4] P. Herman and K. Kozlowski, "Some properties of dynamic equations of motion in terms of the eigenfactor quasi-coordinate velocity vector," *Intelligent Robots and Systems, IEEE International Conference on*, vol. 2, pp. 1924–1929, 2002.

[5] S. Wolf and G. Hirzinger, "A New Variable Stiffness Design: Matching Requirements of the Next Robot Generation," *Robotics and Automation, IEEE International Conference on*, vol. 1, pp. 1741 – 1746, 2008.

[6] M. Okada, S. Ban, and Y. Nakamura, "Skill of compliance with controlled charging/discharging of kinetic energy," *Robotics and Automation, IEEE International Conference on*, vol. 3, pp. 2455–2460, 2002.

[7] O. Eiberger, S. Haddadin, M. Weis, A. Albu-Schäffer, and G. Hirzinger, "On joint design with intrinsic variable compliance: derivation of the DLR QA-Joint," *Robotics and Automation, IEEE International Conference on*, vol. 1, pp. 1687–1694, 2010.

[8] H. Schempf, C. Kraeuter, and M. Blackwell, "ROBOLEG: A robotic soccer-ball kicking leg," *Robotics and Automation, IEEE International Conference on*, vol. 1, pp. 1314–1318, 1995.

[9] S. Haddadin, A. Albu-Schäffer, O. Eiberger, and G. Hirzinger, "New insights concerning intrinsic joint elasticity for safety," *Intelligent Robots and Systems, IEEE International Conference on*, vol. 1, pp. 2181–2187, 2010.

[10] D. Paluska and H. Herr, "The effect of series elasticity on actuator power and work output:implications for robotic and prosthetic joint design," *Robotics and Autonomous Systems*, vol. 1, pp. 667–673, 2006.

[11] Y. Sakagami, R. Watanabe, C. Aoyama, S. Matsunaga, N. Higaki, and K. Fujimura, "The intelligent ASIMO: System overview and integration," *Intelligent Robots and Systems, IEEE International Conference on*, vol. 3, pp. 2478–2483, 2002.

[12] K. Kaneko, F. Kanehiro, S. Kajita, K. Yokoyama, K. Akachi, T. Kawasaki, S. Ota, and T. Isozumi, "Design of prototype humanoid robotics platform for HRP," *Intelligent Robots and Systems, IEEE International Conference on*, vol. 3, pp. 2431–2436, 2002.

[13] M. Kaneko and N. Imamaura, "Development of a tendon-driven finger with single pulley-type TDT sensors," *Intelligent Robots and Systems, IEEE International Conference on*, vol. 1, pp. 752–757, 1991.

[14] M. A. Diftler, R. O. Ambrose, S. M. Goza, K. Tyree, and E. Huber, "Robonaut Mobile Autonomy: Initial Experiments," *Robotics and Automation, IEEE International Conference on*, pp. 1437 – 1442, April 2005.

[15] T. Morita, H. Iwata, and S. Sugano, "Development of human symbiotic robot: Wendy," *Robotics and Automation, IEEE International Conference on*, pp. 3183–3188, 1999.

[16] H. Iwata and S. Sugano, "Design of human symbiotic robot TWENDY-ONE," *Robotics and Automation, IEEE International Conference on*, vol. 1, pp. 580–586, 2009.

[17] S. Jacobsen, J. Wood, D. Knutti, and K. Biggers, "UTAH/MIT Dextroushand - Work in Progress," *Robotics Research, International Journal of*, vol. 3, no. 4, pp. 21–50, 1984.

[18] H. Kobayashi, K. Hyodo, and D. Ogane, "On tendon-driven robotic mechanisms with redundant tendons," *International Journal of Robotic Research*, vol. 17, no. 4, pp. 561–571, 1998.

[19] J. Salisbury and M. T. Mason, "Robot hands and the mechanics of manipulation," *MIT Press*, vol. 2, pp. 59–59, 1985.

[20] F. Lotti and G. Vassura, "A novel approach to mechanical design of articulated fingers for robotic hands," *Robotics and Automation, IEEE International Conference on*, vol. 2, pp. 1687 – 1692, 2002.

[21] F. Lotti, P. Tiezzi, G. Vassura, L. Biagiotti, G. Palli, and C. Melchiorri, "Development of UB Hand 3: Early Results," *Robotics and*

Automation, IEEE International Conference on, vol. 4488 - 4493, p. 1, 2005.

[22] J. Butterfass, M. Grebenstein, H. Liu, and G. Hirzinger, "DLR-Hand II: Next generation of a dextrous robot hand," *Robotics and Automation, IEEE International Conference on*, vol. 1, pp. 109–114, 2001.

[23] M. Chalon and al., "Robotic Components for Space ROKVISS and DEXHAND," *Invited session, Robotics and Automation, IEEE International Conference on*, vol. 1, 2011.

[24] A. Wedler, M. Chalon, and al., "DLRs space qualifiable multi-fingered DEXHAND," in *ASTRA*, 2011.

[25] I. Mizuuchi, R. Tajima, T. Yoshikai, D. Sato, K. Nagashima, M. Inaba, Y. Kuniyoshi, and H. Inoue, "The design and control of the flexible spine of a fully tendon-driven humanoid "kenta"," *Intelligent Robots and Systems, IEEE International Conference on*, vol. 3, pp. 2527 – 2532, 2002.

[26] I. Mizuuchi, Y. Nakanishi, Y. Sodeyama, Y. Namiki, T. Nishino, N. Muramatsu, J. Urata, K. Hongo, T. Yoshikai, and M. Inaba, "An Advanced Musculoskeletal Humanoid Kojiro," *Humanoid Robots, International Conference on*, vol. 1, pp. 294 – 299, 2007.

[27] P. Dario, S. Micera, A. Menciassi, M. Carrozza, M. Zecca, T. Steiglitz, T. Oses, X. Navarro, and D. Ceballos, "CYBERHAND - a consortium project for enhanced control of powered artificial hands based on direct neural interfaces"," *33rd Neural Prosthesis Workshop*, 2002, bethesda, MD, USA.

[28] Ottobock. [Online]. Available: www.ottobock.com

[29] L. Chang and Y. Matsuoka, "A kinematic thumb model for the ACT hand," *Robotics and Automation, IEEE International Conference on*, vol. 1, pp. 1000–1005, 2006.

[30] P. Tuffield and H. Elias, "The Shadow robot mimics human actions," *Industrial Robot*, vol. 30, no. 1, pp. 56–60, 2003.

[31] S. R. C. Limited, "Shadow dextrous hand product specification," Shadow Robot Company Limited, Tech. Rep., February 2004.

[32] D. Guirintano, A. Hollister, W. Buford, D. Thompson, and L. Myers, "A virtual five-link model of the thumb," *Medical Engineering and Physics*, vol. 17, pp. 297–303, 1995.

[33] V. J. Santos and F. J. Valero-Cuevas, "Stochastic analysis of anatomical data suggests three characteristic types of thumb kinematics," in *Summer Bioengineering Conference*, Florida, June 25-29 2003.

[34] V. J.Santos and F. J.Valero-Cuevas, "Reported anatomical variability naturally leads to multimodal distributions of Denavit-Hartenberg parameters for the human thumb," *Biomedical Engineering, IEEE Transactions on*, vol. 53, pp. 155–163, February 2006.

[35] T. Yoshikawa, *Foundation on Robotics : Analysis and Control*. The MIT Press, 1990.

[36] M. T. Rosenstein and R. A. Grupen, "Velocity-dependent dynamic manipulability," *Robotics and Automation, IEEE International Conference on*, vol. 3, pp. 2424–2429, 2002, department of Computer Science University of Massachusetts Amherst, MA 01003 USA mtr@cs.umass.edu, grupen@cs.umass.edu.

[37] M. Raibert and J. Craig, "Hybrid position/force control of manipulators," *ASME Journal of Dynamical Systems, Measurement and Control*, vol. 105, pp. 126–133, 1981.

[38] S. Arimoto, J.-H. Bae, and K. Tahara, "Stability on a manifold: Simultaneous realization of grasp and orientation control of an object by a pair of robot fingers," *Robotics and Automation, IEEE International Conference on*, vol. 2, pp. 2336–2343, 2003.

[39] A. T. Miller and P. K. Allen, "Examples of 3D Grasp Quality Computations," *Robotics and Automation, IEEE International Conference on*, vol. 1, pp. 1240–1246, 1999.

[40] R. Diankov, "Automated construction of robotic manipulation programs," Ph.D. dissertation, Carnegie Mellon University, Robotics Institute, August 2010.

[41] M. Chalon, T. Wimböck, and G. Hirzinger, "Torque and stiffness workspace analysis for flexible tendon mechanisms," *Robotics and Automation, IEEE International Conference on*, 2010.

[42] M. Grebenstein, M. Chalon, G. Hirzinger, and R. Siegwart, "Antagonistically driven finger design for the anthropomorphic DLR hand arm system," *Humanoid Robots, IEEE International Conference on*, vol. 1, pp. 609–616, 2010.

[43] F. Laurin-Kovitz, K. Colgate, J. Carnes, and D. Steven, "Design of components for programmable passive impedance," *Robotics and Automation, IEEE International Conference on*, vol. 2, pp. 1476–1481, 1991.

[44] C. English and D. Russell, "Implementation of variable joint stiffness through antagonistic actuation using rolamite springs," *Mechanism and Machine Theory*, vol. 34, no. 1, pp. 27–40, 1999.

[45] S. A. Migliore, E. A. Brown, and S. P. DeWeerth, "Biologically inspired joint stiffness control," *Robotics and Automation, IEEE International Conference on*, pp. 4508 – 4513, 2005.

[46] B. Vanderborght, B. Verrelst, R. V. Ham, M. V. Damme, D. Lefeber, B. M. Y. Duran, and P. Beyl, "Exploiting natural dynamics to reduce energy consumption by controlling the compliance of soft actuators," *Robotic Research, International Journal of*, vol. 25, no. 4, pp. 343–358, 2006.

[47] G.Palli, C.Melchiorri, T.Wimböck, M.Grebenstein, and G. Hirzinger, "Feedback linearization and simultaneous-position control of robot with antagonistic actuated joints," *Robotics and Automation, IEEE International Conference on*, vol. 1, pp. 4367 – 4372, 2007.

[48] S. Wolf, O. Eiberger, and G. Hirzinger, "The DLR FSJ: energy based design of a variable stiffness joint," *Robotics and Automation, IEEE International Conference on*, vol. 1, pp. 5082 – 5089, 2011.

[49] R. Schiavi, G. Grioli, S. Sen, and A. Bicchi, "VSA-II: a novel prototype of variable stiffness actuator for safe and performing robots interacting with humans," *Robotics and Automation, IEEE International Conference on*, vol. 1, pp. 2171–2176, 2008.

[50] R. M. Murray, Z. Li, and S. S. Sastry, *A Mathematical Introduction to Robotic Manipulation*. CRC Press, 1994.

[51] M. U. Iu and H. D. Gazimagusa, "Kinematic analysis of tendon-driven robotic mechanisms using oriented graphs," *Acta mechanica*, vol. 3-4, no. 182, pp. 265–277, 2006.

[52] A. Albu-Schäffer, M. Fischer, G. Schreiber, F. Schoeppe, and G. Hirzinger, "Soft robotics: What cartesian stiffness can we obtain with passively compliant, uncoupled joints?" *Intelligent Robots and Systems, IEEE International Conference on*, vol. 1, pp. 3295–3301, 2004.

[53] T. Wimböck, C. Ott, A. Albu-Schäffer, and G. Hirzinger, "Impedance control for variable stiffness mechanisms with nonlinear joint coupling," *Intelligent Robots and Systems, IEEE International Conference on*, vol. 1, pp. 3796–3803, 2008.

[54] T. Wimböck, C. Ott, A. Albu-Schäffer, and G. H. A. Kugi, "Impedance control for variable stiffness mechanisms with nonlinear joint coupling," *Intelligent Robots and Systems, IEEE International Conference on*, vol. 1, pp. 3796–3803, 2008.

[55] J. Reinecke, "Joint impedance control of a stiffness adjustable tendon driven anthropomorphic hand," Master's thesis, Technische Universitẗ Dresden, 2012.

[56] A. Albu-Schäffer and G. Hirzinger, "Parameter identification and passivity based joint control for a 7dof torque controlled light weight robot," *Robotics and Automation, IEEE International Conference on*, vol. 1, pp. 1087–1093, 2001.

[57] H. Olsson, K. Astroemand, C. C. de Wit, M. Gaefvert, and P. Lischinsky, "Friction models and friction compensation," 1997.

[58] L. L. Tien, A. Albu-Schäffer, A. D. Luca, and G. Hirzinger, "Friction observer and compensation for control of robots with joint torque measurement," *Intelligent Robots and Systems, IEEE International Conference on*, vol. 1, pp. 3789–3795, 2008.

[59] A. Serio, G. Grioli, I. Sardellitti, N. Tsagarakis, and A. Bicchi, "A decoupled impedance observer for a variable stiffness robot," *Robotics and Automation, IEEE International Conference on*, vol. 1, pp. 5548 – 5553, 2011.

[60] S. Nicosia and P. Tomei, "A global output feedback controller for flexible joint robots," *Automatica*, vol. 31, no. 10, pp. 1465–1469, 1995.

[61] L. Zollo, A. D. Luca, and B. Siciliano, "Regulation with on-line gravity compensation for robots with elastic joints," *Robotics and Automation, IEEE International Conference on*, vol. 3, pp. 2687–2692, 2004.

[62] P. Tomei, "A simple PD controller for robots with elastic joints," *Automatic Control, IEEE Transactions on*, vol. 35, pp. 1208–1213, 1991.

[63] S. Nicosia and P. Tomei, "Design of global tracking controllers for flexible-joint robots," *Journal of Robotic Systems*, vol. 10, no. 6, pp. 835–846, 1993.

[64] A. De Luca and P. Tomei, *Theory of Robot Control*. Springer-Verlag, London, 1996, ch. Elastic Joints, pp. 179–218.

[65] A. Albu-Schäffer and G. Hirzinger, "A globally stable state-feedback controller for flexible joint robots," *Journal of Advanced Robotics, Special Issue: Selected Papers from IROS 2000*, vol. 15, no. 8, pp. 799–814, 2001.

[66] A. Albu-Schäffer, "Regelung von robotern mit elastischen gelenken am beispiel der dlr-leichtbauarme," Ph.D. dissertation, Technische Universität München, 2001.

[67] C. Ott, A. Albu-Schäffer, and G. Hirzinger, "A cartesian compliance controller for a flexible-structure mounted manipulator," *Intelligent Robots and Systems, IEEE International Conference on*, vol. 1, pp. 4502 – 4508, 2006.

[68] C. Ott, "Cartesian impedance control of flexible joint manipulators," Ph.D. dissertation, Saarland University, 2005.

[69] V. Santibanez and R. Kelly, "Energy shaping based controllers for rigid and elastic joint robots: Analysis via passivity theorems," *Robotics and Automation, IEEE International Conference on*, pp. 2225–2231, 1997.

[70] R. Kelly and V. Santibanez, "Global regulation of elastic joint robots based on energy shaping," *IEEE Transactions on Automatic Control*, vol. 43, no. 10, pp. 1451–1456, 1998.

[71] A. van der Schaft, *L_2-Gain and Passivity Techniques in Nonlinear Control*, 2nd ed. Springer-Verlag, 2000.

[72] S. Stramigioli, C. Secchi, A. van der Schaft, and C. Fantuzzi, "Sampled data systems passivity and discrete port-hamiltonian systems," *IEEE Transactions on Robotics and Automation*, vol. 21, pp. 574–587, 2005.

[73] ——, "A novel theory for sample data system passivity," *Intelligent Robots and Systems, IEEE International Conference on*, vol. 2, pp. 1936–1941, 2002.

[74] T. Wimböck, Ch. Ott, and G. Hirzinger, "Passivity-based object-level impedance control for a multifingered hand," *Intelligent Robots and Systems, IEEE International Conference on*, vol. 1, pp. 4621–4627, 2006.

[75] G. Niemeyer and J.-J. E. Slotine, "Telemanipulation with time delays," *International Journal of Robotic Research*, vol. 23, no. 9, pp. 873–890, 2004.

[76] R. Ortega, A. J. van der Schaft, B. Maschke, and G. Escobar, "Interconnection and damping assignment passivity-based control of port-controlled hamiltonian systems," *Automatica*, vol. 38, no. 4, pp. 585–596, 2002.

[77] F. Petit, A. Albu-Schäffer, and G. Hirzinger, "Cartesian impedance control of a stiffness adjustable arm," *Intelligent Robots and Systems, IEEE International Conference on*, vol. 1, pp. 4180 – 4186, 2011.

[78] F. Caccavale, B. Siciliano, and L. Villani, "Robot impedance control with nondiagonal stiffness," *Automatic Control, IEEE Transactions on*, vol. 44, no. 10, pp. 1943–1946, october 1999.

[79] M. Abdallah, , U. Warren, MI, R. Platt, B. Hargrave, and F. Permenter, "Position control of tendon-driven fingers," *Robotics and Automation, IEEE International Conference on*, vol. 1, pp. 2859 – 2864, 2012.

[80] M. E. Abdallah, R. Platt, C. W. Wampler, and B. Hargrave, "Applied joint-space torque and stiffness control of tendon-driven fingers," *Humanoid Robots, IEEE International Conference on*, vol. 1, pp. 74–79, 2010.

[81] R. Platt, M. Abdallah, C. Wampler, and B. Hargrave, "Joint-space torque and stiffness control of tendon-driven manipulators," *Intelligent Robots and Systems, IEEE International Conference on*, vol. 1, pp. 74–79, 2010.

[82] S. Jacobsen, H. Ko, E. Iversen, and C. Davis, "Antagonistic control of a tendon driven manipulator," *Robotics and Automation, IEEE International Conference on*, 1989.

[83] G. Palli, "Model and control of tendon actuated robots," Ph.D. dissertation, DEIS, University of Bologna, 2007.

[84] H. K. Khalil, *Nonlinear Systems*, 3rd ed. Prentice Hall, 2002.

[85] J. Oh and J. Lee, "Control of flexible joint robot system by backstepping design approach," *Robotics and Automation, IEEE International Conference on*, pp. 3435–3440, 1997.

[86] L. Pontryagin, V. Boltyanskii, R. V. Gamkrelidze, and E. F. Mishchenko, *The Mathematical Theory of Optimal Processes*. Gordon and Breach Science Publisher, 1962.

[87] R. Bellman and S. Dreyfus, *An application of dynamic programming to the determination of optimal satellite trajectories.* J. Brit.Interplanet., 1959, vol. 17.

[88] D. J. Braun, M. Howard, and S. Vijayakumar, "Exploiting variable stiffness in explosive movement tasks," *Robotics: Science and System*, vol. 1, pp. 25–32, June 2011.

[89] J. Pearson, "Approximation methods in optimal control." *Electronics and Control, Journal of*, vol. 13, pp. 453–469, 1962.

[90] A. Wernli and G. Cook., "Suboptimal control for the nonlinear quadratic regulator problem." *Automatica*, vol. 11, pp. 75–84, 1975.

[91] J. Cloutier and J. Cockburn, "The state-dependent nonlinear regulator with state constraints," *Proc. of the American Control Conference*, vol. 1, pp. 390–395, 2001.

[92] C. D. Cloutier, J.R. and C. Mracek, "Nonlinear regulation and nonlinear hinf control via the state-dependent riccati equation technique: Part 1, theory; part 2, examples." *Proc. of the First International Conference on Nonlinear Problems in Aviation and Aerospace*, vol. 1, pp. 117–141, 1996.

[93] J. Cloutier and D. Stansbery, "All-aspect acceleration-limited homing guidance." in *Proc. of the AIAA Guidance, Navigation, and Control Conference*, 1999.

[94] ——, "Control of a continuously stirred tank reactor using an asymmetric solution of the state-dependent riccati equation." *Control Applications, IEEE Conference on*, vol. 1, pp. 893–898, 1999.

[95] J. Cloutier and P. Zipfel, "Hypersonic guidance via the state-dependent riccati equation control method." *Control Applications, IEEE Conference on*, vol. 1, pp. 219–224, 1999.

[96] J. S. Shamma and J. R. Cloutier, "Existence of sdre stabilizing feedback," *Automatic Control, IEEE Transactions on*, vol. 48, pp. 513 – 517, 3 september 2002.

[97] T. Cimen, "State-Dependent Riccati Equation (SDRE) Control: A Survey," *Automatic Control, The International Federation of*, vol. 1, pp. 3761–3775, July 2008.

[98] M. Grebenstein, M. Chalon, G. Hirzinger, and R. Siegwart, "A method for hand kinematics designers 7 billion perfect hands," in *ICABB*, 2010.

[99] M. W.Spong, S. Hutchinson, and M. Vidyasagar, *Robot Modeling and Control*. ISBN 81-265-0766-7, 2006.

[100] W. M. Silver, "On the equivalence of lagrangian and newton-euler dynamics for manipulators," *International Journal of Robotic Research*, vol. 1, no. 2, pp. 60–70, june 1982.

[101] S. Toz, M. Kucuk, "A comparative study for computational cost of fundamental robot manipulators," *Industrial Technology, IEEE International Conference on*, vol. 1, pp. 289–293, 2011.

[102] J. J.Craig, *Introduction to Robotics: Mechanics and Control*, 3rd ed. Prentice Hall, 2004.

[103] W. Khalil and D. Creusot, "Symoro+: A system for the symbolic modelling of robots," *Robotica*, vol. 15, pp. 153–161, 1997.

[104] A. D. Luca and L. Ferrajoli, "A modified Newton-Euler method for dynamic computations in robot fault detection and control," *Robotics and Automation, IEEE International Conference on*, vol. 1, pp. 3359 – 3364, juillet 2009.

[105] T. Tjahjowidodo, F. Al-Bender, and H. V. Brussel, "Model Based Friction Compensation in a DC Motor," *Benelux Meeting on Systems and Control*, 2005.

[106] V. Lampaert, F. Al-Bender, and J. Swevers, "A generalized maxwell-slip friction model appropriate for control purposes," *Physics and Control, IEEE International Conference on*, vol. 4, pp. 1170 – 1177, 2003.

[107] P. Hamon, M. Gautier, and P. Garrec, "Dynamic Identification of Robots with a Dry Friction Model Depending on Load and Velocity," *Intelligent Robots and Systems, IEEE International Conference on*, 2010.

[108] P. Hamon, M. Gautier, , and P. Garrec, "New Dry Friction Model with Load- and Velocity-Dependence and Dynamic Identification of Multi-DOF Robots," *Robotics and Automation, IEEE International Conference on*, pp. 1077–1084, 2011.

[109] P. Hamon, "Modélisation et identification dynamiques des robots avec un modèle de frottement sec fonction de la charge et de la vitesse," Ph.D. dissertation, Université de Nantes, 2011.

[110] "http://www.robodrive.de/produkte/," october 2012.

[111] "http://www.biss-interface.com," november 2012.

[112] ESA, "Ecss-e-st-50-12c," European Space Agency, Tech. Rep., 2008.

[113] G. Blankenstein, R. Ortega, and A. J. van der Schaft, "The matching conditions of controlled lagrangians and interconnection and damping assignment passivity based control," *International Journal of Control*, vol. 75, no. 9, pp. 645–665, 2002.

[114] L. Holtz, J. Springob, "Identification and compensation of torque ripple in high-precision permanent magnet motor drives," *Industrial Electronics, IEEE Transactions on*, vol. 43, no. 2, pp. 309–320, April 1996.

[115] J. M. J P Hauschild, G Heppler, "Friction compensation of harmonic drive actuators," *Design*, vol. V, pp. 683–692, 2004.

[116] K. Hollander, T. Sugar, and D. Herring, "Adjustable robotic tendon using a jack spring," *Rehabilitation Robotics, International Conference on*, vol. 1, pp. 113–118, 2005.

[117] "http://www.ichaus.de/keyword/encoder," august 2012.

[118] "http://www.zwick.fr/fr/produits/machine-de-traction-compression-cyclage-statique/machine-de-traction-mono-colonne-jusqua-5-kn/machine-dessai-mono-colonne-precision-line.html," october 2012.

[119] T. IMAEDA, A. KAI-NAN, and W. P. COONEY, *Biomechanics of the thumb*. Saunders, 1992.

[120] K. Kuczynski, "The thumb and the saddle," p. 120, 1975.

[121] F. Adrian E.Flatt MD, "Ours thumbs," in *BUMC Proceeding*, vol. 15, 2002, pp. 380–387.

[122] M. Chalon, T. Wimböck, M. Grebenstein, and G. Hirzinger, "The thumb: Guidelines for a robotic design," *Robotics and Automation, IEEE International Conference on*, 2010.

[123] T. Wimböck, J. Reinecke, and M. Chalon, "Derivation and verification of synergy coordinates for the DLR Hand Arm System," *CASE*, vol. 1, p. 112, 2012.

[124] H. Kobayashi and R. Ozawa, "Adaptive neural network control of tendon driven mechanisms with elastic tendons," *Automatica*, vol. 39, no. 9, pp. 1509–1519, 2003.

[125] J. W. Demmel, *Applied Numerical Linear Algebra*. SIAM, 1997.

[126] H. Berghuis and H. Nijmeijer, "A passivity approach to controller-observer design for robots," *Robotics and Automation, IEEE Transactions on*, vol. 9, pp. 740 – 754, 1993.

[127] A. D. Luca, A. Albu-Schäffer, S. Haddadin, and G. Hirzinger, "Collision Detection and Safe Reaction with the DLR-III Lightweight Manipulator Arm," *Intelligent Robots and Systems, IEEE International Conference on*, vol. 1, pp. 1623–1630, 2006.

[128] P. A. Fuhrmann, "Observer theory," *Linear Algebra Application*, vol. 428, pp. 44–136, 2008.

[129] R. Goussault, "Friction reduction and compensation of an anthropomorphic tendon driven finger with adjustable stiffness," Master's thesis, Ecole des Mines de Paris, 2012.

[130] C. Ott, *Cartesian Impedance Control of Redundant and Flexible-Joint Robots*. Springer Tracts in Advanced Robotics (STAR), 2008, vol. 49.

[131] R. M. Murray and K. J. Astreom, "Feedback systems, an introduction for scientists and engineers," PRINCETON UNIVERSITY PRESSPRINCETON AND OXFORD, Tech. Rep., 2009.

[132] J. Medanic, "Design of nonlinear controls using structured representations," *Decision and Control, IEEE Conference on*, vol. 4, pp. 4163–4168, 2003.

[133] C. J. Taylor, A. Chotai, and P. C. Young, "Nonlinear pole assignment control of state dependent parameter models with time delays." *Control, UKACC International Conference on,*, 2008.

[134] H. K. Khalil, *Nonlinear Systems*, 2nd ed. Prentice Hall, 1996.

[135] V. Utkin, "Sliding mode control design principles and applications to electric drives," *Industrial Electronics, IEEE Transactions on*, vol. 40, no. 1, pp. 23 –36, feb 1993.

[136] G. Niemeyer, N. Diolaiti, and N. Tanner, "Wave haptics: Encoderless virtual stiffnesses," in *International Symposium on Robotics Research*, 2005.

[137] J. Artigas, C. Preusche, and G. Hirzinger, "Wave variables based bilateral control with a time delay model for space robot applications," in *Robotik*, 2004.

[138] N. Tanner and G. Niemeyer, "Improving perception in time-delayed telerobotics," *Robotic Research, International Journal of*, vol. 24, no. 8, pp. 631–644, 2005.

Modélisation et contrôle d'une main anthropomorphe actionnée par des tendons antagonistes

Résumé : Un des freins majeurs au développement de la manipulation d'objet avec une main robotisée est sans aucun doute leur fragilité. C'est l'une des raisons pour laquelle un système bras-main anthropomorphe, extrêmement robuste, est développé au centre de robotique et de mécatronique de DLR. Le système est unique à la fois par sa complexité, utilisant 52 moteurs et plus de 200 capteurs, ainsi que par ses capacités dynamiques. En effet, ce nouveau système a la particularité d'être mécaniquement flexible ce qui offre la possibilité de stocker de l'énergie à court terme et remplit ainsi deux fonctions essentielles pour un robot humanoïde : les impacts sont filtrés et les performances dynamiques sont augmentées.

Dans cette thèse, on se concentre plus particulièrement sur la main. Elle dispose de 19 degrés de liberté dont chacun est actionné par deux tendons flexibles antagonistes. La rigidité des tendons étant non linéaire il est possible, tout comme peut le faire l'être humain, de co-contracter les «muscles» et donc d'ajuster la rigidité des doigts afin de s'adapter au mieux aux tâches à effectuer. Cependant, cette flexibilité entraine de nouveau défis de modélisation et de contrôle. L'état de l'art se concentre majoritairement sur le problème de la répartition des forces internes ou du contrôle d'articulation flexible mais peu de travaux considèrent les deux problèmes simultanément.

Le travail présenté dans la première partie de la thèse se concentre sur la modélisation de la main et du poignet. Les problématiques spécifiques aux systèmes actionnés par des tendons, tels que les matrices de couplage et l'estimation du déplacement des articulations à partir du déplacement des tendons, sont étudiées. La seconde partie se concentre sur le contrôle d'articulations actionnées par des tendons flexibles antagonistes. Les problèmes de distribution des forces internes et de correction de la rigidité perçue par l'utilisateur sont présentés. Des approches de contrôle linéaire et non linéaire sont utilisées et des expériences sont réalisées pour comparer ces approches. En particulier, il est montré que le «backstepping», une méthode de contrôle non linéaire peut être utilisée et permet d'obtenir le comportement d'impédance souhaité tout en garantissant la stabilité en boucle fermée.

Mots clés : Modélisation robotique, main anthropomorphique, système actionné par tendons, contrôle d'articulation flexible, contrôle non linéaire, contrôle appliqué.

Modeling and control of an antagonistically actuated tendon driven anthropomorphic hand

Abstract: One of the major limitations of object manipulation with a robotic hand is the fragility of the hardware. This is one of the motivations for developing the new anthropomorphic and extremely robust Hand Arm System at the robotics and mecatronics center of DLR. The system is unique in terms of complexity, with 52 motors and more than 200 sensors, and also in terms of dynamics. Indeed, the system is mechanically compliant, thus offers the possibility to store and release energy, thereby providing two essential functions: The impacts are filtered and the dynamics are enhanced.

This thesis focuses on the hand. It has 19 degrees of freedom, each being actuated by two flexible antagonistic tendons. Because the stiffnes of the tendons is not linear, it is possible to adjust the mechanical stiffness of the joints, similar to the co-contraction of human muscles, in order to adapt to a task. However, the stiffness adjustability rises new challenges in modeling and control. The state of the art usually focuses on the problems of tendon-driven systems or flexible joint robots but seldomly both simultaneously.

In the first part, the modeling of the hand and the wrist is conducted. Several problems specific to tendon-driven systems are presented, such as the coupling matrices and the joint position estimation based on the tendon displacement. The second part focuses on the control of a single joint actuated by two flexible tendons. The distribution of the tendon forces and the correction of the effective stiffness are reported. Linear and nonlinear approaches are used and multiple experiments are realised to compare them. The major result is that the backstepping, a nonlinear control method, can be used and provides the desired impedance behavior while guaranting closed-loop stability.

Keywords: Robotic modeling, anthropomorphic hand, tendon-driven system, flexible joint control, nonlinear control, applied control.

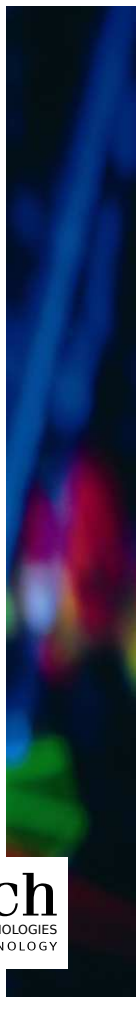

MINES ParisTech

ParisTech
INSTITUT DES SCIENCES ET TECHNOLOGIES
PARIS INSTITUTE OF TECHNOLOGY